

SEEK AND YE SHALL FIND:  
MACHINE LEARNING AND SEARCHES FOR NEW PHYSICS

by

LAYNE N. BRADSHAW

A DISSERTATION

Presented to the Department of Physics  
and the Division of Graduate Studies of the University of Oregon  
in partial fulfillment of the requirements  
for the degree of  
Doctor of Philosophy

June 2023

## DISSERTATION APPROVAL PAGE

Student: Layne N. Bradshaw

Title: Seek and Ye Shall Find:  
Machine Learning and Searches for New Physics

This dissertation has been accepted and approved in partial fulfillment of the requirements for the Doctor of Philosophy degree in the Department of Physics by:

Tien-Tien Yu	Chair
Spencer Chang	Advisor
Laura Jeanty	Core Member
Boris Botvinnik	Institutional Representative

and

Krista Chronister	Vice Provost of Graduate Studies
-------------------	----------------------------------

Original approval signatures are on file with the University of Oregon Division of Graduate Studies.

Degree awarded June 2023

© 2023 Layne N. Bradshaw  
This work is licensed under a Creative Commons  
**Attribution-NonCommercial-NoDerivatives 4.0 International License.**



## DISSERTATION ABSTRACT

Layne N. Bradshaw

Doctor of Philosophy

Department of Physics

June 2023

Title: Seek and Ye Shall Find:  
Machine Learning and Searches for New Physics

The discovery of the Higgs boson confirmed that the Standard Model is the correct description of nature below some high energy scale. However, we know the Standard Model is incomplete and have yet to find significant deviations from it. Without well-motivated directions to guide new physics searches, we need to reconsider where and how we search. We explore this in 3 parts here.

We start by identifying 3- and 4-point on-shell amplitudes involving top quarks that are most susceptible to new physics. Using the Hilbert series as a cross-check, we are able to create an independent set of amplitudes for four-fermion and two-fermion, two-boson interactions. After translating these amplitudes to the lowest-dimension SMEFT-like operator, we use perturbative unitarity to place an upper bound on the coupling, under the assumption that the new physics appears around the TeV scale. With this, we find a number of top quark decay modes that could be probed at the HL-LHC.

Next, we compare the efficacy of a number of methods to decorrelate the output of a machine learned classifier from the invariant jet mass. This decorrelation preserves the background dominated sidebands in the invariant mass distribution as tighter cuts

are made on the network’s output. This increases the potential discovery significance of the new physics. We compare 4 techniques which broadly fall into one of 2 categories—data augmentation or training augmentation. We find that the simpler and computationally cheaper data augmentation techniques perform comparably to the training augmentation techniques across a variety of qualitatively different signals.

Finally, we turn to machine learning based anomaly detection, with the aim of explaining the physics learned by an image-based autoencoder. Adapting techniques from the literature, we make use of two strategies to mimic the autoencoder. Despite fundamental differences, we find that both techniques, when compared to the autoencoder, order background events similarly and perform comparably as anomaly detectors across a wide swath of signals. The mimicker networks independently use the same high-level observables, giving us confidence that these features are indeed those learned by the autoencoder.

This dissertation includes previously published co-authored material.

## CURRICULUM VITAE

NAME OF AUTHOR: Layne N. Bradshaw

GRADUATE AND UNDERGRADUATE SCHOOLS ATTENDED:

University of Oregon, Eugene, Oregon, USA  
Arizona State University, Tempe, AZ, USA

DEGREES AWARDED:

Doctor of Philosophy in Physics, 2023, University of Oregon  
Master of Science in Physics, 2021, University of Oregon  
Bachelor of Science, 2017, Arizona State University

AREAS OF SPECIAL INTEREST:

Interpretable Machine Learning, Machine Learning in Particle Physics, Physics  
Beyond the Standard Model

PROFESSIONAL EXPERIENCE:

Graduate Research Assistant, University of Oregon, 2018-2023  
Graduate Teaching Fellow, University of Oregon, 2017-2023

GRANTS, AWARDS AND HONORS:

Graduate Teaching Fellowship, University of Oregon, 2017-2023  
New American University Scholarship—President's Award, Arizona State  
University, 2013-2017

PUBLICATIONS:

- L. Bradshaw and S. Chang, “Primary Observables for Top Quark Collider Signals,” [arXiv:2304.06063 \[hep-ph\]](#) (Submitted for publication at *Physical Review D*)
- L. Bradshaw, S. Chang, and B. Ostdiek, “Creating Simple, Interpretable Anomaly Detectors for New Physics in Jet Substructure,” *Phys. Rev. D* **106** (2022) no. 3, 035014, [arXiv:2203.01342 \[hep-ph\]](#)
- L. Bradshaw, R. K. Mishra, A. Mitridate, and B. Ostdiek, “Mass Agnostic Jet Taggers,” *SciPost Phys.* **8** (2020) no. 1, 011, [arXiv:1902.05556 \[hep-ph\]](#)

## ACKNOWLEDGEMENTS

It would only be right to begin by thanking my mother, Lori Bradshaw, for your unconditional love and support. Thank you for encouraging me to always go after my dreams, even as they took me far from home. I truly could not have done this without you. Thank you to Kaitlyne & Milo Nixon as well as Lana, Loren, & Rolan McRee for traveling all the way out to Eugene to celebrate my defense with me. I love you all more than I can put into words, and your support these past six years has meant the world to me (and sorry for not saying thank you at the end of the presentation).

Thank you to my advisor, Spencer Chang, for all of your guidance over the years. Whether it was making sense of a result or navigating the stress and anxiety of the pandemic, I will always appreciate you meeting me where I was at.

Thank you to Bryan Ostdiek for taking a bright-eyed, first-year grad student under your wing and showing me how physics research should be done.

To everyone in the High Energy Theory group here at Oregon—Cristien Arzate, Pouya Asadi, Autsin Batz, Tom Bouley, Spencer Chang, Tim Cohen, Joel Doss, Haidar Essieli, Graham Kribs, Ben Lillard, Xiaochuan Lu, Chester Mantel, Bryan Ostdiek, Aria Radick, Tom Schwemberger, Dave Soper, Anna-Maria Taki, Tom Tong, and Tien-Tien Yu—thank you for helping me be a better physicist, researcher, and communicator.

Thank you to Ian Kenney for your friendship over the past eight years. I still look back on those late nights working through E&M over some espresso and a Franziskaner (or two) fondly.



To all of the fantastic people I've had the privilege to meet and befriend while doing physics—Paul Abers, Trevor Brunnenmeyer, Joel Doss, Marija Glisic, Ryan Heilman, Rachael Klaiss, Daniel Moore, Brandon Sumner, Stephanie Urbano, Brian Veit, and so many others—thank you for all of the insightful and inane conversations at the wee hours of the morning and way too late at night.

Thank you to Joseph Comfort and Richard Kirian at Arizona State University for taking a chance on me, and giving me my first exposure to physics outside the context of a lecture hall.

Thank you to all of my friends from outside physics—Luke Bennett, Eric Brown-Malone, Brianna Griffith, Ashley Mas, Kelly McCormish, Curtis Spence, and everyone else—for all of the laughs and for accepting me as I am.

Finally, thank you to my wonderful partner Katie Desautels. Thanks for putting up with all of the late nights, practice talks, and anxious pacing over the past year. You've made what would have otherwise been an unbearable year one that I'll look back on fondly.

For my mother, Lori, and my late father, Ross.

There are no words to thank you for all of your love and support.

I hope I've made you proud.

## TABLE OF CONTENTS

Chapter	Page
I. INTRODUCTION . . . . .	1
1.1. Primary Observables for Top Quark Collider Signals . . . . .	5
1.2. Mass Agnostic Jet Taggers . . . . .	6
1.3. Creating Simple, Interpretable Anomaly Detectors for New Physics in Jet Substructure . . . . .	9
1.4. Outline . . . . .	11
II. PRIMARY OBSERVABLES FOR TOP QUARK COLLIDER SIGNALS	13
2.1. Finding Independent Amplitudes/Couplings for Top Quarks . . .	14
2.2. Hilbert Series . . . . .	17
2.3. Phenomenology . . . . .	20
2.3.1. Unitarity . . . . .	20
2.3.2. Top Quark Decays . . . . .	21
2.4. Independent Amplitudes for Top Quark Physics . . . . .	24
2.4.1. $ffVV$ Amplitudes . . . . .	24
2.4.2. $ffff$ Amplitudes . . . . .	34
2.5. Interesting Top Decay Amplitudes for the HL-LHC . . . . .	42
III. MASS AGNOSTIC JET TAGGERS . . . . .	47
3.1. Simulation details . . . . .	48
3.2. Classification of Methods . . . . .	51
3.2.1. Classification without decorrelation . . . . .	52

Chapter	Page
3.2.2. Decorrelation based on data augmentation . . . . .	58
3.2.2.1. Analytic decorrelation . . . . .	59
3.2.2.2. Planing . . . . .	60
3.2.2.3. PCA . . . . .	63
3.2.3. Decorrelation based on training augmentation . . . . .	65
3.2.3.1. uBoost . . . . .	65
3.2.3.2. Adversarial . . . . .	67
3.3. Results . . . . .	71
3.3.1. Augmented training . . . . .	73
3.3.2. Augmented data . . . . .	77
3.3.3. Comparison . . . . .	81
 IV. CREATING SIMPLE, INTERPRETABLE ANOMALY DETECTORS FOR NEW PHYSICS IN JET SUBSTRUCTURE . . . . .	 84
4.1. Datasets . . . . .	85
4.2. Methodology . . . . .	86
4.2.1. Creating a Target Anomaly Detector with a Convolutional Autoencoder . . . . .	87
4.2.2. Mimicking the Target Anomaly Detector . . . . .	91
4.2.2.1. High Level Observables . . . . .	92
4.2.2.2. Decision Ordering . . . . .	93
4.2.2.3. Paired Neural Network . . . . .	96
4.2.2.4. High-Level Neural Network . . . . .	98
4.3. Results . . . . .	99
4.3.1. Background Decision Ordering . . . . .	99
4.3.2. Anomaly Detection . . . . .	102

Chapter	Page
4.3.3. Using Only Prime EFPs . . . . .	107
4.3.4. Comparison with Isolation Forests . . . . .	108
4.4. Conclusion . . . . .	110
V. CONCLUSIONS . . . . .	112
5.1. Primary Observables for Top Quark Collider Signals . . . . .	112
5.2. Mass Agnostic Jet Taggers . . . . .	113
5.3. Creating Simple, Interpretable Anomaly Detectors for New Physics in Jet Substructure . . . . .	116
APPENDICES	
A. SUPPLEMENTAL MATERIAL FOR MASS AGNOSTIC JET TAGGERS	118
A.1. Adversary decorrelation parameter . . . . .	118
A.2. Comparison of histogram distances . . . . .	120
A.3. Histogram Sculpting Comparison . . . . .	120
B. SUPPLEMENTAL MATERIAL FOR CREATING SIMPLE, INTERPRETABLE ANOMALY DETECTORS FOR NEW PHYSICS IN JET SUBSTRUCTURE . . . . .	125
B.1. Simulation Details . . . . .	125
B.2. Network Training Hyperparameters . . . . .	125
REFERENCES CITED . . . . .	127

## LIST OF FIGURES

Figure	Page
1.	Distributions of the transverse momentum of the hardest jet. . . . . 51
2.	The architecture of a BDT. We take the BDT to be made of 150 DTs, with a max depth of 4. The input to the BDT are the variables that span the 5-body jet phase space, see Eq. (3.4). The indicated parameters $\alpha_i$ represent the weight associated with the particular DT. . . . . 54
3.	Many of the methods explored in this paper use a neural network classifier. For consistency, we always use a network with three hidden layers, each of which has 50 nodes and uses the ReLu activation function. The output is a single node with a sigmoid activation function. Our input data are the 11 $\tau_N^{(\beta)}$ variables of 5-body jet phase space shown in Eq. (3.4). . . . . 56
4.	The left panel shows the ROC curves for three traditional methods, two based on machine learning, to classify a 2-prong signal jet from a QCD jet. The machine learning based methods achieve an area significantly higher than the single variable $\tau_{21}$ based classifier. The right panels show the <i>background only</i> distributions for successively tighter cuts in the solid lines: signal efficiency of 1.0 (black), 0.95 (green), 0.9 (red), 0.8 (purple), 0.7 (brown), 0.6 (pink) and 0.5 (yellow). The signal with no cuts is shown in the filled-in, grey distribution. The only background events which pass the cuts end up having masses similar to that of the signal, even though the machine learning models do not have access to the mass. . . . . 58
5.	The left panel shows the ROC curves for the data augmented neural network methods of PCA and planing as well as the single variable DDT. The network trained on PCA-rescaled data is the best classifier, followed by the network trained on planed data. Both MV decorrelation techniques result in better classification than the single variable $\tau_{21}^{\text{DDT}}$ based classification. The right panels show the <i>background only</i> distributions for successively tighter thresholds for the DDT, Planed, and PCA classifiers: signal efficiency of 1.0 (black), 0.95 (green), 0.9 (red), 0.8 (purple), 0.7 (brown), 0.6 (pink) and 0.5 (yellow). For context, the 2-pronged signal distribution is shown as grey filled-in region. All three methods reduce the background sculpting when compared to their Fig. 4 counterparts. A full side-by-side comparison for 2, 3, and 4 prong signals is shown in App. A.3. . . . . 60
6.	The upper and lower panels show distributions before and after planing away the jet mass, respectively. The left panels show the jet mass distribution for the 2-pronged signal and QCD background. By design, both distributions are (nearly) identical, and uniform across the entire mass range after planing. The center panels show $\tau_1^{(1)}$ , one of the input variables for the classifiers. Before planing, this variable has discriminating power, but that was correlated with the jet mass and got removed by the planing process. The right panels show $\tau_2^{(1)}$ , which has more separation between signal and background <i>after</i> planing. . . . . 62

7. Scatterplot of two benchmark  $\tau$  variables for QCD events in three different mass windows. The left panel shows the original variables, before any kind of preprocessing. The events from different mass bins are well separated. The center panel shows the same events after removing the mean and setting the variance of each variable in each bin to unity. The different mass bins now have the same range, but the 2D correlations are still distinct. In the right panel, the events have been standardized and PCA transformed on a linearly independent basis. The different mass ranges are now hard to distinguish. . . . . 65
8. The network architecture used in the uBoost algorithm. Each BDT has the same layout as those in Fig. 2, and is tasked with keeping the background uniform at a given target signal efficiency. We use 20 BDTs to cover the entire efficiency range, and results are interpolated between target efficiencies to keep the background uniform over the whole efficiency range. The Gini index is used to measure the quality of a split, and the best split is taken when creating new branches. . . . . 67
9. The left panel shows the ROC curves for the adversarially trained neural network and uBoost, along with the results of the base neural network and  $\tau_{21}$ , for comparison. The adversarial results use  $\lambda = 50$ , and the uBoost results use  $\beta_u = 1$ . The right panels show the *background only* distributions as successively tighter cuts are made on the output of these classifiers: signal efficiency of 1.0 (black), 0.95 (green), 0.9 (red), 0.8 (purple), 0.7 (brown), 0.6 (pink) and 0.5 (yellow). The full 2-pronged signal is shown in the filled-in grey distribution for context. Both these methods are able to preserve the background shape well, with only a marginal decrease in performance, but take a factor of 10 to 100 more time to train. Compared to their MV counterparts in the upper panels, it is clear that the training augmentation based approaches significantly reduce the extent of the background sculpting. A full side-by-side comparison for 2, 3, and 4 prong signals is shown in App. A.3. 68
10. The setup of our adversarially trained neural network. The classifier has the same hyperparameters as in Fig. 3. The output of the classifier becomes the input of the adversary, which attempts to predict which bin of the jet mass the QCD events came from. We use tanh activation for the hidden layers of the adversary, and softmax activation for the final layer, with 10 outputs. The multi-class cross entropy loss function is used for the adversary. . . . . 69
11. ROC curves for the 2-, 3-, and 4-prong signal jets versus QCD background for the methods which augment the training method to decorrelate the jet mass. The solid, dashed, and dotted curves show results for neural networks, boosted decision trees, and single variable analysis, respectively. The light blue curves are for the traditional method benchmarks. The purple and dark-blue lines denote the adversarially trained network and uBoost decision tree. For the 3- and 4-prong cases, uBoost cannot classify as well as the adversarially trained neural networks, but still does much better than using a single variable,  $\tau_3/\tau_2$  and  $\tau_4/\tau_3$ , respectively 74
12. The Bhattacharyya distance for the QCD background distributions compared to the original distributions. The distance is defined in Eq. (3.9), and a larger distance represents more sculpting—lower on the plot is better. The upper and lower rows plot the distance as a function of signal efficiency or background rejection, respectively.  $\tau_{21}^{\text{DDT}}$  produces the smallest distances for fixed signal efficiency, but does not generalize to higher-prong jets. The adversarially trained network yields a close approximation and generalizes to more prongs. uBoost falls between the original methods and the adversarially trained network, but takes a factor of 30 less time to train. . . . . 75

13. ROC curves for the 2-, 3-, and 4-prong signal jets versus QCD background for the methods which augment the data to decorrelate the jet mass rather than augment the training. The dashed and solid lines show the gradient boosted decision trees (BDT) and neural networks (NN), respectively. The blue, red, and green curves are for the data which has not been altered, data which uses the PCA rescaling, and data which has the jet mass planed away. The dotted lines show the results using a single combination of the N-subjettiness variables. Generally the BDTs have slightly worse background rejection than the NNs. Similarly, the PCA rescaling based methods tend to be between the unaltered methods and the planing methods, which are better than the single variable analyses. . . . . 78
14. The Bhattacharyya distance for the QCD background distributions compared to the original distributions. The distance is defined in Eq. (3.9), and a larger distance represents more sculpting—lower on the plot is better. The neural networks tend to sculpt the distributions worse than the BDT, regardless of the data. Both the PCA rotations and Planing the jet mass result in smaller distances than the classifiers trained on the original data. . . . . 80
15. A comparison of all the MV based methods to decorrelate the jet mass from the classifier output. The shown PCA and Planed results are for NN architecture. The analytical  $\tau_{21}^{\text{DDT}}$  method sculpts the least for moderate background rejection, but for larger values does not do as good as the adversarially trained neural network. The network trained on data augmented by planing the jet mass do almost as good as the adversarially trained network, with uBoost and the PCA based networks showing slightly more sculpting. With more prongs, planing and adversaries are nearly identical to each other while PCA and uBoost are very similar to each other. 82
16. The average jet image for the background, 80 GeV  $W$ , 174 GeV top, and 80 GeV Higgs. Note that the Higgs bosons are pair produced from the decay of a heavier Higgs, leading to potentially 4 prongs in the large-radius jet. . . . . 87
17. The architecture of the convolutional autoencoder (AE). The AE consists of two separate networks, an encoder that compresses the original image down to a smaller latent space, and a decoder tasked with recreating the original image from the latent space representation. . . . . 89
18. The AE's performance as an anomaly detector on 3 of the anomalous signals, the 80 GeV  $W$ , the 174 GeV top, and the 80 GeV Higgs. Note that the Higgs bosons are pair produced from the decay of a heavier Higgs, leading to potentially 4 prongs in the large-radius jet. The left panel shows the normalized distribution of the log of the AE's anomaly score for the background and each of the signals. The right panel shows the ROC curves for each signal. . . . . 90
19. The architecture of the Paired Neural Network. The interior model consists of 4 hidden layers each with 50 nodes and using the ELU activation function. The interior model outputs a single node for each input and uses the ReLU activation function. The final output of the model is a single node which is the difference between the two interior model outputs and uses a sigmoid activation function. Our input data are the jet's mass,  $p_T$ , and up to 14 EFPs. . . . . 97
20. The architecture of the High- Level Neural Network. This network consists of four hidden layers, with each having 50 nodes and using the ELU activation function. The network output is a single node. Like the PNN, our input data are the jet's mass,  $p_T$ , and up to 14 EFPs. . . . . 98



21. The ADOs for each PNN and HLN. The center line shows the ADO of the model that was used to select the EFPs. The shaded bands show the maximum and minimum ADO values obtained when recalculating the ADO an additional 50 times, using a different set of pairs of events each time. The  $x$ -axis denotes the iteration step of the iterative process. See Table 17 for the multigraph and mathematical representations of the selected EFPs and the iteration step at which they were added. The blue ‘+’ (orange ‘×’) shows the ADO of a PNN (HLN) trained on only the 5 prime EFPs picked out by each method (see Eq. 4.12). The ADO of each model trained on  $m, p_T$ , and all of the  $d \leq 5$  EFPs is the same to 3 significant digits, and is plotted as a single dashed line. . . . . 100
22. The performance of the AE, PNN<sub>14</sub>, and HLN<sub>14</sub> as anomaly detectors on the 80 GeV  $W$ , 174 GeV top, and 80 GeV Higgs. Note that the Higgs bosons are pair produced from the decay of a heavier Higgs, leading to potentially 4 prongs in the large-radius jet. The left panels show the normalized distribution of each method’s respective anomaly score for the background and each signal. The right panel shows the ROC curves for each signal, with the solid lines being the ROC curves for the AE, the dashed lines for HLN<sub>14</sub>, and the dashed-dot lines for PNN<sub>14</sub>. . . . . 103
23. AUCs for the PNN and HLN at each iteration for each of the eight signals reserved for testing. Note that the Higgs bosons are pair produced from the decay of a heavier Higgs, leading to potentially 4 prongs in the large-radius jet. The solid center lines are the AUC of the model used in the iterative process, the shaded bands show the maximum and minimum AUCs from retraining each network an additional 10 times. The dashed black line corresponds to the AE’s AUC. The dotted lines correspond to the isolation forest anomaly detectors and the blue ‘+’ (orange ‘×’) is the PNN(HLN) trained using mass,  $p_T$ , and the five prime factors in Eqn. 4.12. . . . . 104
- A.24. The top row shows the ROC curves for all of the adversarially-trained neural networks tasked with distinguishing the 2-, 3-, and 4-prong signal jets from the QCD background. Lighter shades correspond to increasingly larger values of  $\lambda$ . Larger values of  $\lambda$  put an increased emphasis on making the network output less dependent on the mass, at the cost of worse classification. The middle row shows how the Bhattacharyya distance for the QCD background changes as tighter cuts are made on the network output. As expected, higher values of  $\lambda$  lead to less sculpting than lower values of  $\lambda$ . The bottom row shows a parametric plot of the Bhattacharyya distance for the QCD background versus the background rejection. The adversarially-trained networks are all able to achieve similarly large background rejections, but networks using higher values of  $\lambda$  are able to reject much of the background while preserving the profile of the underlying distribution. All three rows show that the benefits of adversarial training saturate at  $\lambda = 50$ . . . . . 119
- A.25. Comparison of Bhattacharyya distance and Jensen-Shannon distance for 2-, 3-, and 4-pronged signals, as a function of signal efficiency for various decorrelation methods studied in this work. The general trend for both metrics is seen to be the same. . . . . 121
- A.26. Comparison of all decorrelation methods to the benchmarks for the 2-prong signal.  $\tau_N/\tau_{N-1}$  is  $\tau_2/\tau_1$ . 122
- A.27. Comparison of all decorrelation methods to the benchmarks for the 3-prong signal.  $\tau_N/\tau_{N-1}$  is  $\tau_3/\tau_2$ . 123
- A.28. Comparison of all decorrelation methods to the benchmarks for the 4-prong signal.  $\tau_N/\tau_{N-1}$  is  $\tau_4/\tau_3$ . 124

## LIST OF TABLES

Table		Page
1.	Primary 5- and 6-dimension operators for $\bar{q}qW^+W^-$ interactions. As outlined in the text, these operators can be modified to yield the operators for $\bar{q}q'WZ$ interactions. Under the assumption that $\bar{q}$ and $q$ are each other's anti-particles, the operators are Hermitean and have the listed CP properties. If they are not, each of these operators has a Hermitean conjugate, which can be used to create a CP even and a CP odd operator. To simplify the expressions, we use the shorthand $\overleftrightarrow{D}_{\mu\nu} = \overleftrightarrow{D}_\mu \overleftrightarrow{D}_\nu$ , and similarly, $D_{\mu\nu} = D_\mu D_\nu$ . To get the descendant operators, once can add contracted derivatives to get arbitrary Mandelstam factors of $s, t$ .	26
2.	Primary 7- and 8-dimension operators for $\bar{q}qW^+W^-$ interactions, where $\tilde{W}_{\mu\nu} = \frac{1}{2}\epsilon_{\mu\nu\rho\sigma}W^{\rho\sigma}$ . As outlined in the text, these operators can be modified to yield the operators for $\bar{q}q'WZ$ interactions. Under the assumption that $\bar{q}$ and $q$ are each other's anti-particles, the operators are Hermitean and have the listed CP properties. If they are not, each of these operators has a Hermitean conjugate, which can be used to create a CP even and a CP odd operator. To simplify the expressions, we use the shorthand $\overleftrightarrow{D}_{\mu\nu} = \overleftrightarrow{D}_\mu \overleftrightarrow{D}_\nu$ , and similarly, $D_{\mu\nu} = D_\mu D_\nu$ . To get the descendant operators, once can add contracted derivatives to get arbitrary Mandelstam factors of $s, t$ . At dimension 9, $s\mathcal{O}_{26}$ and $s\mathcal{O}_{27}$ become redundant to other operators and thus one only needs their descendants $t^n\mathcal{O}_{26}$ and $t^n\mathcal{O}_{27}$ for an independent set of operators.	27
3.	Primary 5-, 6-, and 7-dimension operators for $\bar{q}qZZ$ interactions. Under the assumption that $\bar{q}$ and $q$ are each other's anti-particles, the operators are Hermitean and have the listed CP properties. If they are not, each of these operators has a Hermitean conjugate, which can be used to create a CP even and a CP odd operator. To simplify the expressions, we use the shorthand $\overleftrightarrow{D}_{\mu\nu} = \overleftrightarrow{D}_\mu \overleftrightarrow{D}_\nu$ , and similarly, $\partial_{\mu\nu} = \partial_\mu \partial_\nu$ . To get the descendant operators, once can add contracted derivatives to get arbitrary Mandelstam factors of $s, (t-u)^2$ .	28
4.	Primary 8-, 9-, and 10-dimension operators for $\bar{q}qZZ$ interactions. Under the assumption that $\bar{q}$ and $q$ are each other's anti-particles, the operators are Hermitean and have the listed CP properties. If they are not, each of these operators has a Hermitean conjugate, which can be used to create a CP even and a CP odd operator. To simplify the expressions, we use the shorthand $\overleftrightarrow{D}_{\mu\nu} = \overleftrightarrow{D}_\mu \overleftrightarrow{D}_\nu$ , and similarly, $\partial_{\mu\nu} = \partial_\mu \partial_\nu$ . To get the descendant operators, once can add contracted derivatives to get arbitrary Mandelstam factors of $s, (t-u)^2$ . At dimension 11, $s\mathcal{O}_{31}$ and $s\mathcal{O}_{32}$ become redundant to other operators. Thus, for these two, we need only their $(t-u)^{2n}\mathcal{O}_{31}$ and $(t-u)^{2n}\mathcal{O}_{32}$ descendants.	29
5.	Primary operators for $\bar{q}qZ\gamma$ interactions. As outlined in the text, these operators can be modified to yield the operators for $\bar{q}qZg, \bar{q}q'W\gamma$ , and $\bar{q}q'Wg$ interactions. Under the assumption that $\bar{q}$ and $q$ are each other's anti-particles, the operators are Hermitean and have the listed CP properties. If they are not, each of these operators has a Hermitean conjugate, which can be used to create a CP even and a CP odd operator. To simplify the expressions, we use the shorthand $\overleftrightarrow{D}_{\mu\nu} = \overleftrightarrow{D}_\mu \overleftrightarrow{D}_\nu$ , and similarly, $D_{\mu\nu} = D_\mu D_\nu$ . To get the descendant operators, once can add contracted derivatives to get arbitrary Mandelstam factors of $s, t$ . At dimension 9, $s\mathcal{O}_7$ and $s\mathcal{O}_8$ become redundant to other operators. For these two, one only needs their $t^n\mathcal{O}_7$ and $t^n\mathcal{O}_8$ descendants.	31

6. Primary operators for  $\bar{q}qg\gamma$  interactions. Under the assumption that  $\bar{q}$  and  $q$  are each other's anti-particles, the operators are Hermitean and have the listed CP properties. If they are not, each of these operators has a Hermitean conjugate, which can be used to create a CP even and a CP odd operator. To simplify the expressions, we use the shorthand  $\overleftrightarrow{D}_{\mu\nu} = \overleftrightarrow{D}_\mu \overleftrightarrow{D}_\nu$ . To get the descendant operators, one can add contracted derivatives to get arbitrary Mandelstam factors of  $s, t$ . At dimension 9,  $s\mathcal{O}_5$  and  $s\mathcal{O}_6$  become redundant to other operators. For these two, one only needs their  $t^n\mathcal{O}_5$  and  $t^n\mathcal{O}_6$  descendants. . . . . 32
7. Primary operators for  $\bar{q}q\gamma\gamma$  interactions. Under the assumption that  $\bar{q}$  and  $q$  are each other's anti-particles, the operators are Hermitean and have the listed CP properties. If they are not, each of these operators has a Hermitean conjugate, which can be used to create a CP even and a CP odd operator. To simplify the expressions, we use the shorthand  $\overleftrightarrow{D}_{\mu\nu} = \overleftrightarrow{D}_\mu \overleftrightarrow{D}_\nu$ , and similarly,  $\partial_{\mu\nu} = \partial_\mu \partial_\nu$ . To get the descendant operators, one can add contracted derivatives to get arbitrary Mandelstam factors of  $s, (t-u)^2$ . At dimension 11,  $s\mathcal{O}_7$  and  $s\mathcal{O}_8$  become redundant to other operators. For these two, one only needs their  $(t-u)^{2n}\mathcal{O}_7$  and  $(t-u)^{2n}\mathcal{O}_8$  descendants. . . . . 33
8. Primary 7-, 8-, and 9-dimension operators for  $\bar{q}qgg$  interactions. There are three allowed  $SU(3)$  contractions, 2 symmetric ones— $\delta_{AB}$  and  $d_{ABC}$ —and one antisymmetric one— $f_{ABC}$ . For example,  $\mathcal{O}_1^{\bar{q}qgg} = (\bar{q}\delta_{AB}q)(G^{A\mu\nu}G_{\mu\nu}^B)$ ,  $\mathcal{O}_2^{\bar{q}qgg} = d_{ABC}(\bar{q}T^A q)(G^{B\mu\nu}G_{\mu\nu}^C)$ , and  $\mathcal{O}_9^{\bar{q}qgg} = f_{ABC}(\bar{q}T^A\sigma_{\mu\nu}q)(G^{B\mu\rho}G_{\rho\nu}^C)$ . Under the assumption that  $\bar{q}$  and  $q$  are each other's anti-particles, the operators are Hermitean and have the listed CP properties. If they are not, each of these operators has a Hermitean conjugate, which can be used to create a CP even and a CP odd operator. To simplify the expressions, we use the shorthand  $\overleftrightarrow{D}_{\mu\nu} = \overleftrightarrow{D}_\mu \overleftrightarrow{D}_\nu$ . To get the descendant operators, one can add contracted derivatives to get arbitrary Mandelstam factors of  $s, (t-u)^2$ . At dimension 9,  $s\mathcal{O}_9$  and  $s\mathcal{O}_{10}$  become redundant to other operators and at dimension 11,  $s\mathcal{O}_{21}$ ,  $s\mathcal{O}_{22}$ ,  $s\mathcal{O}_{23}$  and  $s\mathcal{O}_{24}$  become redundant to other operators. For the  $\mathcal{O}_{9,10,21,22,23,24}$  operators, one only needs descendants with factors of  $(t-u)^2$ . . . . . 35
9. Primary 10- and 11-dimension operators for  $\bar{q}qgg$  interactions. There are three allowed  $SU(3)$  contractions, 2 symmetric ones— $\delta_{AB}$  and  $d_{ABC}$ —and one antisymmetric one— $f_{ABC}$ . Under the assumption that  $\bar{q}$  and  $q$  are each other's anti-particles, the operators are Hermitean and have the listed CP properties. If they are not, each of these operators has a Hermitean conjugate, which can be used to create a CP even and a CP odd operator. To simplify the expressions, we use the shorthand  $\overleftrightarrow{D}_{\mu\nu} = \overleftrightarrow{D}_\mu \overleftrightarrow{D}_\nu$ , and similarly  $D_{\mu\nu} = D_\mu D_\nu$ . To get the descendant operators, one can add contracted derivatives to get arbitrary Mandelstam factors of  $s, (t-u)^2$ . . . . . 36
10. Primary operators for  $\bar{q}q\bar{\ell}\ell$  interactions (As described in the text, these operators can be modified to yield the operators for baryon-lepton interactions  $uu'de$  and  $udd'\nu$ ). Under the assumption the  $\bar{q}, q$  and  $\bar{\ell}, \ell$  are each other's anti-particles, the operators are Hermitean and have the listed CP properties. If they are not, each of these operators has a Hermitean conjugate, which can be used to create a CP even and a CP odd operator. To get the descendant operators, one can add contracted derivatives to get arbitrary Mandelstam factors of  $s, t$ . At dimension 8,  $s\mathcal{O}_9$  and  $s\mathcal{O}_{10}$  become redundant and thus, one only needs to consider  $\mathcal{O}_9$  and  $\mathcal{O}_{10}$  with arbitrary factors of  $t$ . . . . . 37

11. Primary operators for  $uude$  interactions, where  $d^c$  and  $e^c$  are the charge conjugated down-type quark and charged lepton 4-component spinor and  $SU(3)$  indices are contracted with an epsilon tensor (These operators can be modified to yield the operators for  $uddv$  interactions by simply taking  $u \rightarrow d, \bar{d}^c \rightarrow \bar{u}^c, e^c \rightarrow \bar{\nu}/\bar{\nu}^c$ ). To simplify the expressions, we've defined a back-forth derivative , which only acts on the  $u$  fields, and similarly  $\overset{u,Q}{\mu}$  which acts on  $u_R$  and  $Q_L$  (but not  $\bar{Q}_L^c$ ). To get the descendant operators, one can add contracted derivatives to get arbitrary Mandelstam factors that respect the exchange symmetry between the two up-type quarks, i.e.  $s, (t-u)^2$ . At dimension 8,  $s\mathcal{O}_3$  and  $s\mathcal{O}_4$  become redundant and thus, one only needs to consider  $\mathcal{O}_3$  and  $\mathcal{O}_4$  descendants with arbitrary factors of  $(t-u)^2$ . . . . . 38
12. Primary operators for  $\bar{q}q\bar{q}'q'$  interactions. There are two allowed  $SU(3)$  contractions, the  $S$  indicates where  $q, q'$  form a symmetric 6 representation under  $SU(3)$ , while  $A$  has the antisymmetric  $\bar{3}$  representation. For example, with explicit indices we have  $\mathcal{O}_{1,S}^{\bar{q}q\bar{q}'q'} = (\bar{q}^{\{\alpha} q_{\{\alpha})(\bar{q}'^{\beta\}} q'_{\beta\})}$  and  $\mathcal{O}_{1,A}^{\bar{q}q\bar{q}'q'} = (\bar{q}^{\{\alpha} q_{[\alpha})(\bar{q}'^{\beta\}} q'_{\beta]})$ , where  $q_{\{\alpha}q_{\beta\}} = q_{\alpha}q_{\beta} + q_{\beta}q_{\alpha}$  and  $q_{[\alpha}q_{\beta]} = q_{\alpha}q_{\beta} - q_{\beta}q_{\alpha}$ . Under the assumption the  $\bar{q}, q$  and  $\bar{q}', q'$  are respectively each other's anti-particles, the operators are Hermitean and have the listed CP properties. If they are not, each of these operators has a Hermitean conjugate, which can be used to create a CP even and a CP odd operator. To get the descendant operators, one can add contracted derivatives to get arbitrary Mandelstam factors of  $s, t$ . At dimension 8,  $s\mathcal{O}_9$  and  $s\mathcal{O}_{10}$  become redundant and thus, one only needs to consider  $\mathcal{O}_9$  and  $\mathcal{O}_{10}$  with arbitrary factors of  $t$ . . . . . 40
13. Primary operators for  $qq\bar{q}\bar{q}$  interactions with two indistinguishable quarks, for the specific case of  $uu\bar{t}\bar{c}$  interactions (Hermitean conjugate yields  $tc\bar{u}\bar{u}$  and down-type interactions can be found by exchange for down quarks.). The  $SU(3)$  contractions are determined by  $S(A)$  to be symmetric (antisymmetric) in the  $uu$  indices. We've defined a back-forth derivative , which only acts on the  $u$  fields, and similarly  $\overset{u,Q_1}{\mu}$  which acts on  $u_R$  and  $Q_{1L}$ . For descendant operators, one adds contracted derivatives to get arbitrary Mandelstam factors that respect the exchange symmetry, i.e.  $s, (t-u)^2$ . At dimension 8,  $s\mathcal{O}_3$  and  $s\mathcal{O}_4$  become redundant, while at dimension 10,  $s\mathcal{O}_{27}$  and  $s\mathcal{O}_{28}$  become redundant. Thus one only needs to consider  $\mathcal{O}_{3,4,27,28}$  descendants with arbitrary factors of  $(t-u)^2$ . . . . . 41
14. Primary operators for  $qq\bar{q}\bar{q}$  interactions with two indistinguishable quarks and two indistinguishable antiquarks, for the specific case of  $uu\bar{t}\bar{t}$  interactions (The Hermitean conjugate yields the  $tt\bar{u}\bar{u}$  interactions and the down-type interactions can be found by exchange for down quarks.). The  $SU(3)$  contractions are determined by  $S$  to be symmetric in the  $uu$  indices and  $A$  to be antisymmetric. To simplify the expressions, we've defined a back-forth derivative , which only acts on the  $u$  fields, and similarly  $\overset{u,Q_1}{\mu}$  which acts on  $u_R$  and  $Q_{1L}$ . To get the descendant operators, one can add contracted derivatives to get arbitrary Mandelstam factors that respect the exchange symmetries, i.e.  $s, (t-u)^2$ . At dimension 8,  $s\mathcal{O}_2$  and  $s\mathcal{O}_3$  become redundant, while at dimension 10,  $s\mathcal{O}_{19}$  and  $s\mathcal{O}_{20}$  become redundant. Thus, one only needs to consider  $\mathcal{O}_2, \mathcal{O}_3, \mathcal{O}_{19}, \mathcal{O}_{20}$  with arbitrary factors of  $(t-u)^2$ . . . . . 43
15. Details of the signal process used in the event generation, along with the choice of parameters and generation level kinematic cuts. . . . . 51

16. The time in seconds to train a classifier on dual E5-2690v4 (28 core) processors. The mean and standard deviation are calculated over 10 independent trainings. The large variance in the neural network times is due to the early stopping condition, leading to a non-fixed number of epochs. Note that the adversarially trained neural network statistics are over sampled once over each of the nine different values of  $\lambda$  due to the long training time. In addition, the adversarial networks used GPU nodes. BDTs are faster to train, but are not as effective classifiers. The Adversarial and uBoost decorrelation methods take much longer than the PCA or Planing methods. . . . . 72

17. The EFP multigraphs and corresponding expressions for each of the EFPs selected by both the HLN and PNN. In the last two columns, we list the iteration step where the PNN or HLN selects the corresponding EFP. 102

18. The background rejection ( $1/\varepsilon_B$ ) at two different fixed signal efficiencies ( $\varepsilon_S$ )—0.5 and 0.1—and the signal efficiency at two different fixed values of the background rejection—10 and 100—for all 8 anomalous signals. We present these metrics for 5 different networks, the AE, PNN<sub>0</sub>, HLN<sub>0</sub>, PNN<sub>14</sub>, and HLN<sub>14</sub>. The values shown in red are those where  $\varepsilon_B > \varepsilon_S$ . . . . . 106

# CHAPTER I

## INTRODUCTION

The Standard Model (SM) of particle physics is perhaps the most successful scientific theory in human history, culminating with the discovery of the Higgs Boson at the Large Hadron Collider (LHC) in 2012 [1, 2]. The agreement between theory and experiment is remarkable, and is best highlighted by the measurement of the electron’s anomalous magnetic moment [3], where the SM prediction and the experimentally measured value agree to more than one part per trillion. For all of its successes, though, we know that the SM cannot be a complete description of nature. There are a number of observed phenomena, such as the existence of dark matter [4, 5, 6, 7, 8, 9] and neutrino oscillations <sup>1</sup> [10, 11], that cannot be explained by the known particle content of the SM.

As experiments at the LHC mature, much of the easily accessible parameter space for theoretically well-motivated models to explain Beyond the Standard Model (BSM) physics, such as supersymmetry [12], has been closed [13]. Experimental hints as to where new physics may lie have been few and far between, and recent measurements of the muon’s anomalous magnetic moment [14] or the mass of the W boson with CDF II [15] demonstrate how difficult these searches can be. This reality suggests a complementary approach to look for new physics—leveraging theoretical tools to highlight production/decay modes that are most likely to be susceptible to BSM operators while still being accessible to active experiments and using more powerful computational tools to search for rare signs of BSM physics.

---

<sup>1</sup>Fermions in the SM acquire their mass through interactions with the Higgs, which requires both a left- and right-handed copy of the fermion. As of now, only left-handed neutrinos have been observed. There are simple modifications to the SM that either add in a right-handed neutrino, or allow neutrinos to acquire a mass through a Majorana mass term. Here, we take the SM to be the theory that predicts that neutrinos should be exactly massless.

Effective field theories (EFTs) are a well-established method of organizing the effects of physics above a certain energy scale, and have been by both theorists and experimentalists to guide searches for BSM physics at both the LHC and future colliders. Today, it is common to treat the SM as an EFT, where the effects of new physics above the electroweak scale appear only indirectly as modifications to parameters in the SM Lagrangian. The two commonly used paradigms used to parameterize the indirect effects of new physics are the Standard Model EFT (SMEFT) [16, 17] and the Higgs EFT (HEFT) [18]. These two paradigms have different assumptions about physics at high energy scales—SMEFT is expressed in the electroweak symmetric phase and utilizes the Higgs doublet whereas HEFT is expressed in the broken phase and consequently utilizes the physical Higgs boson and an independent set of Goldstones. These differences give rise to contrasting predictions about the relative importance of certain effects. See Ref. [19] for a more comprehensive review of the differences between SMEFT and HEFT.

Despite the ease with which EFTs allow us to neatly organize the effects of new physics on the low-energy degrees of freedom, there are a number of Lagrangian-side issues that can obfuscate the connections between EFT operators and their corresponding experimental signals. Operators which give the same physical amplitude can be written in a number of seemingly different ways. Equations of motion and integration-by-parts can give rise to redundancies in operator bases. Additionally, the large number of allowed interactions make it difficult to know when one has a complete basis. These issues have motivated work to understand the direct connection between dimension-6 SMEFT operators and the physical observables they parameterize [20, 21, 22, 23].

As alluded to above, these issues stemming from the Lagrangian have no impact on the predictions of the physical amplitudes when all external particles are on shell. These amplitudes are physically observable, and thus serve as a useful intermediary between theory and experiment. Recent work in the study of amplitudes has resulted in greater insight into the independent amplitudes for a given process. In particular, the general structure of BSM amplitudes, given just  $SU(3)_c \times U(1)_{em}$  invariance has been analyzed with both spinor-helicity [24, 25, 26, 27] and standard variables [28].

While EFTs and amplitudes are useful to guide searches, these searches still need to be carried out, and the data they collect analyzed. Finding rare physics amounts to solving an increasingly difficult binary classification problem. If the relevant signals are particularly uncommon, it can be hard to find these new signals in the first place, and even more difficult to make any statistically significant statements. This problem is only exacerbated if one needs to first define a new observable (or set of observables) that can be used as a discriminant.

Over the past decade, advances in computational power and machine learning (ML) have paved the way for the use of so-called ‘deep’ learning to search for BSM physics. Compared to the ‘shallow’ ML models of yore, deep ML models have an increased capacity to learn complex, non-linear functions of their inputs<sup>2</sup>. This difference is highlighted well in Ref. [29], where a deep neural network given only low-level information outperforms a shallow neural network with access to both the same low-level information, as well as relevant high-level information. This increase in performance has a corresponding increase in the potential discovery significance.

When searching for new resonances at the LHC, it is increasingly important to develop and apply search strategies that are sensitive to a wide class of signals.

---

<sup>2</sup>Shallow ML models typically have 1 (or 0) hidden layers. Deep ML models will contain multiple hidden layers.



For hadronically decaying resonances, there has been considerable effort in the past to develop various methods, targeted at the boosted regime ( $p_T \gg m$ ) of these resonances. Such boosted resonances appear in many generic BSM scenarios, as well as in hadronic channels of boosted W/Z in the SM itself. In the boosted regime, the resulting jets from the hadronic decay of these resonances are merged, and the result is a fat jet of wide radius. Using the difference in radiation pattern inside these fat jets, captured by various substructure variables, single variable (SV) [30, 31] as well as multi-variable (MV) machine learning based methods [32, 33, 34, 35, 36, 37, 38, 39, 40, 41, 42, 43, 44, 45, 46, 47, 48, 49, 50, 51, 52, 53] have been shown to allow a good discrimination of these signals from QCD background (see [54, 55] for a review of machine learning based techniques in high energy physics).

Many analyses have been carried out at the LHC to look for new physics beyond the Standard Model, but unfortunately these have yet to yield statistically significant deviations from the expected background. This may indicate that there is no new physics to be found in the data or, more optimistically, it may be a result of not looking for the right signals. There remain many well-motivated models to search for, but designing and carrying out dedicated analyses for each quickly becomes intractable. This motivates the need for broad, model-agnostic searches. The advent of modern machine learning has seen the creation of a variety of unsupervised anomaly detection techniques, all capable of searching for new physics with no reliance on a particular signal model. See Ref. [56] for a recent review of anomaly detection and unsupervised techniques.

## 1.1 Primary Observables for Top Quark Collider Signals

Ref. [28] was able to characterize the structure of on-shell 3- and 4-point amplitudes involving the Higgs. To complete this procedure, a set of potential on-shell amplitudes was constructed out of Lorentz invariant combinations of momenta and polarizations. By studying their Taylor expansion in the kinematic variables, a set of independent amplitudes was determined. These could then be converted into a basis of Lagrangian operators. As a cross-check, the number of independent operators at each mass dimension could be determined using the Hilbert Series approach [57, 58, 59, 60, 61, 62, 63]. For the four point couplings, this lead to a number of primary amplitudes/operators whose multiplication by Mandelstam variables gave descendant amplitudes/operators. If these new interactions are mediated by the exchange of a massive particle, the lowest order primary amplitude would be a first approximation to the relevant phenomenology. Finally, by requiring unitarity up to an energy  $E_{\max}$ , one can place upper bounds on their coupling strength. These results when combined with simple estimates, suggested that there are new amplitudes in Higgs decays into  $Z\bar{f}f, W\bar{f}f, \gamma\bar{f}f$ , and  $Z\gamma\gamma$  that could be searched for at the HL-LHC.

In Chapter II, we extend this study to amplitudes involving the top quark. At the High-Luminosity LHC (HL-LHC) and future TeV colliders, over a billion top quarks will be produced, allowing the study for rare decays as well as new production mechanisms. This requires understanding the general structure of four fermion operators and two fermion operators with two gauge bosons, which can result in primaries up to dimension 11. Interestingly, we find interactions (e.g.  $\gamma\gamma\bar{f}f$ ) whose Hilbert series numerator has a complete cancellation in the coefficient for one of the terms, where a naïve inspection incorrectly concludes that there are no

primary operators at a mass dimension. In our analysis, we have also checked that the primary and descendant structure up to at least dimension 12, going beyond the existing dimension 8 results using spinor-helicity variables [26, 27]. As an initial look at the phenomenology of these operators, we give simple estimates that top quark decays for which FCNC modes (e.g.  $t \rightarrow c(\bar{\ell}\ell, h\gamma, hg, Z\gamma, Zg, \gamma\gamma, \gamma g)$ ) and charged current decay modes could be interesting to search for at the HL-LHC. These simple estimates indicate that there are some decay modes that appear at dimension 8 and 10 in SMEFT that are worth studying in more detail.

## 1.2 Mass Agnostic Jet Taggers

While entirely focusing on the best discriminant to distinguish between signal and background is desirable, it is only a first step. In realistic searches for these resonances, one needs to model the background with confidence, given that QCD is hard to estimate entirely analytically. This is usually accomplished by looking at distributions of variables in which the background is smooth and featureless, while the signal is not—an example of such a variable being the invariant mass of the jet. Using sideband analysis or control regions, one can model the background, and therefore look for new resonances using a bump hunt strategy.

The substructure of a fat jet is related to kinematic variables such as the jet mass,  $m$ , and transverse momentum,  $p_T$ . As a result, the application of any classifier for signal isolation tends to distort the background distribution for  $m$  and  $p_T$ . This leads to introducing spurious features in the distributions, making a bump hunt harder to implement with statistical confidence. It is not surprising that such a distortion for the background distribution occurs, because a good discriminant should reject a large fraction of background events, so that the events that survive are necessarily

signal like, and hence the background distribution starts to look signal like. The right optimization requires taking these two competing effects into account—a strong signal discrimination vs an undistorted background distribution.

Specifically, there are two side effects that come as a result of the correlation of the jet mass with the classifier output. The first is that the classifier is only good for a signal of a given mass. This is less than ideal as a broad search strategy for new physics. One would either need to train multiple classifiers to cover the mass range, or need to use other techniques such as parametrized networks [34, 64]. The other side effect is related to systematics. If the only background that makes it through the selection criteria looks exactly like the signal, it can be hard to estimate the level of background contamination. While unintuitive, it can be better to have a classifier which removes less background, if it does so in such a way that the systematics are decreased. The overall goal is to maximize the significance, which is approximately given by  $S/\sqrt{B + \sigma_{\text{sys}}^2}$ . Allowing more background can lead to a better significance if it decreases the systematic uncertainty  $\sigma_{\text{sys}}$ .

Recent work, based on both single variable and multivariate approaches have addressed this constrained optimization problem. For example, a decorrelated  $\tau_{21}$ , called  $\tau_{21}^{\text{DDT}}$  has been shown to be effective in keeping background distributions unaffected [65, 66]. While this single variable method has the advantage of being simpler to implement, it will not be useful for more complicated boosted jets. Multivariate methods, while more powerful in general as compared to single variable based methods, are also prone to distorting the background distributions more, and require more sophisticated *training augmentation* based approaches. For example, multivariate methods based on Boosted Decision Trees (BDT) use a modified algorithm called uBoost to perform this constrained optimization [67]. Multivariate

methods based on Neural Networks (NN) use an adversarial architecture [68, 64, 69] to accomplish the same. However, these multivariable methods are significantly more involved and require tuning additional hyperparameters for optimal performance. In a recent work [70], the ATLAS collaboration has studied mass decorrelation in hadronic 2-body decays for both single and multivariate approaches.

In addition to these, there are *data augmentation* based approaches that aim for a middle ground.<sup>3</sup> The idea is to decorrelate the input to multivariate methods, so that any dependence on a given background variable is reduced significantly. While these methods are not as efficient in keeping the distributions undistorted, they are quick to implement and still enjoy the power of multivariate discrimination. Two such approaches, PCA [36, 65] (based on principal component analysis, from which it derives the name) and Planing [33, 38] are shown to be efficient in benchmark cases.

There is a general need to compare and understand the advantages and limitations of these methods, when requiring both high signal isolation and undistorted background distribution. A classification of these methods, and quantifying their performance using suitable metrics, for varying levels of signal complexity (in terms of prongedness) is desired. Depending on the situation at hand, one may want to work with higher/lower signal efficiency or lower/higher background rejection, for a given background distortion. This should be quantified for various methods and signal topologies. This can give a clear picture of when is a given method suitable, and how to augment one with the other if needed.

---

<sup>3</sup>In the machine learning literature, data augmentation is a technique to modify an input and add to the existing training set. This can make a classifier more robust to noise or underlying symmetries. We use data augmentation instead to remove information that we don't want to be learned.

### 1.3 Creating Simple, Interpretable Anomaly Detectors for New Physics in Jet Substructure

Anomaly detection techniques rely on an ability to characterize the background in some way, with the hope that this characterization does not generalize to out-of-distribution events, thus making signal events appear “anomalous.” Broadly speaking, anomaly detection can be split into two categories, depending on how similar one expects the signal and background to look. If they are expected to look similar, one has to work to exploit differences in the underlying probability distributions, and many techniques have been developed to highlight those differences [71, 44, 72, 73, 74, 75, 76, 77, 78, 79, 80, 81, 82, 83, 84, 85, 86, 87, 88, 89, 90, 91, 92]. However, one often expects there to be qualitative differences between signal and background. In that case, there are a variety of methods that can determine whether events are anomalous or not on an event-by-event basis [93, 36, 94, 69, 50, 95, 96, 97, 98, 99, 100, 101, 102, 103, 104, 105, 106, 107, 108, 109, 110, 111, 112, 113, 114, 115, 116, 117, 118, 119, 120].

Machine learning (ML) techniques, including unsupervised anomaly detection, typically make use of low-level, high-dimensional data. This is in contrast to human-engineered strategies, which tend to use high-level, low-dimensional data. When the two perform equally well on a given task, we tend to assume that the ML strategy must have used some combination of its low-level inputs to create an approximation of the high-level variables used by humans. It could be, however, that the ML strategy has found an alternative that is just as efficient. Unfortunately, the “black box” nature of ML techniques make it difficult to understand what the machine is actually learning. This problem is only amplified when the ML strategy outperforms the human-engineered one. Has the machine learned a simple observable humans didn’t consider or has it perhaps found something new?

There have been efforts to understand a neural network by using existing high level observables [29, 121, 38, 122, 123], as well as “knowledge distillation” techniques to gain insights about complex networks by analyzing simpler ones [124, 125, 126, 127]. In a recent paper (Ref. [128]), a promising iterative technique was introduced to build an interpretable classifier. This classifier mimics a “black box” deep neural network classifier, where the mimicker’s inputs consists of a limited set of human-interpretable high-level variables (see also [129, 130]). In this paper, we extend this technique to anomaly detectors by presenting two strategies for mapping the low-level information utilized by an anomaly detector into a handful of simple to understand high-level observables. As a concrete example, we attempt to mimic both the decisions and performance of an anomaly detector based on a convolutional autoencoder, which is trained on background jet images. The convolutional autoencoder then helps to iteratively select high-level observables that serve as the inputs to the mimicker networks. As our pool of high-level observables, we use the Energy Flow Polynomials [131] because they form a basis for all infrared- and collinear-safe observables.

We introduce two strategies to mimic an autoencoder. The first strategy, the *High-Level Network*, uses a small number of high-level observables to match the autoencoder’s anomaly score on an event-by-event basis. The other strategy, the *Paired Neural Network*, is tasked with using a potentially different set of observables to learn to make the same ordering decisions as the autoencoder. Given a pair of events, the *Paired Neural Network* learns which of the two was deemed to be less anomalous by the autoencoder. Note that like the convolutional autoencoder we want to mimic, both the *Paired* and *High-Level* neural networks are only trained on background events and so are unsupervised with respect to signal events. Despite

their philosophical differences, we find that both strategies agree on which high-level observables are useful for ordering background events like the autoencoder. These two strategies also have comparable performance, where we find that they both make the same ordering decisions as the autoencoder  $\sim 83\%$  of the time.

Since these networks are unsupervised, applying these networks as anomaly detectors allows us to test whether the decision ordering on background events transfers to signal events. Interestingly, for seven of the eight different signals we consider, we find that the mimickers perform as well or better as anomaly detectors than the autoencoder. Thus, this shows that it is possible to create interpretable anomaly detectors that have a limited number of high-level inputs without compromising performance. This reduction of complexity is an obvious advantage for experimental applications of anomaly detection, reducing work needed for variable validation and determination of systematic uncertainties. Theoretically, this result gives insights into the features of a QCD jet image which are harder to compress into a lower dimensional latent space.

## 1.4 Outline

This dissertation is comprised of three analyses that aid in the search for BSM physics.

In Chapter II, we adapt the methods outlined in Ref. [28] to characterize the structure of 3- and 4-point on shell amplitudes involving the top quark. We create a set of independent amplitudes, cross-checked by the appropriate Hilbert series, and translate these amplitudes into a set of SMEFT-like operators. We then use perturbative unitarity to place an upper bound on the coupling strength of these



operators. With this, we highlight a number of new top production/decay amplitudes that are accessible to the HL-LHC.

In Chapter III, we compare and quantify the efficacy of data augmentation and training augmentation techniques in decorrelating a deep ML classifier from the invariant jet mass. All of these techniques help to preserve the background dominated sidebands in the invariant mass distribution, even as tighter cuts are made on the classifier's output. This allows experimentalists to better understand systematic sources of error in the signal region, which allows us to make more statistically significant statements about the data.

Finally, in Chapter IV, we focus on the interpretability of ML-based anomaly detection. Adapting techniques from the literature, we iteratively build a series of deep anomaly detectors with the aim of mimicking a more complex, image-based convolutional autoencoder. One series of deep networks is tasked with regressing the reconstruction error of the autoencoder, the other is tasked with mimicking the background decision ordering of the autoencoder. The iterative process picks out the high-level physics observables that best explain the physics being learned by the convolutional autoencoder. We find that both techniques are able to successfully mimic the autoencoder, both in the relative ordering of background events and when used as anomaly detectors, and agree on the relevant underlying physics learned by the autoencoder.

Chapter II contains material that has yet to be published (though a preprint is available [132]) and co-authored with Spencer Chang. Chapter III contains material that has been published [133] and was co-authored with Rashmish K. Mishra, Andrea Mitridate, and Bryan Ostdiek. Chapter IV contains material that has been published [134] and was co-authored with Spencer Chang

## CHAPTER II

### PRIMARY OBSERVABLES FOR TOP QUARK COLLIDER SIGNALS

Future colliders, such as the HL-LHC, are expected to produce over a billion top quarks over the lifetime of the experiment. This large number will allow for the study of rare decays and new production mechanisms, which could point to BSM physics. In this chapter, we adapt the techniques outlined in Ref. [28] to on-shell amplitudes involving top quarks. We use a number of theoretical tools from the modern amplitudes program to identify a set of independent operators up to dimensions 12 and 13 for four fermion ( $ffff$ ) operators and two fermion, two gauge boson ( $ffvv$ ) operators, respectively. We can then translate these amplitudes into the lowest possible dimension SMEFT-like operator, and use perturbative unitarity to place a bound on that operator's coupling. This allows us to highlight which production/decay modes are accessible to future experiments like the HL-LHC, and warrant being studied in more detail.

This chapter is organized as follows. Section 2.1 describes what amplitudes we will explore and how to determine independent amplitudes. Section 2.2 discusses the Hilbert series results for our top quark operators. In Section 2.3, we discuss some relevant phenomenological issues, such as unitarity bounds on coupling strengths and also rough estimates for top quark decays at the HL-LHC. Section 2.4 is the main body of results, where we list the operators for the primary amplitudes. In Section 2.5, we estimate which top decay amplitudes are interesting for exploration at HL-LHC.

The characterization of  $ffVV$  amplitudes and operators was done by LB and Spencer Chang. Spencer Chang characterized the  $ffff$  amplitudes and operators.

## 2.1 Finding Independent Amplitudes/Couplings for Top Quarks

The general on-shell amplitudes needed for top quark phenomenology are invariant under  $SU(3)_c \times U(1)_{em}$  and Lorentz symmetry. For 3 and 4 point interactions, imposing  $SU(3)_c$  and Lorentz symmetry gives the following list:

$$3\text{pt} : \bar{q}qV, \bar{q}qh, \quad 4\text{pt} : \bar{q}q\bar{\ell}\ell, qq\ell, \bar{q}q\bar{q}q, \bar{q}qhh, \bar{q}qhV, \bar{q}qVV \quad (2.1)$$

where  $q$  is a quark,  $\ell$  is a lepton (charged or neutral),  $h$  is a Higgs boson, and  $V$  is any gauge boson. To fully characterize these 4 point interactions, we also need additional 3 point interactions for exchange diagrams, which add

$$3\text{pt additional} : VVV, hVV, hhh, \bar{\ell}\ell h, \bar{\ell}\ell V. \quad (2.2)$$

Of these couplings, the three point couplings and  $\bar{q}qhh, \bar{q}qhV$  have been fully characterized (e.g [28]), so in this paper this leaves the following four point couplings to determine:

$$\bar{q}qVV : WW\bar{q}q, WZ\bar{q}q', ZZ\bar{q}q, Z\gamma\bar{q}q, Zg\bar{q}q, W\gamma\bar{q}q', Wg\bar{q}q', g\gamma\bar{q}q, \gamma\gamma\bar{q}q, gg\bar{q}q, \quad (2.3)$$

$$\text{Four fermion} : \bar{q}q\bar{\ell}\ell, \bar{q}q'\bar{e}\nu, qq\ell, \bar{q}q\bar{q}q. \quad (2.4)$$

When there are identical particles involved, the form of the amplitude must respect the relevant exchange symmetry and for these, there are no amplitudes with 3 or more identical particles (note that, if we were characterizing down quark interactions, we would have to consider  $ddd\bar{e}$ ).

In [28], a general approach for finding independent amplitudes for 3 and 4 point on-shell amplitudes was presented. Here, we give a brief overview of the process and refer to that paper for further details, but will also note where changes in that approach need to be made. To characterize four point on-shell amplitudes, we form Lorentz invariants out of particle momenta, fermion wavefunctions, and gauge boson polarizations. For massless gauge bosons, we use the field strength contribution  $\epsilon_\mu p_\nu - \epsilon_\nu p_\mu$ , so that the amplitude is manifestly gauge invariant. Three point interactions with a covariant derivative can also give a four point contact interaction with a gauge boson; for our cases, the only one that will be relevant is  $\bar{q}\sigma_{\mu\nu}q'W^{\mu\nu}$ , which generates a  $\bar{q}q'W\gamma$  interaction. This results in a set of amplitudes  $\mathcal{M}_a$ , giving a linear parameterization of the general amplitudes  $\mathcal{M} = \sum_a C_a \mathcal{M}_a$ . For each on-shell amplitude  $\mathcal{M}_a$ , we can associate a local Lagrangian operator, which we choose to have the lowest mass dimension possible,  $\frac{c_a}{v^{d_{\mathcal{O}}-4}}\mathcal{O}_a$ , where we've normalized its coefficient with factors of the Higgs vev to give a dimensionless coupling  $c_a$ , resulting in a Lagrangian which parameterizes the on-shell amplitudes

$$\mathcal{L}_{\text{amp}} = \sum_a \frac{c_a}{v^{d_{\mathcal{O}}-4}}\mathcal{O}_a. \quad (2.5)$$

By connecting these amplitudes to Lagrangian operators, we can work in increasing mass dimension of the corresponding operators. For example,  $\bar{q}qWW$  starts at dimension 5, since the lowest local operator needs two fermions and two gauge bosons, while  $\bar{q}q\gamma\gamma$  will start at dimension 7. At a given mass dimension, we write out all of the amplitudes for the allowed particle helicities. In cases where there are two particles that are identical, we symmetrize and anti-symmetrize with respect to those two particles. After finding the allowed primary amplitudes for the distinguishable case, we can achieve the indistinguishable case by imposing the

Bose/Fermi symmetry. We'll have more to say on that later, when we have the Hilbert series results.

For our four point amplitudes, we consider  $1 + 2 \rightarrow 3 + 4$  scattering in the center of mass frame, where  $p_1 = (E_1, 0, 0, p_i), p_2 = (E_2, 0, 0, -p_i), p_3 = (E_3, 0, p_f \sin \theta, p_f \cos \theta), p_4 = (E_4, 0, -p_f \sin \theta, -p_f \cos \theta)$ . On-shell these have the constraints

$$E_1 = \frac{E_{com}^2 + m_1^2 - m_2^2}{2E_{com}}, E_2 = \frac{E_{com}^2 + m_2^2 - m_1^2}{2E_{com}}, E_3 = \frac{E_{com}^2 + m_3^2 - m_4^2}{2E_{com}}, E_4 = \frac{E_{com}^2 + m_4^2 - m_3^2}{2E_{com}} \quad (2.6)$$

A general kinematic configuration is determined by the two continuous parameters  $E_{com}$  and  $\cos \theta$  as well as the choice of helicities. However, treating  $p_i, p_f$ , and  $\sin \theta$  as independent is advantageous for finding amplitude redundancies. On-shell, one can replace even powers of these variables as  $\sin^2 \theta = (1 - \cos^2 \theta), p_i^2 = \frac{(E_{com}^2 - (m_1 + m_2)^2)(E_{com}^2 - (m_1 - m_2)^2)}{4E_{com}^2}, p_f^2 = \frac{(E_{com}^2 - (m_3 + m_4)^2)(E_{com}^2 - (m_3 - m_4)^2)}{4E_{com}^2}$ . After doing this, as shown in detail in [28], the Taylor series coefficients of the amplitudes expansion in  $E_{com}, p_i, p_f, \cos \theta, \sin \theta$  must all vanish if there is an amplitude redundancy. Schematically, if there are Taylor series coefficients  $B_\alpha$ , we then form the matrix  $\frac{\partial B_\alpha}{\partial C_a}$ , evaluate it for random numerical values for the particle masses, and numerically evaluate its singular value decomposition. The number of nonzero values in that decomposition is the number of independent amplitudes and one can find the independent ones by removing  $C_a$ 's one at a time.

There are a few modifications to [28] needed to address the amplitudes of this paper. First of all, for four fermion amplitudes, we are required to have fermions in the final state. Similar to that paper, we can choose a mass configuration, either  $m_3 = 0, m_4 \neq 0$  or  $m_3 = m_4$ , to constrain the variable dependence of the kinematic variables

in the fermion wavefunctions. We have checked that this mass assumption doesn't affect the basis of independent amplitudes. Having final state fermions also results in dependence on  $\cos \frac{\theta}{2}, \sin \frac{\theta}{2}$ , which can be treated by replacing  $\cos \theta = 2 \cos^2 \frac{\theta}{2} - 1$  and  $\sin \theta = 2 \cos \frac{\theta}{2} \sin \frac{\theta}{2}$  and using  $\cos \frac{\theta}{2}$  and  $\sin \frac{\theta}{2}$  as our variables. Another complication is that the allowed  $SU(3)$  gauge invariant contractions are more diverse than before. This issue interplays with the Bose/Fermi symmetries of the amplitudes. As an example, for  $\bar{q}qgg$ , interchange of the gluons must result in the same amplitude. If the gluons are contracted with an  $f_{ABC}$  then the amplitude must also be odd under exchange of the momenta and polarizations of the gluons. On the other hand if the gluons are contracted with a  $d_{ABC}$  then the amplitude must also be even under exchange of the momenta and polarizations of the gluons.

## 2.2 Hilbert Series

The Hilbert series gives a systematic way to count the number of gauge invariant independent operators, up to equation of motion and integration by part redundancies [57, 58, 59, 60, 61, 62, 63], which provides a useful cross check on our amplitude counting. It gives a function, whose Taylor series expansion in a parameter  $q$  gives the number of independent operators at each mass dimension <sup>1</sup>. In Eqn. 2.7, we list the Hilbert series for each of the four point operators that we will characterize. The

---

<sup>1</sup>How to treat massive gauge bosons has only recently been worked out and is best explained in [63].

three point and the other four point operator results can be found in [28].

$$\begin{aligned}
H_{WW\bar{f}f} &= H_{WZ\bar{f}f'} = \frac{4q^5 + 12q^6 + 16q^7 + 6q^8 - 2q^9}{(1 - q^2)^2}, \\
H_{ZZ\bar{f}f} &= \frac{2q^5 + 6q^6 + 12q^7 + 6q^8 + 6q^9 + 6q^{10} - 2q^{11}}{(1 - q^2)(1 - q^4)}, \\
H_{Z\gamma\bar{f}f} &= H_{Zg\bar{f}f} = H_{W\gamma\bar{f}f'} = H_{Wg\bar{f}f'} = \frac{4q^6 + 12q^7 + 8q^8 + (2 - 2)q^9}{(1 - q^2)^2}, \\
H_{g\gamma\bar{f}f} &= \frac{6q^7 + 8q^8 + (4 - 2)q^9}{(1 - q^2)^2}, \quad H_{\gamma\gamma\bar{f}f} = \frac{4q^7 + 2q^8 + 4q^9 + 6q^{10} + (2 - 2)q^{11}}{(1 - q^2)(1 - q^4)}, \\
H_{gg\bar{f}f} &= \frac{10q^7 + 10q^8 + (14 - 2)q^9 + 14q^{10} + (6 - 4)q^{11}}{(1 - q^2)(1 - q^4)}, \\
H_{\bar{q}q\bar{\ell}\ell} &= H_{\bar{q}q'\bar{e}\nu} = H_{q_1q_2q_3\ell} = \frac{10q^6 + 8q^7 - 2q^8}{(1 - q^2)^2}, \\
H_{qqq'\ell} &= \frac{4q^6 + 6q^7 + (6 - 2)q^8 + 2q^9}{(1 - q^2)(1 - q^4)}, \quad H_{\bar{q}\bar{q}'qq'} = \frac{2(10q^6 + 8q^7 - 2q^8)}{(1 - q^2)^2}, \\
H_{\bar{q}\bar{q}'qq} &= H_{\bar{q}\bar{q}qq'} = \frac{10q^6 + 8q^7 + (10 - 2)q^8 + 8q^9 - 2q^{10}}{(1 - q^2)(1 - q^4)}, \\
H_{\bar{q}\bar{q}qq} &= \frac{8q^6 + 4q^7 + (8 - 2)q^8 + 4q^9 - 2q^{10}}{(1 - q^2)(1 - q^4)}.
\end{aligned} \tag{2.7}$$

These fractional forms are interpretable in the following way: the numerator counts the number of primary operators and the denominator allows for the dressing of these operators with Mandelstam factors.

For example, looking at  $H_{\bar{q}q\bar{\ell}\ell} = \frac{10q^6 + 8q^7 - 2q^8}{(1 - q^2)^2}$ , the numerator says that there are 10 dimension 6 primary operators and 8 dimension 7 primary operators. Ignore for now the  $-2q^8$ , which we'll see denotes two constraints that appear at dimension 8. The denominator of  $1/(1 - q^2)^2$  has an expansion of  $(1 + q^2 + q^4 + \dots)^2$  which is just counting the number of operators from multiplying the primaries by Mandelstam factors of  $s, t$  ( $u$  is redundant to the on-shell condition). As we will see when we analyze the amplitudes of this interaction, two primary amplitudes at dimension 6,

say  $M_a, M_b$  (with respective operators  $\mathcal{O}_a, \mathcal{O}_b$ ), when multiplied by a factor of  $s$  are redundant to a linear combination of other amplitudes, so are no longer independent at dimension 8. This explains the  $-2q^8$  since treating this as the loss of the two related operators  $s\mathcal{O}_a$  and  $s\mathcal{O}_b$  and all of their descendants gives the correct counting of the number of independent terms. Also for some denominators, the factors are  $(1 - q^2)(1 - q^4)$ . This results for situations where there are two identical particles in the amplitude. Assuming the two initial state particles are the identical pair,  $s$  and  $(t - u)^2$  are the Mandelstam factors that have the correct exchange symmetry between the two particles, so we are allowed to multiply the primary by an arbitrary set of  $s$  and  $(t - u)^2$  factors (note that the primary already has a factor of  $+/-$  when exchanging bosons/fermions).

As you'll notice in the Hilbert series list, some of the numerator coefficients are written in an unusual way, for example the  $(14 - 2)q^9$  and  $(6 - 4)q^{11}$  in  $H_{gg\bar{f}f}$ . When we evaluated the Hilbert series, these would of course have been  $12q^9$  and  $2q^{11}$ . However, when examining the number of independent amplitudes at dimension 9, we found 14 new primaries and 2 redundancies when 2 of the dimension 7 amplitudes were multiplied by  $s$ . In this way, the Hilbert series must be interpreted with care, as there can be hidden cancellations. In some case, there is even a complete cancellation like the  $(2 - 2)q^{11}$  term for  $\gamma\gamma\bar{f}f$ , where a naïve interpretation would have missed the new primaries at dimension 11.

The Hilbert series also allows for understanding of the constraints of Bose/Fermi symmetry. For example, for  $gg\bar{f}f$  there are two symmetric contractions for the gluon  $SU(3)$  indices ( $\delta_{AB}, d_{ABC}$ ) and one antisymmetric contraction ( $f_{ABC}$ ), then swapping the kinematic variables of the two gluons would result respectively in a  $+$  sign for the first two and a  $-$  sign for the last one. Now, if we calculated the Hilbert series



assuming photons were odd under interchange, then  $H_{\gamma\gamma\bar{f}f}^{asym} = \frac{2q^7+6q^8+(6-2)q^9+2q^{10}+2q^{11}}{(1-q^2)(1-q^4)}$ .

One can then check that  $H_{gg\bar{f}f} = 2H_{\gamma\gamma\bar{f}f} + H_{\gamma\gamma\bar{f}f}^{asym}$  as expected from the behavior under kinematic variable exchange and the allowed  $SU(3)$  contractions.

Note that unlike in [28], due to complications of enumerating all of the terms, we do not claim to have examined the full, allowed tensor structures of the amplitudes. Instead, we have checked that we agree with the Hilbert series up to dimension 13 for  $\bar{q}qVV$  amplitudes and dimension 12 for four fermion amplitudes. Up to those dimensions, the numerator of these Hilbert series do not have any additional cancellations. As the Hilbert series shows, the redundancies that appear at higher dimension appear in pairs so it seems unlikely there are more, but still we cannot guarantee that others do not appear at higher dimension.

## 2.3 Phenomenology

### 2.3.1 Unitarity

As in [28], we utilize unitarity to constrain the coupling strengths of these operators. Since these are new couplings beyond the Standard Model, they violate unitarity at high energies. Requiring the amplitudes to satisfy perturbative unitarity up to a scale  $E_{\max}$ , gives an upper bound on the couplings. The technique follows the work [135, 136, 137, 138], where the unitarity bounds due to high multiplicity scattering was developed (see also [139, 140, 141, 142, 143]).

To stand in for a more detailed calculation of each amplitude, we utilize a SMEFT operator realization of the amplitude to act as a proxy. As an example, consider the case of  $\frac{c}{v}\bar{q}qWW$ . This is realized by the dimension 8 SMEFT operator  $\frac{1}{\Lambda^4}(\bar{Q}_L\tilde{H}u_R + \text{h.c.})|D^\mu H|^2$ <sup>2</sup>. Since we are only looking for an approximate bound, we ignore  $O(1)$  factors like  $\sqrt{2}, g, g', \sin\theta_W, \cos\theta_W$  and only take into account factors of  $v$ . Under this

---

<sup>2</sup>Note that the dimension 6 operator  $\frac{1}{\Lambda^2}(\bar{Q}_L(D^2\tilde{H})u_R + \text{h.c.})$  can be reduced by equations of motion and does not result in the correct high energy behavior of the  $\bar{q}qWW$  interaction.

approximation,  $c \approx v^4/\Lambda^4$ . The SMEFT operator has many contact interactions that violate unitarity, but we find that either the lowest and highest multiplicity give the best bound as a function of  $E_{\max}$ , so we will calculate these for all interactions and include them in our tables. For this example, the lowest multiplicity amplitude is for two quarks and two Goldstones, with a matrix element that goes as  $M_{2 \rightarrow 2} \approx \frac{vE_{\max}^3}{\Lambda^4}$ , where one factor of  $E_{\max}$  comes from the fermion bilinear and the other two come from the two derivatives acting on the Goldstones. This is bounded by phase space factors  $M_{2 \rightarrow 2} \leq 8\pi$  [135], which translates into  $c \leq (8\pi)v^3/E_{\max}^3 \approx \frac{0.4}{E_{\text{TeV}}^3}$  where  $E_{\text{TeV}} = E_{\max}/\text{TeV}$ . The highest multiplicity amplitude is for two quarks and 3 Goldstones, with  $M_{2 \rightarrow 3} \approx \frac{E_{\max}^3}{\Lambda^4} \leq \frac{32\pi^2}{E_{\max}}$ , where the bound again depends on the phase space. This gives the bound  $c \leq (32\pi^2)v^4/E_{\max}^4 \approx \frac{1.2}{E_{\text{TeV}}^4}$ . As this example illustrates, we generally find that the low multiplicity constraint is stronger for  $E_{\max} < 4\pi v$  and the high multiplicity one is stronger for energies above that.

### 2.3.2 Top Quark Decays

The HL-LHC will produce about 5 billion top quarks, allowing searches for rare decays as well as new production modes. Here we will consider decay modifications due to our amplitudes. The on-shell 2 and 3 body decay modes of the top quark allowed by the Standard Model quantum numbers are

$$t \rightarrow dW, u(Z, h), d(e\nu, \bar{d}u, WZ, W\gamma, Wg), u(\bar{\ell}\ell, \bar{q}q, WW, Z\gamma, Zg, \gamma\gamma, \gamma g, gg) \quad (2.8)$$

along with changes in flavors of quarks and leptons.

Searches for the flavor changing two body decays are actively being pursued at the LHC (e.g. [144, 145, 146, 147, 148, 149, 150]), where theoretical analyses are often performed in SMEFT (e.g. [151, 152, 153, 154]). Some of the three body decays are higher order decays that exist in the Standard Model at tree level

(e.g.  $dW(Z, \gamma, g), uWW$ ), while the others require flavor changing neutral current interactions which should be suppressed in the Standard Model. Searches for new decay modes can be triggered by requiring one of the tops decays in the standard leptonic channel and then looking for the new decay mode for the other top quark.

For this simple analysis of the phenomenology, we will approximate top decay amplitudes as a constant, assuming the top quark mass is the only relevant mass scale

$$\mathcal{M}_{\mathcal{O}}(t \rightarrow 2) \simeq \frac{c_{\mathcal{O}}}{v^{d_{\mathcal{O}}-4}} m_t^{d_{\mathcal{O}}-3} \approx c_{\mathcal{O}} \left(\frac{m_t}{v}\right)^{d_{\mathcal{O}}-4} m_t \approx c_{\mathcal{O}} 2^{2-d_{\mathcal{O}}/2} m_t, \quad (2.9)$$

$$\mathcal{M}_{\mathcal{O}}(t \rightarrow 3) \simeq \frac{c_{\mathcal{O}}}{v^{d_{\mathcal{O}}-4}} m_t^{d_{\mathcal{O}}-4} \approx c_{\mathcal{O}} \left(\frac{m_t}{v}\right)^{d_{\mathcal{O}}-4} \approx c_{\mathcal{O}} 2^{2-d_{\mathcal{O}}/2}, \quad (2.10)$$

where we've approximated  $v \approx \sqrt{2}m_t$ . Note that this ignores  $O(1)$  enhancements of the form  $(m_t/m_W)$  that can come from longitudinal polarizations, but is sufficient for our estimates.

Let's first consider non-FCNC top decays that are not suppressed in the Standard Model, such as  $t \rightarrow b(W, \ell\nu, W\gamma, Wg)$ . In such cases, one has at least the Standard Model top background to contend with. For new amplitudes which are CP even, they will interfere with the Standard Model amplitude and have enhanced sensitivities (unless one designs CP violating observables). In this case, we want to compare the number of new decays to the fluctuation in the Standard Model top background. Under our approximation the branching ratios in the Standard Model and the modification due to interference are

$$Br(t \rightarrow 2)_{SM} \approx \frac{1}{16\pi m_t \Gamma_t} |\mathcal{M}(t \rightarrow 2)_{SM}|^2, \quad (2.11)$$

$$\delta Br(t \rightarrow 2) \approx \frac{1}{16\pi m_t \Gamma_t} |\mathcal{M}(t \rightarrow 2)_{SM}| |\mathcal{M}(t \rightarrow 2)_{BSM}|. \quad (2.12)$$

To estimate sensitivity, we require that the new top decays must be as large as a one sigma deviation in the Standard Model top background, which for a sample of  $N_t$  top quarks gives  $N_t \delta Br(t \rightarrow 2) \gtrsim \sqrt{N_t Br(t \rightarrow 2)_{SM}}$ . Such a calculation gives for two and three body decays the constraints

$$\begin{aligned}
 \text{2 Body Decays : } \quad c &\gtrsim 5 \times 10^{-6} \left(\frac{10^9}{N_t}\right)^{1/2} 2^{d_{\mathcal{O}}/2}, \\
 \text{3 Body Decays : } \quad c &\gtrsim 6 \times 10^{-5} \left(\frac{10^9}{N_t}\right)^{1/2} 2^{d_{\mathcal{O}}/2}
 \end{aligned}
 \tag{2.13}$$

where we've normalized to a total sample of a billion top quarks.

For FCNC decays, such as  $t \rightarrow c(Z, \gamma, g, WW, Z\gamma, Zg, \gamma\gamma, \gamma g, gg)$ , the branching ratios predicted in the Standard Model ( $10^{-12}$  to  $10^{-17}$ ) are too small to occur at the HL-LHC (e.g. [?, ?, ?, ?, 155]). Thus, for these decays we can ignore interference and give an estimate that works for both CP even and odd interactions. If we make an optimistic assumption that other backgrounds can be neglected, this requires that the new branching ratios  $Br_{BSM}$  give a few events at the HL-LHC or  $N_t Br_{BSM} \gtrsim 1$ . Under our approximation, this gives the same bounds as Eqn. 2.13.

To get some sense of how well this approximation works, we've checked in a few existing FCNC searches, whether the background free assumption works at the  $O(1)$  level. As one might expect, one finds that for final states with a single gluon or photon, where hadronic backgrounds and fakes are relevant, that this is a poor assumption and gives a branching ratio bound that is too strong by two and three orders of magnitude for photon and gluon decays, respectively. Thus, estimates for these final states should be viewed as very optimistic. However, we found that the searches with a Higgs decaying into two photons agree roughly with our bounds. Similarly, the final states with  $e, \mu$ 's give bounds that are correct to a factor of 2 – 3

as long as one takes into account tagging efficiencies for  $b$  ( $\sim 0.5$ ),  $e/\mu$  ( $\sim 0.8$ ) and, when relevant,  $Z$  and  $W$  leptonic branching ratios ( $\sim 0.06$  and  $0.2$ ). Thus, as long as one take these factors into account, these final states should be more reliable. Later, when combined with our upper bounds from perturbative unitarity, these calculations will enable us to give a simple estimate of which decay amplitudes that are worth exploring further at the HL-LHC.

## 2.4 Independent Amplitudes for Top Quark Physics

In the following subsections, we will list operators corresponding to the primary amplitudes for  $ffVV$  and  $ffff$  interactions involving the top quark. We will make comparisons to the Hilbert series to show consistency with the number of independent operators, including discussions of redundancies that occur at certain mass dimensions. We will also give  $CP$  properties of the operators and unitarity bounds on the coupling constants for these interactions.

### 2.4.1 $ffVV$ Amplitudes

Tables 1 and 2 list the primary operators for  $\bar{q}qWW$  interactions. Note that for the primary operators, covariant derivatives are with respect to  $SU(3)_c \times U(1)_{em}$  and thus only involve the photon and gluon. From the Hilbert series, we expect that there should be 4 operators at dimension 5, 12 operators at dimension 6, 16 operators at dimension 7, 6 operators at dimension 8, and at least two redundancies at dimension 9. This is precisely what we find, with the 38 listed operators and at dimension 9,  $s\mathcal{O}_{26}$  and  $s\mathcal{O}_{27}$  become redundant to other operators, where  $s = (p_q + p_{\bar{q}})^2$ . To generate an independent set of operators, one needs to add descendants of the primaries, which involve multiplying by arbitrary powers of  $s$  and  $t$ . However, because of the redundancies at dimension 9, for  $\mathcal{O}_{26}$  and  $\mathcal{O}_{27}$ , one only needs their descendants  $t^n\mathcal{O}_{26}$  and  $t^n\mathcal{O}_{27}$ . We've also listed the lowest dimensional SMEFT-like operator

(that we could find) which realizes each operator, where the covariant derivatives are with respect to  $SU(3)_c \times SU(2)_L \times U(1)_Y$ . We also list the unitarity bounds for each SMEFT operator, assuming the lowest and highest particle multiplicity. These operators can also be reworked to account for  $\bar{q}q'WZ$  amplitudes provided we take  $q \rightarrow q'$  and  $W \rightarrow Z$ . Here, we use  $q'$  to denote a different quark flavor of the correct charge.

In Tables 3 and 4, we list the primary operators for  $\bar{q}qZZ$  interactions. Reading off from the Hilbert series, we expect to see 2 operators at dimension 5, 6 operators at dimension 6, 12 operators at dimension 7, 6 operators at dimensions 8, 9, and 10, and at least 2 constraints at dimension 11. We do indeed find that there are 38 primary operators, as well as two redundancies at dimension 11, for  $s\mathcal{O}_{31}$  and  $s\mathcal{O}_{32}$ . To generate an independent set of operators, one needs to add descendants of the primaries, which involve multiplying by arbitrary powers of  $s$  and  $(t - u)^2$  (note that  $(t - u)^2$  respects the exchange symmetry of the  $Z$ 's). However because of the redundancies at dimension 11, for  $\mathcal{O}_{31}$  and  $\mathcal{O}_{32}$ , one only needs their descendants  $(t - u)^{2n}\mathcal{O}_{31}$  and  $(t - u)^{2n}\mathcal{O}_{32}$ .

We have listed all of the primary operators for  $\bar{q}qZ\gamma$  interactions in Table 5. The Hilbert series tells us to expect 4 operators at dimension 6, 12 new operators at dimension 7, 8 operators at dimension 8, and 2 new operators and 2 new redundancies at dimension 9. We note that a naïve interpretation of the Hilbert series would have missed the 2 new primary operators that appear at dimension 9. We find that there are 26 primary operators, in agreement with the Hilbert series, as well as two constraints at dimension 9— $s\mathcal{O}_7$  and  $s\mathcal{O}_8$ . Thus for those two operators, one only needs their descendant operators  $t^n\mathcal{O}_7$  and  $t^n\mathcal{O}_8$ . These operators can also be adapted to account for  $\bar{q}q'W\gamma$ ,  $\bar{q}q'Zg$ , and  $\bar{q}q'Wg$  where we use a prime to denote a different quark flavor.

$i$	$\mathcal{O}_i^{\bar{q}qW^+W^-}$	CP	$d\mathcal{O}_i$	SMEFT Operator	c Unitarity Bound
1	$(\bar{q}q) (W_\mu^+ W^{-\mu})$	+	5	$(\bar{Q}_L \bar{H} u_R + \text{h.c.}) ( D^\mu H ^2)$	$\frac{0.4}{E_{\text{TeV}}^3}, \frac{1.2}{E_{\text{TeV}}^4}$
2	$(i\bar{q}\gamma_{55}q) (W_\mu^+ W^{-\mu})$	-		$(i\bar{Q}_L \bar{H} u_R + \text{h.c.}) ( D^\mu H ^2)$	
3	$(\bar{q}\sigma^{\mu\nu}q) (iW_\mu^+ W_\nu^-)$	+		$(\bar{Q}_L \sigma^{\mu\nu} \bar{H} u_R + \text{h.c.}) (i[D_\mu H]^\dagger [D_\nu H] + \text{h.c.})$	
4	$(i\bar{q}\sigma^{\mu\nu}\gamma_{55}q) (iW_\mu^+ W_\nu^-)$	-		$(i\bar{Q}_L \sigma^{\mu\nu} \gamma_{55} \bar{H} u_R + \text{h.c.}) (i[D_\mu H]^\dagger [D_\nu H] + \text{h.c.})$	
5	$(\bar{q}\gamma^\nu q) (iW_\mu^{+\mu} \overleftrightarrow{D}_\nu W_\mu^-)$	+	6	$(\bar{Q}_L \gamma^\nu Q_L + \bar{u}_R \gamma^\nu u_R) (i[D^\mu H]^\dagger \overleftrightarrow{D}_\nu [D_\mu H] + \text{h.c.})$	
6	$(\bar{q}\gamma^\nu \gamma_{55}q) (iW_\mu^{+\mu} \overleftrightarrow{D}_\nu W_\mu^-)$	+		$(\bar{Q}_L \gamma^\nu Q_L - \bar{u}_R \gamma^\nu u_R) (i[D^\mu H]^\dagger \overleftrightarrow{D}_\nu [D_\mu H] + \text{h.c.})$	
7	$(i\bar{q}\gamma^\nu \overleftrightarrow{D}_\mu q) (W^{+\mu} W_\nu^- + \text{h.c.})$	+		$(i\bar{Q}_L \gamma^\nu \overleftrightarrow{D}_\mu Q_L + i\bar{u}_R \gamma^\nu \overleftrightarrow{D}_\mu u_R) ( D^\mu H ^\dagger [D_\nu H] + \text{h.c.})$	
8	$(i\bar{q}\gamma^\nu \gamma_{55} \overleftrightarrow{D}_\mu q) (W^{+\mu} W_\nu^- + \text{h.c.})$	+		$(i\bar{Q}_L \gamma^\nu \overleftrightarrow{D}_\mu Q_L - i\bar{u}_R \gamma^\nu \overleftrightarrow{D}_\mu u_R) ( D^\mu H ^\dagger [D_\nu H] + \text{h.c.})$	
9	$(\bar{q}\gamma^\nu q) (iW_\mu^{+\mu} D_\mu W_\nu^- + \text{h.c.})$	+		$(\bar{Q}_L \gamma^\nu Q_L + \bar{u}_R \gamma^\nu u_R) (i[D^\mu H]^\dagger [D_{\mu\nu} H] + \text{h.c.})$	
10	$(\bar{q}\gamma^\nu \gamma_{55}q) (iW_\mu^{+\mu} D_\mu W_\nu^- + \text{h.c.})$	+		$(\bar{Q}_L \gamma^\nu Q_L - \bar{u}_R \gamma^\nu u_R) (i[D^\mu H]^\dagger [D_{\mu\nu} H] + \text{h.c.})$	
11	$(i\bar{q}\gamma^\mu \overleftrightarrow{D}_\nu q) (iW_\mu^+ W^{-\nu} + \text{h.c.})$	-		$(i\bar{Q}_L \gamma^\mu \overleftrightarrow{D}_\nu Q_L + i\bar{u}_R \gamma^\mu \overleftrightarrow{D}_\nu u_R) (i[D_\mu H]^\dagger [D^\nu H] + \text{h.c.})$	
12	$(i\bar{q}\gamma^\mu \gamma_{55} \overleftrightarrow{D}_\nu q) (iW_\mu^+ W^{-\nu} + \text{h.c.})$	-		$(i\bar{Q}_L \gamma^\mu \overleftrightarrow{D}_\nu Q_L - i\bar{u}_R \gamma^\mu \overleftrightarrow{D}_\nu u_R) (i[D_\mu H]^\dagger [D^\nu H] + \text{h.c.})$	
13	$(\bar{q}\gamma^\nu q) (W^{+\mu} D_\mu W_\nu^- + \text{h.c.})$	-		$(\bar{Q}_L \gamma^\nu Q_L + \bar{u}_R \gamma^\nu u_R) ( D^\mu H ^\dagger [D_{\mu\nu} H] + \text{h.c.})$	
14	$(\bar{q}\gamma^\nu \gamma_{55}q) (W^{+\mu} D_\mu W_\nu^- + \text{h.c.})$	-		$(\bar{Q}_L \gamma^\nu Q_L - \bar{u}_R \gamma^\nu u_R) ( D^\mu H ^\dagger [D_{\mu\nu} H] + \text{h.c.})$	
15	$\epsilon_{\mu\nu\rho\sigma} (\bar{q}\gamma^\nu q) (W^{+\rho} \overleftrightarrow{D}^\mu W^{-\sigma})$	+		$\epsilon_{\mu\nu\rho\sigma} (\bar{Q}_L \gamma^\nu Q_L + \bar{u}_R \gamma^\nu u_R) ( D^\rho H ^\dagger \overleftrightarrow{D}^\mu [D^\sigma H] + \text{h.c.})$	
16	$\epsilon_{\mu\nu\rho\sigma} (\bar{q}\gamma^\nu \gamma_{55}q) (W^{+\rho} \overleftrightarrow{D}^\mu W^{-\sigma})$	+		$\epsilon_{\mu\nu\rho\sigma} (\bar{Q}_L \gamma^\nu Q_L - \bar{u}_R \gamma^\nu u_R) ( D^\rho H ^\dagger \overleftrightarrow{D}^\mu [D^\sigma H] + \text{h.c.})$	

Table 1. Primary 5- and 6-dimension operators for  $\bar{q}qW^+W^-$  interactions. As outlined in the text, these operators can be modified to yield the operators for  $\bar{q}qWZ$  interactions. Under the assumption that  $\bar{q}$  and  $q$  are each other's anti-particles, the operators are Hermitian and have the listed CP properties. If they are not, each of these operators has a Hermitian conjugate, which can be used to create a CP even and a CP odd operator. To simplify the expressions, we use the shorthand  $\overleftrightarrow{D}_{\mu\nu} = \overleftrightarrow{D}_\mu \overleftrightarrow{D}_\nu$ , and similarly,  $D_{\mu\nu} = D_\mu D_\nu$ . To get the descendant operators, one can add contracted derivatives to get arbitrary Mandelstam factors of  $s, t$ .

$i$	$\mathcal{O}_{\bar{q}q}^{\bar{q}q} W^+ W^-$	CP	$d\mathcal{O}_i$	SMEFT Operator	$c$ Unitarity Bound
17	$(\overleftrightarrow{q} \overleftrightarrow{D}_{\mu\nu} q) (W^{+\mu} W^{-\nu})$	+		$(\overleftrightarrow{Q}_L \overleftrightarrow{D}_{\mu\nu} \overleftrightarrow{H} u_R + \text{h.c.}) ( [D^\nu H]^\dagger [D^\nu H] + \text{h.c.} )$	
18	$(i \overleftrightarrow{q} \overleftrightarrow{D}_{\mu\nu} q) (W^{+\mu} W^{-\nu})$	-		$(i \overleftrightarrow{Q}_L \overleftrightarrow{D}_{\mu\nu} \overleftrightarrow{H} u_R + \text{h.c.}) ( [D^\mu H]^\dagger [D^\nu H] + \text{h.c.} )$	
19	$(i \overleftrightarrow{q} \overleftrightarrow{D}_{\mu\nu} q) (W^{+\nu} D_\nu W^{-\mu} + \text{h.c.})$	-		$(i \overleftrightarrow{Q}_L \overleftrightarrow{D}_\mu \overleftrightarrow{H} u_R + \text{h.c.}) ( [D_\nu H]^\dagger [D^\nu H] + \text{h.c.} )$	
20	$(\overleftrightarrow{q} \overleftrightarrow{D}_{\mu\nu} q) (W^{+\nu} D_\nu W^{-\mu} + \text{h.c.})$	+		$(\overleftrightarrow{Q}_L \overleftrightarrow{D}_\mu \overleftrightarrow{H} u_R + \text{h.c.}) ( [D_\nu H]^\dagger [D^\nu H] + \text{h.c.} )$	
21	$(i \overleftrightarrow{q} \overleftrightarrow{D}_{\mu\nu} q) (i W^{+\nu} D_\nu W^{-\mu} + \text{h.c.})$	+		$(i \overleftrightarrow{Q}_L \overleftrightarrow{D}_\mu \overleftrightarrow{H} u_R + \text{h.c.}) (i [D_\nu H]^\dagger [D^\nu H] + \text{h.c.})$	
22	$(\overleftrightarrow{q} \overleftrightarrow{D}_{\mu\nu} q) (i W^{+\nu} D_\nu W^{-\mu} + \text{h.c.})$	-	7	$(\overleftrightarrow{Q}_L \overleftrightarrow{D}_\mu \overleftrightarrow{H} u_R + \text{h.c.}) (i [D_\nu H]^\dagger [D^\nu H] + \text{h.c.})$	$\frac{0.02}{E_{\text{TeV}}^5}, \frac{0.07}{E_{\text{TeV}}^6}$
23	$\epsilon_{\mu\nu\rho\sigma} (i \overleftrightarrow{q} \overleftrightarrow{D}_{\mu\nu} q) (W^{+\rho} \overleftrightarrow{D}^\nu W^{-\sigma})$	+		$\epsilon_{\mu\nu\rho\sigma} (i \overleftrightarrow{Q}_L \overleftrightarrow{D}^\mu \overleftrightarrow{H} u_R + \text{h.c.}) ( [D^\rho H]^\dagger \overleftrightarrow{D}^\nu [D^\sigma H] + \text{h.c.} )$	
24	$\epsilon_{\mu\nu\rho\sigma} (\overleftrightarrow{q} \overleftrightarrow{D}_{\mu\nu} q) (W^{+\rho} \overleftrightarrow{D}^\nu W^{-\sigma})$	-		$\epsilon_{\mu\nu\rho\sigma} (\overleftrightarrow{Q}_L \overleftrightarrow{D}^\mu \overleftrightarrow{H} u_R + \text{h.c.}) ( [D^\rho H]^\dagger \overleftrightarrow{D}^\nu [D^\sigma H] + \text{h.c.} )$	
25	$(i \overleftrightarrow{q} \sigma^{\mu\nu} \overleftrightarrow{D}_{\rho q}) (i W_\nu^\dagger \overleftrightarrow{D}_\mu W^{-\rho} + \text{h.c.})$	-		$(i \overleftrightarrow{Q}_L \sigma^{\mu\nu} \overleftrightarrow{D}_\rho \overleftrightarrow{H} u_R + \text{h.c.}) (i [D_\nu H]^\dagger \overleftrightarrow{D}_\mu [D^\rho H] + \text{h.c.} )$	
26	$(\overleftrightarrow{q} \sigma^{\mu\nu} q) (i [D_\rho W_\nu^\dagger] \overleftrightarrow{D}_\mu W^{-\rho} + \text{h.c.})$	+		$(\overleftrightarrow{Q}_L \sigma^{\mu\nu} \overleftrightarrow{H} u_R + \text{h.c.}) (i [D_\rho H]^\dagger \overleftrightarrow{D}_\mu [D^\rho H] + \text{h.c.} )$	
27	$(i \overleftrightarrow{q} \sigma^{\mu\nu} \overleftrightarrow{D}_{\rho q}) (i [D_\rho W_\nu^\dagger] \overleftrightarrow{D}_\mu W^{-\rho} + \text{h.c.})$	-		$(i \overleftrightarrow{Q}_L \sigma^{\mu\nu} \overleftrightarrow{H} u_R + \text{h.c.}) (i [D_{\rho\nu} H]^\dagger \overleftrightarrow{D}_\mu [D^\rho H] + \text{h.c.} )$	
28	$(\overleftrightarrow{q} \sigma^{\mu\nu} \overleftrightarrow{D}_{\rho q}) (i W_\nu^\dagger \overleftrightarrow{D}_\mu W^{-\rho} + \text{h.c.})$	+		$(\overleftrightarrow{Q}_L \sigma^{\mu\nu} \overleftrightarrow{D}_\rho \overleftrightarrow{H} u_R + \text{h.c.}) (i [D_\nu H]^\dagger \overleftrightarrow{D}_\mu [D^\rho H] + \text{h.c.} )$	
29	$(\overleftrightarrow{q} q) (W^{\mu\nu} W_{\mu\nu})$	+		$(\overleftrightarrow{Q}_L \overleftrightarrow{H} u_R + \text{h.c.}) (W^{\alpha\mu\nu} W_{\mu\nu}^\alpha)$	
30	$(i \overleftrightarrow{q} \overleftrightarrow{D}_{\mu\nu} q) (W^{\mu\nu} W_{\mu\nu})$	-		$(i \overleftrightarrow{Q}_L \overleftrightarrow{H} u_R + \text{h.c.}) (W^{\alpha\mu\nu} W_{\mu\nu}^\alpha)$	$\frac{0.4}{E_{\text{TeV}}^4}, \frac{1.2}{E_{\text{TeV}}^5}$
31	$(\overleftrightarrow{q} q) (W^{+\mu\nu} \overleftrightarrow{W}_{\mu\nu}^-)$	-		$(\overleftrightarrow{Q}_L \overleftrightarrow{H} u_R + \text{h.c.}) (W^{\alpha\mu\nu} \overleftrightarrow{W}_{\mu\nu}^\alpha + \text{h.c.} )$	
32	$(i \overleftrightarrow{q} \overleftrightarrow{D}_{\mu\nu} q) (W^{+\mu\nu} \overleftrightarrow{W}_{\mu\nu}^-)$	+		$(i \overleftrightarrow{Q}_L \overleftrightarrow{H} u_R + \text{h.c.}) (W^{\alpha\mu\nu} \overleftrightarrow{W}_{\mu\nu}^\alpha + \text{h.c.} )$	
33	$(\overleftrightarrow{q} \gamma^\mu \overleftrightarrow{D}_{\nu\rho} q) (i W^{+\nu} \overleftrightarrow{D}_\mu W^{-\rho})$	+		$(\overleftrightarrow{Q}_L \gamma^\mu \overleftrightarrow{D}_\nu \overleftrightarrow{Q}_L + \overleftrightarrow{u}_R \gamma^\mu \overleftrightarrow{D}_\nu u_R) (i [D^\nu H]^\dagger \overleftrightarrow{D}_\mu [D^\rho H] + \text{h.c.} )$	
34	$(\overleftrightarrow{q} \gamma^\mu \overleftrightarrow{D}_{\nu\rho} q) (i W^{+\nu} \overleftrightarrow{D}_\mu W^{-\rho})$	+		$(\overleftrightarrow{Q}_L \gamma^\mu \overleftrightarrow{D}_\nu \overleftrightarrow{Q}_L - \overleftrightarrow{u}_R \gamma^\mu \overleftrightarrow{D}_\nu u_R) (i [D^\nu H]^\dagger \overleftrightarrow{D}_\mu [D^\rho H] + \text{h.c.} )$	
35	$(i \overleftrightarrow{q} \gamma^\mu \overleftrightarrow{D}_{\rho q}) (i W^{+\nu} \overleftrightarrow{D}_\mu D_\nu W^{-\rho} + \text{h.c.})$	-	8	$(i \overleftrightarrow{Q}_L \gamma^\mu \overleftrightarrow{D}_\rho \overleftrightarrow{Q}_L + i \overleftrightarrow{u}_R \gamma^\mu \overleftrightarrow{D}_\rho u_R) (i [D_\nu H]^\dagger \overleftrightarrow{D}_\mu [D^{\rho\nu} H] + \text{h.c.} )$	
36	$(i \overleftrightarrow{q} \gamma^\mu \overleftrightarrow{D}_{\rho q}) (i W^{+\nu} \overleftrightarrow{D}_\mu D_\nu W^{-\rho} + \text{h.c.})$	-		$(i \overleftrightarrow{Q}_L \gamma^\mu \overleftrightarrow{D}_\rho \overleftrightarrow{Q}_L - i \overleftrightarrow{u}_R \gamma^\mu \overleftrightarrow{D}_\rho u_R) (i [D_\nu H]^\dagger \overleftrightarrow{D}_\mu [D^{\rho\nu} H] + \text{h.c.} )$	
37	$(\overleftrightarrow{q} \gamma^\mu q) (i [D_\rho W_\nu^\dagger] \overleftrightarrow{D}_\mu D^\nu W^{-\rho})$	+		$(\overleftrightarrow{Q}_L \gamma^\mu \overleftrightarrow{Q}_L + \overleftrightarrow{u}_R \gamma^\mu u_R) (i [D_{\nu\rho} H]^\dagger \overleftrightarrow{D}_\mu [D^{\rho\nu} H] + \text{h.c.} )$	
38	$(\overleftrightarrow{q} \gamma^\mu \overleftrightarrow{D}_{\nu\rho} q) (i [D_\rho W_\nu^\dagger] \overleftrightarrow{D}_\mu D^\nu W^{-\rho})$	+		$(\overleftrightarrow{Q}_L \gamma^\mu \overleftrightarrow{Q}_L - \overleftrightarrow{u}_R \gamma^\mu u_R) (i [D_\nu H]^\dagger \overleftrightarrow{D}_\mu [D^{\rho\nu} H] + \text{h.c.} )$	$\frac{0.006}{E_{\text{TeV}}^6}$

Table 2. Primary 7- and 8-dimension operators for  $\bar{q}qW^+W^-$  interactions, where  $\overleftrightarrow{W}_{\mu\nu} = \frac{1}{2}\epsilon_{\mu\nu\rho\sigma}W^{\rho\sigma}$ . As outlined in the text, these operators can be modified to yield the operators for  $\bar{q}q'WZ$  interactions. Under the assumption that  $\bar{q}$  and  $q$  are each other's anti-particles, the operators are Hermitean and have the listed CP properties. If they are not, each of these operators has a Hermitean conjugate, which can be used to create a CP even and a CP odd operator. To simplify the expressions, we use the shorthand  $\overleftrightarrow{D}_{\mu\nu} = \overleftrightarrow{D}_\mu \overleftrightarrow{D}_\nu$ , and similarly,  $D_{\mu\nu} = D_\mu D_\nu$ . To get the descendant operators, one can add contracted derivatives to get arbitrary Mandelstam factors of  $s, t$ . At dimension 9,  $s\mathcal{O}_{26}$  and  $s\mathcal{O}_{27}$  become redundant to other operators and thus one only needs their descendants  $t^n\mathcal{O}_{26}$  and  $t^n\mathcal{O}_{27}$  for an independent set of operators.



$i$	$\mathcal{O}_{\bar{q}qZZ}$	CP	$d\mathcal{O}_i$	SMEFT Operator	$c$ Unitarity Bound
1	$(\bar{q}q) (Z^\mu Z_\mu)$	+	5	$(\bar{Q}_L \tilde{H} u_R + \text{h.c.})  D_\mu H ^2$	$\frac{0.4}{E_{\text{TeV}}^3}, \frac{1.2}{E_{\text{TeV}}^4}$
2	$(\bar{q}i\gamma_5 q) (Z^\mu Z_\mu)$	-		$(i\bar{Q}_L \tilde{H} u_R + \text{h.c.})  D_\mu H ^2$	
3	$(i\bar{q}\gamma^\nu \overleftrightarrow{D}_{\mu q}) (Z^\mu Z_\nu)$	+	6	$(i\bar{Q}_L \gamma^\nu \overleftrightarrow{D}_\mu Q_L + i\bar{u}_R \gamma^\nu \overleftrightarrow{D}_\mu u_R) ([D^\mu H]^\dagger [D_\nu H] + \text{h.c.})$	$\frac{0.09}{E_{\text{TeV}}^5}$
4	$(i\bar{q}\gamma^\nu \gamma_5 \overleftrightarrow{D}_{\mu q}) (Z^\mu Z_\nu)$	+		$(i\bar{Q}_L \gamma^\nu \overleftrightarrow{D}_\mu Q_L - i\bar{u}_R \gamma^\nu \overleftrightarrow{D}_\mu u_R) ([D^\mu H]^\dagger [D_\nu H] + \text{h.c.})$	
5	$(\bar{q}\gamma^\nu q) (Z^\mu \partial_\mu Z_\nu)$	-		$(\bar{Q}_L \gamma^\nu Q_L + \bar{u}_R \gamma^\nu u_R) ([D^\mu H]^\dagger [D_{\mu\nu} H] + \text{h.c.})$	
6	$(\bar{q}\gamma^\nu \gamma_5 q) (Z^\mu \partial_\mu Z_\nu)$	-		$(\bar{Q}_L \gamma^\nu Q_L - \bar{u}_R \gamma^\nu u_R) ([D^\mu H]^\dagger [D_{\mu\nu} H] + \text{h.c.})$	
7	$(\bar{q}\gamma^\nu q) (\tilde{Z}_{\nu\sigma} Z^\sigma)$	+	6	$(\bar{Q}_L \gamma^\nu Q_L + \bar{u}_R \gamma^\nu u_R) (\tilde{B}_{\nu\sigma} H^\dagger D^\sigma H + \text{h.c.})$	$\frac{0.4}{E_{\text{TeV}}^5}, \frac{1.2}{E_{\text{TeV}}^6}$
8	$(\bar{q}\gamma^\nu \gamma_5 q) (\tilde{Z}_{\nu\sigma} Z^\sigma)$	+		$(\bar{Q}_L \gamma^\nu Q_L - \bar{u}_R \gamma^\nu u_R) (\tilde{B}_{\nu\sigma} H^\dagger D^\sigma H + \text{h.c.})$	
9	$(\bar{q}q) (Z_{\mu\nu} Z^{\mu\nu})$	+		$(\bar{Q}_L \tilde{H} u_R + \text{h.c.}) (B^{\mu\nu} B_{\mu\nu})$	
10	$(i\bar{q}\gamma_5 q) (Z^{\mu\nu} Z_{\mu\nu})$	-	7	$(i\bar{Q}_L \tilde{H} u_R + \text{h.c.}) (B^{\mu\nu} B_{\mu\nu})$	$\frac{0.4}{E_{\text{TeV}}^3}, \frac{1.2}{E_{\text{TeV}}^4}$
11	$(\bar{q}q) (Z^{\mu\nu} \tilde{Z}_{\mu\nu})$	-		$(\bar{Q}_L \tilde{H} u_R + \text{h.c.}) (B^{\mu\nu} \tilde{B}_{\mu\nu})$	
12	$(i\bar{q}\gamma_5 q) (Z^{\mu\nu} \tilde{Z}_{\mu\nu})$	+		$(i\bar{Q}_L \tilde{H} u_R + \text{h.c.}) (B^{\mu\nu} \tilde{B}_{\mu\nu})$	
13	$(i\bar{q}\sigma_{\mu\nu} \overleftrightarrow{D}_{\rho q}) (Z^\mu \partial^\rho Z^\nu)$	+		$(i\bar{Q}_L \sigma_{\mu\nu} \overleftrightarrow{D}_\rho \tilde{H} u_R + \text{h.c.}) ([D^\mu H]^\dagger [D^{\rho\nu} H] + \text{h.c.})$	
14	$(\bar{q}\sigma_{\mu\nu} \gamma_5 \overleftrightarrow{D}_{\rho q}) (Z^\mu \partial^\rho Z^\nu)$	-	7	$(\bar{Q}_L \sigma_{\mu\nu} \overleftrightarrow{D}_\rho \tilde{H} u_R + \text{h.c.}) ([D^\mu H]^\dagger [D^{\rho\nu} H] + \text{h.c.})$	$\frac{0.02}{E_{\text{TeV}}^5}, \frac{0.07}{E_{\text{TeV}}^6}$
15	$(\bar{q}\overleftrightarrow{D}_{\mu\nu} q) (Z^\mu Z^\nu)$	+		$(\bar{Q}_L \overleftrightarrow{D}_{\mu\nu} \tilde{H} u_R + \text{h.c.}) ([D^\mu H]^\dagger [D^\nu H] + \text{h.c.})$	
16	$(i\bar{q}\gamma_5 \overleftrightarrow{D}_{\mu\nu} q) (Z^\mu Z^\nu)$	-		$(i\bar{Q}_L \overleftrightarrow{D}_{\mu\nu} \tilde{H} u_R + \text{h.c.}) ([D^\mu H]^\dagger [D^\nu H] + \text{h.c.})$	
17	$(i\bar{q}\overleftrightarrow{D}_{\nu q}) (Z^\mu \partial_\mu Z^\nu)$	-		$(i\bar{Q}_L \overleftrightarrow{D}_\nu \tilde{H} u_R + \text{h.c.}) ([D^\mu H]^\dagger [D_\mu^\nu H] + \text{h.c.})$	
18	$(\bar{q}\gamma_5 \overleftrightarrow{D}_{\nu q}) (Z^\mu \partial_\mu Z^\nu)$	+		$(\bar{Q}_L \overleftrightarrow{D}_\nu \tilde{H} u_R + \text{h.c.}) ([D^\mu H]^\dagger [D_\mu^\nu H] + \text{h.c.})$	
19	$(i\bar{q}\overleftrightarrow{D}^{\mu q}) (\tilde{Z}_{\mu\sigma} Z^\sigma)$	+	7	$(i\bar{Q}_L \overleftrightarrow{D}^{\mu} \tilde{H} u_R + \text{h.c.}) (\tilde{B}_{\mu\sigma} H^\dagger D^\sigma H + \text{h.c.})$	$\frac{0.09}{E_{\text{TeV}}^4}, \frac{0.9}{E_{\text{TeV}}^5}$
20	$(\bar{q}\gamma_5 \overleftrightarrow{D}^{\mu q}) (\tilde{Z}_{\mu\sigma} Z^\sigma)$	-		$(\bar{Q}_L \overleftrightarrow{D}^{\mu} \tilde{H} u_R + \text{h.c.}) (\tilde{B}_{\mu\sigma} H^\dagger D^\sigma H + \text{h.c.})$	

Table 3. Primary 5-, 6-, and 7-dimension operators for  $\bar{q}qZZ$  interactions. Under the assumption that  $\bar{q}$  and  $q$  are each other's anti-particles, the operators are Hermitian and have the listed CP properties. If they are not, each of these operators has a Hermitian conjugate, which can be used to create a CP even and a CP odd operator. To simplify the expressions, we use the shorthand  $\overleftrightarrow{D}_{\mu\nu} = \overleftrightarrow{D}_\mu \overleftrightarrow{D}_\nu$ , and similarly,  $\partial_{\mu\nu} = \partial_\mu \partial_\nu$ . To get the descendant operators, one can add contracted derivatives to get arbitrary Mandelstam factors of  $s, (t-u)^2$ .

$i$	$\mathcal{O}_i^{qqZZ}$	CP	$d\mathcal{O}_i$	SMEFT Operator	$c$ Unitarity Bound
21	$(i\bar{q}\gamma^\nu \overleftrightarrow{D}_{\rho q})$ ( $[\partial_\nu Z^\mu] \partial^\rho Z_\mu$ )	+	8	$(i\bar{Q}_L \gamma^\nu \overleftrightarrow{D}_\rho Q_L + i\bar{u}_R \gamma^\nu \overleftrightarrow{D}_\rho u_R)$ ( $[D_\nu^\mu H]^\dagger [D^\rho_\mu H] + \text{h.c.}$ )	$\frac{0.006}{E_{\text{TeV}}^6}$
22	$(i\bar{q}\gamma^\nu \gamma_5 \overleftrightarrow{D}_{\rho q})$ ( $[\partial_\nu Z^\mu] \partial^\rho Z^\mu$ )	+		$(i\bar{Q}_L \gamma^\nu \overleftrightarrow{D}_\rho Q_L - i\bar{u}_R \gamma^\nu \overleftrightarrow{D}_\rho u_R)$ ( $[D_\nu^\mu H]^\dagger [D^\rho_\mu H] + \text{h.c.}$ )	
23	$(\bar{q}\gamma^\nu \overleftrightarrow{D}_{\mu\rho q})$ ( $Z^\mu \partial^\rho Z_\nu$ )	-		$(\bar{Q}_L \gamma^\nu \overleftrightarrow{D}_{\mu\rho} Q_L + \bar{u}_R \gamma^\nu \overleftrightarrow{D}_{\mu\rho} u_R)$ ( $[D^\mu H]^\dagger [D^\rho_\nu H] + \text{h.c.}$ )	
24	$(\bar{q}\gamma^\nu \gamma_5 \overleftrightarrow{D}_{\mu\rho q})$ ( $Z^\mu \partial^\rho Z_\nu$ )	-		$(\bar{Q}_L \gamma^\nu \overleftrightarrow{D}_{\mu\rho} Q_L - \bar{u}_R \gamma^\nu \overleftrightarrow{D}_{\mu\rho} u_R)$ ( $[D^\mu H]^\dagger [D^\rho_\nu H] + \text{h.c.}$ )	
25	$(i\bar{q}\gamma^\nu \overleftrightarrow{D}_{\rho q})$ ( $Z_\mu \partial^\rho Z_\nu$ )	+		$(i\bar{Q}_L \gamma^\nu \overleftrightarrow{D}_\rho Q_L + i\bar{u}_R \gamma^\nu \overleftrightarrow{D}_\rho u_R)$ ( $[D_\mu H]^\dagger [D^{\rho\mu} H] + \text{h.c.}$ )	
26	$(i\bar{q}\gamma^\nu \gamma_5 \overleftrightarrow{D}_{\rho q})$ ( $Z_\mu \partial^\rho Z_\nu$ )	+		$(i\bar{Q}_L \gamma^\nu \overleftrightarrow{D}_\rho Q_L - i\bar{u}_R \gamma^\nu \overleftrightarrow{D}_\rho u_R)$ ( $[D_\mu H]^\dagger [D^{\rho\mu} H] + \text{h.c.}$ )	
27	$(\bar{q}\overleftrightarrow{D}_{\nu\alpha q})$ ( $Z_\mu \partial^{\alpha\mu} Z^\nu$ )	+	9	$(\bar{Q}_L \overleftrightarrow{D}_{\nu\alpha} \overleftrightarrow{H} u_R + \text{h.c.})$ ( $[D_\mu H]^\dagger [D^{\alpha\mu\nu} H] + \text{h.c.}$ )	$\frac{0.001}{E_{\text{TeV}}^7}, \frac{0.004}{E_{\text{TeV}}^8}$
28	$(i\bar{q}\gamma_5 \overleftrightarrow{D}_{\nu\alpha q})$ ( $Z_\mu \partial^{\alpha\mu} Z^\nu$ )	-		$(i\bar{Q}_L \overleftrightarrow{D}_{\nu\alpha} \overleftrightarrow{H} u_R + \text{h.c.})$ ( $[D_\mu H]^\dagger [D^{\alpha\mu\nu} H] + \text{h.c.}$ )	
29	$(i\bar{q}\sigma_{\mu\nu} \gamma_5 \overleftrightarrow{D}_{\rho\sigma q})$ ( $[\partial^\mu Z^\rho] \partial^\sigma Z^\nu$ )	+		$(i\bar{Q}_L \sigma_{\mu\nu} \overleftrightarrow{D}_{\rho\sigma} \overleftrightarrow{H} u_R + \text{h.c.})$ ( $[D^{\mu\rho} H]^\dagger [D^{\sigma\nu} H] + \text{h.c.}$ )	
30	$(\bar{q}\sigma^{\mu\nu} \overleftrightarrow{D}_{\rho\sigma q})$ ( $Z_{\mu\nu} \partial^\sigma Z^\rho$ )	-	9	$(\bar{Q}_L \sigma^{\mu\nu} \overleftrightarrow{D}_{\rho\sigma} \overleftrightarrow{H} u_R + \text{h.c.})$ ( $B_{\mu\nu} H^\dagger D^{\sigma\rho} H + \text{h.c.}$ )	$\frac{0.006}{E_{\text{TeV}}^6}, \frac{0.05}{E_{\text{TeV}}^8}$
31	$(i\bar{q}\sigma^{\mu\nu} \overleftrightarrow{D}_{\sigma q})$ ( $[\partial_\rho Z_{\mu\nu}] \partial^\sigma Z^\rho$ )	+		$(i\bar{Q}_L \sigma^{\mu\nu} \overleftrightarrow{D}_\sigma \overleftrightarrow{H} u_R + \text{h.c.})$ ( $[\partial_\rho B_{\mu\nu}] H^\dagger D^{\sigma\rho} H + \text{h.c.}$ )	
32	$(i\bar{q}\sigma^{\mu\nu} \overleftrightarrow{D}_{\rho q})$ ( $[\partial_\mu \tilde{Z}_{\nu\sigma}] \partial^\rho Z^\sigma$ )	-		$(i\bar{Q}_L \sigma^{\mu\nu} \overleftrightarrow{D}_\rho \overleftrightarrow{H} u_R + \text{h.c.})$ ( $[\partial_\mu \tilde{B}_{\nu\sigma}] H^\dagger D^{\rho\sigma} H + \text{h.c.}$ )	
33	$(\bar{q}\gamma^\mu \overleftrightarrow{D}_{\nu\sigma q})$ ( $[\partial_{\mu\rho} Z^\nu] \partial^\sigma Z^\rho$ )	-	10	$(\bar{Q}_L \gamma^\mu \overleftrightarrow{D}_{\nu\sigma} Q_L + \bar{u}_R \gamma^\mu \overleftrightarrow{D}_{\nu\sigma} u_R)$ ( $[D^\nu_{\mu\rho} H]^\dagger [D^{\sigma\rho} H] + \text{h.c.}$ )	$\frac{3 \times 10^{-4}}{E_{\text{TeV}}^8}$
34	$(i\bar{q}\gamma^\mu \overleftrightarrow{D}_{\sigma q})$ ( $[\partial_{\mu\rho} Z_\nu] \partial^{\sigma\nu} Z^\rho$ )	+		$(i\bar{Q}_L \gamma^\mu \overleftrightarrow{D}_\sigma Q_L + i\bar{u}_R \gamma^\mu \overleftrightarrow{D}_\sigma u_R)$ ( $[D_{\mu\rho\nu} H]^\dagger [D^{\sigma\nu\rho} H] + \text{h.c.}$ )	
35	$(i\bar{q}\gamma^\mu \gamma_5 \overleftrightarrow{D}_{\sigma q})$ ( $[\partial_{\mu\rho} Z_\nu] \partial^{\sigma\nu} Z^\rho$ )	+		$(i\bar{Q}_L \gamma^\mu \overleftrightarrow{D}_\sigma Q_L - i\bar{u}_R \gamma^\mu \overleftrightarrow{D}_\sigma u_R)$ ( $[D_{\mu\rho\nu} H]^\dagger [D^{\sigma\nu\rho} H] + \text{h.c.}$ )	
36	$(\bar{q}\gamma^\alpha \overleftrightarrow{D}^{\mu\beta} q)$ ( $\tilde{Z}_{\mu\rho} \partial^{\rho\beta} Z_\alpha$ )	+	10	$(\bar{Q}_L \gamma^\alpha \overleftrightarrow{D}^{\mu\beta} Q_L + \bar{u}_R \gamma^\alpha \overleftrightarrow{D}^{\mu\beta} u_R)$ ( $\tilde{B}_{\mu\rho} H^\dagger D^{\rho\beta} H + \text{h.c.}$ )	$\frac{0.001}{E_{\text{TeV}}^7}, \frac{0.004}{E_{\text{TeV}}^8}$
37	$(\bar{q}\gamma^\alpha \gamma_5 \overleftrightarrow{D}^{\mu\beta} q)$ ( $\tilde{Z}_{\mu\rho} \partial^{\rho\beta} Z_\alpha$ )	+		$(\bar{Q}_L \gamma^\alpha \overleftrightarrow{D}^{\mu\beta} Q_L - \bar{u}_R \gamma^\alpha \overleftrightarrow{D}^{\mu\beta} u_R)$ ( $\tilde{B}_{\mu\rho} H^\dagger D^{\rho\beta} H + \text{h.c.}$ )	
38	$(i\bar{q}\gamma^\rho \gamma_5 \overleftrightarrow{D}^{\mu\alpha\beta} q)$ ( $\tilde{Z}_{\mu\rho} \partial^\beta Z^\alpha$ )	-		$(i\bar{Q}_L \gamma^\rho \overleftrightarrow{D}^{\mu\alpha\beta} Q_L - i\bar{u}_R \gamma^\rho \overleftrightarrow{D}^{\mu\alpha\beta} u_R)$ ( $\tilde{B}_{\mu\rho} H^\dagger D^{\alpha\beta} H + \text{h.c.}$ )	

Table 4. Primary 8-, 9-, and 10-dimension operators for  $\bar{q}qZZ$  interactions. Under the assumption that  $\bar{q}$  and  $q$  are each other's anti-particles, the operators are Hermitian and have the listed CP properties. If they are not, each of these operators has a Hermitian conjugate, which can be used to create a CP even and a CP odd operator. To simplify the expressions, we use the shorthand  $\overleftrightarrow{D}_{\mu\nu} = \overleftrightarrow{D}_\mu \overleftrightarrow{D}_\nu$ , and similarly,  $\partial_{\mu\nu} = \partial_\mu \partial_\nu$ . To get the descendant operators, one can add contracted derivatives to get arbitrary Mandelstam factors of  $s, (t-u)^2$ . At dimension 11,  $s\mathcal{O}_{31}$  and  $s\mathcal{O}_{32}$  become redundant to other operators. Thus, for these two, we need only their  $(t-u)^{2n} \mathcal{O}_{31}$  and  $(t-u)^{2n} \mathcal{O}_{32}$  descendants.

To get  $\bar{q}qZg$  operators, one replaces  $F^{\mu\nu} \rightarrow G^{\mu\nu}$ , to get  $\bar{q}q'W\gamma$  operators, one should make the replacement  $q \rightarrow q'$  and  $Z \rightarrow W$ , and to get  $\bar{q}q'Wg$  operators one needs to make the replacements  $q \rightarrow q'$ ,  $F^{\mu\nu} \rightarrow G^{\mu\nu}$ , and  $Z \rightarrow W$ .

Table 6 lists the primary operators for  $\bar{q}qg\gamma$  interactions. Reading the appropriate Hilbert series, we expect to find 6 dimension 7 operators, 8 dimension 8 operators, and 4 dimension 9 operators, as well as 2 operators that become redundant at dimension 9, so the analysis again finds 2 additional dimension 9 primary operators that a quick interpretation of the Hilbert series would have missed. We indeed find the 18 operators we expect from the Hilbert series analysis, as well as two operators that become redundant at dimension 9— $s\mathcal{O}_5$  and  $s\mathcal{O}_6$ . Thus, for those two operators, we can just add their descendants  $t^n\mathcal{O}_5$  and  $t^n\mathcal{O}_6$ .

We list the primary operators for  $\bar{q}q\gamma\gamma$  interactions in Table 7. From the Hilbert series, we expect that there should be 4 operators at dimension 7, 2 operators at dimension 8, 4 operators at dimension 9, 6 operators at dimension 10, and 2 operators at dimension 11. We also find that there are two new redundancies at dimension 11. This again gives rise to a complete cancellation at dimension 11. We find 18 primary operators, in agreement with the Hilbert series. We also find two new constraints at dimension 11,  $s\mathcal{O}_7$  and  $s\mathcal{O}_8$ . For those two operators, we only need to add their descendant operators  $(t-u)^{2n}\mathcal{O}_7$  and  $(t-u)^{2n}\mathcal{O}_8$ .

In Tables 8 and 9, we list all of the primary operators for  $\bar{q}qgg$  interactions. The Hilbert series says that we should expect 10 operators at dimension 7, 10 operators at dimension 8, 14 operators at dimension 9, 14 operators at dimension 10, and 6 operators at dimension 11. Additionally, we find that there are 2 redundancies at dimension 9— $s\mathcal{O}_9$  and  $s\mathcal{O}_{10}$ —and 4 redundancies at dimension 11— $s\mathcal{O}_{21}$ ,  $s\mathcal{O}_{22}$ ,  $s\mathcal{O}_{23}$ , and  $s\mathcal{O}_{24}$ . As noted in Sec. 2.2, there are three ways we can contract the  $SU(3)$  indices,

$i$	$\mathcal{O}_i^{\bar{q}qZ\gamma}$	CP	$d\mathcal{O}_i$	SMEFT Operator	$c$ Unitarity Bound
1	$(\bar{q}\gamma^\nu q)(F_{\nu\mu}Z^\mu)$	-	6	$(\bar{Q}_L\gamma^\nu Q_L + \bar{u}_R\gamma^\nu u_R)(B_{\nu\mu}H^\dagger D^\mu H + \text{h.c.})$	$\frac{0.4}{E_{\text{TeV}}^3}, \frac{1.2}{E_{\text{TeV}}^4}$
2	$(\bar{q}\gamma^\nu\gamma_5 q)(F_{\nu\mu}Z^\mu)$	-		$(\bar{Q}_L\gamma^\nu Q_L - \bar{u}_R\gamma^\nu u_R)(B_{\nu\mu}H^\dagger D^\mu H + \text{h.c.})$	
3	$(\bar{q}\gamma^\nu q)(\bar{F}_{\nu\sigma}Z^\sigma)$	+		$(\bar{Q}_L\gamma^\nu Q_L + \bar{u}_R\gamma^\nu u_R)(\bar{B}_{\nu\sigma}H^\dagger D^\sigma H + \text{h.c.})$	
4	$(\bar{q}\gamma^\nu\gamma_5 q)(\bar{F}_{\nu\sigma}Z^\sigma)$	+		$(\bar{Q}_L\gamma^\nu Q_L - \bar{u}_R\gamma^\nu u_R)(\bar{B}_{\nu\sigma}H^\dagger D^\sigma H + \text{h.c.})$	
5	$(\bar{q}q)(F_{\mu\nu}Z^{\mu\nu})$	+	7	$(\bar{Q}_L\bar{H}u_R + \text{h.c.})(B_{\mu\nu}B^{\mu\nu})$	$\frac{0.4}{E_{\text{TeV}}^3}, \frac{1.2}{E_{\text{TeV}}^4}$
6	$(i\bar{q}\gamma_5 q)(F_{\mu\nu}Z^{\mu\nu})$	-		$(i\bar{Q}_L\bar{H}u_R + \text{h.c.})(B_{\mu\nu}B^{\mu\nu})$	
7	$(\bar{q}q)(\bar{F}_{\mu\nu}Z^{\mu\nu})$	-		$(\bar{Q}_L\bar{H}u_R + \text{h.c.})(B^{\mu\nu}B_{\mu\nu})$	
8	$(i\bar{q}\gamma_5 q)(\bar{F}_{\mu\nu}Z^{\mu\nu})$	+		$(i\bar{Q}_L\bar{H}u_R + \text{h.c.})(B^{\mu\nu}B_{\mu\nu})$	
9	$(i\bar{q}\overleftrightarrow{D}_{\nu q})(F^{\nu\mu}Z_\mu)$	-	7	$(i\bar{Q}_L\overleftrightarrow{D}_{\nu}\bar{H}u_R + \text{h.c.})(B^{\nu\mu}H^\dagger D_\mu H + \text{h.c.})$	$\frac{0.09}{E_{\text{TeV}}^3}, \frac{0.9}{E_{\text{TeV}}^4}$
10	$(q\overleftrightarrow{D}_{\nu\gamma_5 q})(F^{\nu\mu}Z_\mu)$	+		$(\bar{Q}_L\overleftrightarrow{D}_{\nu}\bar{H}u_R + \text{h.c.})(B^{\nu\mu}H^\dagger D_\mu H + \text{h.c.})$	
11	$(i\bar{q}\sigma_{\mu\nu}\overleftrightarrow{D}_{\rho q})(F^{\mu\rho}Z^\nu)$	+		$(i\bar{Q}_L\sigma_{\mu\nu}\overleftrightarrow{D}_{\rho}\bar{H}u_R + \text{h.c.})(B^{\rho\mu}H^\dagger D^\nu H + \text{h.c.})$	
12	$(\bar{q}\sigma_{\mu\nu}q)(F^{\mu\rho}\partial_\rho Z^\nu)$	-		$(\bar{Q}_L\sigma_{\mu\nu}\bar{H}u_R + \text{h.c.})(B^{\mu\rho}H^\dagger D^\nu H + \text{h.c.})$	
13	$(\bar{q}\sigma_{\mu\nu}\gamma_5\overleftrightarrow{D}_{\rho q})(F^{\mu\rho}Z^\nu)$	-		$(\bar{Q}_L\sigma_{\mu\nu}\overleftrightarrow{D}_{\rho}\bar{H}u_R + \text{h.c.})(B^{\mu\rho}H^\dagger D^\nu H + \text{h.c.})$	
14	$(i\bar{q}\sigma_{\mu\nu}\gamma_5 q)(F^{\mu\rho}\partial_\rho Z^\nu)$	+		$(i\bar{Q}_L\sigma_{\mu\nu}\bar{H}u_R + \text{h.c.})(B^{\mu\rho}H^\dagger D^\nu H + \text{h.c.})$	
15	$(i\bar{q}\overleftrightarrow{D}_{\mu q})(\bar{F}_{\mu\sigma}Z^\sigma)$	+		$(i\bar{Q}_L\overleftrightarrow{D}_{\mu}\bar{H}u_R + \text{h.c.})(\bar{B}_{\mu\sigma}H^\dagger D^\sigma H + \text{h.c.})$	
16	$(\bar{q}\gamma_5\overleftrightarrow{D}_{\mu q})(\bar{F}_{\mu\sigma}Z^\sigma)$	-		$(\bar{Q}_L\overleftrightarrow{D}_{\mu}\bar{H}u_R + \text{h.c.})(\bar{B}_{\mu\sigma}H^\dagger D^\sigma H + \text{h.c.})$	
17	$(\bar{q}\gamma^\nu q)(\{\partial_\nu F^{\mu\rho}\}Z_{\mu\rho})$	-	8	$(\bar{Q}_L\gamma^\nu Q_L + \bar{u}_R\gamma^\nu u_R)(\{\partial_\nu B^{\mu\rho}\}B_{\mu\rho})$	$\frac{0.09}{E_{\text{TeV}}^4}$
18	$(\bar{q}\gamma^\nu\gamma_5 q)(\{\partial_\nu F^{\mu\rho}\}Z_{\mu\rho})$	-		$(\bar{Q}_L\gamma^\nu Q_L - \bar{u}_R\gamma^\nu u_R)(\{\partial_\nu B^{\mu\rho}\}B_{\mu\rho})$	
19	$(i\bar{q}\gamma^\nu\overleftrightarrow{D}_{\rho q})(\{\partial_\nu F^{\mu\rho}\}Z_\mu)$	+	8	$(i\bar{Q}_L\gamma^\nu\overleftrightarrow{D}_{\rho}Q_L + i\bar{u}_R\gamma^\nu\overleftrightarrow{D}_{\rho}u_R)(\{\partial_\nu B^{\mu\rho}\}H^\dagger D_\mu H + \text{h.c.})$	$\frac{0.02}{E_{\text{TeV}}^5}, \frac{0.07}{E_{\text{TeV}}^6}$
20	$(i\bar{q}\gamma^\nu\gamma_5\overleftrightarrow{D}_{\rho q})(\{\partial_\nu F^{\mu\rho}\}Z_\mu)$	+		$(i\bar{Q}_L\gamma^\nu\overleftrightarrow{D}_{\rho}Q_L - i\bar{u}_R\gamma^\nu\overleftrightarrow{D}_{\rho}u_R)(\{\partial_\nu B^{\mu\rho}\}H^\dagger D_\mu H + \text{h.c.})$	
21	$(i\bar{q}\gamma^\nu\overleftrightarrow{D}_{\mu q})(F^{\mu\rho}\partial_\rho Z_\nu)$	+		$(i\bar{Q}_L\gamma^\nu\overleftrightarrow{D}_{\mu}Q_L + i\bar{u}_R\gamma^\nu\overleftrightarrow{D}_{\mu}u_R)(B^{\mu\rho}H^\dagger D_{\nu\rho}H + \text{h.c.})$	
22	$(i\bar{q}\gamma^\nu\gamma_5\overleftrightarrow{D}_{\mu q})(F^{\mu\rho}\partial_\rho Z_\nu)$	+		$(i\bar{Q}_L\gamma^\nu\overleftrightarrow{D}_{\mu}Q_L - i\bar{u}_R\gamma^\nu\overleftrightarrow{D}_{\mu}u_R)(B^{\mu\rho}H^\dagger D_{\nu\rho}H + \text{h.c.})$	
23	$(\bar{q}\gamma_\mu\overleftrightarrow{D}_{\nu\rho q})(F^{\mu\rho}Z^\nu)$	-		$(\bar{Q}_L\gamma_\mu\overleftrightarrow{D}_{\nu\rho}Q_L + \bar{u}_R\gamma_\mu\overleftrightarrow{D}_{\nu\rho}u_R)(B^{\mu\rho}H^\dagger D^\nu H + \text{h.c.})$	
24	$(\bar{q}\gamma_\mu\gamma_5\overleftrightarrow{D}_{\nu\rho q})(F^{\mu\rho}Z^\nu)$	-		$(\bar{Q}_L\gamma_\mu\overleftrightarrow{D}_{\nu\rho}Q_L - \bar{u}_R\gamma_\mu\overleftrightarrow{D}_{\nu\rho}u_R)(B^{\mu\rho}H^\dagger D^\nu H + \text{h.c.})$	
25	$(\bar{q}\overleftrightarrow{D}_{\mu\nu}q)(F^{\mu\rho}\partial_\rho Z^\nu)$	+	9	$(\bar{Q}_L\overleftrightarrow{D}_{\mu\nu}\bar{H}u_R + \text{h.c.})(B^{\mu\rho}H^\dagger D^\nu H + \text{h.c.})$	$\frac{0.006}{E_{\text{TeV}}^6}, \frac{0.05}{E_{\text{TeV}}^8}$
26	$(i\bar{q}\gamma_5\overleftrightarrow{D}_{\mu\nu}q)(F^{\mu\rho}\partial_\rho Z^\nu)$	-		$(i\bar{Q}_L\overleftrightarrow{D}_{\mu\nu}\bar{H}u_R + \text{h.c.})(B^{\mu\rho}H^\dagger D^\nu H + \text{h.c.})$	

Table 5. Primary operators for  $\bar{q}qZ\gamma$  interactions. As outlined in the text, these operators can be modified to yield the operators for  $\bar{q}qZg$ ,  $\bar{q}q'W\gamma$ , and  $\bar{q}q'Wg$  interactions. Under the assumption that  $\bar{q}$  and  $q$  are each other's anti-particles, the operators are Hermitean and have the listed CP properties. If they are not, each of these operators has a Hermitean conjugate, which can be used to create a CP even and a CP odd operator.

To simplify the expressions, we use the shorthand  $\overleftrightarrow{D}_{\mu\nu} = \overleftrightarrow{D}_\mu\overleftrightarrow{D}_\nu$ , and similarly,  $D_{\mu\nu} = D_\mu D_\nu$ . To get the descendant operators, once can add contracted derivatives to get arbitrary Mandelstam factors of  $s, t$ . At dimension 9,  $s\mathcal{O}_7$  and  $s\mathcal{O}_8$  become redundant to other operators. For these two, one only needs their  $t^n\mathcal{O}_7$  and  $t^n\mathcal{O}_8$  descendants.

$i$	$\mathcal{O}_i^{\bar{q}qg\gamma}$	CP	$d_{\mathcal{O}_i}$	SMEFT Operator	$c$ Unitarity Bound
1	$(\bar{q}q)(F^{\mu\nu}G_{\mu\nu})$	+	7	$(\bar{Q}_L\tilde{H}u_R + \text{h.c.})(B^{\mu\nu}G_{\mu\nu})$	$\frac{0.4}{E_{\text{TeV}}^3}, \frac{1.2}{E_{\text{TeV}}^4}$
2	$(i\bar{q}\gamma_5q)(F^{\mu\nu}G_{\mu\nu})$	-		$(i\bar{Q}_L\tilde{H}u_R + \text{h.c.})(B^{\mu\nu}G_{\mu\nu})$	
3	$(\bar{q}\sigma_{\mu\nu}q)(F^{\mu\rho}G_{\nu\rho}^\nu)$	-		$(\bar{Q}_L\sigma_{\mu\nu}\tilde{H}u_R + \text{h.c.})(B^{\mu\rho}G_{\nu\rho}^\nu)$	
4	$(i\bar{q}\sigma_{\mu\nu}\gamma_5q)(F^{\mu\rho}G_{\nu\rho}^\nu)$	+		$(i\bar{Q}_L\sigma_{\mu\nu}\gamma_5\tilde{H}u_R + \text{h.c.})(B^{\mu\rho}G_{\nu\rho}^\nu)$	
5	$(\bar{q}q)(F^{\mu\nu}\tilde{G}_{\mu\nu})$	-		$(\bar{Q}_L\tilde{H}u_R + \text{h.c.})(B^{\mu\nu}\tilde{G}_{\mu\nu})$	
6	$(i\bar{q}\gamma_5q)(F^{\mu\nu}\tilde{G}_{\mu\nu})$	+		$(\bar{Q}_R\tilde{H}u_R + \text{h.c.})(B^{\mu\nu}\tilde{G}_{\mu\nu})$	
7	$(\bar{q}\gamma^\nu q)([\partial_\nu F^{\mu\rho}]G_{\mu\rho})$	-	8	$(\bar{Q}_L\gamma^\nu Q_L + \bar{u}_R\gamma^\nu u_R)([\partial_\nu B^{\mu\rho}]G_{\mu\rho})$	$\frac{0.09}{E_{\text{TeV}}^4}$
8	$(\bar{q}\gamma^\nu\gamma_5q)([\partial_\nu F^{\mu\rho}]G_{\mu\rho})$	-		$(\bar{Q}_L\gamma^\nu Q_L - \bar{u}_R\gamma^\nu u_R)([\partial_\nu B^{\mu\rho}]G_{\mu\rho})$	
9	$(i\bar{q}\gamma^\nu\overleftrightarrow{D}_\mu q)(F^{\mu\rho}G_{\nu\rho})$	+		$(i\bar{Q}_L\gamma^\nu\overleftrightarrow{D}_\mu Q_L + i\bar{u}_R\gamma^\nu\overleftrightarrow{D}_\mu u_R)(B^{\mu\rho}G_{\nu\rho})$	
10	$(i\bar{q}\gamma^\nu\gamma_5\overleftrightarrow{D}_\mu q)(F^{\mu\rho}G_{\nu\rho})$	+		$(i\bar{Q}_L\gamma^\nu\overleftrightarrow{D}_\mu Q_L - i\bar{u}_R\gamma^\nu\overleftrightarrow{D}_\mu u_R)(B^{\mu\rho}G_{\nu\rho})$	
11	$(i\bar{q}\gamma^\nu\overleftrightarrow{D}_\rho q)(F_{\nu\mu}G^{\rho\mu})$	+		$(i\bar{Q}_L\gamma^\nu\overleftrightarrow{D}_\rho Q_L + i\bar{u}_R\gamma^\nu\overleftrightarrow{D}_\rho u_R)(B_{\nu\mu}G^{\rho\mu})$	
12	$(i\bar{q}\gamma^\nu\gamma_5\overleftrightarrow{D}_\rho q)(F_{\nu\mu}G^{\rho\mu})$	+		$(i\bar{Q}_L\gamma^\nu\overleftrightarrow{D}_\rho Q_L - i\bar{u}_R\gamma^\nu\overleftrightarrow{D}_\rho u_R)(B_{\nu\mu}G^{\rho\mu})$	
13	$(i\bar{q}\gamma^\nu\overleftrightarrow{D}_\rho q)(\tilde{F}_{\mu\nu}G^{\mu\rho})$	-		$(i\bar{Q}_L\gamma^\nu\overleftrightarrow{D}_\rho Q_L + i\bar{u}_R\gamma^\nu\overleftrightarrow{D}_\rho u_R)(\tilde{B}_{\mu\nu}G^{\mu\rho})$	
14	$(i\bar{q}\gamma^\nu\gamma_5\overleftrightarrow{D}_\rho q)(\tilde{F}_{\mu\nu}G^{\mu\rho})$	-		$(i\bar{Q}_L\gamma^\nu\overleftrightarrow{D}_\rho Q_L - i\bar{u}_R\gamma^\nu\overleftrightarrow{D}_\rho u_R)(\tilde{B}_{\mu\nu}G^{\mu\rho})$	
15	$(\bar{q}\overleftrightarrow{D}_{\mu\nu}q)(F^{\mu\rho}G_{\nu\rho}^\nu)$	+	9	$(\bar{Q}_L\overleftrightarrow{D}_{\mu\nu}\tilde{H}u_R + \text{h.c.})(B^{\mu\rho}G_{\nu\rho}^\nu)$	$\frac{0.02}{E_{\text{TeV}}^5}, \frac{0.07}{E_{\text{TeV}}^6}$
16	$(i\bar{q}\gamma_5\overleftrightarrow{D}_{\mu\nu}q)(F^{\mu\rho}G_{\nu\rho}^\nu)$	-		$(i\bar{Q}_L\overleftrightarrow{D}_{\mu\nu}\tilde{H}u_R + \text{h.c.})(B^{\mu\rho}G_{\nu\rho}^\nu)$	
17	$(i\bar{q}\sigma_{\mu\nu}\overleftrightarrow{D}_\sigma q)(F^{\mu\rho}D_\rho G^{\nu\sigma})$	+		$(i\bar{Q}_L\sigma_{\mu\nu}\overleftrightarrow{D}_\sigma\tilde{H}u_R + \text{h.c.})(B^{\mu\rho}D_\rho G^{\nu\sigma})$	
18	$(\bar{q}\sigma_{\mu\nu}\gamma_5\overleftrightarrow{D}_\rho q)(F^{\mu\sigma}D_\sigma G^{\nu\rho})$	-		$(\bar{Q}_L\sigma_{\mu\nu}\overleftrightarrow{D}_\rho u_R + \text{h.c.})(B^{\mu\sigma}D_\sigma G^{\nu\rho})$	

Table 6. Primary operators for  $\bar{q}qg\gamma$  interactions. Under the assumption that  $\bar{q}$  and  $q$  are each other's anti-particles, the operators are Hermitian and have the listed CP properties. If they are not, each of these operators has a Hermitian conjugate, which can be used to create a CP even and a CP odd operator. To simplify the expressions, we use the shorthand  $\overleftrightarrow{D}_{\mu\nu} = \overleftrightarrow{D}_\mu\overleftrightarrow{D}_\nu$ . To get the descendant operators, one can add contracted derivatives to get arbitrary Mandelstam factors of  $s, t$ . At dimension 9,  $s\mathcal{O}_5$  and  $s\mathcal{O}_6$  become redundant to other operators. For these two, one only needs their  $t^n\mathcal{O}_5$  and  $t^n\mathcal{O}_6$  descendants.

$i$	$\mathcal{O}_i^{\bar{q}q\gamma\gamma}$	CP	$d_{\mathcal{O}_i}$	SMEFT Operator	$c$ Unitarity Bound
1	$(\bar{q}q)(F^{\mu\nu}F_{\mu\nu})$	+	7	$(\bar{Q}_L\tilde{H}u_R + \text{h.c.})(B^{\mu\nu}B_{\mu\nu})$	$\frac{0.4}{E_{\text{TeV}}^3}, \frac{1.2}{E_{\text{TeV}}^4}$
2	$(\bar{q}\gamma_5 q)(F^{\mu\nu}F_{\mu\nu})$	-		$(i\bar{Q}_L\tilde{H}u_R + \text{h.c.})(B^{\mu\nu}B_{\mu\nu})$	
3	$(\bar{q}q)(F^{\mu\nu}\tilde{F}_{\mu\nu})$	-		$(\bar{Q}_L\tilde{H}u_R + \text{h.c.})(B^{\mu\nu}\tilde{B}_{\mu\nu})$	
4	$(i\bar{q}\gamma_5 q)(F^{\mu\nu}\tilde{F}_{\mu\nu})$	+		$(i\bar{Q}_L\tilde{H}u_R + \text{h.c.})(B^{\mu\nu}\tilde{B}_{\mu\nu})$	
5	$(i\bar{q}\gamma^\nu\overleftrightarrow{D}_\mu q)(F^{\mu\rho}F_{\rho\nu})$	+	8	$(i\bar{Q}_L\overleftrightarrow{D}_\mu\gamma^\nu Q_L + i\bar{u}_R\overleftrightarrow{D}_\mu\gamma^\nu u_R)(B^{\mu\rho}B_{\rho\nu})$	$\frac{0.09}{E_{\text{TeV}}^4}$
6	$(i\bar{q}\gamma^\nu\gamma_5\overleftrightarrow{D}_\mu q)(F^{\mu\rho}F_{\rho\nu})$	+		$(i\bar{Q}_L\overleftrightarrow{D}_\mu\gamma^\nu Q_L - i\bar{u}_R\overleftrightarrow{D}_\mu\gamma^\nu u_R)(B^{\mu\rho}B_{\rho\nu})$	
7	$(i\bar{q}\sigma_{\mu\nu}\overleftrightarrow{D}_\rho q)(F^{\mu\sigma}\partial^\rho F^\nu{}_\sigma)$	+	9	$(i\bar{Q}_L\sigma_{\mu\nu}\overleftrightarrow{D}_\rho\tilde{H}u_R + \text{h.c.})(B^{\mu\sigma}\partial^\rho B^\nu{}_\sigma)$	$\frac{0.02}{E_{\text{TeV}}^5}, \frac{0.07}{E_{\text{TeV}}^6}$
8	$(\bar{q}\sigma_{\mu\nu}\gamma_5\overleftrightarrow{D}_\rho q)(F^{\mu\sigma}\partial^\rho F^\nu{}_\sigma)$	-		$(\bar{Q}_L\sigma_{\mu\nu}\overleftrightarrow{D}_\rho\tilde{H}u_R + \text{h.c.})(B^{\mu\sigma}\partial^\rho B^\nu{}_\sigma)$	
9	$(\bar{q}\overleftrightarrow{D}_{\mu\nu}q)(F^{\mu\rho}F^\nu{}_\rho)$	+		$(\bar{Q}_L\overleftrightarrow{D}_{\mu\nu}\tilde{H}u_R + \text{h.c.})(B^{\mu\rho}B^\nu{}_\rho)$	
10	$(i\bar{q}\gamma_5\overleftrightarrow{D}_{\mu\nu}q)(F^{\mu\rho}F^\nu{}_\rho)$	-		$(i\bar{Q}_L\overleftrightarrow{D}_{\mu\nu}\tilde{H}u_R + \text{h.c.})(B^{\mu\rho}B^\nu{}_\rho)$	
11	$(i\bar{q}\gamma^\nu\overleftrightarrow{D}_\rho q)([\partial_\nu F^{\mu\sigma}]\partial^\rho F_{\mu\sigma})$	+	10	$(i\bar{Q}_L\gamma^\nu\overleftrightarrow{D}_\rho Q_L + i\bar{u}_R\gamma^\nu\overleftrightarrow{D}_\rho u_R)([\partial_\nu B^{\mu\sigma}]\partial^\rho B_{\mu\sigma})$	$\frac{0.006}{E_{\text{TeV}}^5}$
12	$(i\bar{q}\gamma^\nu\gamma_5\overleftrightarrow{D}_\rho q)([\partial_\nu F^{\mu\sigma}]\partial^\rho F_{\mu\sigma})$	+		$(i\bar{Q}_L\gamma^\nu\overleftrightarrow{D}_\rho Q_L - i\bar{u}_R\gamma^\nu\overleftrightarrow{D}_\rho u_R)([\partial_\nu B^{\mu\sigma}]\partial^\rho B_{\mu\sigma})$	
13	$(\bar{q}\gamma^\nu\overleftrightarrow{D}_{\mu\sigma}q)(F^{\mu\rho}\partial^\sigma F_{\nu\rho})$	-		$(\bar{Q}_L\gamma^\nu\overleftrightarrow{D}_{\mu\sigma}Q_L + \bar{u}_R\gamma^\nu\overleftrightarrow{D}_{\mu\sigma}u_R)(B^{\mu\rho}\partial^\sigma B_{\nu\rho})$	
14	$(\bar{q}\gamma^\nu\gamma_5\overleftrightarrow{D}_{\mu\sigma}q)(F^{\mu\rho}\partial^\sigma F_{\nu\rho})$	-		$(\bar{Q}_L\gamma^\nu\overleftrightarrow{D}_{\mu\sigma}Q_L - \bar{u}_R\gamma^\nu\overleftrightarrow{D}_{\mu\sigma}u_R)(B^{\mu\rho}\partial^\sigma B_{\nu\rho})$	
15	$(\bar{q}\gamma^\nu\overleftrightarrow{D}_{\alpha\beta}q)(\tilde{F}_{\nu\sigma}\partial^\beta F^{\sigma\alpha})$	+		$(\bar{Q}_L\gamma^\nu\overleftrightarrow{D}_{\alpha\beta}Q_L + \bar{u}_R\gamma^\nu\overleftrightarrow{D}_{\alpha\beta}u_R)(\tilde{B}_{\nu\sigma}\partial^\beta B^{\sigma\alpha})$	
16	$(\bar{q}\gamma^\nu\gamma_5\overleftrightarrow{D}_{\alpha\beta}q)(\tilde{F}_{\nu\sigma}\partial^\beta F^{\sigma\alpha})$	+		$(\bar{Q}_L\gamma^\nu\overleftrightarrow{D}_{\alpha\beta}Q_L - \bar{u}_R\gamma^\nu\overleftrightarrow{D}_{\alpha\beta}u_R)(\tilde{B}_{\nu\sigma}\partial^\beta B^{\sigma\alpha})$	
17	$(\bar{q}\sigma_{\mu\nu}\overleftrightarrow{D}_{\sigma\alpha}q)(F^{\mu\rho}\partial_\rho^\alpha F^{\nu\sigma})$	-	11	$(\bar{Q}_L\sigma_{\mu\nu}\overleftrightarrow{D}_{\sigma\alpha}\tilde{H}u_R + \text{h.c.})(B^{\mu\rho}\partial_\rho^\alpha B^{\nu\sigma})$	$\frac{0.001}{E_{\text{TeV}}^7}, \frac{0.004}{E_{\text{TeV}}^8}$
18	$(i\bar{q}\sigma_{\mu\nu}\gamma_5\overleftrightarrow{D}_{\sigma\alpha}q)(F^{\mu\rho}\partial_\rho^\alpha F^{\nu\sigma})$	+		$(i\bar{Q}_L\sigma_{\mu\nu}\overleftrightarrow{D}_{\sigma\alpha}\tilde{H}u_R + \text{h.c.})(B^{\mu\rho}\partial_\rho^\alpha B^{\nu\sigma})$	

Table 7. Primary operators for  $\bar{q}q\gamma\gamma$  interactions. Under the assumption that  $\bar{q}$  and  $q$  are each other's anti-particles, the operators are Hermitean and have the listed CP properties. If they are not, each of these operators has a Hermitean conjugate, which can be used to create a CP even and a CP odd operator. To simplify the expressions, we use the shorthand  $\overleftrightarrow{D}_{\mu\nu} = \overleftrightarrow{D}_\mu\overleftrightarrow{D}_\nu$ , and similarly,  $\partial_{\mu\nu} = \partial_\mu\partial_\nu$ . To get the descendant operators, one can add contracted derivatives to get arbitrary Mandelstam factors of  $s, (t-u)^2$ . At dimension 11,  $s\mathcal{O}_7$  and  $s\mathcal{O}_8$  become redundant to other operators. For these two, one only needs their  $(t-u)^{2n}$   $\mathcal{O}_7$  and  $(t-u)^{2n}$   $\mathcal{O}_8$  descendants.

two symmetric and one antisymmetric. For example,  $\mathcal{O}_1$  and  $\mathcal{O}_2$  in Table 8 should be read as  $(\bar{q}\delta_{AB}q)(G^{A\mu\nu}G_{\mu\nu}^B)$  and  $d_{ABC}(\bar{q}T^A q)(G^{B\mu\nu}G_{\mu\nu}^C)$ , respectively, where  $T^A$  are the generators of  $SU(3)$ .  $\mathcal{O}_7$  in Table 8 should be ready as  $f_{ABC}(\bar{q}T^A q)(G^{B\mu\nu}G_{\mu\nu}^C)$ . Thus, for  $\mathcal{O}_{9,10,21,22,23,24}$ , we only need to add their descendants with factors of  $(t-u)^2$ .

### 2.4.2 $ffff$ Amplitudes

In Table 10, we've listed the primary operators for  $\bar{q}q\bar{\ell}\ell$  interactions. As the numerators of the Hilbert series suggests, there should be 10 primaries at dimension 6, 8 primaries at dimension 7, and at least two redundancies at dimension 8. This is precisely what we find with the listed 18 operators, where at dimension 8,  $s\mathcal{O}_9$  and  $s\mathcal{O}_{10}$  are redundant to the other operators, where  $s = (p_q + p_{\bar{q}})^2$ . Thus, for those two operators, one only needs their descendants  $t^n\mathcal{O}_9$  and  $t^n\mathcal{O}_{10}$ . We've listed a potential SMEFT operator to realize this interaction. In some cases, a linear combination of the amplitudes may have a lower dimension SMEFT operator. For example,  $\bar{q}q\bar{\ell}\ell - \bar{q}i\gamma_5 q\bar{\ell}i\gamma_5 \ell$  can be realized by the SMEFT operator  $(\epsilon^{ab}\bar{Q}_{La}u_R\bar{L}_{Lb}e_R + \text{h.c.})$ . This would affect the unitarity bound by removing the higher multiplicity bound of  $15/E_{\text{TeV}}^4$ . We can also convert these operators to account for baryon-lepton interactions between  $uu'd\bar{e}$  and  $udd'\nu$ . The primes indicate different flavors and thus, we do not need to consider any issues with indistinguishable particles. For example,  $tcde$  interactions can be found by replacing  $\bar{q} \rightarrow \bar{t}^c, q \rightarrow c, \bar{\ell} \rightarrow \bar{e}^c, \ell \rightarrow d$  where  $t^c$  and  $e^c$  are the charge conjugated 4-component spinor for the top quark and the electron and the  $SU(3)$  indices are contracted with an epsilon tensor. For the baryon-neutrino coupling, the number of operators would depend on whether the neutrino is Majorana or Dirac, where the Dirac case has twice the operators, since one can use either  $\bar{\nu}$  or  $\bar{\nu}^c$ .

$i$	$\mathcal{O}_i^{\bar{q}qgg}$	CP	$d\mathcal{O}_i$	$SU(3)$	SMEFT Operator	$c$ Unitarity Bound
1, 2	$(\bar{q}q) (G^{\mu\nu} G_{\mu\nu})$	+	7	$\delta_{AB}, d_{ABC}$	$(\bar{Q}_L \tilde{H}_{uR} + \text{h.c.}) (G^{\mu\nu} G_{\mu\nu})$	$\frac{0.4}{E_{\text{TeV}}^3}, \frac{1.2}{E_{\text{TeV}}^4}$
3, 4	$(i\bar{q}\gamma_{15}q) (G^{\mu\nu} G_{\mu\nu})$	-			$(i\bar{Q}_L \tilde{H}_{uR} + \text{h.c.}) (G^{\mu\nu} G_{\mu\nu})$	
5, 6	$(\bar{q}q) (G^{\mu\nu} \tilde{G}_{\mu\nu})$	-			$(\bar{Q}_L \tilde{H}_{uR} + \text{h.c.}) (G^{\mu\nu} \tilde{G}_{\mu\nu})$	
7, 8	$(i\bar{q}\gamma_{15}q) (G^{\mu\nu} \tilde{G}_{\mu\nu})$	+			$(i\bar{Q}_L \tilde{H}_{uR} + \text{h.c.}) (G^{\mu\nu} \tilde{G}_{\mu\nu})$	
9	$(\bar{q}\sigma_{\mu\nu}q) (G^{\mu\rho} G_{\nu\rho}^c)$	+	7	$f_{ABC}$	$(\bar{Q}_L \sigma_{\mu\nu} \tilde{H}_{uR} + \text{h.c.}) (G^{\mu\rho} G_{\nu\rho}^c)$	$\frac{0.4}{E_{\text{TeV}}^3}, \frac{1.2}{E_{\text{TeV}}^4}$
10	$(i\bar{q}\sigma_{\mu\nu}\gamma_{15}q) (G^{\mu\rho} G_{\nu\rho}^c)$	-			$(i\bar{Q}_L \sigma_{\mu\nu} \tilde{H}_{uR} + \text{h.c.}) (G^{\mu\rho} G_{\nu\rho}^c)$	
11, 12	$(i\bar{q}\gamma^\nu \overleftrightarrow{D}_\mu q) (G^{\mu\rho} G_{\nu\rho}^c)$	+	8	$\delta_{AB}, d_{ABC}$	$(i\bar{Q}_L \gamma^\nu \overleftrightarrow{D}_\mu Q_L + i\bar{u}_R \gamma^\nu \overleftrightarrow{D}_\mu u_R) (G^{\mu\rho} G_{\nu\rho}^c)$	$\frac{0.09}{E_{\text{TeV}}^4}$
13, 14	$(i\bar{q}\gamma^\nu \gamma_{15} \overleftrightarrow{D}_\mu q) (G^{\mu\rho} G_{\nu\rho}^c)$	+			$(i\bar{Q}_L \gamma^\nu \overleftrightarrow{D}_\mu Q_L - i\bar{u}_R \gamma^\nu \overleftrightarrow{D}_\mu u_R) (G^{\mu\rho} G_{\nu\rho}^c)$	
15	$(\bar{q}\gamma^\nu q) (D_\nu G^{\mu\rho}) \tilde{G}_{\mu\rho}$	+			$(\bar{Q}_L \gamma^\nu Q_L + \bar{u}_R \gamma^\nu u_R) (D_\nu G^{\mu\rho}) \tilde{G}_{\mu\rho}$	
16	$(\bar{q}\gamma^\nu \gamma_{15} q) (D_\nu G^{\mu\rho}) \tilde{G}_{\mu\rho}$	+			$(\bar{Q}_L \gamma^\nu Q_L - \bar{u}_R \gamma^\nu u_R) (D_\nu G^{\mu\rho}) \tilde{G}_{\mu\rho}$	
17	$(i\bar{q}\gamma^\nu \overleftrightarrow{D}_\mu q) (G^{\mu\rho} G_{\nu\rho}^c)$	-	8	$f_{ABC}$	$(i\bar{Q}_L \gamma^\nu \overleftrightarrow{D}_\mu Q_L + i\bar{u}_R \gamma^\nu \overleftrightarrow{D}_\mu u_R) (G^{\mu\rho} G_{\nu\rho}^c)$	$\frac{0.09}{E_{\text{TeV}}^4}$
18	$(i\bar{q}\gamma^\nu \gamma_{15} \overleftrightarrow{D}_\mu q) (G^{\mu\rho} G_{\nu\rho}^c)$	-			$(i\bar{Q}_L \gamma^\nu \overleftrightarrow{D}_\mu Q_L - i\bar{u}_R \gamma^\nu \overleftrightarrow{D}_\mu u_R) (G^{\mu\rho} G_{\nu\rho}^c)$	
19	$(i\bar{q}\gamma^\mu \overleftrightarrow{D}_\rho q) (G^{\nu\rho} \tilde{G}_{\mu\nu})$	+			$(i\bar{Q}_L \gamma^\mu \overleftrightarrow{D}_\rho q + i\bar{u}_R \gamma^\mu \overleftrightarrow{D}_\rho u_R) (G^{\nu\rho} \tilde{G}_{\mu\nu})$	
20	$(i\bar{q}\gamma^\mu \gamma_{15} \overleftrightarrow{D}_\rho q) (G^{\nu\rho} \tilde{G}_{\mu\nu})$	+			$(i\bar{Q}_L \gamma^\mu \overleftrightarrow{D}_\rho q - i\bar{u}_R \gamma^\mu \overleftrightarrow{D}_\rho u_R) (G^{\nu\rho} \tilde{G}_{\mu\nu})$	
21, 22	$(i\bar{q}\sigma_{\mu\nu} \overleftrightarrow{D}_\sigma q) (G^{\mu\rho} D^\sigma G_{\nu\rho}^c)$	+	9	$\delta_{AB}, d_{ABC}$	$(i\bar{Q}_L \sigma_{\mu\nu} \overleftrightarrow{D}_\sigma \tilde{H}_{uR} + \text{h.c.}) (G^{\mu\rho} D^\sigma G_{\nu\rho}^c)$	$\frac{0.02}{E_{\text{TeV}}^5}, \frac{0.07}{E_{\text{TeV}}^6}$
23, 24	$(\bar{q}\sigma_{\mu\nu}\gamma_{15} \overleftrightarrow{D}_\sigma q) (G^{\mu\rho} D^\sigma G_{\nu\rho}^c)$	-			$(\bar{Q}_L \sigma_{\mu\nu} \overleftrightarrow{D}_\sigma \tilde{H}_{uR} + \text{h.c.}) (G^{\mu\rho} D^\sigma G_{\nu\rho}^c)$	
25, 26	$(\bar{q}\overleftrightarrow{D}_{\mu\nu} q) (G^{\mu\rho} G_{\nu\rho}^c)$	+			$(\bar{Q}_L \overleftrightarrow{D}_{\mu\nu} \tilde{H}_{uR} + \text{h.c.}) (G^{\mu\rho} G_{\nu\rho}^c)$	
27, 28	$(i\bar{q}\gamma_{15} \overleftrightarrow{D}_{\mu\nu} q) (G^{\mu\rho} G_{\nu\rho}^c)$	-			$(i\bar{Q}_L \overleftrightarrow{D}_{\mu\nu} \tilde{H}_{uR} + \text{h.c.}) (G^{\mu\rho} G_{\nu\rho}^c)$	
29	$(\bar{q}\overleftrightarrow{D}_{\rho q}) (G^{\mu\nu} D^\rho G_{\mu\nu})$	+			$(\bar{Q}_L \overleftrightarrow{D}_\rho \tilde{H}_{uR} + \text{h.c.}) (G^{\mu\nu} D^\rho G_{\mu\nu})$	
30	$(i\bar{q}\gamma_{15} \overleftrightarrow{D}_{\rho q}) (G^{\mu\nu} D^\rho G_{\mu\nu})$	-			$(i\bar{Q}_L \overleftrightarrow{D}_\rho \tilde{H}_{uR} + \text{h.c.}) (G^{\mu\nu} D^\rho G_{\mu\nu})$	
31	$(\bar{q}\overleftrightarrow{D}_{\rho q}) (G^{\mu\nu} D^\rho \tilde{G}_{\mu\nu})$	-			$(\bar{Q}_L \overleftrightarrow{D}_\rho \tilde{H}_{uR} + \text{h.c.}) (G^{\mu\nu} D^\rho \tilde{G}_{\mu\nu})$	
32	$(i\bar{q}\gamma_{15} \overleftrightarrow{D}_{\rho q}) (G^{\mu\nu} D^\rho \tilde{G}_{\mu\nu})$	+			$(i\bar{Q}_L \overleftrightarrow{D}_\rho \tilde{H}_{uR} + \text{h.c.}) (G^{\mu\nu} D^\rho \tilde{G}_{\mu\nu})$	
33	$(i\bar{q}\sigma_{\mu\nu} \overleftrightarrow{D}_\sigma q) (G^{\mu\rho} D_\rho G^{\nu\sigma})$	-			$(i\bar{Q}_L \sigma_{\mu\nu} \overleftrightarrow{D}_\sigma u_R + \text{h.c.}) (G^{\mu\rho} D_\rho G^{\nu\sigma})$	$\frac{0.02}{E_{\text{TeV}}^5}, \frac{0.07}{E_{\text{TeV}}^6}$
34	$(\bar{q}\sigma_{\mu\nu}\gamma_{15} \overleftrightarrow{D}_\sigma q) (G^{\mu\rho} D_\rho G^{\nu\sigma})$	+			$(\bar{Q}_L \sigma_{\mu\nu} \overleftrightarrow{D}_\sigma u_R + \text{h.c.}) (G^{\mu\rho} D_\rho G^{\nu\sigma})$	

Table 8. Primary 7-, 8-, and 9-dimension operators for  $\bar{q}qgg$  interactions. There are three allowed  $SU(3)$  contractions, 2 symmetric ones— $\delta_{AB}$  and  $d_{ABC}$ —and one antisymmetric one— $f_{ABC}$ . For example,  $\mathcal{O}_1^{\bar{q}qgg} = (\bar{q}\delta_{AB}q) (G^{A\mu\nu} G_{\mu\nu}^B)$ ,  $\mathcal{O}_2^{\bar{q}qgg} = d_{ABC} (\bar{q}T^A q) (G^{B\mu\nu} G_{\mu\nu}^C)$ , and  $\mathcal{O}_9^{\bar{q}qgg} = f_{ABC} (\bar{q}T^A \sigma_{\mu\nu} q) (G^{B\mu\rho} G_{\rho\nu}^C)$ . Under the assumption that  $\bar{q}$  and  $q$  are each other's anti-particles, the operators are Hermitean and have the listed CP properties. If they are not, each of these operators has a Hermitean conjugate, which can be used to create a CP even and a CP odd operator. To simplify the expressions, we use the shorthand  $\overleftrightarrow{D}_{\mu\nu} = \overleftrightarrow{D}_\mu \overleftrightarrow{D}_\nu$ . To get the descendant operators, one can add contracted derivatives to get arbitrary Mandelstam factors of  $s, (t-u)^2$ . At dimension 9,  $s\mathcal{O}_9$  and  $s\mathcal{O}_{10}$  become redundant to other operators and at dimension 11,  $s\mathcal{O}_{21}$ ,  $s\mathcal{O}_{22}$ ,  $s\mathcal{O}_{23}$  and  $s\mathcal{O}_{24}$  become redundant to other operators. For the  $\mathcal{O}_{9,10,21,22,23,24}$  operators, one only needs descendants with factors of  $(t-u)^2$ .



$i$	$\mathcal{O}_i^{\bar{q}qg}$	CP	$d_{\mathcal{O}_i}$	$SU(3)$	SMEFT Operator	$c$ Unitarity Bound
35, 36	$(i\bar{q}\gamma^\nu \overleftrightarrow{D}_{\sigma q}) (D_\nu G^{\mu\rho}) D^\sigma G_{\mu\rho}$	+	10	$\delta_{AB}, d_{ABC}$	$(i\bar{Q}_L \gamma^\nu \overleftrightarrow{D}_{\sigma Q_L} + i\bar{u}_R \gamma^\nu \overleftrightarrow{D}_{\sigma u_R}) (D_\nu G^{\mu\rho}) D^\sigma G_{\mu\rho}$	$\frac{0.006}{E_{\text{TeV}}^5}$
37, 38	$(i\bar{q}\gamma^\nu \gamma_5 \overleftrightarrow{D}_{\sigma q}) (D_\nu G^{\mu\rho}) D^\sigma G_{\mu\rho}$	+			$(i\bar{Q}_L \gamma^\nu \overleftrightarrow{D}_{\sigma Q_L} - i\bar{u}_R \gamma^\nu \overleftrightarrow{D}_{\sigma u_R}) (D_\nu G^{\mu\rho}) D^\sigma G_{\mu\rho}$	
39, 40	$(\bar{q}\gamma^\nu \overleftrightarrow{D}_{\mu\sigma q}) (G^{\mu\rho} D^\sigma G_{\nu\rho})$	-			$(\bar{Q}_L \gamma^\nu \overleftrightarrow{D}_{\mu\sigma Q_L} + \bar{u}_R \gamma^\nu \overleftrightarrow{D}_{\mu u_R}) (G^{\mu\rho} D^\sigma G_{\nu\rho})$	
41, 42	$(\bar{q}\gamma^\nu \gamma_5 \overleftrightarrow{D}_{\mu\sigma q}) (G^{\mu\rho} D^\sigma G_{\nu\rho})$	-			$(\bar{Q}_L \gamma^\nu \overleftrightarrow{D}_{\mu\sigma Q_L} - \bar{u}_R \gamma^\nu \overleftrightarrow{D}_{\mu u_R}) (G^{\mu\rho} D^\sigma G_{\nu\rho})$	
43, 44	$(\bar{q}\gamma^\mu \overleftrightarrow{D}_{\rho\sigma q}) (G^{\nu\rho} D^\sigma \tilde{G}_{\mu\nu})$	+			$(\bar{Q}_L \gamma^\mu \overleftrightarrow{D}_{\rho\sigma Q_L} + \bar{u}_R \gamma^\mu \overleftrightarrow{D}_{\rho\sigma u_R}) (G^{\nu\rho} D^\sigma \tilde{G}_{\mu\nu})$	
45, 46	$(\bar{q}\gamma^\mu \gamma_5 \overleftrightarrow{D}_{\rho\sigma q}) (G^{\nu\rho} D^\sigma \tilde{G}_{\mu\nu})$	+			$(\bar{Q}_L \gamma^\mu \overleftrightarrow{D}_{\rho\sigma Q_L} - \bar{u}_R \gamma^\mu \overleftrightarrow{D}_{\rho\sigma u_R}) (G^{\nu\rho} D^\sigma \tilde{G}_{\mu\nu})$	
47	$(\bar{q}\gamma^\nu \overleftrightarrow{D}_{\mu\sigma q}) (G^{\mu\rho} D^\sigma G_{\nu\rho})$	+	10	$f_{ABC}$	$(\bar{Q}_L \gamma^\nu \overleftrightarrow{D}_{\mu\sigma Q_L} + \bar{u}_R \gamma^\nu \overleftrightarrow{D}_{\mu\sigma u_R}) (G^{\mu\rho} D^\sigma G_{\nu\rho})$	$\frac{0.006}{E_{\text{TeV}}^5}$
48	$(\bar{q}\gamma^\nu \gamma_5 \overleftrightarrow{D}_{\mu\sigma q}) (G^{\mu\rho} D^\sigma G_{\nu\rho})$	+			$(\bar{Q}_L \gamma^\nu \overleftrightarrow{D}_{\mu\sigma Q_L} - \bar{u}_R \gamma^\nu \overleftrightarrow{D}_{\mu\sigma u_R}) (G^{\mu\rho} D^\sigma G_{\nu\rho})$	
49, 50	$(\bar{q}\sigma_{\mu\nu} \overleftrightarrow{D}_{\sigma\alpha q}) (G^{\mu\rho} D_\rho^\alpha G^{\nu\sigma})$	-	11	$\delta_{AB}, d_{ABC}$	$(\bar{Q}_L \sigma_{\mu\nu} \overleftrightarrow{D}_{\sigma\alpha} \overleftrightarrow{H}_{u_R} + \text{h.c.}) (G^{\mu\rho} D_\rho^\alpha G^{\nu\sigma})$	$\frac{0.001}{E_{\text{TeV}}^7}, \frac{0.004}{E_{\text{TeV}}^8}$
51, 52	$(i\bar{q}\sigma_{\mu\nu} \gamma_5 \overleftrightarrow{D}_{\sigma\alpha q}) (G^{\mu\rho} D_\rho^\alpha G^{\nu\sigma})$	+			$(i\bar{Q}_L \sigma_{\mu\nu} \overleftrightarrow{D}_{\sigma\alpha} \overleftrightarrow{H}_{u_R} + \text{h.c.}) (G^{\mu\rho} D_\rho^\alpha G^{\nu\sigma})$	
53	$(i\bar{q} \overleftrightarrow{D}_{\mu\nu\sigma q}) (G^{\mu\rho} D^\sigma G_\rho^\nu)$	+	11	$f_{ABC}$	$(i\bar{Q}_L \overleftrightarrow{D}_{\mu\nu\sigma} \overleftrightarrow{H}_{u_R} + \text{h.c.}) (G^{\mu\rho} D^\sigma G_\rho^\nu)$	$\frac{0.001}{E_{\text{TeV}}^7}, \frac{0.004}{E_{\text{TeV}}^8}$
54	$(\bar{q}\gamma_5 \overleftrightarrow{D}_{\mu\nu\sigma q}) (G^{\mu\rho} D^\sigma G_\rho^\nu)$	-			$(\bar{Q}_L \overleftrightarrow{D}_{\mu\nu\sigma} \overleftrightarrow{H}_{u_R} + \text{h.c.}) (G^{\mu\rho} D^\sigma G_\rho^\nu)$	

Table 9. Primary 10- and 11-dimension operators for  $\bar{q}qg$  interactions. There are three allowed  $SU(3)$  contractions, 2 symmetric ones— $\delta_{AB}$  and  $d_{ABC}$ —and one antisymmetric one— $f_{ABC}$ . Under the assumption that  $\bar{q}$  and  $q$  are each other's anti-particles, the operators are Hermitean and have the listed CP properties. If they are not, each of these operators has a Hermitean conjugate, which can be used to create a CP even and a CP odd operator. To simplify the expressions, we use the shorthand  $\overleftrightarrow{D}_{\mu\nu} = \overleftrightarrow{D}_\mu \overleftrightarrow{D}_\nu$ , and similarly  $D_{\mu\nu} = D_\mu D_\nu$ . To get the descendant operators, one can add contracted derivatives to get arbitrary Mandelstam factors of  $s, (t-u)^2$ .

$i$	$\mathcal{O}_{\bar{q}\bar{q}\ell\ell}$	CP	$d_{\mathcal{O}_i}$	SMEFT Operator	$c$ Unitarity Bound
1	$(\bar{q}q)(\bar{\ell}\ell)$	+		$(\bar{Q}_L\tilde{H}u_R + \text{h.c.})(\bar{L}_L H e_R + \text{h.c.})$	
2	$(\bar{q}\gamma_{15}q)(\bar{\ell}\ell)$	-	6	$(i\bar{Q}_L\tilde{H}u_R + \text{h.c.})(\bar{L}_L H e_R + \text{h.c.})$	$\frac{1.5}{E_{\text{TeV}}^2}, \frac{15}{E_{\text{TeV}}^4}$
3	$(\bar{q}q)(\bar{\ell}i\gamma_{15}\ell)$	-		$(Q_L\tilde{H}u_R + \text{h.c.})(i\bar{L}_L H e_R + \text{h.c.})$	
4	$(\bar{q}i\gamma_{15}q)(\bar{\ell}i\gamma_{15}\ell)$	+		$(i\bar{Q}_L\tilde{H}u_R + \text{h.c.})(i\bar{L}_L H e_R + \text{h.c.})$	
5	$(\bar{q}\gamma^\mu q)(\bar{\ell}\gamma_\mu\ell)$	+		$(Q_L\gamma^\mu Q_L + \bar{u}_R\gamma^\mu u_R)(\bar{L}_L\gamma_\mu L_L + \bar{e}_R\gamma_\mu e_R)$	
6	$(\bar{q}\gamma^\mu\gamma_{15}q)(\bar{\ell}\gamma_\mu\ell)$	+	6	$(Q_L\gamma^\mu Q_L - \bar{u}_R\gamma^\mu u_R)(\bar{L}_L\gamma_\mu L_L + \bar{e}_R\gamma_\mu e_R)$	
7	$(\bar{q}\gamma^\mu q)(\bar{\ell}\gamma_\mu\gamma_{15}\ell)$	+		$(Q_L\gamma^\mu Q_L + \bar{u}_R\gamma^\mu u_R)(\bar{L}_L\gamma_\mu L_L - \bar{e}_R\gamma_\mu e_R)$	
8	$(\bar{q}\gamma^\mu\gamma_{15}q)(\bar{\ell}\gamma_\mu\gamma_{15}\ell)$	+		$(Q_L\gamma^\mu Q_L - \bar{u}_R\gamma^\mu u_R)(\bar{L}_L\gamma_\mu L_L - \bar{e}_R\gamma_\mu e_R)$	$\frac{1.5}{E_{\text{TeV}}^2}$
9	$(\bar{q}\sigma^{\mu\nu}q)(\bar{\ell}\sigma_{\mu\nu}\ell)$	+	6	$(Q_L\sigma^{\mu\nu}\tilde{H}u_R + \text{h.c.})(\bar{L}_L\sigma_{\mu\nu}H e_R + \text{h.c.})$	$\frac{1.5}{E_{\text{TeV}}^2}, \frac{15}{E_{\text{TeV}}^4}$
10	$\epsilon_{\mu\nu\rho\sigma}(\bar{q}\sigma^{\mu\nu}q)(\bar{\ell}\sigma^{\rho\sigma}\ell)$	-		$\epsilon_{\mu\nu\rho\sigma}(Q_L\sigma^{\mu\nu}\tilde{H}u_R + \text{h.c.})(\bar{L}_L\sigma^{\rho\sigma}H e_R + \text{h.c.})$	
11	$(\bar{q}\gamma^\mu q)(i\bar{\ell}D_\mu\ell)$	+		$(\bar{Q}_L\gamma^\mu Q_L + \bar{u}_R\gamma^\mu u_R)(i\bar{L}_L\overleftrightarrow{H}D_\mu e_R + \text{h.c.})$	
12	$(\bar{q}\gamma^\mu q)(\bar{\ell}\gamma_{15}D_\mu\ell)$	-		$(\bar{Q}_L\gamma^\mu Q_L + \bar{u}_R\gamma^\mu u_R)(\bar{L}_L\overleftrightarrow{H}D_\mu e_R + \text{h.c.})$	
13	$(\bar{q}\gamma^\mu\gamma_{15}q)(i\bar{\ell}D_\mu\ell)$	+	7	$(Q_L\gamma^\mu Q_L - \bar{u}_R\gamma^\mu u_R)(i\bar{L}_L\overleftrightarrow{H}D_\mu e_R + \text{h.c.})$	
14	$(\bar{q}\gamma^\mu\gamma_{15}q)(\bar{\ell}\gamma_{15}D_\mu\ell)$	-		$(\bar{Q}_L\gamma^\mu Q_L - \bar{u}_R\gamma^\mu u_R)(\bar{L}_L\overleftrightarrow{H}D_\mu e_R + \text{h.c.})$	
15	$(i\bar{q}D^\mu q)(\bar{\ell}\gamma_\mu\ell)$	+		$(i\bar{Q}_L\overleftrightarrow{H}D^\mu u_R + \text{h.c.})(\bar{L}_L\gamma_\mu L_L + \bar{e}_R\gamma_\mu e_R)$	
16	$(\bar{q}\gamma_{15}D^\mu q)(\bar{\ell}\gamma_\mu\ell)$	-		$(\bar{Q}_L\overleftrightarrow{H}D^\mu u_R + \text{h.c.})(\bar{L}_L\gamma_\mu L_L + \bar{e}_R\gamma_\mu e_R)$	
17	$(i\bar{q}D^\mu q)(\bar{\ell}\gamma_\mu\gamma_{15}\ell)$	+		$(i\bar{Q}_L\overleftrightarrow{H}D^\mu u_R + \text{h.c.})(\bar{L}_L\gamma_\mu L_L - \bar{e}_R\gamma_\mu e_R)$	$\frac{0.4}{E_{\text{TeV}}^3}, \frac{1.2}{E_{\text{TeV}}^4}$
18	$(\bar{q}\gamma_{15}D^\mu q)(\bar{\ell}\gamma_\mu\gamma_{15}\ell)$	-		$(\bar{Q}_L\overleftrightarrow{H}D^\mu u_R + \text{h.c.})(\bar{L}_L\gamma_\mu L_L - \bar{e}_R\gamma_\mu e_R)$	

Table 10. Primary operators for  $\bar{q}q\bar{\ell}\ell$  interactions (As described in the text, these operators can be modified to yield the operators for baryon-lepton interactions  $uu'de$  and  $udd'\nu$ ). Under the assumption the  $\bar{q}, q$  and  $\bar{\ell}, \ell$  are each other's anti-particles, the operators are Hermitean and have the listed CP properties. If they are not, each of these operators has a Hermitean conjugate, which can be used to create a CP even and a CP odd operator. To get the descendant operators, one can add contracted derivatives to get arbitrary Mandelstam factors of  $s, t$ . At dimension 8,  $s\mathcal{O}_9$  and  $s\mathcal{O}_{10}$  become redundant and thus, one only needs to consider  $\mathcal{O}_9$  and  $\mathcal{O}_{10}$  with arbitrary factors of  $t$ .

$i$	$\mathcal{O}_i^{uude}$	$d\mathcal{O}_i$	SMEFT Operator	$c$ Unitarity Bound
1	$(\bar{d}^c u)(\bar{e}^c u)$	6	$(\bar{d}_R^c \bar{H}^\dagger Q_L + \bar{Q}_L^c H u_R)(\bar{e}_R^c \bar{H}^\dagger Q_L + \bar{L}_L^c H u_R)$	$\frac{1.5}{E_{\text{TeV}}^2}, \frac{1.5}{E_{\text{TeV}}^4}$
2	$(\bar{d}^c i\gamma_5 u)(\bar{e}^c u)$		$(i\bar{d}_R^c \bar{H}^\dagger Q_L - i\bar{Q}_L^c H u_R)(i\bar{e}_R^c \bar{H}^\dagger Q_L + \bar{L}_L^c H u_R)$	
3	$(\bar{d}^c u)(\bar{e}^c i\gamma_5 u)$		$(\bar{d}_R^c \bar{H}^\dagger Q_L + \bar{Q}_L^c H u_R)(i\bar{e}_R^c \bar{H}^\dagger Q_L - i\bar{L}_L^c H u_R)$	
4	$(\bar{d}^c i\gamma_5 u)(\bar{e}^c i\gamma_5 u)$		$(i\bar{d}_R^c \bar{H}^\dagger Q_L - i\bar{Q}_L^c H u_R)(i\bar{e}_R^c \bar{H}^\dagger Q_L - i\bar{L}_L^c H u_R)$	
5	$(\bar{d}^c \gamma^\mu u)(\bar{e}^c D_\mu u)$	7	$(\bar{Q}_L^c \gamma^\mu Q_L + \bar{d}_R^c \gamma^\mu u_R)(\bar{e}_R^c D_\mu \bar{H}^\dagger Q_L + \bar{L}_L^c H D_\mu u_R)$	$\frac{0.4}{E_{\text{TeV}}^3}, \frac{1.2}{E_{\text{TeV}}^4}$
6	$(\bar{d}^c \gamma^\mu u)(\bar{e}^c i\gamma_5 D_\mu u)$		$(\bar{Q}_L^c \gamma^\mu Q_L + \bar{d}_R^c \gamma^\mu u_R)(i\bar{e}_R^c D_\mu \bar{H}^\dagger Q_L - i\bar{L}_L^c H D_\mu u_R)$	
7	$(\bar{d}^c \gamma^\mu \gamma_5 u)(\bar{e}^c D_\mu u)$		$(\bar{Q}_L^c \gamma^\mu Q_L - \bar{d}_R^c \gamma^\mu u_R)(\bar{e}_R^c D_\mu \bar{H}^\dagger Q_L + \bar{L}_L^c H D_\mu u_R)$	
8	$(\bar{d}^c \gamma^\mu \gamma_5 u)(\bar{e}^c i\gamma_5 D_\mu u)$		$(\bar{Q}_L^c \gamma^\mu Q_L - \bar{d}_R^c \gamma^\mu u_R)(i\bar{e}_R^c D_\mu \bar{H}^\dagger Q_L - i\bar{L}_L^c H D_\mu u_R)$	
9	$(\bar{d}^c D_\mu u)(\bar{e}^c \gamma^\mu u)$		$(\bar{d}_R^c D_\mu \bar{H}^\dagger Q_L + \bar{Q}_L^c H D_\mu u_R)(\bar{L}_L^c \gamma^\mu Q_L + \bar{e}_R^c \gamma^\mu u_R)$	
10	$(\bar{d}^c i\gamma_5 D_\mu u)(\bar{e}^c \gamma^\mu u)$		$(i\bar{d}_R^c D_\mu \bar{H}^\dagger Q_L - i\bar{Q}_L^c H D_\mu u_R)(\bar{L}_L^c \gamma^\mu Q_L + \bar{e}_R^c \gamma^\mu u_R)$	
11	$(\bar{d}^c u)(\overleftrightarrow{D}_\mu^u \bar{e}^\dagger D_\mu^u u)$	8	$(\bar{d}_R^c \bar{H}^\dagger Q_L + \bar{Q}_L^c H u_R)(\overleftrightarrow{D}_\mu^u \bar{e}_R^\dagger D_\mu^u \bar{H}^\dagger Q_L + \overleftrightarrow{D}_\mu^u \bar{L}_L^\dagger H D_\mu^u u_R)$	$\frac{0.09}{E_{\text{TeV}}^4}, \frac{0.9}{E_{\text{TeV}}^5}$
12	$(\bar{d}^c i\gamma_5 u)(\overleftrightarrow{D}_\mu^u \bar{e}^\dagger D_\mu^u u)$		$(i\bar{d}_R^c \bar{H}^\dagger Q_L - i\bar{Q}_L^c H u_R)(\overleftrightarrow{D}_\mu^u \bar{e}_R^\dagger D_\mu^u \bar{H}^\dagger Q_L + \overleftrightarrow{D}_\mu^u \bar{L}_L^\dagger H D_\mu^u u_R)$	
13	$(\bar{d}^c u)(\overleftrightarrow{D}_\mu^u \bar{e}^\dagger i\gamma_5 D_\mu^u u)$		$(\bar{d}_R^c \bar{H}^\dagger Q_L + \bar{Q}_L^c H u_R)(i\overleftrightarrow{D}_\mu^u \bar{e}_R^\dagger D_\mu^u \bar{H}^\dagger Q_L - i\overleftrightarrow{D}_\mu^u \bar{L}_L^\dagger H D_\mu^u u_R)$	
14	$(\bar{d}^c i\gamma_5 u)(\overleftrightarrow{D}_\mu^u \bar{e}^\dagger i\gamma_5 D_\mu^u u)$		$(i\bar{d}_R^c \bar{H}^\dagger Q_L - i\bar{Q}_L^c H u_R)(i\overleftrightarrow{D}_\mu^u \bar{e}_R^\dagger D_\mu^u \bar{H}^\dagger Q_L - i\overleftrightarrow{D}_\mu^u \bar{L}_L^\dagger H D_\mu^u u_R)$	
15	$(\bar{d}^c \gamma^\mu u)(\overleftrightarrow{D}_\nu^u \bar{e}^\dagger \gamma_\mu D_\nu^u u)$	8	$(\bar{Q}_L^c \gamma^\mu Q_L + \bar{d}_R^c \gamma^\mu u_R)(\overleftrightarrow{D}_\nu^u \bar{L}_L^\dagger \gamma_\mu D_\nu^u \bar{e}_R^\dagger Q_L + \overleftrightarrow{D}_\nu^u \bar{e}_R^\dagger \gamma_\mu D_\nu^u \bar{Q}_L)$	$\frac{0.09}{E_{\text{TeV}}^4}$
16	$(\bar{d}^c \gamma^\mu \gamma_5 u)(\overleftrightarrow{D}_\nu^u \bar{e}^\dagger \gamma_\mu D_\nu^u u)$		$(\bar{Q}_L^c \gamma^\mu Q_L - \bar{d}_R^c \gamma^\mu u_R)(\overleftrightarrow{D}_\nu^u \bar{L}_L^\dagger \gamma_\mu D_\nu^u \bar{e}_R^\dagger Q_L + \overleftrightarrow{D}_\nu^u \bar{e}_R^\dagger \gamma_\mu D_\nu^u \bar{Q}_L)$	
17	$(\bar{d}^c \gamma^\mu u)(\overleftrightarrow{D}_\nu^u \bar{e}^\dagger \overleftrightarrow{D}_\mu^u D_\nu u)$	9	$(\bar{Q}_L^c \gamma^\mu Q_L + \bar{d}_R^c \gamma^\mu u_R)(\overleftrightarrow{D}_\nu^u \bar{e}_R^\dagger \overleftrightarrow{D}_\mu^u \bar{Q}_L + \overleftrightarrow{D}_\nu^u \bar{L}_L^\dagger H \overleftrightarrow{D}_\mu^u D_\nu u_R)$	$\frac{0.02}{E_{\text{TeV}}^5}, \frac{0.07}{E_{\text{TeV}}^6}$
18	$(\bar{d}^c \gamma^\mu u)(\overleftrightarrow{D}_\nu^u \bar{e}^\dagger i\gamma_5 \overleftrightarrow{D}_\mu^u D_\nu u)$		$(\bar{Q}_L^c \gamma^\mu Q_L + \bar{d}_R^c \gamma^\mu u_R)(i\overleftrightarrow{D}_\nu^u \bar{e}_R^\dagger \overleftrightarrow{D}_\mu^u D_\nu u_R - i\overleftrightarrow{D}_\nu^u \bar{L}_L^\dagger H \overleftrightarrow{D}_\mu^u D_\nu u_R)$	

Table 11. Primary operators for  $uude$  interactions, where  $d^c$  and  $e^c$  are the charge conjugated down-type quark and charged lepton 4-component spinor and  $SU(3)$  indices are contracted with an epsilon tensor (These operators can be modified to yield the operators for  $udd\nu$  interactions by simply taking  $u \rightarrow d, \bar{d}^c \rightarrow \bar{u}^c, \bar{e}^c \rightarrow \bar{\nu}/\bar{\nu}^c$ ). To simplify the expressions, we've defined a back-forth derivative  $\overleftrightarrow{D}_\mu^u$ , which only acts on the  $u$  fields, and similarly  $\overleftrightarrow{D}_\mu^{u,Q}$  which acts on  $u_R$  and  $Q_L$  (but not  $\bar{Q}_L^c$ ). To get the descendant operators, one can add contracted derivatives to get arbitrary Mandelstam factors that respect the exchange symmetry between the two up-type quarks, i.e.  $s, (t-u)^2$ . At dimension 8,  $s\mathcal{O}_3$  and  $s\mathcal{O}_4$  become redundant and thus, one only needs to consider  $\mathcal{O}_3$  and  $\mathcal{O}_4$  descendants with arbitrary factors of  $(t-u)^2$ .

In Table 11, we've listed the primary operators for  $uude$  interactions, where all  $SU(3)$  indices are contracted by an epsilon tensor. As the Hilbert series suggests, there should be 4 primaries at dimension 6, 6 primaries at dimension 7, 6 primaries with 2 redundancies at dimension 8, and 2 primaries at dimension 9. The table shows the stated number of independent primaries and we find that at dimension 8,  $s\mathcal{O}_3$  and  $s\mathcal{O}_4$  are redundant to the other operators, where  $s = (p_u + p_{\bar{u}})^2$ . Thus, for those two, one only needs their descendants  $(t - u)^{2n}\mathcal{O}_3$  and  $(t - u)^{2n}\mathcal{O}_4$ . To account for  $udd\nu$  interactions, one replaces  $u \rightarrow d, \bar{d}^c \rightarrow \bar{u}^c, \bar{e}^c \rightarrow \bar{\nu}/\bar{\nu}^c$ , where again the case of Dirac neutrinos allows twice as many operators.

In Table 12, we've listed the primary operators for  $\bar{q}q\bar{q}'q'$  interactions. Notably the Hilbert series for this has a numerator that is twice the  $\bar{q}q\bar{\ell}\ell$  Hilbert series. This factor of two is simply for the two allowed  $SU(3)$  contractions, one where the  $qq'$  are either in the 6 or  $\bar{3}$  representation, leading to the symmetric ( $S$ ) and antisymmetric ( $A$ ) operators. Again, at dimension 8,  $s\mathcal{O}_9$  and  $s\mathcal{O}_{10}$  are redundant to the other operators, where  $s = (p_q + p_{\bar{q}})^2$ . Thus one only needs to add their descendants  $t^n\mathcal{O}_9$  and  $t^n\mathcal{O}_{10}$ .

In Table 13, we've listed the primary operators for  $\bar{q}q\bar{q}q$  interactions when two of the quarks are identical for the specific case of  $uu\bar{t}\bar{c}$ . There are again two allowed  $SU(3)$  contractions, specified by whether the  $uu$  are in symmetric ( $S$ ) or antisymmetric ( $A$ ) combination. Since we're suppressing the  $SU(3)$  indices, this makes some of the expressions look identical, which occurs in the blocks (1-4) and (5-8), (11-12) and (17-18), (19-22) and (25-28), and (29-30) and (31-32). At dimension 8,  $s\mathcal{O}_3$  and  $s\mathcal{O}_4$  become redundant and at dimension 10,  $s\mathcal{O}_{27}$  and  $s\mathcal{O}_{28}$  become redundant, where  $s = (p_u + p_{\bar{u}})^2$ . Thus one only needs to add descendants for  $\mathcal{O}_{3,4,27,28}$

$i$	$\mathcal{O}_{i,S/A}^{\bar{q}q\bar{q}'q'}$	CP	$d_{\mathcal{O}_i}$	SMEFT Operator	$c$ Unitarity Bound
1	$(\bar{q}q)(\bar{q}'q')$	+	6	$(\bar{Q}_L\tilde{H}u_R + \text{h.c.})(\bar{Q}'_L\tilde{H}u'_R + \text{h.c.})$	$\frac{1.5}{E_{\text{TeV}}^2}, \frac{15}{E_{\text{TeV}}^4}$
2	$(\bar{q}i\gamma_5q)(\bar{q}'q')$	-		$(i\bar{Q}_L\tilde{H}u_R + \text{h.c.})(\bar{Q}'_L\tilde{H}u'_R + \text{h.c.})$	
3	$(\bar{q}q)(\bar{q}'i\gamma_5q')$	-		$(\bar{Q}_L\tilde{H}u_R + \text{h.c.})(i\bar{Q}'_L\tilde{H}u'_R + \text{h.c.})$	
4	$(\bar{q}i\gamma_5q)(\bar{q}'i\gamma_5q')$	+		$(i\bar{Q}_L\tilde{H}u_R + \text{h.c.})(i\bar{Q}'_L\tilde{H}u'_R + \text{h.c.})$	
5	$(\bar{q}\gamma^\mu q)(\bar{q}'\gamma_\mu q')$	+	6	$(\bar{Q}_L\gamma^\mu Q_L + \bar{u}_R\gamma^\mu u_R)(\bar{Q}'_L\gamma_\mu Q'_L + \bar{u}'_R\gamma_\mu u'_R)$	$\frac{1.5}{E_{\text{TeV}}^2}$
6	$(\bar{q}\gamma^\mu\gamma_5q)(\bar{q}'\gamma_\mu q')$	+		$(\bar{Q}_L\gamma^\mu Q_L - \bar{u}_R\gamma^\mu u_R)(\bar{Q}'_L\gamma_\mu Q'_L + \bar{u}'_R\gamma_\mu u'_R)$	
7	$(\bar{q}\gamma^\mu q)(\bar{q}'\gamma_\mu\gamma_5q')$	+		$(\bar{Q}_L\gamma^\mu Q_L + \bar{u}_R\gamma^\mu u_R)(\bar{Q}'_L\gamma_\mu Q'_L - \bar{u}'_R\gamma_\mu u'_R)$	
8	$(\bar{q}\gamma^\mu\gamma_5q)(\bar{q}'\gamma_\mu\gamma_5q')$	+		$(\bar{Q}_L\gamma^\mu Q_L - \bar{u}_R\gamma^\mu u_R)(\bar{Q}'_L\gamma_\mu Q'_L - \bar{u}'_R\gamma_\mu u'_R)$	
9	$(\bar{q}\sigma^{\mu\nu}q)(\bar{q}'\sigma_{\mu\nu}q')$	+	6	$(\bar{Q}_L\sigma^{\mu\nu}\tilde{H}u_R + \text{h.c.})(\bar{Q}'_L\sigma_{\mu\nu}\tilde{H}u'_R + \text{h.c.})$	$\frac{1.5}{E_{\text{TeV}}^2}, \frac{15}{E_{\text{TeV}}^4}$
10	$\epsilon_{\mu\nu\rho\sigma}(\bar{q}\sigma^{\mu\nu}q)(\bar{q}'\sigma^{\rho\sigma}q')$	-		$\epsilon_{\mu\nu\rho\sigma}(\bar{Q}_L\sigma^{\mu\nu}\tilde{H}u_R + \text{h.c.})(\bar{Q}'_L\sigma^{\rho\sigma}\tilde{H}u'_R + \text{h.c.})$	
11	$(\bar{q}\gamma^\mu q)(i\bar{q}'\overleftrightarrow{D}_\mu q')$	+	7	$(\bar{Q}_L\gamma^\mu Q_L + \bar{u}_R\gamma^\mu u_R)(i\bar{Q}'_L\overleftrightarrow{H}\overleftrightarrow{D}_\mu u'_R + \text{h.c.})$	$\frac{0.4}{E_{\text{TeV}}^3}, \frac{1.2}{E_{\text{TeV}}^4}$
12	$(\bar{q}\gamma^\mu q)(\bar{q}'\gamma_5\overleftrightarrow{D}_\mu q')$	-		$(\bar{Q}_L\gamma^\mu Q_L + \bar{u}_R\gamma^\mu u_R)(\bar{Q}'_L\overleftrightarrow{H}\overleftrightarrow{D}_\mu u'_R + \text{h.c.})$	
13	$(\bar{q}\gamma^\mu\gamma_5q)(i\bar{q}'\overleftrightarrow{D}_\mu q')$	+		$(\bar{Q}_L\gamma^\mu Q_L - \bar{u}_R\gamma^\mu u_R)(i\bar{Q}'_L\overleftrightarrow{H}\overleftrightarrow{D}_\mu u'_R + \text{h.c.})$	
14	$(\bar{q}\gamma^\mu\gamma_5q)(\bar{q}'\gamma_5\overleftrightarrow{D}_\mu q')$	-		$(\bar{Q}_L\gamma^\mu Q_L - \bar{u}_R\gamma^\mu u_R)(\bar{Q}'_L\overleftrightarrow{H}\overleftrightarrow{D}_\mu u'_R + \text{h.c.})$	
15	$(i\bar{q}\overleftrightarrow{D}^\mu q)(\bar{q}'\gamma_\mu q')$	+		$(i\bar{Q}_L\overleftrightarrow{H}\overleftrightarrow{D}^\mu u_R + \text{h.c.})(\bar{Q}'_L\gamma_\mu Q'_L + \bar{u}'_R\gamma_\mu u'_R)$	
16	$(\bar{q}\gamma_5\overleftrightarrow{D}^\mu q)(\bar{q}'\gamma_\mu q')$	-		$(\bar{Q}_L\overleftrightarrow{H}\overleftrightarrow{D}^\mu u_R + \text{h.c.})(\bar{Q}'_L\gamma_\mu Q'_L + \bar{u}'_R\gamma_\mu u'_R)$	
17	$(i\bar{q}\overleftrightarrow{D}^\mu q)(\bar{q}'\gamma_\mu\gamma_5q')$	+		$(i\bar{Q}_L\overleftrightarrow{H}\overleftrightarrow{D}^\mu u_R + \text{h.c.})(\bar{Q}'_L\gamma_\mu Q'_L - \bar{u}'_R\gamma_\mu u'_R)$	
18	$(\bar{q}\gamma_5\overleftrightarrow{D}^\mu q)(\bar{q}'\gamma_\mu\gamma_5q')$	-		$(\bar{Q}_L\overleftrightarrow{H}\overleftrightarrow{D}^\mu u_R + \text{h.c.})(\bar{Q}'_L\gamma_\mu Q'_L - \bar{u}'_R\gamma_\mu u'_R)$	

Table 12. Primary operators for  $\bar{q}q\bar{q}'q'$  interactions. There are two allowed  $SU(3)$  contractions, the  $S$  indicates where  $q, q'$  form a symmetric 6 representation under  $SU(3)$ , while  $A$  has the antisymmetric  $\bar{3}$  representation. For example, with explicit indices we have  $\mathcal{O}_{1,S}^{\bar{q}q\bar{q}'q'} = (\bar{q}^{\{\alpha}q_{\{\alpha})(\bar{q}'^{\beta\}}q'_{\beta\})}$  and  $\mathcal{O}_{1,A}^{\bar{q}q\bar{q}'q'} = (\bar{q}^{\alpha}q_{[\alpha})(\bar{q}'^{\beta\]}q'_{\beta]})$ , where  $q_{\{\alpha}q_{\beta\}} = q_{\alpha}q_{\beta} + q_{\beta}q_{\alpha}$  and  $q_{[\alpha}q_{\beta]} = q_{\alpha}q_{\beta} - q_{\beta}q_{\alpha}$ . Under the assumption the  $\bar{q}, q$  and  $\bar{q}', q'$  are respectively each other's anti-particles, the operators are Hermitean and have the listed CP properties. If they are not, each of these operators has a Hermitean conjugate, which can be used to create a CP even and a CP odd operator. To get the descendant operators, one can add contracted derivatives to get arbitrary Mandelstam factors of  $s, t$ . At dimension 8,  $s\mathcal{O}_9$  and  $s\mathcal{O}_{10}$  become redundant and thus, one only needs to consider  $\mathcal{O}_9$  and  $\mathcal{O}_{10}$  with arbitrary factors of  $t$ .

$i$	$\mathcal{O}_i^{uuf\bar{c}}$	$d\mathcal{O}_i$	$SU(3)$	SMEFT Operator	$c$ Unitarity Bound
1	$(\bar{t}u)(\bar{c}u)$	6	A	$(Q_{3L}\bar{H}u_R + \bar{t}_R\bar{H}^\dagger Q_{1L})(Q_{2L}\bar{H}u_R + \bar{c}_R\bar{H}^\dagger Q_{1L})$	$\frac{1.5}{E^2\text{TeV}}, \frac{1.5}{E^4\text{TeV}}$
2	$(\bar{t}\bar{t}\gamma_5 u)(\bar{c}u)$			$(Q_{3L}\bar{H}u_R + \bar{t}_R\bar{H}^\dagger Q_{1L})(Q_{2L}\bar{H}u_R + \bar{c}_R\bar{H}^\dagger Q_{1L})$	
3	$(\bar{t}\bar{t}\gamma_5 u)(\bar{c}\bar{t}\gamma_5 u)$			$(Q_{3L}\bar{H}u_R + \bar{t}_R\bar{H}^\dagger Q_{1L})(Q_{2L}\bar{H}u_R + \bar{c}_R\bar{H}^\dagger Q_{1L})$	
4	$(\bar{t}\bar{t}\gamma_5 u)(\bar{c}\bar{t}\gamma_5 u)$			$(Q_{3L}\bar{H}u_R + \bar{t}_R\bar{H}^\dagger Q_{1L})(Q_{2L}\bar{H}u_R + \bar{c}_R\bar{H}^\dagger Q_{1L})$	
5	$(\bar{t}u)(\bar{c}u)$	6	S	$(Q_{3L}\bar{H}u_R + \bar{t}_R\bar{H}^\dagger Q_{1L})(Q_{2L}\bar{H}u_R + \bar{c}_R\bar{H}^\dagger Q_{1L})$	$\frac{1.5}{E^2\text{TeV}}, \frac{1.5}{E^4\text{TeV}}$
6	$(\bar{t}\bar{t}\gamma_5 u)(\bar{c}u)$			$(Q_{3L}\bar{H}u_R + \bar{t}_R\bar{H}^\dagger Q_{1L})(Q_{2L}\bar{H}u_R + \bar{c}_R\bar{H}^\dagger Q_{1L})$	
7	$(\bar{t}u)(\bar{c}\bar{t}\gamma_5 u)$			$(Q_{3L}\bar{H}u_R + \bar{t}_R\bar{H}^\dagger Q_{1L})(Q_{2L}\bar{H}u_R + \bar{c}_R\bar{H}^\dagger Q_{1L})$	
8	$(\bar{t}\bar{t}\gamma_5 u)(\bar{c}\bar{t}\gamma_5 u)$			$(Q_{3L}\bar{H}u_R + \bar{t}_R\bar{H}^\dagger Q_{1L})(Q_{2L}\bar{H}u_R + \bar{c}_R\bar{H}^\dagger Q_{1L})$	
9	$(\bar{t}\bar{t}\gamma_5 u)(\bar{c}\bar{t}\gamma_5 u)$			$(Q_{3L}\bar{H}u_R + \bar{t}_R\bar{H}^\dagger Q_{1L})(Q_{2L}\bar{H}u_R + \bar{c}_R\bar{H}^\dagger Q_{1L})$	
10	$(\bar{t}\bar{t}\gamma_5 u)(\bar{c}\bar{t}\gamma_5 u)$			$(Q_{3L}\bar{H}u_R + \bar{t}_R\bar{H}^\dagger Q_{1L})(Q_{2L}\bar{H}u_R + \bar{c}_R\bar{H}^\dagger Q_{1L})$	
11	$(\bar{t}\bar{t}\gamma_5 u)(\bar{c}D_\mu u)$			$(Q_{3L}\bar{H}u_R + \bar{t}_R\bar{H}^\dagger Q_{1L})(Q_{2L}\bar{H}u_R + \bar{c}_R\bar{H}^\dagger Q_{1L})$	
12	$(\bar{t}\bar{t}\gamma_5 u)(\bar{c}\bar{t}\gamma_5 D_\mu u)$			$(Q_{3L}\bar{H}u_R + \bar{t}_R\bar{H}^\dagger Q_{1L})(Q_{2L}\bar{H}u_R + \bar{c}_R\bar{H}^\dagger Q_{1L})$	
13	$(\bar{t}\bar{t}\gamma_5 u)(\bar{c}D_\mu u)$			$(Q_{3L}\bar{H}u_R + \bar{t}_R\bar{H}^\dagger Q_{1L})(Q_{2L}\bar{H}u_R + \bar{c}_R\bar{H}^\dagger Q_{1L})$	
14	$(\bar{t}\bar{t}\gamma_5 u)(\bar{c}\bar{t}\gamma_5 D_\mu u)$			$(Q_{3L}\bar{H}u_R + \bar{t}_R\bar{H}^\dagger Q_{1L})(Q_{2L}\bar{H}u_R + \bar{c}_R\bar{H}^\dagger Q_{1L})$	
15	$(\bar{t}D_\mu u)(\bar{c}\bar{t}\gamma_5 u)$			$(Q_{3L}\bar{H}u_R + \bar{t}_R\bar{H}^\dagger Q_{1L})(Q_{2L}\bar{H}u_R + \bar{c}_R\bar{H}^\dagger Q_{1L})$	
16	$(\bar{t}\bar{t}\gamma_5 D_\mu u)(\bar{c}\bar{t}\gamma_5 u)$			$(Q_{3L}\bar{H}u_R + \bar{t}_R\bar{H}^\dagger Q_{1L})(Q_{2L}\bar{H}u_R + \bar{c}_R\bar{H}^\dagger Q_{1L})$	
17	$(\bar{t}\bar{t}\gamma_5 u)(\bar{c}D_\mu u)$			$(Q_{3L}\bar{H}u_R + \bar{t}_R\bar{H}^\dagger Q_{1L})(Q_{2L}\bar{H}u_R + \bar{c}_R\bar{H}^\dagger Q_{1L})$	
18	$(\bar{t}\bar{t}\gamma_5 u)(\bar{c}\bar{t}\gamma_5 D_\mu u)$			$(Q_{3L}\bar{H}u_R + \bar{t}_R\bar{H}^\dagger Q_{1L})(Q_{2L}\bar{H}u_R + \bar{c}_R\bar{H}^\dagger Q_{1L})$	
19	$(\bar{t}u)((D^\mu\bar{c})\bar{D}_\mu^u u)$			$(Q_{3L}\bar{H}u_R + \bar{t}_R\bar{H}^\dagger Q_{1L})(Q_{2L}\bar{H}u_R + \bar{c}_R\bar{H}^\dagger Q_{1L})$	
20	$(\bar{t}\bar{t}\gamma_5 u)((D^\mu\bar{c})\bar{D}_\mu^u u)$			$(Q_{3L}\bar{H}u_R + \bar{t}_R\bar{H}^\dagger Q_{1L})(Q_{2L}\bar{H}u_R + \bar{c}_R\bar{H}^\dagger Q_{1L})$	
21	$(\bar{t}u)((D^\mu\bar{c})\bar{t}\gamma_5\bar{D}_\mu^u u)$			$(Q_{3L}\bar{H}u_R + \bar{t}_R\bar{H}^\dagger Q_{1L})(Q_{2L}\bar{H}u_R + \bar{c}_R\bar{H}^\dagger Q_{1L})$	
22	$(\bar{t}\bar{t}\gamma_5 u)((D^\mu\bar{c})\bar{t}\gamma_5\bar{D}_\mu^u u)$			$(Q_{3L}\bar{H}u_R + \bar{t}_R\bar{H}^\dagger Q_{1L})(Q_{2L}\bar{H}u_R + \bar{c}_R\bar{H}^\dagger Q_{1L})$	
23	$(\bar{t}\bar{t}\gamma_5 u)((D^\nu\bar{c})\bar{t}\gamma_\mu\bar{D}_\nu^u u)$			$(Q_{3L}\bar{H}u_R + \bar{t}_R\bar{H}^\dagger Q_{1L})(Q_{2L}\bar{H}u_R + \bar{c}_R\bar{H}^\dagger Q_{1L})$	
24	$(\bar{t}\bar{t}\gamma_5 u)((D^\nu\bar{c})\bar{t}\gamma_\mu\bar{D}_\nu^u u)$			$(Q_{3L}\bar{H}u_R + \bar{t}_R\bar{H}^\dagger Q_{1L})(Q_{2L}\bar{H}u_R + \bar{c}_R\bar{H}^\dagger Q_{1L})$	
25	$(\bar{t}u)((D^\mu\bar{c})\bar{D}_\mu^u u)$			$(Q_{3L}\bar{H}u_R + \bar{t}_R\bar{H}^\dagger Q_{1L})(Q_{2L}\bar{H}u_R + \bar{c}_R\bar{H}^\dagger Q_{1L})$	
26	$(\bar{t}\bar{t}\gamma_5 u)((D^\mu\bar{c})\bar{D}_\mu^u u)$			$(Q_{3L}\bar{H}u_R + \bar{t}_R\bar{H}^\dagger Q_{1L})(Q_{2L}\bar{H}u_R + \bar{c}_R\bar{H}^\dagger Q_{1L})$	
27	$(\bar{t}u)((D^\mu\bar{c})\bar{t}\gamma_5\bar{D}_\mu^u u)$			$(Q_{3L}\bar{H}u_R + \bar{t}_R\bar{H}^\dagger Q_{1L})(Q_{2L}\bar{H}u_R + \bar{c}_R\bar{H}^\dagger Q_{1L})$	
28	$(\bar{t}\bar{t}\gamma_5 u)((D^\mu\bar{c})\bar{t}\gamma_5\bar{D}_\mu^u u)$			$(Q_{3L}\bar{H}u_R + \bar{t}_R\bar{H}^\dagger Q_{1L})(Q_{2L}\bar{H}u_R + \bar{c}_R\bar{H}^\dagger Q_{1L})$	
29	$(\bar{t}\bar{t}\gamma_5 u)((D^\nu\bar{c})\bar{t}\gamma_\mu\bar{D}_\nu^u u)$			$(Q_{3L}\bar{H}u_R + \bar{t}_R\bar{H}^\dagger Q_{1L})(Q_{2L}\bar{H}u_R + \bar{c}_R\bar{H}^\dagger Q_{1L})$	
30	$(\bar{t}\bar{t}\gamma_5 u)((D^\nu\bar{c})\bar{t}\gamma_\mu\bar{D}_\nu^u u)$			$(Q_{3L}\bar{H}u_R + \bar{t}_R\bar{H}^\dagger Q_{1L})(Q_{2L}\bar{H}u_R + \bar{c}_R\bar{H}^\dagger Q_{1L})$	
31	$(\bar{t}\bar{t}\gamma_5 u)((D^\nu\bar{c})\bar{t}\gamma_\mu\bar{D}_\nu^u u)$			$(Q_{3L}\bar{H}u_R + \bar{t}_R\bar{H}^\dagger Q_{1L})(Q_{2L}\bar{H}u_R + \bar{c}_R\bar{H}^\dagger Q_{1L})$	
32	$(\bar{t}\bar{t}\gamma_5 u)((D^\nu\bar{c})\bar{t}\gamma_\mu\bar{D}_\nu^u u)$			$(Q_{3L}\bar{H}u_R + \bar{t}_R\bar{H}^\dagger Q_{1L})(Q_{2L}\bar{H}u_R + \bar{c}_R\bar{H}^\dagger Q_{1L})$	
33	$(\bar{t}\bar{t}\gamma_5 u)((D^\nu\bar{c})\bar{t}\gamma_\mu\bar{D}_\nu^u u)$			$(Q_{3L}\bar{H}u_R + \bar{t}_R\bar{H}^\dagger Q_{1L})(Q_{2L}\bar{H}u_R + \bar{c}_R\bar{H}^\dagger Q_{1L})$	
34	$(\bar{t}\bar{t}\gamma_5 u)((D^\nu\bar{c})\bar{t}\gamma_\mu\bar{D}_\nu^u u)$			$(Q_{3L}\bar{H}u_R + \bar{t}_R\bar{H}^\dagger Q_{1L})(Q_{2L}\bar{H}u_R + \bar{c}_R\bar{H}^\dagger Q_{1L})$	
35	$(\bar{t}D_\mu u)((D^\nu\bar{c})\bar{t}\gamma_\mu\bar{D}_\nu^u u)$			$(Q_{3L}\bar{H}u_R + \bar{t}_R\bar{H}^\dagger Q_{1L})(Q_{2L}\bar{H}u_R + \bar{c}_R\bar{H}^\dagger Q_{1L})$	
36	$(\bar{t}\bar{t}\gamma_5 D_\mu u)((D^\nu\bar{c})\bar{t}\gamma_\mu\bar{D}_\nu^u u)$			$(Q_{3L}\bar{H}u_R + \bar{t}_R\bar{H}^\dagger Q_{1L})(Q_{2L}\bar{H}u_R + \bar{c}_R\bar{H}^\dagger Q_{1L})$	

Table 13. Primary operators for  $qq\bar{q}\bar{q}$  interactions with two indistinguishable quarks, for the specific case of  $u\bar{u}\bar{t}\bar{c}$  interactions (Hermitian conjugate yields  $t\bar{c}\bar{u}\bar{u}$  and down-type interactions can be found by exchange for down quarks.). The  $SU(3)$  contractions are determined by  $S(A)$  to be symmetric (antisymmetric) in the  $uu$  indices. We've defined a back-forth derivative  $\bar{D}_\mu^u$ , which only acts on the  $u$  fields, and similarly  $\bar{D}_\mu^{u,Q_1}$  which acts on  $u_R$  and  $Q_{1L}$ . For descendant operators, one adds contracted derivatives to get arbitrary Mandelstam factors that respect the exchange symmetry, i.e.,  $(t-u)^2$ . At dimension 8,  $s\mathcal{O}_3$  and  $s\mathcal{O}_4$  become redundant, while at dimension 10,  $s\mathcal{O}_{27}$  and  $s\mathcal{O}_{28}$  become redundant. Thus one only needs to consider  $\mathcal{O}_{3,4,27,28}$  descendants with arbitrary factors of  $(t-u)^2$ .

with factors of  $(t - u)^2$ . These four redundancies explain the two  $-2$  terms in the Hilbert series numerator.

In Table 14, we've listed the primary operators for  $\bar{q}q\bar{q}q$  interactions when the two quarks are identical and the two anti-quarks are identical, for the specific case of  $u\bar{u}t\bar{t}$ . There are again two allowed  $SU(3)$  contractions, specified by whether the  $uu$  are in symmetric ( $S$ ) or antisymmetric ( $A$ ) combination. Since we're suppressing the  $SU(3)$  indices, this makes some of the expressions look identical, with (1-3) and (4-6) being the same, as well as (13-15) and (18-20). At dimension 8,  $s\mathcal{O}_2$  and  $s\mathcal{O}_3$  become redundant and at dimension 10,  $s\mathcal{O}_{19}$  and  $s\mathcal{O}_{20}$  become redundant. Thus one only needs the descendants of  $\mathcal{O}_{2,3,19,20}$  with factors of  $(t - u)^2$ . These four redundancies explain the two  $-2$  terms in the Hilbert series.

## 2.5 Interesting Top Decay Amplitudes for the HL-LHC

Now that we have all of the results, we can compare our unitarity upper bounds on the coupling strengths with our estimate of the couplings needed for HL-LHC sensitivity to the new top quark decays in Eqn. 2.13, to highlight which top decay amplitudes are worth studying in more detail at the HL-LHC. In the following, we will assume we have top quark pair production, where one top quark decays into a  $b$  quark and a leptonic  $W$ , with a  $b$ -tagging efficiency of 0.5, a lepton tagging efficiency of 0.8, and a  $W$  leptonic branching ratio of 0.2. For the Higgs modes, we will assume it decays to photons with a branching ratio of  $\sim 2 \times 10^{-3}$ .

First, let's consider two body decays of the top quark. For the charged current decays, we have  $t \rightarrow W(b, s, d)$ , which have left and right handed vector and tensor couplings, which can be distinguished by the lepton angular distributions [156]. In addition, the tensor operators can be constrained by top quark production [157]. For flavor changing neutral current decays, we have  $t \rightarrow (u, c)(h, Z, \gamma, g)$ , which are all

$i$	$\mathcal{O}_i^{u\bar{u}t\bar{t}}$	$d\mathcal{O}_i$	$SU(3)$	SMEFT Operator	c Unitarity Bound
1	$(\bar{t}u)(\bar{t}u)$	6	A	$(\bar{Q}_{3L}\bar{H}u_R + \bar{t}_R\bar{H}^\dagger Q_{1L})(\bar{Q}_{3L}\bar{H}u_R + \bar{t}_R\bar{H}^\dagger Q_{1L})$	$\frac{1.5}{E_{\text{TeV}}^2}, \frac{1.5}{E_{\text{TeV}}^4}$
2	$(\bar{t}\bar{t}\gamma_5 u)(\bar{t}u)$			$(i\bar{Q}_{3L}\bar{H}u_R - i\bar{t}_R\bar{H}^\dagger Q_{1L})(\bar{Q}_{3L}\bar{H}u_R + \bar{t}_R\bar{H}^\dagger Q_{1L})$	
3	$(\bar{t}\bar{t}\gamma_5 u)(\bar{t}\bar{t}\gamma_5 u)$			$(\bar{Q}_{3L}\bar{H}u_R - \bar{t}_R\bar{H}^\dagger Q_{1L})(\bar{Q}_{3L}\bar{H}u_R - \bar{t}_R\bar{H}^\dagger Q_{1L})$	
4	$(\bar{t}u)(\bar{t}u)$	6	S	$(\bar{Q}_{3L}\bar{H}u_R + \bar{t}_R\bar{H}^\dagger Q_{1L})(\bar{Q}_{3L}\bar{H}u_R + \bar{t}_R\bar{H}^\dagger Q_{1L})$	$\frac{1.5}{E_{\text{TeV}}^2}, \frac{1.5}{E_{\text{TeV}}^4}$
5	$(\bar{t}\bar{t}\gamma_5 u)(\bar{t}u)$			$(i\bar{Q}_{3L}\bar{H}u_R - i\bar{t}_R\bar{H}^\dagger Q_{1L})(\bar{Q}_{3L}\bar{H}u_R + \bar{t}_R\bar{H}^\dagger Q_{1L})$	
6	$(\bar{t}\bar{t}\gamma_5 u)(\bar{t}\bar{t}\gamma_5 u)$			$(\bar{Q}_{3L}\bar{H}u_R - \bar{t}_R\bar{H}^\dagger Q_{1L})(\bar{Q}_{3L}\bar{H}u_R - \bar{t}_R\bar{H}^\dagger Q_{1L})$	
7	$(\bar{t}\gamma^\mu u)(\bar{t}\gamma_\mu u)$	6	S	$(\bar{Q}_{3L}\gamma^\mu Q_{1L} + \bar{t}_R\gamma^\mu u_R)(\bar{Q}_{3L}\gamma_\mu Q_{1L} + \bar{t}_R\gamma_\mu u_R)$	$\frac{1.5}{E_{\text{TeV}}^2}$
8	$(\bar{t}\gamma^\mu \gamma_5 u)(\bar{t}\gamma_\mu u)$			$(\bar{Q}_{3L}\gamma^\mu Q_{1L} - \bar{t}_R\gamma^\mu u_R)(\bar{Q}_{3L}\gamma_\mu Q_{1L} + \bar{t}_R\gamma_\mu u_R)$	
9	$(\bar{t}\gamma^\mu u)(\bar{t}D_\mu u)$	7	A	$(\bar{Q}_{3L}\gamma^\mu Q_{1L} + \bar{t}_R\gamma^\mu u_R)(\bar{Q}_{3L}\bar{H}D_\mu u_R - i\bar{t}_R D_\mu \bar{H}^\dagger Q_{1L})$	$\frac{0.4}{E_{\text{TeV}}^2}, \frac{1.2}{E_{\text{TeV}}^4}$
10	$(\bar{t}\gamma^\mu u)(\bar{t}\bar{t}\gamma_5 D_\mu u)$			$(\bar{Q}_{3L}\gamma^\mu Q_{1L} + \bar{t}_R\gamma^\mu u_R)(i\bar{Q}_{3L}\bar{H}D_\mu u_R - i\bar{t}_R D_\mu \bar{H}^\dagger Q_{1L})$	
11	$(\bar{t}\gamma^\mu \gamma_5 u)(\bar{t}D_\mu u)$			$(\bar{Q}_{3L}\gamma^\mu Q_{1L} - \bar{t}_R\gamma^\mu u_R)(\bar{Q}_{3L}\bar{H}D_\mu u_R + \bar{t}_R D_\mu \bar{H}^\dagger Q_{1L})$	
12	$(\bar{t}\gamma^\mu \gamma_5 u)(\bar{t}\bar{t}\gamma_5 D_\mu u)$			$(\bar{Q}_{3L}\gamma^\mu Q_{1L} - \bar{t}_R\gamma^\mu u_R)(i\bar{Q}_{3L}\bar{H}D_\mu u_R - i\bar{t}_R D_\mu \bar{H}^\dagger Q_{1L})$	
13	$(\bar{t}u)([D^\mu \bar{t}] \bar{D}_\mu u)$	8	A	$(\bar{Q}_{3L}\bar{H}u_R + \bar{t}_R\bar{H}^\dagger Q_{1L})([D^\nu \bar{Q}_{3L}\bar{H}][\bar{D}_\mu^{\nu, Q_1} u_R + [D^\mu \bar{t}_R] \bar{D}_\mu^{\nu, Q_1} \bar{H}^\dagger Q_{1L})$	$\frac{0.09}{E_{\text{TeV}}^4}, \frac{0.9}{E_{\text{TeV}}^6}$
14	$(\bar{t}\bar{t}\gamma_5 u)([D^\mu \bar{t}] \bar{D}_\mu u)$			$(i\bar{Q}_{3L}\bar{H}u_R - i\bar{t}_R\bar{H}^\dagger Q_{1L})([D^\nu \bar{Q}_{3L}\bar{H}][\bar{D}_\mu^{\nu, Q_1} u_R + [D^\mu \bar{t}_R] \bar{D}_\mu^{\nu, Q_1} \bar{H}^\dagger Q_{1L})$	
15	$(\bar{t}\bar{t}\gamma_5 u)([D^\mu \bar{t}] i\gamma_5 \bar{D}_\mu u)$			$(i\bar{Q}_{3L}\bar{H}u_R - i\bar{t}_R\bar{H}^\dagger Q_{1L})(i[D^\nu \bar{Q}_{3L}\bar{H}][\bar{D}_\mu^{\nu, Q_1} u_R - i[D^\mu \bar{t}_R] \bar{D}_\mu^{\nu, Q_1} \bar{H}^\dagger Q_{1L})$	
16	$(\bar{t}\gamma^\mu u)([D^\nu \bar{t}] \gamma_\mu \bar{D}_\nu^u u)$	8	A	$(\bar{Q}_{3L}\gamma^\mu Q_{1L} + \bar{t}_R\gamma^\mu u_R)([D^\nu \bar{Q}_{3L}\bar{H}][\bar{D}_\mu^{\nu, Q_1} u_R + [D^\nu \bar{t}_R] \gamma_\mu \bar{D}_\nu^u u)$	$\frac{0.09}{E_{\text{TeV}}^4}$
17	$(\bar{t}\gamma^\mu \gamma_5 u)([D^\nu \bar{t}] \gamma_\mu \bar{D}_\nu^u u)$			$(\bar{Q}_{3L}\gamma^\mu Q_{1L} - \bar{t}_R\gamma^\mu u_R)([D^\nu \bar{Q}_{3L}\bar{H}][\bar{D}_\mu^{\nu, Q_1} u_R + [D^\nu \bar{t}_R] \gamma_\mu \bar{D}_\nu^u u)$	
18	$(\bar{t}u)([D^\mu \bar{t}] \bar{D}_\mu u)$			$(\bar{Q}_{3L}\bar{H}u_R + \bar{t}_R\bar{H}^\dagger Q_{1L})([D^\mu \bar{Q}_{3L}\bar{H}][\bar{D}_\mu^{\nu, Q_1} u_R + [D^\mu \bar{t}_R] \bar{D}_\mu^{\nu, Q_1} \bar{H}^\dagger Q_{1L})$	
19	$(\bar{t}\bar{t}\gamma_5 u)([D^\mu \bar{t}] \bar{D}_\mu u)$	8	S	$(i\bar{Q}_{3L}\bar{H}u_R - i\bar{t}_R\bar{H}^\dagger Q_{1L})([D^\mu \bar{Q}_{3L}\bar{H}][\bar{D}_\mu^{\nu, Q_1} u_R + [D^\mu \bar{t}_R] \bar{D}_\mu^{\nu, Q_1} \bar{H}^\dagger Q_{1L})$	$\frac{0.09}{E_{\text{TeV}}^4}, \frac{0.9}{E_{\text{TeV}}^6}$
20	$(\bar{t}\bar{t}\gamma_5 u)([D^\mu \bar{t}] i\gamma_5 \bar{D}_\mu u)$			$(i\bar{Q}_{3L}\bar{H}u_R - i\bar{t}_R\bar{H}^\dagger Q_{1L})(i[D^\mu \bar{Q}_{3L}\bar{H}][\bar{D}_\mu^{\nu, Q_1} u_R - i[D^\mu \bar{t}_R] \bar{D}_\mu^{\nu, Q_1} \bar{H}^\dagger Q_{1L})$	
21	$(\bar{t}\gamma^\mu u)([D^\nu \bar{t}] D_\mu \bar{D}_\nu^u u)$			$(\bar{Q}_{3L}\gamma^\mu Q_{1L} + \bar{t}_R\gamma^\mu u_R)([D^\nu \bar{Q}_{3L}\bar{H}][\bar{D}_\mu^{\nu, Q_1} u_R + [D^\nu \bar{t}_R] \bar{D}_\mu^{\nu, Q_1} D_\mu \bar{H}^\dagger Q_{1L})$	
22	$(\bar{t}\gamma^\mu u)([D^\nu \bar{t}] i\gamma_5 D_\mu \bar{D}_\nu^u u)$	9	S	$(\bar{Q}_{3L}\gamma^\mu Q_{1L} + \bar{t}_R\gamma^\mu u_R)(i[D^\nu \bar{Q}_{3L}\bar{H}][\bar{D}_\mu^{\nu, Q_1} u_R - i[D^\nu \bar{t}_R] \bar{D}_\mu^{\nu, Q_1} D_\mu \bar{H}^\dagger Q_{1L})$	$\frac{0.02}{E_{\text{TeV}}^5}, \frac{0.07}{E_{\text{TeV}}^6}$
23	$(\bar{t}\gamma^\mu \gamma_5 u)([D^\nu \bar{t}] D_\mu \bar{D}_\nu^u u)$			$(\bar{Q}_{3L}\gamma^\mu Q_{1L} - \bar{t}_R\gamma^\mu u_R)([D^\nu \bar{Q}_{3L}\bar{H}][\bar{D}_\mu^{\nu, Q_1} u_R + [D^\nu \bar{t}_R] \bar{D}_\mu^{\nu, Q_1} D_\mu \bar{H}^\dagger Q_{1L})$	
24	$(\bar{t}\gamma^\mu \gamma_5 u)([D^\nu \bar{t}] i\gamma_5 D_\mu \bar{D}_\nu^u u)$			$(\bar{Q}_{3L}\gamma^\mu Q_{1L} - \bar{t}_R\gamma^\mu u_R)(i[D^\nu \bar{Q}_{3L}\bar{H}][\bar{D}_\mu^{\nu, Q_1} u_R - i[D^\nu \bar{t}_R] \bar{D}_\mu^{\nu, Q_1} D_\mu \bar{H}^\dagger Q_{1L})$	

Table 14. Primary operators for  $qq\bar{q}\bar{q}$  interactions with two indistinguishable quarks and two indistinguishable antiquarks, for the specific case of  $u\bar{u}t\bar{t}$  interactions (The Hermitian conjugate yields the  $t\bar{t}u\bar{u}$  interactions and the down-type interactions can be found by exchange for down quarks.). The  $SU(3)$  contractions are determined by  $S$  to be symmetric in the  $uu$  indices and  $A$  to be antisymmetric. To simplify the expressions, we've defined a back-forth derivative  $\bar{D}_\mu^{\nu, Q_1}$ , which only acts on the  $u$  fields, and similarly  $\bar{D}_\mu^{\nu, Q_1}$  which acts on  $u_R$  and  $Q_{1L}$ . To get the descendant operators, one can add contracted derivatives to get arbitrary Mandelstam factors that respect the exchange symmetries, i.e.  $s, (t-u)^2$ . At dimension 8,  $s\mathcal{O}_2$  and  $s\mathcal{O}_3$  become redundant, while at dimension 10,  $s\mathcal{O}_{19}$  and  $s\mathcal{O}_{20}$  become redundant. Thus, one only needs to consider  $\mathcal{O}_2, \mathcal{O}_3, \mathcal{O}_{19}, \mathcal{O}_{20}$  with arbitrary factors of  $(t-u)^2$ .



actively being searched for at the LHC [146, 147, 149, 148, 150, 145, 144]. For all of these two body decays, there is a dimension 6 SMEFT operator that realizes the coupling, which explains why they are actively being studied. Our constraints on the coupling strengths agree that these are interesting and could potentially probe unitarity violating scales up to several tens of TeV.

Now, let's consider three body decays. We do not consider all hadronic decays of the top quark since those suffer from large combinatorial backgrounds at the LHC and our estimates would be entirely too optimistic. The charged current contact interaction  $t \rightarrow (b, s, d)(\bar{e}, \bar{\mu}, \bar{\tau})\nu$  has a different lepton pair invariant mass, which could be interesting to look for in terms of the quark-charged lepton invariant mass distribution. Here our estimates say that all of the dimension 6 CP even amplitudes could be interesting, even with unitarity violation occurring around 5 TeV, while the dimension 7 CP even amplitudes are interesting if unitarity violation occurs at about  $\sim 3$  TeV. Thus, these are worth exploring as there is room to increase the coupling for lower scales of unitarity violation. The other three body decays with a charged current interaction are  $t \rightarrow (b, s, d)W(\gamma, g)$ , which are generated at higher order in the Standard Model (we do not consider  $t \rightarrow dWZ$  since this is so close to being kinematically closed and thus, our assumptions about the phase space and matrix element would be wrong.). Contact amplitudes, unlike the Standard Model processes, are not enhanced in the collinear/soft limits so these might be distinguishable. Here, we find that of the operators in Table 5 the operators 3-4, 5 and 8 could be interesting for unitarity violation occurring at  $\sim 6$  TeV, operators 10 and 14-15 need unitarity violation by  $\sim 3$  TeV, and operators 19-22 and 25 need unitarity violation just above a TeV. However, since we should interpret our estimates carefully for these photon

and gluon decays, the lowest dimension operators are probably the most realistic to explore.

Flavor changing decays are highly suppressed in the Standard Model, so these are very promising to search for. To start with, four fermion contact terms  $t \rightarrow (c, u)(e, \mu, \tau)(\bar{e}, \bar{\mu}, \bar{\tau})$  are being searched for at the LHC in the lepton flavor violating modes to  $e\mu$  [158]. Here our estimates say that dimension 6 CP even and odd amplitudes are interesting for unitarity violation above 9 TeV, while dimension 7 CP even and odd amplitudes require unitarity violation by  $\sim 4$  TeV. The existing CMS search probes the dimension 6 amplitudes [158], but does not look for the dimension 7 amplitudes since they appear at dimension 8 in SMEFT. We can also consider flavor changing neutral current decays involving gauge bosons, including  $t \rightarrow (c, u)(h\gamma, hg, Z\gamma, Zg, \gamma\gamma, \gamma g, gg)$ , but not  $t \rightarrow (c, u)WW$  since it is also nearly kinematically closed. Again, our estimates are too optimistic for the decay modes that are completely hadronic, so we will focus on the other cases. For the decays with a Higgs and a photon or gluon, using the amplitudes and unitarity bounds in Table 3 of [28] and assuming the diphoton Higgs decay, we find that the dimension 6, 7, 8 operators require unitarity violation respectively by  $\sim 5, 2, 1$  TeV, so the dimension 6 and 7 ones are the most promising. For the decays into a  $Z$  and a photon or gluon, assuming the  $Z$  decays to  $ee$  or  $\mu\mu$ , we find that the dimension 6, 7, 8, 9 operators in Table 5, require unitarity violation respectively by  $\sim 3.5, 2.5, 1.2, 0.8$  TeV so the dimension 6, 7, 8 ones should be explored more closely, but the dimension 9 operators are likely out of reach. For the decays with two photons or a photon and gluon, we find that the dimension 7, 8, 9, 10, 11 operators in Tables 6, 7 require unitarity violation respectively by  $\sim 5, 2, 1.3, 1, 0.7$  TeV and given that we should be careful

with these estimates (especially for the  $\gamma g$  case), the dimension 7 ones are likely the only relevant ones.

There are also baryon number violating three body decays mediated by our amplitudes,  $t \rightarrow (\bar{c}, \bar{u})(\bar{b}, \bar{s}, \bar{d})(\bar{e}, \bar{\mu}, \bar{\tau})$ . These would have combinatorial backgrounds, but have been searched for in the past by CMS [159]. Again, theory explorations of these have focused on the dimension 6 SMEFT operators [160, 161], so it would be interesting if the ones parameterized by dimension 8 SMEFT operators give distinguishable signals.

To conclude, our unitarity bounds combined with our estimates for the interesting size of couplings for top quark decays has allowed us a quick survey of which of the decay amplitudes may be worth pursuing at the HL-LHC. As the dimension of the amplitude gets larger, these two constraints become more challenging to satisfy without lowering the scale of unitarity to the TeV scale. Since the SMEFT operator realization must be at the same or higher dimension, this motivates studying in more detail top decays from many dimension 8 and a few dimension 10 SMEFT operators to determine their sensitivity at HL-LHC and future colliders.

## CHAPTER III

### MASS AGNOSTIC JET TAGGERS

In Ch. II, we outlined a procedure for identifying on-shell amplitudes involving top quarks that are most susceptible to new physics. By combining techniques from the modern amplitudes program with perturbative unitarity, we were able to highlight a number of SMEFT-like operators whose couplings could feasibly be probed at the HL-LHC.

These SMEFT operators arise from integrating out a heavy new state. In addition to looking for the imprint of new physics on deviations to SM couplings, we can also search for signs of this new heavy state directly. This is often done by looking for a new resonance in the invariant mass spectrum, with the resonance centered at the mass of the new heavy state. If the production cross section of this new state is small, it can be difficult to distinguish this ‘bump’ in the invariant mass spectrum from a statistical fluctuation in the SM background. Traditional ‘cut and count’ methods exacerbate this problem, as any background events that make it past the cut must inevitably mimic the signal.

In this chapter, we compare a number of ML methods that aim to decorrelate the output of a classifier from the invariant jet mass. The advantage of these methods is two-fold. By removing the dependence on jet mass, this makes the classifier more useful for a broader search, rather than a search that is only looking for a new resonance at a specific mass. The second, perhaps more important advantage, is that by intentionally forcing our ML classifiers to be agnostic to the invariant mass of the jet, we preserve the background dominated sidebands around the new resonance, even as tighter cuts are made on the classifier’s output. This is crucial, as preserving these sidebands allows us to get a better handle on the underlying systematic uncertainties.

The methods we study fall broadly into one of two classes—data augmentation and training augmentation.

The outline of this chapter is as follows. A brief overview of the Monte Carlo simulation used to generate the signal and background events is given in Sec. 3.1. In Sec. 3.2, we classify and describe the representative methods for decorrelation, first focusing on the general idea and then on specific details. We present the results in Sec. 4.3. Appendix A.1 shows the results of the parameter sweep used to choose the adversarial network studied in this work. A comparison of popular histogram distance metrics is shown in App. A.2. A side-by-side graphical comparison of all of the decorrelation methods applied to all of the signals considered is shown in App. A.3.

The characterization of how data planing impacts mass decorrelation was done by LB. Rashmish K. Mishra characterized how the uBoost algorithm impacts mass decorrelation and provided the simulated data from a previous project. Andrea Mitridate characterized how PCA rotations impact mass decorrelation. Bryan Ostdiek characterized how generative adversarial neural networks impact mass decorrelation.

### **3.1 Simulation details**

In this section, we provide the details about the Monte Carlo simulated dataset used in this study. While this study does not rely on any specific model where the fat jets with some level of prongedness come from, we choose to work with a model which can give signals with 2- as well as 3- and 4-pronged jets, in suitable parts of parameter space. Studying higher pronged signals is useful in the context of mass decorrelation methods—apart from broadening the scope of the study, higher pronged jets are also sufficiently distinct from the background QCD jets, so that the importance of

de-sculpting of mass distribution is changed compared to lower pronged jets. We quantify these statements in the next sections.

The model considered is based on warped extra-dimensional RS models with more than 2 branes (see Ref. [162] for theory and [163, 164, 165] for phenomenological details). The relevant degrees of freedom for our case are the KK modes of the EW gauge boson (massive spin-1 EW charged particles, denoted by  $Z_{\text{KK}}/W_{\text{KK}}$ ) and the radion (a massive spin-0 singlet under SM, denoted by  $R$ ). In this “extended” RS model, the radion coupling to tops/higgs/gluons is highly suppressed as compared to usual RS models, so that the dominant way to produce the radion is through the spin-1 KK EW gauge boson’s decay into SM gauge bosons and a radion. This further leads to the dominant decay modes of the radion to be into SM W/Z. In the fully hadronic decay channel of W/Z from radion decay, one expects 4-pronged jets when the radion and/or the intermediate W/Z are boosted (see Ref. [165] for a detailed discussion on various regimes of boosted topology depending on the mass of the radion). The spin-1 KK EW gauge boson couples to SM particles like its SM counterpart. For preparing a 2-pronged signal sample, we use the process  $p+p \rightarrow Z_{\text{KK}}+j$ ,  $Z_{\text{KK}} \rightarrow jj$ , for a 200 GeV mass  $Z_{\text{KK}}$ . The produced  $Z_{\text{KK}}$  is boosted due to recoil with the first jet, so that in its fully hadronic decay, we get a 2-pronged jet. For a 3-pronged jet, we use the process  $p+p \rightarrow Z_{\text{KK}} \rightarrow t\bar{t}$ , with the usual 3-pronged fully hadronic top decay. In this case, the  $Z_{\text{KK}}$  is not boosted. Choosing the mass of  $Z_{\text{KK}}$  to be 1500 GeV, the tops from its decay are sufficiently boosted, so that we get a boosted 3-pronged sample. Finally, for the 4-pronged case, we consider  $p+p \rightarrow Z_{\text{KK}} \rightarrow Z(\rightarrow \nu\bar{\nu}) R(\rightarrow WW \rightarrow jjjj)$ . The  $Z_{\text{KK}}$  mass is taken to be 1500 GeV, and is produced unboosted. For a light radion of mass 200 GeV, the radion is produced boosted, and in its fully hadronic decay mode through Ws, we get a 4-pronged jet. Note that if one of the W from the radion

decays leptonically, we would get non-isolated leptons inside a 2-pronged jet, which would be rejected by usual isolation criteria. Further, in the case of radion decay to two Zs, if one of the Z decays invisibly, we would again be led to a 2-pronged jet. We avoid these complications by simply focusing on the fully hadronic decay mode of the radion through Ws.

The details of the signal process considered are shown in Tab. 15, along with the masses and the kinematic cuts chosen (at generation level) to produce boosted jets of desired prongedness. The background for these signals is taken to be QCD jet, generated by  $p + p \rightarrow Z + j$ ,  $Z \rightarrow \nu\bar{\nu}$ , at leading order in QCD coupling. A sample size of 500K is generated for each signal category, while 1M events are generated for the QCD background,<sup>1</sup> using MADGRAPH@AMC 2.6.4 [166] for parton-level events generation (14 TeV center of mass energy), PYTHIA 8 [167] for parton showers and hadronization, and DELPHES 3.4.1 [168] for detector simulation. Jets are constructed from the track and tower hits, using the anti- $k_t$  algorithm implementation in FASTJET, with a jet radius  $R = 1.2$ . The clustered jets are required to satisfy  $p_{T,J} > 500$  GeV and  $-2.5 \leq \eta_J \leq 2.5$ . A mass cut of  $50 \leq m_J(\text{GeV}) \leq 400$  is further imposed on the groomed mass of the jet, where grooming is performed by Pruning [169] with Cambridge-Aachen algorithm, with  $z_{\text{cut}} = 0.1$  and  $R_{\text{cut}} = 0.5$ . The highest  $p_T$  jet is considered as the candidate jet, from which the higher level NN inputs are constructed using the NSUBJETTINESS module in FASTJET for axis choice of ONEPASS KT AXES, for the same jet radius used in the construction of the original jet.

After the pre-selection cuts, the original 1M sample of QCD jets is cut down to 151 559. Similarly, the 500k events for the different BSM jets are reduced to

---

<sup>1</sup>We do not use jet matching or merging and only take the hardest jet in the event.

Prong	Process	Parameters (TeV)	Kinematic Cuts (GeV)
2P	$p + p \rightarrow j + Z_{KK}, Z_{KK} \rightarrow j j$	$m_{KK} = 0.2$	$p_{T,\min} = 50, p_{T,\min}^{\geq 1} = 400$
3P	$p + p \rightarrow Z_{KK} \rightarrow t \bar{t}$	$m_{KK} = 1.5$	$p_{T,\min} = 50$
4P	$p + p \rightarrow Z_{KK} \rightarrow Z(\nu\bar{\nu}) + R(jjjj)$	$m_{KK} = 1.5, m_R = 0.2$	$p_{T,\min} = 50$

Table 15. Details of the signal process used in the event generation, along with the choice of parameters and generation level kinematic cuts.

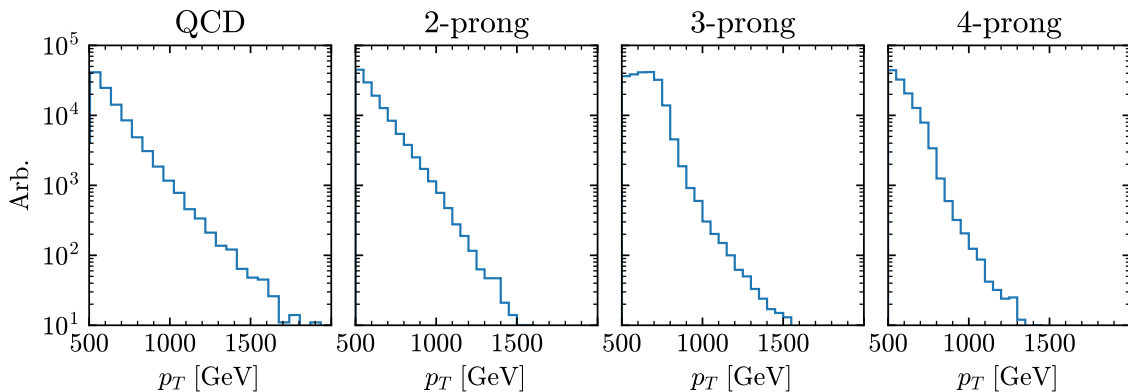


Figure 1. Distributions of the transverse momentum of the hardest jet.

187 659, 303 917, and 177 418 for the 2-, 3-, and 4-prong signals, respectively. The  $p_T$  distributions for the different samples are shown in Fig. 1. Training the machine learning algorithms is done on 70% of the combined datasets with 15% set aside for validation and 15% for independent testing.

### 3.2 Classification of Methods

In this section, we introduce various methods for decorrelating the mass distribution from classifier output. For classifiers, we consider single variable, such as  $\tau_{21}$ , as well as multivariate based architectures such as BDTs and NNs. We note that typically, multivariate analysis refer to shallow NNs or BDTs, as opposed to the more modern machine learning architectures. For mass decorrelation, we consider either augmenting the data, to reduce the correlation of jet mass from the input to the



classifier, or augmenting the training, where the optimization procedure is modified to decorrelate the classifier output from mass. We also introduce the benchmark classifiers, which are needed for comparison.

### 3.2.1 Classification without decorrelation

To allow a comparison for the performance of various decorrelation methods, we need to introduce the corresponding benchmark methods, which do not take any decorrelation into account. Jet classification is often done using the substructure within the jet. The  $N$ -subjettiness observables  $\tau_N^{(\beta)}$  [170, 31, 30] can quantify the substructure, and are defined as

$$\tau_N^{(\beta)} = \frac{1}{p_{T_J}} \sum_{i \in \text{Jet}} p_{T_i} \min \left\{ \Delta R_{1i}^\beta, \Delta R_{2i}^\beta, \dots, \Delta R_{Ni}^\beta \right\}, \quad (3.1)$$

where  $p_{T_J}$  is the transverse momentum of the whole jet,  $p_{T_i}$  is the transverse momentum of the  $i^{\text{th}}$  constituent of the jet,  $\Delta R_{Ai}$  is the distance between axis  $A$  and constituent  $i$  and  $\beta$  is a real number. The distance is defined as

$$\Delta R_{Ai} = \sqrt{\Delta\phi_{Ai}^2 + \Delta\eta_{Ai}^2}. \quad (3.2)$$

Suitable choices of the sub-jet axes lead to small values for different  $\tau_N^{(\beta)}$ . For instance, a boosted, hadronically-decaying  $W$  will have two hard partons in the jet. If the axes are chosen to be along the directions of these two partons, the value of  $\tau_2^{(\beta)}$  will be much lower than  $\tau_1^{(\beta)}$  where only one axis is considered. In contrast, a QCD jet will have a radiation pattern taking up more of the jet area, leading to constituents further away from the axes; both  $\tau_1^{(\beta)}$  and  $\tau_2^{(\beta)}$  will be relatively large. With this, a common method for classifying jets with 2-prong structure is to examine the ratio between the

two,

$$\tau_{21} \equiv \frac{\tau_2^{(1)}}{\tau_1^{(1)}}. \quad (3.3)$$

For our 2-prong signal (described in more detail in Sec. 3.1), using  $\tau_{21}$  results in an area under the receiver operating characteristic curve (AUC) of 0.747. An AUC of 0.5 is the equivalent of randomly guessing, and an AUC of 1.0 is a perfect classifier. Thus,  $\tau_{21}$  is a simple, single observable which significantly aids in discriminating 2-prong jets. When looking for boosted jets with more prongs, an analogous strategy is applied. For 3-prong jets, we use  $\tau_{32} = \tau_3^{(1)}/\tau_2^{(1)}$  and the observable  $\tau_{43} = \tau_4^{(1)}/\tau_3^{(1)}$  is used for 4-prong jets. The corresponding AUCs are 0.819 and 0.938. Once again, these simple single variable observables are strong discriminators of the corresponding signal topologies.

We use  $\tau_{21}$ ,  $\tau_{32}$ , and  $\tau_{43}$  as examples of single variable based classifiers. The benefit of these is that the variable is physics based and the systematics can be readily studied. However, a single variable may not be able to take advantage of the correlations of other observables in the data (e.g. see [171] for a BSM example). To fully incorporate all of the information, multivariate analysis is needed. We study two such multivariate methods, based on boosted decision tree and neural network architectures, which have been shown to lead to increased discrimination.<sup>2</sup>

The authors of [172] introduced a minimal but complete basis for a jet with  $M$ -body phase space. In particular, they showed that the dimension of the  $M$  body phase space is  $3M - 4$  and can be spanned using combinations of the  $\tau_N^{(\beta)}$ . In our study, we examine jets with up to 4-prong structure. We use a 5-body phase space for

---

<sup>2</sup>We do not use convolutional neural networks (jet images), but only focus on the jet substructure variables to keep the data representation constant across all methods.

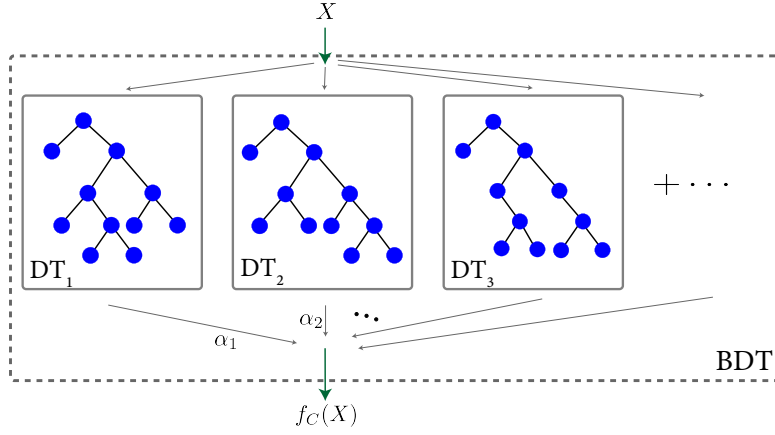


Figure 2. The architecture of a BDT. We take the BDT to be made of 150 DTs, with a max depth of 4. The input to the BDT are the variables that span the 5-body jet phase space, see Eq. (3.4). The indicated parameters  $\alpha_i$  represent the weight associated with the particular DT.

our multivariate analyses, as the performance is seen to saturate for 4-prong signals for a larger basis. For jets with fewer prongs, the 5-body basis is over-complete and the results saturate as well. This 5-body phase space basis is given as

$$X = \left\{ \tau_1^{(0.5)}, \tau_1^{(1)}, \tau_1^{(2)}, \tau_2^{(0.5)}, \tau_2^{(1)}, \tau_2^{(2)}, \tau_3^{(0.5)}, \tau_3^{(1)}, \tau_3^{(2)}, \tau_4^{(1)}, \tau_4^{(2)} \right\} . \quad (3.4)$$

These observables are used as the inputs for all of the multivariate approaches studied here. While this basis covers the substructure, the overall scale of the jet is not taken into account. Including the overall scale by using the transverse momentum or jet mass allows the classifiers to achieve better background rejection for a given signal efficiency, but at the expense of more sculpting. In the interest of not sculpting, and to have a fair comparison with the single variable taggers, we do not use the transverse momentum or the jet mass as an input for the machine learning algorithms.<sup>3</sup>

<sup>3</sup>The  $\tau_1^{(2)}$  observable is related to the ratio of  $m/p_T$ , so including the transverse momentum would allow the multivariate analysis the possibility to learn the jet mass.

The first multivariate method we consider is based on a boosted decision tree (BDT) architecture. A BDT is made of decision trees (DT), which are a tree of binary decisions on various variables, leading to a final binary classification of data. Boosting is the technique to allow an ensemble of DT with weak predictions to build an overall strong classifier, thereby *boosting* the performance. The DTs are ordered such that each subsequent DT learns on the failures of its predecessors, by assigning higher weights to the misclassified events. Figure 2 shows the architecture of a BDT successively made from many DTs. BDTs have the advantage of being faster to train, less prone to overfitting and easier to see inside the box, as compared to methods based on Neural Networks (NN). However, they are more sensitive to noisy data and outliers.

Before training, the inputs are first scaled using the `STANDARDSCALER` of `SCIKIT-LEARN` so that each variable has zero mean and unit variance on the training set. The data is split into three separate sets, one for training, one for validation, and one for testing. The same `STANDARDSCALER` is used for all of the sets. We use the standard implementation of the gradient boosting classifier within the `SCIKIT-LEARN` framework [173]. In particular, we use 150 estimators, a max depth of 4, and a learning rate of 0.1. This leads to good discrimination, with an AUC of 0.863—a 15% increase compared to using just  $\tau_{21}$ —for the same two-prong jets as before.

The second multivariate method we consider is based on neural networks. Figure 3 shows the basic setup of our network, which is implemented in the `KERAS` [174] package with the `TENSORFLOW` backend [175]. Unless otherwise stated, all neural networks in this study use the same architecture, with three hidden layers of 50 nodes each. The nodes are activated using the Rectified Linear Unit (ReLU). The last layer contains a single node with a Sigmoid activation function so that the output

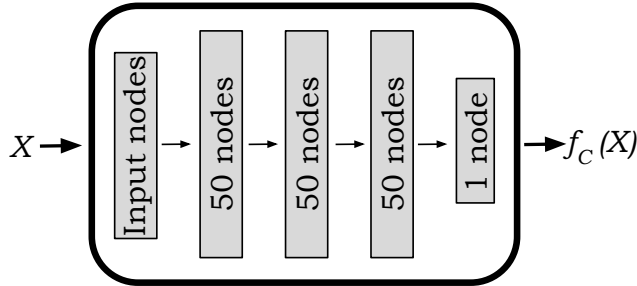


**Figure 3.** Many of the methods explored in this paper use a neural network classifier. For consistency, we always use a network with three hidden layers, each of which has 50 nodes and uses the ReLu activation function. The output is a single node with a sigmoid activation function. Our input data are the 11  $\tau_N^{(\beta)}$  variables of 5-body jet phase space shown in Eq. (3.4).

is a number between 0 and 1. We experimented with increasing or decreasing the number of layers, and found that three hidden layers is where performance saturated. Adding more nodes was not found to be helpful.

Training is done using the ADAM optimizer [176] to minimize the binary cross entropy loss function, which is given by:

$$L_{\text{classifier}} = -\frac{1}{N} \sum_i^N w_i \left[ y_i \ln f_C(X_i) + (1 - y_i) \ln (1 - f_C(X_i)) \right], \quad (3.5)$$

where  $y_i$  is the true label,  $f_C(X_i)$  is the network output, and  $w_i$  is the weight for the  $i^{\text{th}}$  event. It is standard for all of  $w_i$  to be taken to be one, but in the case of unbalanced classes with significant difference in the number of training samples, it is useful to set  $w_i$  to a specific value per class so that the effective number of training samples for each class becomes equal; these are called class weights. We implement class weights throughout as it was found to improve the classifiers, even though we do not have badly imbalanced classes. In Sec. 3.2.2.2, we explore another application of using weights during training.

The learning rate is initially set to  $10^{-3}$ . The loss is computed on the validation set after each epoch of training to ensure that the network is not over fitting. If the

validation loss has not improved for 5 epochs, the learning rate is decreased by a factor of 10, with a minimum of  $10^{-6}$ . Training is stopped when the validation loss has not improved for 10 epochs. Training usually takes between 30-40 epochs.

To have a fair comparison with the BDT, the network is trained on the same training set, using the same pre-processing. In addition, a common test set is used for all comparisons. The depth of the network allows it to learn more of the non-linearities between the input features than the boosted decision tree, yielding a AUC of 0.872. This is only a 1% increase in the AUC, but this can have large impacts on the potential discovery of new physics. For instance, at a fixed signal efficiency of 0.5, the background rejection increases from a factor of 13 to a factor of 15, allowing for 16% more background rejection.<sup>4</sup>

A summary of the application of the three different methods presented so far is in Fig. 4. The left panel shows the ROC curves, where better classifiers are up and to the right. In what follows, we will always use a solid line to denote a neural network based classifier, a dashed line for a BDT, and a dotted line for a single variable analysis. The two multi-variate analysis are similar and do much better than the single variable  $\tau_{21}$ . The right panels highlight the main problem explored in this work. The solid black line and the grey, shaded regions show the jet mass distributions for the QCD background and the 2-prong signal, respectively. The different colored lines show the resulting QCD only distribution when cutting to signal efficiencies of 0.95, 0.9, 0.8, 0.7, 0.6, and 0.5. The  $\tau_{21}$  classifier removes much of the QCD background at low jet masses, but allows many more events at high masses, so the background efficiency changes drastically as a function of the jet mass. This is even worse for the

---

<sup>4</sup>Here, and in the rest of the paper, we define the background rejection over the whole jet mass range considered:  $50 \leq m_J(\text{GeV}) \leq 400$ . We expect this choice to give the same qualitatively result which would be obtained by defining the background rejection on a smaller mass window (more details on this can be found in section 4.3.).

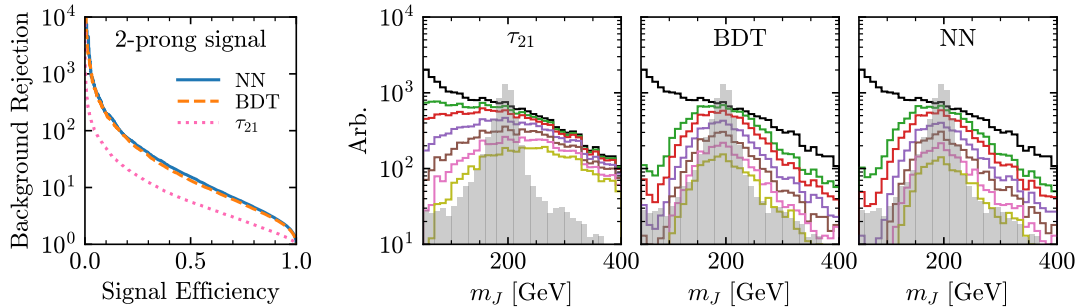


Figure 4. The left panel shows the ROC curves for three traditional methods, two based on machine learning, to classify a 2-prong signal jet from a QCD jet. The machine learning based methods achieve an area significantly higher than the single variable  $\tau_{21}$  based classifier. The right panels show the *background only* distributions for successively tighter cuts in the solid lines: signal efficiency of 1.0 (black), 0.95 (green), 0.9 (red), 0.8 (purple), 0.7 (brown), 0.6 (pink) and 0.5 (yellow). The signal with no cuts is shown in the filled-in, grey distribution. The only background events which pass the cuts end up having masses similar to that of the signal, even though the machine learning models do not have access to the mass.

multivariate analyses, which drastically sculpt the background distributions. Even though they are only using substructure information, and do not have access to the overall scale of the jet, the QCD events that make it through are peaked at the signal mass. This better background rejection comes at the cost of having both the signal and background shapes becoming very similar, which makes estimating systematic uncertainties much harder.

With this motivation, we now turn to the different approaches of decorrelating the output of a classifier with a given variable such as jet mass. These approaches broadly fall into two categories. The first is to augment the data on which the model is trained, while leaving the training procedure unchanged. The second category is to not augment the data, but to alter the training algorithm itself. We discuss these two in turn next.

### 3.2.2 Decorrelation based on data augmentation

The general idea of data augmentation is to reduce as much as possible the correlation of the classifier input to the jet mass. This can be done for both single and multivariable methods. For single variable classifier, this can be done analytically,

which we review below. For multivariable classifiers, the decorrelation must be done numerically, which we study using two recently proposed methods: *Planing* [38] and *PCA-based rescaling* [36, 65]. Both of these methods can be used for NNs and BDTs; in this section we only show the examples for the NN. These methods are fast, and have little application-time computation cost.

### 3.2.2.1 Analytic decorrelation

For classification based on a single variable such as  $\tau_{21}$ , analytic decorrelation methods have been proposed [65, 66], where a modified variable is constructed which is explicitly designed to preserve the background distribution. The appropriate scaling variable for QCD jets is the dimensionless ratio  $\rho = \log(m^2/p_T^2)$ . A plot of  $\tau_{21}$  vs  $\rho$  shows that background jets in different  $p_T$  ranges are linearly shifted from one another, and that there is a linear relation between  $\tau_{21}$  and  $\rho$  for a certain range of  $\rho$ . With this information, the decorrelation with mass can be performed in two steps. The  $p_T$  dependence is removed by defining  $\rho' = \rho + \log(p_T/\mu)$  where the value of  $\mu$  is chosen phenomenologically (taken to be 1 GeV in [65]). The linear correlation between  $\tau_{21}$  and  $\rho'$  can be removed by considering a modified variable—the so-called “Designed Decorrelated Tagger”,  $\tau_{21}^{\text{DDT}} = \tau_{21} - M\rho'$ , where  $M$  is the numerically calculated slope of the  $\tau_{21}$  vs  $\rho'$  curve. Apart from being simple to implement, the background systematics are easier to study because the method only involves a linear shift of the original observable. However, this method fails to generalize to more complex topologies, as there is not a simple linear relation between  $\tau_N^{(1)}/\tau_{N-1}^{(1)}$  and  $\rho'$  for  $N > 2$ .

Using  $\tau_{21}^{\text{DDT}}$  as a single variable classifier on a 2-prong signal gives an AUC of 0.687, which is the lowest among the decorrelation methods considered in this work. Compared to  $\tau_{21}$ , the Designed Decorrelated Tagger has an AUC that is 8% lower,



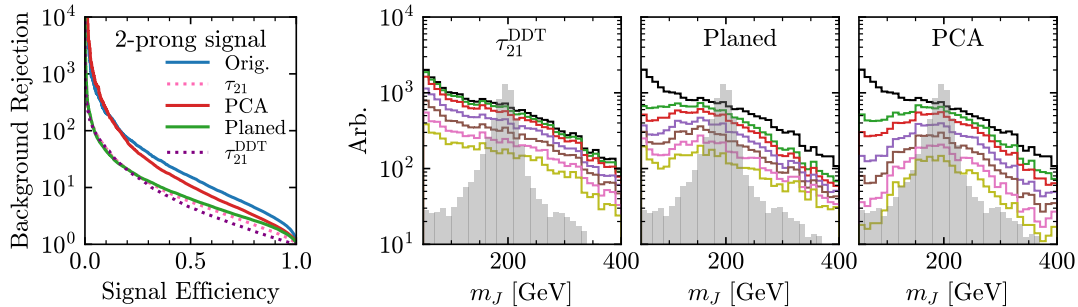


Figure 5. The left panel shows the ROC curves for the data augmented neural network methods of PCA and planing as well as the single variable DDT. The network trained on PCA-rescaled data is the best classifier, followed by the network trained on planed data. Both MV decorrelation techniques result in better classification than the single variable  $\tau_{21}^{\text{DDT}}$  based classification. The right panels show the *background only* distributions for successively tighter thresholds for the DDT, Planed, and PCA classifiers: signal efficiency of 1.0 (black), 0.95 (green), 0.9 (red), 0.8 (purple), 0.7 (brown), 0.6 (pink) and 0.5 (yellow). For context, the 2-pronged signal distribution is shown as grey filled-in region. All three methods reduce the background sculpting when compared to their Fig. 4 counterparts. A full side-by-side comparison for 2, 3, and 4 prong signals is shown in App. A.3.

though only a nominally smaller background rejection at a fixed signal efficiency of 50%, as seen in the left panel of Fig. 5. The right panels of Fig. 5 show how the background distribution changes as tighter cuts are made on the signal efficiency.  $\tau_{21}^{\text{DDT}}$  sculpts far less than  $\tau_{21}$  (See App. A.3 for a side-by-side comparison), and by eye, seems to perfectly preserve the shape of the QCD background distribution. We quantify these statements in the next sections.

### 3.2.2.2 *Planing*

Data planing [38] is a procedure that was initially designed to better understand what information an MV model is learning. This is accomplished by using the “uniform phase space” scheme introduced in [33] to restrict the model’s access to a certain observable, and looking for a subsequent drop in performance during testing. It turns out, however, that limiting what information the neural network is capable of learning and decorrelating the network output from a given observable are similar tasks.

At its core, planing is a weighting technique that takes a given distribution, and weights the data such that this distribution is now uniform over the range of values

in consideration. Our choice to weight both the signal and the background to be uniform is not unique—one could instead weight the signal to the background shape or vice versa, as long as they have the same distribution after the procedure. For a set of input features,  $X_i$ , where  $i$  denotes a given event, and  $m$  is the feature to be planed, the weights can be computed as:

$$[w(X_i)]^{-1} = C \left. \frac{d\sigma(X_i)}{dm} \right|_{m=m_i}, \quad (3.6)$$

where  $\sigma(X_i)$  is the distribution of the data as a function of feature  $X$ , and  $C$  is a dimensionful constant common to both signal and background. This is required, as signal and background are planed separately. In practice, these weights are determined by uniformly binning the events, and then inverting the resulting histogram. This introduces some finite binning effects, which tend to be more pronounced near the ends of the distribution. However, these effects can be easily mitigated, and do not have a significant impact on training, see Ref. [177] for a method to compute the weights without binning.

The planed feature does not necessarily have to be an input to the network. In this work, we are interested in decorrelating the network output from the jet mass, so this is the variable we apply the planing procedure to. As mentioned in Sec. 3.2.1, it is possible to add event-by-event weights to the loss function when training, treating some events as more or less important than others. Planing uses the weights in Eq. (3.6) and treats events that weigh less (more) as more (less) important. When training a network on planed data, the weights in the binary cross-entropy, Eq. (??), are the product of the planing weights, Eq. (3.6), and the class weights discussed previously.

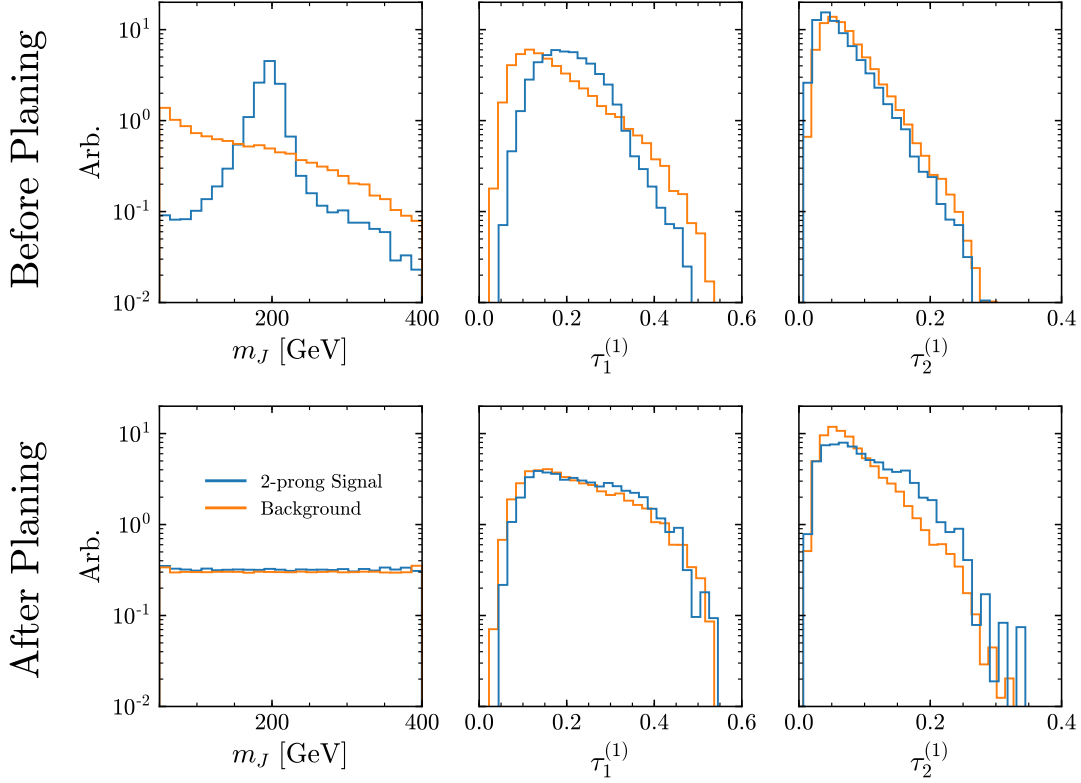


Figure 6. The upper and lower panels show distributions before and after planing away the jet mass, respectively. The left panels show the jet mass distribution for the 2-pronged signal and QCD background. By design, both distributions are (nearly) identical, and uniform across the entire mass range after planing. The center panels show  $\tau_1^{(1)}$ , one of the input variables for the classifiers. Before planing, this variable has discriminating power, but that was correlated with the jet mass and got removed by the planing process. The right panels show  $\tau_2^{(1)}$ , which has more separation between signal and background *after* planing.

Figure 6 highlights the key features of planing. In the left panels, we show the jet mass distributions for the 2-pronged signal events and the QCD background events. These distributions are planed separately, and the lower left panel shows the resulting distributions after planing away the jet mass information. Both are uniform over the relevant mass range, though there are some finite binning effects visible near the high- and low-mass ends of the planed distributions. The two center panels show one of the network inputs,  $\tau_1^{(1)}$ , before and after planing. Before planing there is a clear separation between the signal and background distributions, which means that there is discriminating power available to the network from this feature

alone. After weighting this input, we see that the signal and background  $\tau_1^{(1)}$  look much more similar, so there is now less discriminating power in this planed feature. However, planing does not reduce the discriminating power of every input feature. In the rightmost panels, we see that before planing, the distributions of  $\tau_2^{(1)}$  are nearly identical for signal and background. After applying the weights from the planing procedure, we see that there is now more distinction between the two, with the added benefit that this extra classifying power does not come at the cost of further sculpting the background jet mass distribution.

The MV classifier is trained on planed data, but is tested using unaltered data. Compared to a network with the same architecture, but trained on unaugmented data, the network trained on planed data is only able to achieve an AUC of 0.778—nearly 11% lower. This reduction in AUC corresponds to a background rejection nearly 3 times smaller at a fixed signal efficiency of 50% compared to the network trained on data which has not been planed, as seen in the left panel of Fig. 5. The right panels of Fig. 5 shows how the background distribution changes as tighter cuts are made on the signal efficiency. Comparing these distributions to the right panels of Fig. 4, it is clear that a network trained on planed data sculpts far less than any of the MV techniques discussed thus far. A side-by-side comparison can be found in App. A.3. We quantify these statements in the next sections.

### **3.2.2.3 PCA**

Another preprocessing procedure which aims to decorrelate the discrimination power of the NN from the jet mass was proposed in [36]. The basic idea is to preprocess the  $\tau_N^{(\beta)}$  variables in such a way that their distribution for QCD events is no longer correlated to the jet mass. This is achieved by first binning the standardized data (zero mean and unit standard deviation for each variable) in jet mass, with a variable

binning size to have the same number of QCD events in each bin. Then, in each bin, the standardized input variables are transformed as follows:

$$\vec{\tau}_i^{\text{std}} \rightarrow \vec{\tau}_i^{\text{PCA}} = R_i^{-1} S_i R_i \vec{\tau}_i^{\text{std}}, \quad (3.7)$$

where  $\vec{\tau}_i^{\text{std}}$  ( $\vec{\tau}_i^{\text{PCA}}$ ) is a 11 dimensional vector made of standardized (PCA transformed) variables in bin  $i$ ,  $R_i$  is the matrix that diagonalizes the covariance matrix for the QCD  $\tau$  variables in that given bin, and  $S_i$  makes the covariance matrix unity in that bin. The action of  $R_i$  is to induce a rotation into a basis where all the variables are linearly uncorrelated (this is the typical procedure used in principal component analysis (PCA), from which the method derives its name). Typically, after this rotation the data needs to be standardized again, requiring the action of the diagonal  $S_i$  matrix. The effect of PCA preprocessing procedure is illustrated by the scatter plot in Fig. 7, for two of the variables  $\tau_1^{(1)}$  and  $\tau_2^{(1)}$ , for three mass bins. In the scatter plot, the differences for the mass bins in the original variables are very easy to see, and also noticeable in the standardized variable. However, the mass bins look much more similar for PCA transformed variables. Notice that, while both the  $R$  and  $S$  are computed (bin-by-bin) only using the QCD sample, the transformation, Eq. (3.7), is then applied both to the QCD and signal events (both during the training of the NN and when applying the tagger to the test data).<sup>5</sup>

The network trained on PCA scaled data is able to achieve an AUC of 0.829, which is only a 4% reduction compared to the network with the same architecture trained on the unaltered data. This is shown in the left panel of Fig. 5. The right panel of Fig. 5 shows how the background distribution changes as tighter cuts are

---

<sup>5</sup>This is different than the case of planing, where the test set does not use data augmentation.

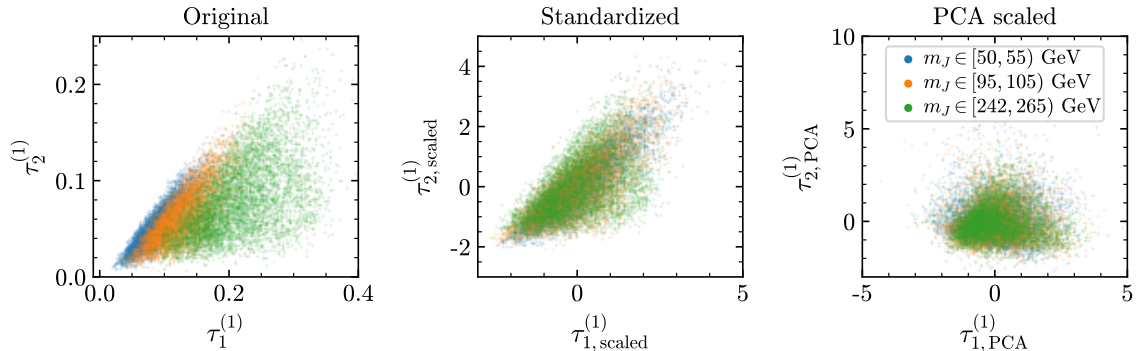


Figure 7. Scatterplot of two benchmark  $\tau$  variables for QCD events in three different mass windows. The left panel shows the original variables, before any kind of preprocessing. The events from different mass bins are well separated. The center panel shows the same events after removing the mean and setting the variance of each variable in each bin to unity. The different mass bins now have the same range, but the 2D correlations are still distinct. In the right panel, the events have been standardized and PCA transformed on a linearly independent basis. The different mass ranges are now hard to distinguish.

made on the signal efficiency. Comparing these distributions to the right panels of Fig. 4 (see App. A.3 for the side-by-side comparison), it is again clear that a network trained on PCA scaled data sculpts less. We quantify these statements in the next sections.

### 3.2.3 Decorrelation based on training augmentation

The general idea of training augmentation is to assign a penalty to distorting a background distribution that is desired to be uncorrelated with the classifier. This allows the optimal solution to balance the performance with decorrelation. Further, the decorrelation is not requested at just one step in the process, like in data augmentation based approach, but rather at each step in the process. In this category, we study two of recently proposed methods *uBoost* and *Adversarial Neural Networks*.

#### 3.2.3.1 *uBoost*

A BDT algorithm can be modified to leave some distributions of a given class unaffected in the classification procedure, as proposed in [67], called *uBoost*.<sup>6</sup> The

---

<sup>6</sup>A follow up to the *uBoost* algorithm was developed in Ref. [178]. This new method achieves similar classification and uniformity as *uBoost*, but only trains a single BDT with a modified loss function, rather than training multiple BDTs.

basic idea is to incorporate the cost of affecting the distribution that is desired to be unaffected in the optimization procedure. This procedure necessarily depends on the efficiency of classification, since the cost of affecting a distribution has to be measured for fixed efficiency. In other words, a trivial way to not affect a distribution for a variable for a given class is to have a very small efficiency to select the other class, so that no events of the other class are selected and the distribution stays the same. Hence, the non-trivial optimization algorithm is implicitly defined for a given efficiency, taken to be the average efficiency of the BDT. The average efficiency of the overall BDT corresponds to a local efficiency for each event. This local efficiency is calculated using  $k$ -nearest-neighbor (kNN) events that pass the BDT cut, constructed from DTs up to this point. Hence this local efficiency depends on both the event and the tree. Data points with a local efficiency lower than average efficiency are given more importance, and those with a local efficiency higher than average efficiency are given lesser importance. The relative importance is controlled by a parameter  $\beta_u$  (see Eq.(2.3) in Ref. [67]). The BDT then is optimized for a given efficiency. One can then construct an even bigger ensemble of BDTs, each optimized for a given efficiency, and design the response function in such a way that the right one is chosen for a given efficiency. An illustration of this is sketched in Fig. 8.

The uBoost architecture we consider uses 20 BDTs to cover the full signal efficiency range, with each BDT being comprised of 150 individual DTs, each with a maximum depth of 4. The decision trees use the Gini Index to measure the quality of a split. Additionally, we use  $k = 50$  nearest neighbor events to compute the local efficiencies. As the authors of [67] point out, there is very little change in the performance of uBoost for  $k \in [50, 1000]$ , but choosing  $k < 20$  drastically increases the statistical uncertainty on the local efficiency, which worsens the performance of

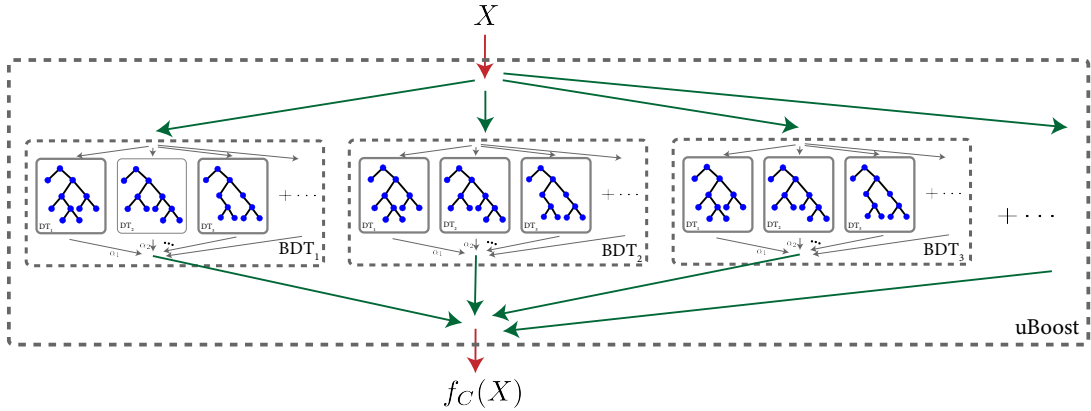


Figure 8. The network architecture used in the uBoost algorithm. Each BDT has the same layout as those in Fig. 2, and is tasked with keeping the background uniform at a given target signal efficiency. We use 20 BDTs to cover the entire efficiency range, and results are interpolated between target efficiencies to keep the background uniform over the whole efficiency range. The Gini index is used to measure the quality of a split, and the best split is taken when creating new branches.

the uBoost algorithm. The parameter  $\beta_u$  which sets the relative training importance of events with local efficiency more/less than the average efficiency, is set to 1.

Using the uBoost algorithm for classification results in an AUC of 0.783, which is a 9% reduction when compared to classification using standard gradient boosted decision trees. At a fixed signal efficiency of 50%, this translates into uBoost rejecting 23% less background than a standard BDT operating at the same signal efficiency. However, this reduction in classification power comes with the benefit of decreased background sculpting. The right panel in Fig. 9 shows how the background distribution changes as tighter cuts are made on the uBoost network output. By eye, uBoost sculpts the background considerably less than a traditional BDT. Quantitative assessments are made in Section 4.3.

### 3.2.3.2 Adversarial

The idea to use adversarial networks to decorrelate jet mass from the output of a classifier was first introduced in [64]. The authors showed that in the case of small systematic errors, both adversarially trained networks and traditional neural



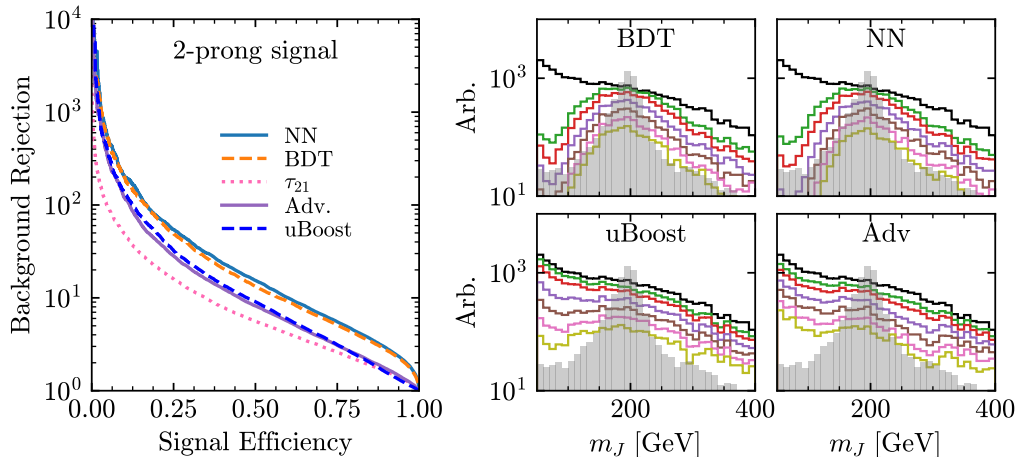


Figure 9. The left panel shows the ROC curves for the adversarially trained neural network and uBoost, along with the results of the base neural network and  $\tau_{21}$ , for comparison. The adversarial results use  $\lambda = 50$ , and the uBoost results use  $\beta_u = 1$ . The right panels show the *background only* distributions as successively tighter cuts are made on the output of these classifiers: signal efficiency of 1.0 (black), 0.95 (green), 0.9 (red), 0.8 (purple), 0.7 (brown), 0.6 (pink) and 0.5 (yellow). The full 2-pronged signal is shown in the filled-in grey distribution for context. Both these methods are able to preserve the background shape well, with only a marginal decrease in performance, but take a factor of 10 to 100 more time to train. Compared to their MV counterparts in the upper panels, it is clear that the training augmentation based approaches significantly reduce the extent of the background sculpting. A full side-by-side comparison for 2, 3, and 4 prong signals is shown in App. A.3.

networks lead to better chances of discovery for 2-pronged jets than using traditional jet substructure or the DDT [65]. However, when the systematic uncertainty on the background is large, the traditional neural network never does as well as the adversarially trained network or the analytic taggers. The adversarially trained network remains better than the analytic methods.

The key aspect of adversarial training is using multiple neural networks, instead of single one. First, the inputs are fed through a traditional classifier, as in Sec. 3.2.1. The output of the classifier is a number between 0 and 1. The next stage trains a second network to infer the feature to be decorrelated (the mass for us) using only the output of the classifier. An illustration of this is shown in Fig. 10.

The overall goal then becomes to train a classifier which not only classifies well, but which also does not allow the adversary to infer the jet mass. This is done using

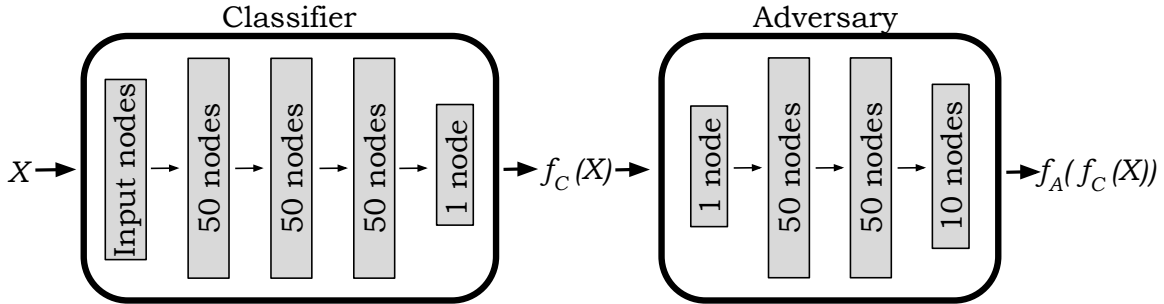


Figure 10. The setup of our adversarially trained neural network. The classifier has the same hyperparameters as in Fig. 3. The output of the classifier becomes the input of the adversary, which attempts to predict which bin of the jet mass the QCD events came from. We use tanh activation for the hidden layers of the adversary, and softmax activation for the final layer, with 10 outputs. The multi-class cross entropy loss function is used for the adversary.

a combined loss function of the form

$$L_{\text{tagger}} = L_{\text{classifier}} - \lambda L_{\text{adversary}}, \quad (3.8)$$

where  $L_{\text{classifier}}$  and  $L_{\text{adversary}}$  are usual classification loss functions. However, we only calculate  $L_{\text{adversary}}$  for the QCD sample and not the signal samples. The parameter  $\lambda$  is a positive hyperparameter set by the user, giving the relative importance of the two tasks; classifying and decorrelating. A larger value of  $\lambda$  puts more emphasis on not allowing the adversary to be able to infer the mass at the cost of poorer classification.

As done in Ref. [64], we use ten nodes for the output of the adversary, with the jet mass digitized to ten bins with equal numbers of QCD jets per bin, treating the problem as a multi-class classification problem. The activation for the last layer is the softmax function and  $L_{\text{adversary}}$  is the multiclass cross entropy. This was found to lead to more stable training than trying to regress the exact jet mass. In addition, we found that a tanh activation function for the hidden layers of the adversary to be more stable than ReLU activation. The ATLAS study in Ref. [70] also uses adversarial neural networks for mass decorrelation, but does so by having the adversary predict

the probability distribution function of the background, as in Ref. [68], rather than predicting the mass bin.

The adversarial set-up makes training the networks more involved. First, we train the classifier using only the binary cross entropy loss function. Next, the adversary is trained alone, only using the output of the classifier. We found the training procedure which led to the most stable results for the combined networks to be as follows. The adversary is set to not be trainable, and the classifier weights are updated using the total loss of Eq. (3.8). However, only a small number of updates to the weights of the classifier are allowed. Then, the classifier weights are frozen and the adversary becomes trainable. It is given substantially more time to adjust to the updated classifier, minimizing its own  $L_{\text{adversary}}$  for many epochs. The process is then repeated many times, first making minor updates to the classifier followed by ample time for the adversary to respond. This procedure takes about a factor of 10-100 more time to train than other methods.

The other aspect of adversarial training which makes it more challenging is the choice of the hyperparameter  $\lambda$ . *A priori*, the value of  $\lambda$  should be chosen so that the loss of the classifier is of order the same size as the loss of the adversary. However, the best value will depend on the use case. The necessity of this optimization produces a family of classifiers with trade-offs between classifying power and decorrelation abilities. This is in contrast to analytic and data augmentation based decorrelation methods, which only give a single classifier. For our studies, we scanned over ranges of  $\lambda \in \{1, 2, 5, 10, 20, 50, 100, 200, 500, 1000\}$ . The results seem to saturate at  $\lambda = 50$ . The result of this hyperparameter scan are shown in App. A.1. We tried smaller values as well, but these were seen to be nearly equivalent with the traditional neural

network. The longer training times, coupled with the need to optimize  $\lambda$  greatly increases the computational overhead for using adversarial methods.

The adversarially-trained neural network (with  $\lambda = 50$ ) achieves an AUC of 0.807, which is a 7% reduction in AUC compared to the neural network considered in section 3.2.1. At a fixed signal efficiency of 50%, this difference in AUC translates to the adversarially trained network rejecting 33% less background than a traditionally trained neural network. However, the adversarial approach still results in a better classifier than single variable analyses, as shown in Fig. 9. The right panel of Fig. 9 shows how the background distribution changes as tighter cuts are made on the output of the adversarially trained network. It is clear that the adversarial approach sculpts the background far less than traditional neural networks. We make this statement more quantitative in Sec. 4.3.

### 3.3 Results

One of the considerations when choosing an analysis method is the computational overhead. Table 16 shows the amount of time it takes to train the different classifiers. The difference between the number of prongs is mostly dominated by the different sample sizes, but also comes from how easy the minimum of the loss function is to find.

The neural network based methods take longer to train than the boosted decision trees. As expected, the methods which augment the training process take longer to return a good classifier. The uBoost method trains 20 different BDTs so it takes around 20 times longer than the base BDT.<sup>7</sup> Decorrelating the NN by using an adversary network takes substantially longer to train, although as we show below,

---

<sup>7</sup>The updated boosting methods found in [178] do not require training multiple BDTs, so their training time is similar to a standard BDT.

Method	2-prong	3-prong	4-prong
Base Network	$409 \pm 56.8$	$601 \pm 82.9$	$483 \pm 64.9$
Base BDT	$66 \pm 2.7$	$88 \pm 0.4$	$64 \pm 1.1$
PCA Network	$421 \pm 48.7$	$566 \pm 63.6$	$366 \pm 32.8$
PCA BDT	$70 \pm 1.3$	$97 \pm 1.3$	$69 \pm 0.9$
Planed Network	$406 \pm 44.2$	$604 \pm 90.7$	$462 \pm 81.7$
Planed BDT	$64 \pm 1.0$	$88 \pm 1.2$	$63 \pm 0.8$
Adversarial	$49\,429 \pm 520.8$	$54\,953 \pm 683.3$	$49\,003 \pm 1892.0$
uBoost	$1495 \pm 6.6$	$2047 \pm 6.5$	$1430 \pm 10.0$

Table 16. The time in seconds to train a classifier on dual E5-2690v4 (28 core) processors. The mean and standard deviation are calculated over 10 independent trainings. The large variance in the neural network times is due to the early stopping condition, leading to a non-fixed number of epochs. Note that the adversarially trained neural network statistics are over sampled once over each of the nine different values of  $\lambda$  due to the long training time. In addition, the adversarial networks used GPU nodes. BDTs are faster to train, but are not as effective classifiers. The Adversarial and uBoost decorrelation methods take much longer than the PCA or Planing methods.

it does achieve the best results. In contrast, the methods which augment the data beforehand show very little change in the time it takes to train.

The computational overhead is not the only consideration. In the rest of this section, we examine both the amount of background rejection and the degree to which the background is sculpted. Depending on the particular analysis, it may be optimal to allow more or less sculpting depending on the needed background rejection. The background rejection is defined over the whole jet mass range considered:  $50 \leq m_J(\text{GeV}) \leq 400$ . For the taggers considered in this work, we expect this choice to give qualitatively the same results that would be obtained by defining it in a narrower mass window centered around the signal. This is because they are structured exactly to achieve this goal: to keep the background rejection constant over the whole mass range.

To quantitatively define how much the classifier sculpts the background, we use the Bhattacharyya distance, which is a popular measure of the distance between two probability distributions. For two given histograms  $H_1$  and  $H_2$  with  $N$  bins each, the distance is given as:

$$d_B(H_1, H_2) = \sqrt{1 - \frac{1}{N\sqrt{\langle H_1 \rangle \langle H_2 \rangle}} \sum_I \left( \sqrt{H_1(I)H_2(I)} \right)}, \quad \langle H_K \rangle = \frac{1}{N} \sum_J H_K(J). \quad (3.9)$$

This distance has the nice property that it is normalized between 0 and 1, allowing for a comparison of the sculpting from various taggers more easily. This choice of metric is not unique. In App. A.2, we compare the Bhattacharyya distance with another distance measure, the Jensen-Shannon distance (used in Ref. [70]). The two are seen to have similar features.

### 3.3.1 Augmented training

In this section we examine the decorrelation methods which change the way the training is done, namely the adversarial neural networks and uBoost. While these methods take longer to train, their input data is unaltered, which is better for calibration and other systematics. In all of the comparisons, we include the base neural network and the single-variable analysis as benchmark references.

Figure 11 shows the ROC curves for decorrelation methods along with the benchmarks. The left, middle, and right columns are for the 2-prong (boosted  $Z_{KK} \rightarrow q\bar{q}$ ), 3-prong (boosted top), and 4-prong (boosted  $R \rightarrow q\bar{q}q'\bar{q}'$ ) jets as described in Sec. 3.1, respectively. The first noticeable trend is that the more prongs the signal sample contains, the easier it is to distinguish from the QCD background, which is typically single pronged. In fact, for many of our classifiers for the 4-prong

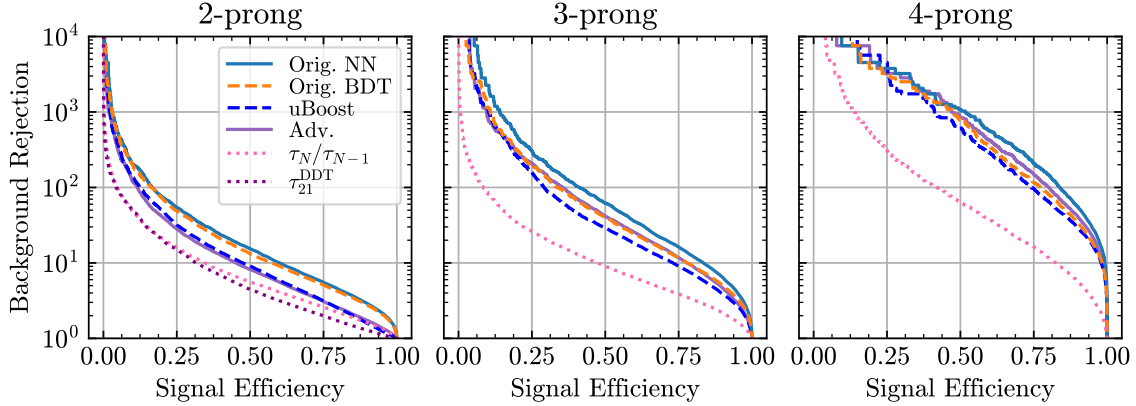


Figure 11. ROC curves for the 2-, 3-, and 4-prong signal jets versus QCD background for the methods which augment the training method to decorrelate the jet mass. The solid, dashed, and dotted curves show results for neural networks, boosted decision trees, and single variable analysis, respectively. The light blue curves are for the traditional method benchmarks. The purple and dark-blue lines denote the adversarially trained network and uBoost decision tree. For the 3- and 4-prong cases, uBoost cannot classify as well as the adversarially trained neural networks, but still does much better than using a single variable,  $\tau_3/\tau_2$  and  $\tau_4/\tau_3$ , respectively

signal, we run out of background events at a signal efficiency of around 0.1. We will see evidence of this in the remaining metrics even though the rapid removal of background events yields more statistical uncertainty on these results.

The adversarially trained network with  $\lambda = 50$  is shown in the solid light-purple line and uBoost classifier is shown by the dashed blue line. This value of  $\lambda$  was around where the performance saturated; Appendix A.1 shows the results for all values of  $\lambda$  tested. For the 2-prong signal, uBoost and the adversarially trained network have very similar curves. These are roughly in the middle of the base MV methods and the single variable analysis. Moving to the 3- and 4- prong signals, the adversarially trained network achieves better background rejection than uBoost, but both of these are significantly better than a single variable analysis. Note that currently there are no DDT type methods for 3- and 4-prong jets.

The Bhattacharyya distance calculated on the *QCD background only* distributions is shown in Fig. 12. Specifically, we calculate the distance between the original (no cuts) jet mass distribution and the background distribution which passes

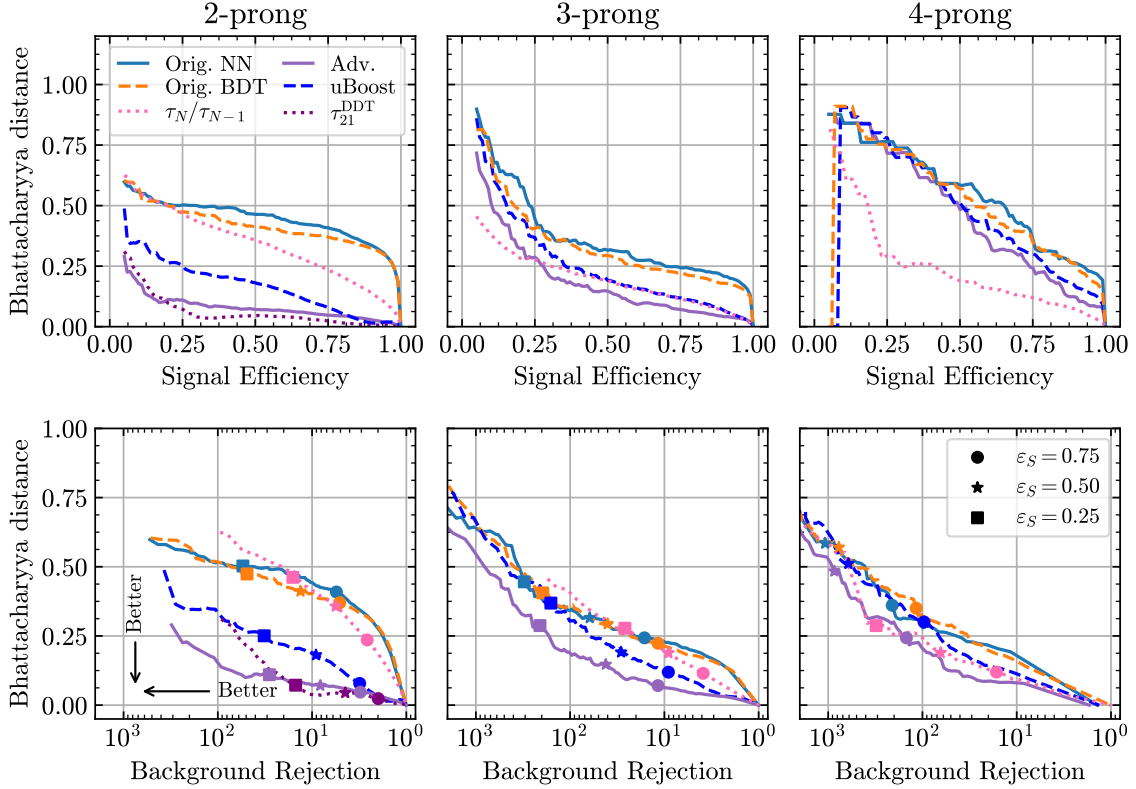


Figure 12. The Bhattacharyya distance for the QCD background distributions compared to the original distributions. The distance is defined in Eq. (3.9), and a larger distance represents more sculpting—lower on the plot is better. The upper and lower rows plot the distance as a function of signal efficiency or background rejection, respectively.  $\tau_{21}^{\text{DDT}}$  produces the smallest distances for fixed signal efficiency, but does not generalize to higher-prong jets. The adversarially trained network yields a close approximation and generalizes to more prongs. uBoost falls between the original methods and the adversarially trained network, but takes a factor of 30 less time to train.

a cut for the specified signal efficiency (top row) or background rejection (bottom row). We see clearly that the original NN and BDT give the greatest amount of distortion to the distributions, resulting in larger distances. For the 2-prong jets, the distance for original MVs is around 0.5 for most of the signal efficiencies, and  $\tau_{21}$  slowly grows to the same values. For 3- and 4-prong, the single N-subjettiness variable produce smaller distances than the original MVs over the whole region.

The  $\tau_{21}^{\text{DDT}}$  classifier was specifically designed to remove the mass correlation; as such, it produces the smallest distances for fixed signal efficiency. However, there are no 3- or 4-prong versions. That being said, the adversarially trained neural network



produces distances that are comparable to  $\tau_{21}^{\text{DDT}}$  over the range of signal efficiencies. It also has the smallest distances for the MV methods for the 3- and 4-prong signals. uBoost does not achieve as low of distance scores but its distances are still generally closer to the adversarially trained network than the originals, and trains about a factor of 30 faster than the adversary.

Only looking at the distance compared to the signal efficiency does not take into account how well the classifier separates the signal jets from QCD. Balancing the need for unaltered distributions against the necessary background rejection is task specific, but can be aided by plotting the two against each other. In the lower row of Fig. 12, we show the parametric plots of the histogram distance versus the background rejection. In these plots, the optimal classifier will be to the lower-left corner, yielding a small distance between the distributions before and after cuts and simultaneously rejecting large backgrounds. These are made by scanning over the values of the signal efficiency from 1 to 0.05, which is why the curves do not extend all the way to the left. The points marked by circles, stars, and squares are for fixed signal efficiencies of 0.75, 0.5, and 0.25, respectively.

The original MV methods, along with the single variable analysis, yield similar shaped curves, offering the same amount of sculpting for a fixed amount of background rejection. This is interesting because the  $\tau_N/\tau_{N-1}$  distances were quite different when plotted against the signal efficiency. This can be observed by examining the location of the marked points along the curve, where the pink ones fall further to the left than do the light blue and orange points.

The adversarially trained classifier sculpts the least for a given background rejection for the different pronged jets, other than a small region where  $\tau_{21}^{\text{DDT}}$  is the

least. uBoost again falls between the original methods and the adversarially trained network, providing a good compromise on computation time and decorrelation.

For the 4-prong jets, all of the classifiers give similar results with fairly large distances. This indicates that the QCD is not 4-pronged, so all of the classifiers can cut out large amounts of the background. Even the methods which are supposed to produce smaller histogram distances end up sculpting the backgrounds quite heavily. In any real analysis, this is most likely not an issue because of the extensive background rejection.

Plotting the distance versus signal efficiency (top row of Fig. 12) makes it hard to see trends in sculpting between the various pronged jets. However, in the bottom row, we get a sense that the decorrelation techniques yield a certain distortion of the background shape given the amount of rejection. For instance, with a background rejection of 10,  $\tau_{21}^{\text{DDT}}$ , uBoost, and adversarially trained networks yield Bhattacharyya distances  $\sim 0.1$  for all of the prongs. Additionally, the distance is  $\sim 0.25$  for a background rejection of 100 for all prongs. This is expected because our different pronged signal distributions peak at roughly the same mass (200 GeV for 2- and 4-pronged, and 173 GeV for 3-pronged). Thus, for a fixed background rejection, the background events which remain mimic a signal region that is approximately independent of the signal prongedness.

### 3.3.2 Augmented data

The previous section examined the extent to which uBoost and adversarially trained neural networks can decorrelate the jet mass from the classifier output, which is achieved by changing the training procedure. We now move on to focus on the methods proposed in Sec. 3.2.2: altering the input data rather than the training. Augmenting the data rather than the training procedure greatly reduces the amount

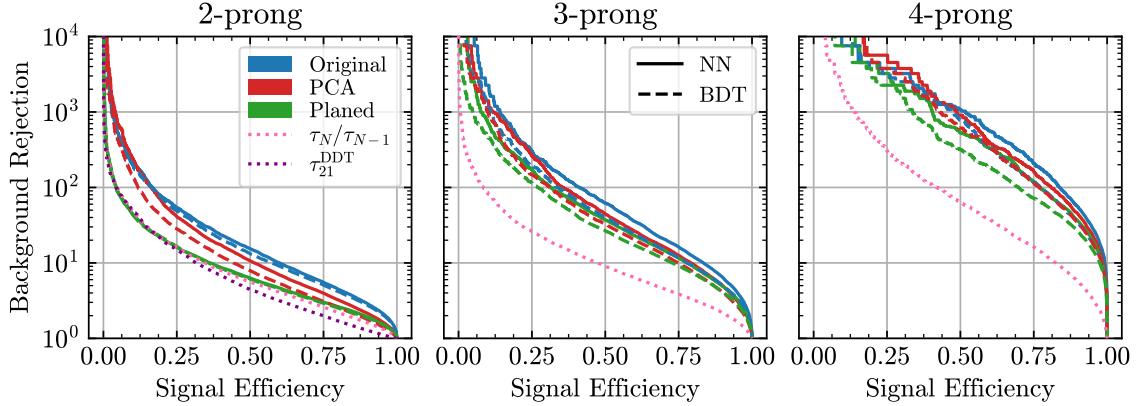


Figure 13. ROC curves for the 2-, 3-, and 4-prong signal jets versus QCD background for the methods which augment the data to decorrelate the jet mass rather than augment the training. The dashed and solid lines show the gradient boosted decision trees (BDT) and neural networks (NN), respectively. The blue, red, and green curves are for the data which has not been altered, data which uses the PCA rescaling, and data which has the jet mass planed away. The dotted lines show the results using a single combination of the N-subjettiness variables. Generally the BDTs have slightly worse background rejection than the NNs. Similarly, the PCA rescaling based methods tend to be between the unaltered methods and the planing methods, which are better than the single variable analyses.

of time required to train the models, as shown in Tab. 16. Additionally, it allows us to test the methods using both boosted decision trees and neural networks.

The overall ability to classify is shown in the ROC curves in Fig. 13. As with the last section, the left, middle, and right plots have the signal jets with boosted two-body, three-body, and four-body decays, respectively. In all of the plots, the blue, red, and green lines are for the unaltered data, the PCA rotated data, and the Planed data respectively. The solid lines represent the neural network results, and the dashed lines are the gradient boosted decision tree. Additionally, we show the single N-subjettiness variable analyses in the dotted lines.

In all of the plots, the unaltered neural network achieves the best classification. This is expected, because neural networks can use more non-linearities, and the data has not been processed to remove correlations with the jet mass. The 2-prong signal shows some difference in the PCA and Planed neural network results, but for the 3- and 4-prong signal neural nets, these methods yield similar classification. The BDTs show similar trends, performing slightly worse than the neural networks in terms of

pure classification. The methods to decorrelate the jet mass from the MV output still achieve better background rejection than the single variable analysis.

The degree of decorrelation is examined in Fig. 14 where the Bhattacharyya distance is plotted against the signal efficiency in the upper row. The distance is calculated on the background-only distributions and the color scheme is the same as the previous figure. In almost every case, the BDT has smaller distances (less distortion) than the NN. The classifiers trained on the PCA rotated data show much less distortion than the original data other than for the 4-prong jets. For instance, the 2-prong jet mass distribution distances are about half the value as the corresponding unaltered method. The method of planing away the jet mass information shows nearly an additional factor of two less sculpting than the PCA method for the 2-prong jets. However, the planing curves do not reach as low of distances as  $\tau_{21}^{\text{DDT}}$  for most signal efficiencies.

The planing method produces the smallest distances out of the different methods considered here for the 3-prong jets. The 4-prong signal is particularly easy for the classifiers to distinguish from the QCD background. As a result, even the MVs with attempts at mass decorrelation have large Bhattacharyya distances for fixed signal efficiency. Out of these, the planing method sculpts the distributions the least.

In the bottom row of Fig. 14 we again show the background rejection plotted against the Bhattacharyya distance. We again find that for 2-prong jets,  $\tau_{21}^{\text{DDT}}$  sculpts the least for a given background rejection. However, it does not reach the largest background rejection values. The next best method is the neural network trained on planed data, which even produces smaller distances for background rejection above around 20, as compared to  $\tau_{21}^{\text{DDT}}$ . The planing methods seem different than the others in that the NN has less sculpting than the BDT. The BDT trained on the PCA

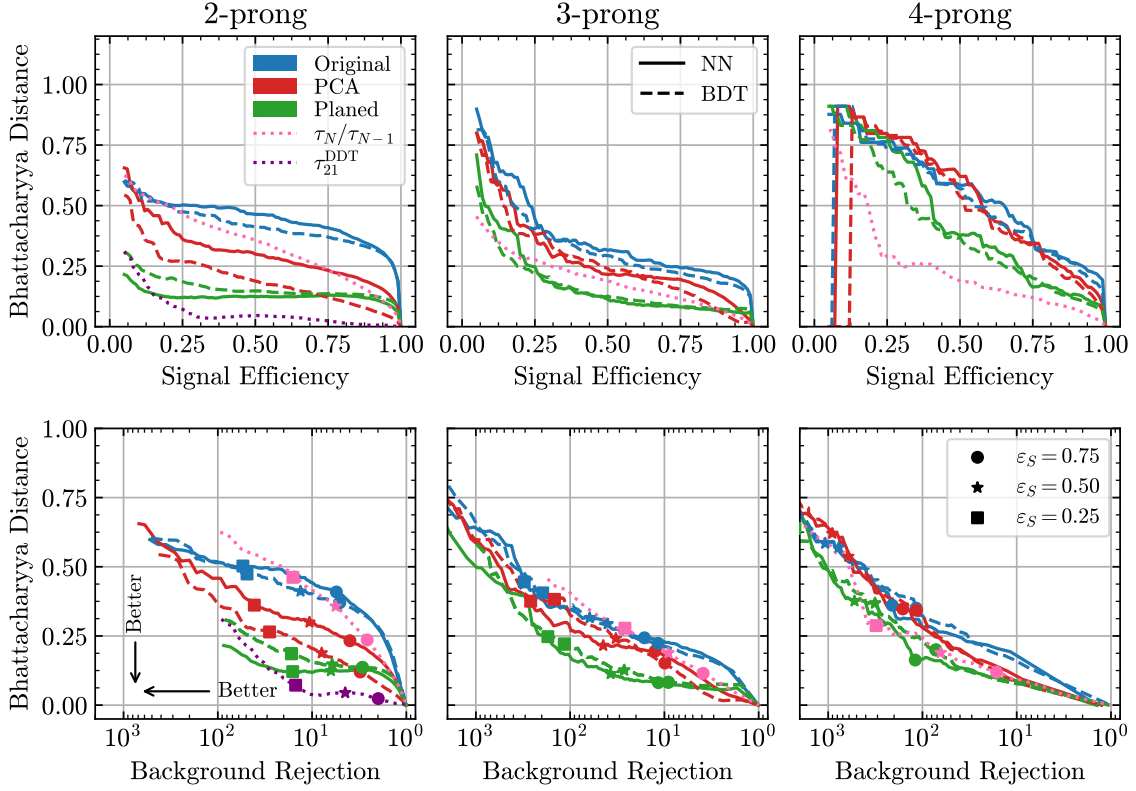


Figure 14. The Bhattacharyya distance for the QCD background distributions compared to the original distributions. The distance is defined in Eq. (3.9), and a larger distance represents more sculpting—lower on the plot is better. The neural networks tend to sculpt the distributions worse than the BDT, regardless of the data. Both the PCA rotations and Planing the jet mass result in smaller distances than the classifiers trained on the original data.

scaled data behaves similar to the BDT trained on planed data, but reaches to larger background rejections and for a fixed background rejection has better signal efficiency. The PCA scaled neural network has slightly more sculpting for fixed background rejection than the other decorrelation methods, but still has much smaller distances than the unaltered methods.

The 3-prong jet signal Bhattacharyya distance shows an interesting change when plotted against the background rejection as opposed to the signal efficiency. In the middle panel of Fig. 14,  $\tau_3/\tau_2$  produces smaller distances for fixed signal efficiency than all of the methods other than planing. However, for a fixed background rejection,

it sculpts the data more than nearly all of the MV methods. We again find that the neural network trained on planed data provides the smallest distances for a given background rejection, but the BDT is not far behind. The PCA-based methods also provide less sculpting than the original methods.

The 4-prong jet results are more clustered, but  $\tau_4/\tau_3$  (shown in pink) has smaller distances for fixed background rejection than the original methods—and surprisingly—the PCA based methods. That being said, the signal efficiencies are also much smaller. The neural network trained on data which has had the jet mass planed away produces the best curve.

The data augmentation methods explored in this section allow for using both BDTs and NNs and training takes about the same amount of time as the unaltered data. However, by augmenting the data, it is possible to make the MVs sculpt the jet mass much less than the original MVs. This does lower the overall background rejection for a given signal efficiency, but for fixed background rejection, the degree of sculpting can be much less. In this regard, these methods achieve similar results to the methods which augment the training process instead of the input data which have already been studied in the literature.

### 3.3.3 Comparison

Finally, we want to get a sense for how the augmented training methods perform, as compared to the data augmentation methods. In Fig. 15 we show the Bhattacharyya distance versus the signal efficiency (top) and background rejection (bottom) for *only* the decorrelation methods and not the original methods. We only show the neural networks for the data augmentation methods because they achieve better background rejection than BDTs, for fixed signal efficiency. For 2-prong jets,  $\tau_{21}^{\text{DDT}}$  has the least sculpting for background rejections smaller than around a factor

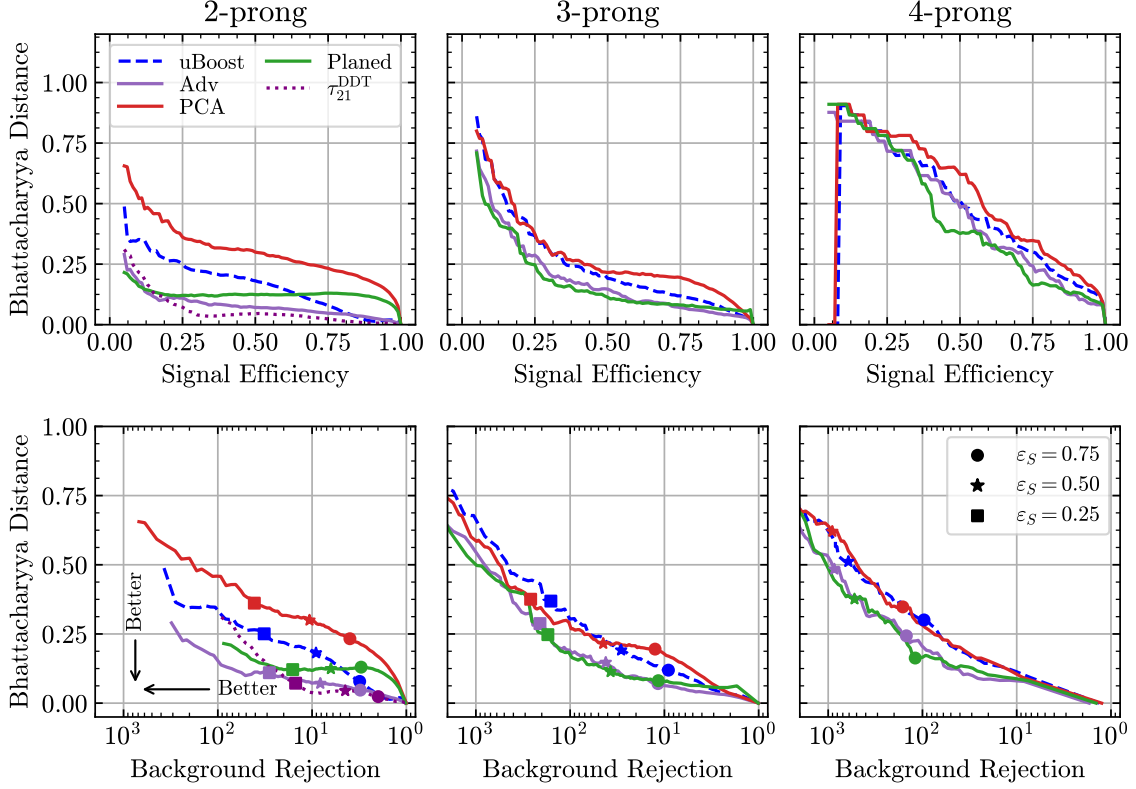


Figure 15. A comparison of all the MV based methods to decorrelate the jet mass from the classifier output. The shown PCA and Planed results are for NN architecture. The analytical  $\tau_{21}^{\text{DDT}}$  method sculpts the least for moderate background rejection, but for larger values does not do as good as the adversarially trained neural network. The network trained on data augmented by planing the jet mass do almost as good as the adversarially trained network, with uBoost and the PCA based networks showing slightly more sculping. With more prongs, planing and adversaries are nearly identical to each other while PCA and uBoost are very similar to each other.

of 10, but for larger than this, the adversarially trained network has the smallest distances. The network trained on planed data has the next smallest distances for large background rejection. While the green line is close to the purple adversary line, the marked points are further to the right, indicating that the planed network does not have as much signal efficiency for the corresponding background rejection/histogram distance. However, it is worth pointing out that planing sculpts less than uBoost, and takes about a factor of three less time to train. For the 2-prong jets, the PCA based method sculpts the most out of the decorrelation methods. PCA, however, seems to perform far better when paired with BDTs rather than NNs. Comparing Figs. 14

and 15, we see that augmenting the data using the PCA approach and then training a BDT—as opposed to a NN—sculpts just about the same as uBoost does for fixed background rejections, but takes less than 1/20 of the time to train.

The 3- and 4-prong jets show similar patterns in their results. As emphasized before, there is currently not an analytic decorrelation method similar to  $\tau_{21}^{\text{DDT}}$  for higher prong jets. The neural networks trained on the data with the jet mass planed away achieve very similar curves to the adversarial network curves—and train about a factor of 100 times faster. One may worry that this is a sign that the adversary is not actually doing well for the higher pronged jets. In App. A.3 we show the jet mass distributions and do not think this is the case.

With these higher-pronged jets, the PCA based rotation method gives similar curves to uBoost. However, the PCA method has two benefits over uBoost. First, the marked points are further to the left, indicating that for fixed signal efficiency, the PCA networks have more background rejection than uBoost. Second, the amount of time required to train the machine is around a factor of four less.



## CHAPTER IV

### CREATING SIMPLE, INTERPRETABLE ANOMALY DETECTORS FOR NEW PHYSICS IN JET SUBSTRUCTURE

In Ch. III, we reviewed and compared a number of methods that could be used to decorrelate the output of an ML classifier from the invariant mass of the jet. Not only did these methods allow for the classifier to be used across a broader range of new resonance masses, but they also allowed us to make more statistically significant statements about the new physics by preserving the background dominated sidebands used to reduce systematic sources of error. While these classifiers have a reduced dependence on the mass of the new state, they still have some dependence on the underlying UV model.

Without a clear, theoretically well-motivated model of UV physics, this problem quickly becomes intractable. Every new model of UV physics would require a unique classifier to search for it. One can instead, however, turn to a number of ML-based anomaly detection techniques. A dedicated classifier will outperform an anomaly detector. But what the anomaly detector lacks in out-and-out classification power, it makes up for in generality. Anomaly detectors only rely on a solid model of the background, and can consequently be used to search for any BSM physics.

At the LHC, anomaly detectors tend to use low-level information as their inputs, and rely on the deep ML model to learn a number of high level observables that will prove to be a useful discriminant. Since these features are learned in the hidden layers of the model, it is inaccessible to us. In this chapter, we adapt techniques from the literature to anomaly detection, and iteratively map out the physics learned by a complex, image-based anomaly detector by building a number of simpler ML models with easily interpretable inputs.

This chapter is outlined as follows. In Sec. 4.1, we describe the Monte Carlo generated dataset, as well as the relevant selection criteria and preprocessing. Sec. 4.2 starts by describing the details of the convolutional autoencoder. We then review all of the pieces needed to mimic the autoencoder—the pool of high-level observables we use to explain the autoencoder, a metric to determine how similar the decisions of two networks are, the details of our two simplified anomaly detectors, and the iterative procedure we use to construct the mimickers from the pool of high-level observables. We present our results in Sec. 4.3, detailing the construction and performance of the mimickers. Details of the simulated events and network training hyperparameters appear in the App. B.1 and App. B.2, respectively.

The computational work was performed by LB, with advisory help from Spencer Chang and Bryan Ostdiek.

## 4.1 Datasets

In this section, we briefly describe the simulated datasets we use in this study. In particular, our focus is on anomaly detection in boosted jets at the LHC. We utilize the publicly available datasets provided by Ref. [103], using QCD dijet events [179] as background and  $W$ , top, and Higgs jets [180] as the anomalous events. We consider four different  $W$  masses,  $m_W = 59, 80, 120, 174$  GeV, two different top masses,  $m_t = 80, 174$  GeV, and two different Higgs masses,  $m_h = 20, 80$  GeV. Note that when  $m_t = 80$  GeV, the mass of the decay product  $W$  is set to 20 GeV. The full simulation details are given in App. B.1. These signals give a broad range of signals with varying amounts of substructure (two to four prongs), which will prove useful when testing the ability of our anomaly detectors.

These datasets contain approximately 700,000 QCD dijet events and 100,000 events for each of the  $W$ , top, and Higgs signals. After applying a  $p_T$  cut (see

App. B.1), we are left with  $\sim 150,000$  QCD events and  $\sim 30,000$  events for each of the anomalous signals. We use 2/3 of the QCD dijet events for training the autoencoder, with the remaining 1/3 being reserved for testing and validation. We are not considering training on real data at this point, so we do not include the possibility of contamination in the background set from signal samples when training the autoencoder. However, previous work has shown that autoencoders are robust to up to  $\sim 10\%$  signal contamination [50, 69, 95, 181].

Our procedure for preprocessing the raw four vectors into images follows that outlined in Ref. [49] and is implemented with the ENERGYFLOW package [182]. For the leading jet in each event, we boost and rotate along the beam direction, such that the  $p_T$  weighted centroid lies at  $(\eta, \phi) = (0, 0)$ . The jet is then rotated about its centroid until its principal axis lies along the vertical. Finally, the jet is reflected about the horizontal and vertical axes so that the maximum intensity lies in the upper-right quadrant. Only after centering, rotating, and reflecting the jet do we pixelate the image. Our final pixelated images are  $40 \times 40$ , covering  $\Delta\eta = \Delta\phi = 2.0$ . The last step of our preprocessing procedure is to divide by the total  $p_T$  in the image. This final normalization step ensures that each image has the same scale, which helps with training. Figure 16 shows the average jet image for the background and three representative signals—the 80 GeV  $W$ , 174 GeV top, and 80 GeV Higgs.

## 4.2 Methodology

While neural networks have been used for classification and anomaly detection with great success, they are often viewed as black boxes, leading one to wonder what information they are using to match or outperform traditional techniques. With this in mind, the authors of Ref. [128] showed that modern classification networks are able to be mimicked by interpretable networks using a few high level physics variables as

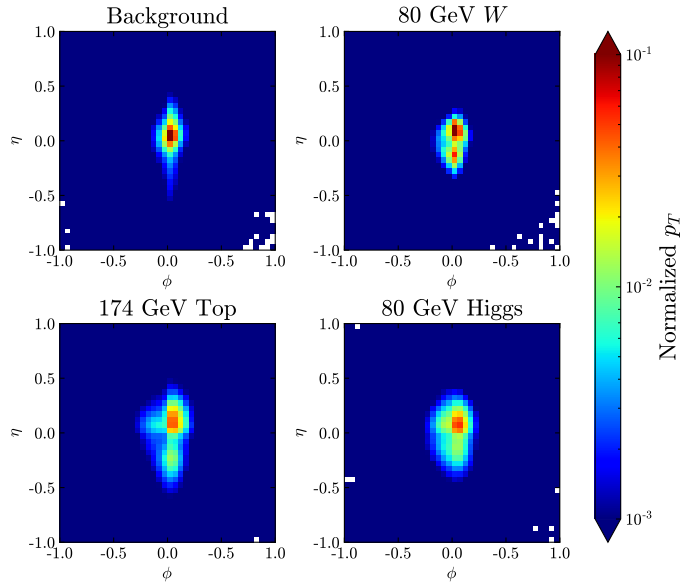


Figure 16. The average jet image for the background, 80 GeV  $W$ , 174 GeV top, and 80 GeV Higgs. Note that the Higgs bosons are pair produced from the decay of a heavier Higgs, leading to potentially 4 prongs in the large-radius jet.

inputs. In this work, we adapt this method to the task of anomaly detection. In order to do this, we first need a good anomaly detector to mimic with physics variables.

#### 4.2.1 Creating a Target Anomaly Detector with a Convolutional Autoencoder

The anomaly detector we chose is a convolutional autoencoder (hereafter referred to as the AE). Given an input image, the AE is tasked with encoding the image down into a smaller latent space, then reconstructing the original image from its latent space representation. The idea behind compressing the data to a smaller representation is that it forces the network to learn what is important about the jet image, while ignoring noisy or less crucial aspects. The hope is that when the autoencoder is applied to anomalous data, the important characteristics will be different, and thus the image will be poorly encoded, leading to a decoded image which is quite different from the initial image. Thus, we can distinguish between the background data and

the anomalous signal data by the size of the reconstruction error. AEs were first introduced to the high energy community as anomaly detectors in Refs. [94, 69, 50].<sup>1</sup>

The architecture of our AE is shown in Fig. 17 and is described below. The encoder consists of multiple layers. The first two layers are a set of five  $3 \times 3$  pixel convolutional filters. We use a stride of one and pad the output to keep the same height and width as the original image. After each convolution we apply an exponential linear unit (ELU) activation [183]. Following these convolutions, the representation is down sampled with a  $2 \times 2$  max pooling layer, leading to a height and width of 20 pixels. This reduced image is then passed through another two convolutional layers with five filters before being passed through a final convolutional layer with a single filter. This final  $20 \times 20$  image is then flattened and connected to a Dense layer with 100 nodes, which is in turn connected to our 32-dimensional latent space. We chose a 32-dimensional latent space, as that is where we found the performance of the AE as an anomaly detector began to saturate.

The decoder mirrors the encoder and consists of a Dense layer with 100 nodes, followed by another Dense layer with 400 nodes. Both of these Dense layers use the ELU activation function. The output of this layer is then reshaped into a  $20 \times 20$  image, and is then passed through two convolutional layers with five filters each. All of the convolutional layers in the decoder use a  $3 \times 3$  convolutional kernel and the ELU activation function, with the exception of the last convolutional layer in the decoder, which uses the SOFTMAX activation function along the pixel dimension so that the sum of the pixel intensities is unity. These are then upsampled with a transposed convolutional layer to  $40 \times 40$ , passed through a convolutional layer with

---

<sup>1</sup>Often, AEs can be improved with Variational Autoencoders (VAEs), in which the latent space representation becomes a distribution, rather than a single point. As a proof of principle, we use the simpler AE, and leave the extension to VAEs for further study.

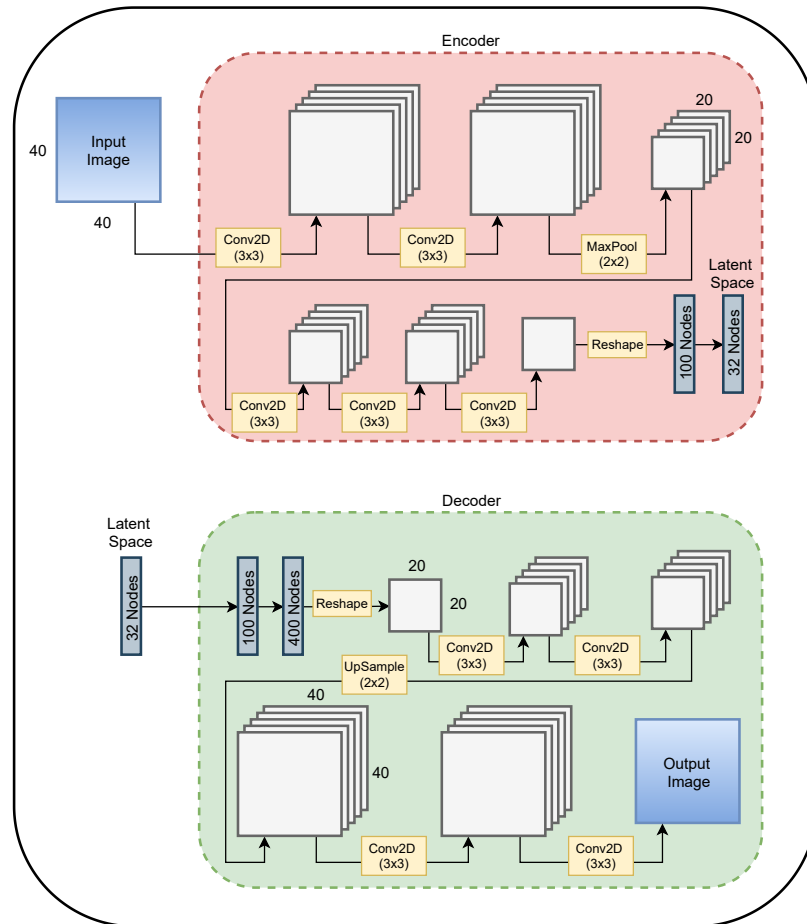


Figure 17. The architecture of the convolutional autoencoder (AE). The AE consists of two separate networks, an encoder that compresses the original image down to a smaller latent space, and a decoder tasked with recreating the original image from the latent space representation.

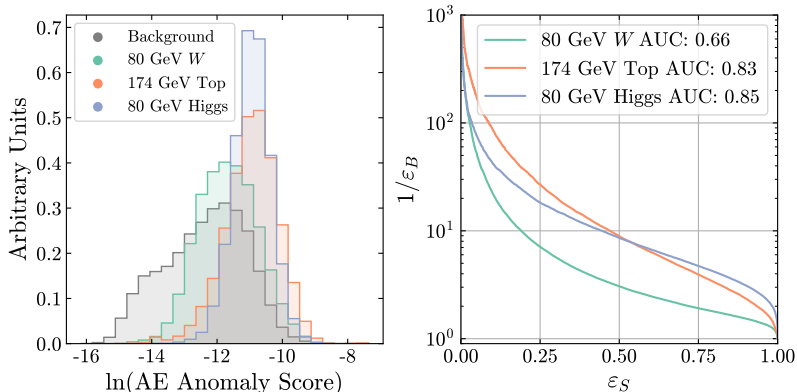


Figure 18. The AE’s performance as an anomaly detector on 3 of the anomalous signals, the 80 GeV  $W$ , the 174 GeV top, and the 80 GeV Higgs. Note that the Higgs bosons are pair produced from the decay of a heavier Higgs, leading to potentially 4 prongs in the large-radius jet. The left panel shows the normalized distribution of the log of the AE’s anomaly score for the background and each of the signals. The right panel shows the ROC curves for each signal.

5 filters, and finally passed through one last convolutional layer to create the output image. We train the AE to reproduce QCD jet images, by minimizing the mean squared error of their reconstruction. Explicitly, this is given as

$$L_{\text{AE}} = \frac{1}{N_i N_p} \sum_k^{N_i} \sum_j^{N_p} \left( f_A(I_k^j) - I_k^j \right)^2 \quad (4.1)$$

where  $N_i$  is the total number of images,  $N_p$  is the number of pixels in each image,  $I_k^j$  is the  $j$ th pixel of the  $k$ th input image, and  $f_A(I_k^j)$  is the AE’s reconstruction of that pixel for that input image. The training details for the AE are provided in App. B.2. Our AE, along with all of the other neural network architectures discussed in Sec. 4.2 are implemented with KERAS [174] using the TENSORFLOW [175] backend.

Figure 18 shows some examples of how the trained AE can act as an anomaly detector. The left panels display the distribution of the reconstruction errors as the anomaly score for the background training set as well as three different anomalous signals. At first glance, the reconstruction errors are very small, but this is explained by the normalization and the sparsity of our jet images. Because each image is

normalized to sum to one, all pixels have a value of less than one. The images are also very sparse, so most pixels are identically 0, and the network is very good at predicting that. When we take the mean squared error over the pixels, we actually average over the number of pixels, so the number of pixels with no intensity leads to a very good average reconstruction. Importantly, we see that the background distribution is at lower scores than the signal distributions. The encoder has never seen jets with inherent substructure from the decay of a heavy resonance, so it doesn't recognize the important information to encode into the latent space, and the decoder therefore performs worse when reconstructing the images. The right panel displays the Receiver Operating Characteristic (ROC) curves for these three signals. While the  $W$  is harder for the AE to distinguish from the background, the top and Higgs jets have decent Area Under the ROC Curve (AUC) scores.

As we've seen, our constructed AE is capable of detecting jets which are different from the QCD background it was trained on. In the next section we build up a method to mimic the ordering decisions the AE makes using physics observables.

#### 4.2.2 Mimicking the Target Anomaly Detector

As shown in the previous section, the AE is able to tag various signals as being different from QCD. However, it is unclear what information in the event image is being used to do this. In order to mimic the behavior of the AE, we need a few ingredients. The first is a wide set of physics observables which could possibly explain the anomaly detector. For these, we use the Energy Flow Polynomials, described in detail in Sec. 4.2.2.1. Next, we use the idea of *decision ordering* to select which observables are important as described in Sec. 4.2.2.2. Finally, we need a flexible function which can use the physics observables to produce an anomaly score which mimics that of the AE. We describe two complementary methods which achieve this



goal. The first method, a Paired Neural Network, is a neural network which takes in the physics observables from two events at the same time and is trained to determine which event had the worse reconstruction error from the AE. We construct this in such a way that at inference, we can feed in a single event and get an anomaly score. This technique is described in Sec. 4.2.2.3. The second method, a High-Level Neural Network, instead takes in only a single event at a time and is trained to regress the reconstruction error of the AE for that event. This second method is described in Sec. 4.2.2.4.

#### 4.2.2.1 *High Level Observables*

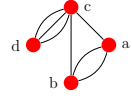
Since there is no way to know which human-constructed, high-level observables will be relevant *a priori*, we need to rely on using a basis of observables. To that end, we make use of the Energy Flow Polynomials (EFPs) [131], a formally infinite set of jet substructure observables inspired by previous work on energy correlation functions [184, 185, 186, 187, 188, 189]. The EFPs form a discrete linear basis for all infrared- and collinear-safe (IRC-safe) observables and are defined in terms of the momentum fraction,  $z_a$ , and pairwise angular distances,  $\theta_{ab}$ . The EFPs are computed using the four-momentum of each particle in the jet, where  $z_a$  is the momentum fraction carried by particle  $a$ , and  $\theta_{ab}$  is the pairwise angular distance between particles  $a$  and  $b$ . Each EFP is conveniently represented by a multigraph, using the following correspondences:

$$\text{each node } a \leftrightarrow \sum_{a=1}^N z_a \tag{4.2}$$

and

$$\text{each } k\text{-fold edge between nodes } a \text{ and } b \leftrightarrow (\theta_{ab})^k . \tag{4.3}$$

As an example, we have



$$= \sum_{a=1}^N \sum_{b=1}^N \sum_{c=1}^N \sum_{d=1}^N z_a z_b z_c z_d \theta_{ab}^2 \theta_{ac} \theta_{bc} \theta_{cd}^3. \quad (4.4)$$

In this example, we've labeled the nodes for clarity, but will not do so for future graphs. To build some intuition for this framework, we note that the fully connected graphs with  $N$  vertices correspond to the  $N$ -point energy correlation functions.

The EFPs corresponding to each multigraph can be modified with a pair of parameters,  $(\kappa, \beta)$ , which determine the precise meaning of  $z_a$  and  $\theta_{ab}$ . More specifically,

$$z_a^{(\kappa)} = \left( \frac{p_{T_a}}{\sum_b p_{T_b}} \right)^\kappa, \quad (4.5)$$

$$\theta_{ab}^{(\beta)} = (\Delta\eta_{ab}^2 + \Delta\phi_{ab}^2)^{\beta/2} \quad (4.6)$$

where  $p_{T_a}$  is the transverse momentum of particle  $a$ ,  $\Delta\eta_{ab}$  is the difference in pseudorapidity between particles  $a$  and  $b$ , and  $\Delta\phi_{ab}$  is the difference in azimuthal angle between particles  $a$  and  $b$ . The original IRC-safe EFPs require  $\kappa = 1$ . While there are well-motivated reasons to explore a broader space of observables at the cost of IR and/or C safety [190, 191, 192], we restrict ourselves to only IRC-safe observables in this work. For our iterative procedure to mimic the AE, we choose  $\kappa = 1$ ,  $\beta = 1$ , and consider all EFPs with degree (i.e. the number of edges)  $d \leq 5$ . With these parameters, we have a total of 102 EFPs to explore.

#### 4.2.2.2 Decision Ordering

To create an interpretable alternative to the AE, we will iteratively add EFP observables as inputs to the mimicking networks. To compare how well a network (or

EFP input) orders events relative to the AE, we use a series of metrics implemented in Ref. [128]. Here we briefly summarize these metrics. Given two decision functions,  $f(x)$  and  $g(x)$ , the *decision ordering* (DO) for a pair of events  $x_1$  and  $x_2$  is defined as

$$\text{DO}[f, g](x_1, x_2) = \Theta\left([f(x_1) - f(x_2)][g(x_1) - g(x_2)]\right) \quad (4.7)$$

where  $\Theta(x)$  is the Heaviside theta function, and we choose  $\Theta(0) = 1$ . Here, we can think of  $f(x)$  as being the anomaly score/reconstruction error for the AE and  $g(x)$  being the output of one of our methods. Later, we will also use  $f(x) = \text{AE}(x)$  and  $g(x) = \text{EFP}(x)$  to determine which EFP observables to include for our mimickers. A DO of 1 means that  $f$  and  $g$  agree that one event is more anomalous than another; a DO of 0 indicates the two methods disagree on which event is more anomalous. If two decision functions have  $\text{DO} = 1$  for all possible pairs  $x_1$  and  $x_2$ , then the two are effectively identical decision functions on the domain tested.

To create a summary statistic, we then average the DO over all possible pairs, weighted by the underlying distributions that  $x_1$  and  $x_2$  are drawn from. The resulting statistic, the *average decision ordering* (ADO) is given by

$$\text{ADO}[f, g] = \int dx_1 dx_2 p_1(x_1) p_2(x_2) \text{DO}[f, g](x_1, x_2) \quad (4.8)$$

This evaluates to 1 if both decision functions order every possible pair of events in the same manner (making them equivalent decision functions), 0 if they order the pairs in the opposite manner, and  $\frac{1}{2}$  if there is no consistency to the way the decision functions order the events. Due to computing constraints, we could not compute the ADO on the entirety of the background training set. Instead, when computing the

ADO, we choose 10,000 events at random, and then evaluate on the  $\binom{10000}{2} \sim 5 \times 10^7$  pairs of events.

We now follow the *Black-Box Guided Search Strategy* from Ref. [128] to iteratively construct neural networks whose decision functions should become better and better approximations of the AE's. We start by training a neural network,  $\text{NN}_0$  on some initial set of observables,  $X_0 = (m_J, p_T)$ . We will later describe the two possible architectures for  $\text{NN}_0$ , but for now it is enough to say it aims to produce decision functions that mimic the AE on background events. We then compute the ADO between  $\text{NN}_0$  and the AE, and isolate all of the pairs of events misordered by  $\text{NN}_0$ . From our set of high-level observables,  $O$ , we then want to find the observable  $O_1 \in O$  with the highest ADO on the pairs misordered by  $\text{NN}_0$ .<sup>2</sup> We then train a new neural network,  $\text{NN}_1$ , whose input observables are  $X_1 = X_0 \cup O_1$ . Given its inputs, we would expect  $\text{NN}_1$  to have a decision function that more closely resembles that of the AE—and consequently, a higher ADO compared to  $\text{NN}_0$ —since it has access to the same information  $\text{NN}_0$  had, as well as information that can help order the pairs misordered by  $\text{NN}_0$ .

From here, we continue to iterate using the remaining observables in  $O$ . On the  $n$ th iteration, we start by finding the observable  $O_n \in O$  with the highest ADO on the pairs misordered by  $\text{NN}_{n-1}(X_{n-1})$  that is not already part of  $X_{n-1}$ . We then build a new set of inputs,  $X_n = X_{n-1} \cup O_n$ , and train a new neural network,  $\text{NN}_n$  on  $X_n$ . At each iteration, we expect the ADO between the neural network and AE to increase, since the neural network we construct on the  $n$ th iteration has access to all of the same information available to the previous network, as well as a new observable  $O_n$  that helps order the events misordered by the  $(n - 1)$ th neural network.

---

<sup>2</sup>If the ADO of an observable is less than 0.5, we take 1-ADO, since a highly anticorrelated variable is also useful.

Now that we have described both the physics observables and the general method for choosing which observables to give the networks, we describe the two network architectures in more detail.

#### **4.2.2.3 Paired Neural Network**

Our first attempt to mimic the AE is an approach we call the Paired Neural Network (PNN). The aim of the Paired Neural Network is to mimic the AE by learning to predict the relative anomaly score between two events. To do this, the PNN takes pairs of events as its input and classifies which has a larger anomaly score. This is in contrast to other methods such as trying to match the AE’s output or anomaly score on an event-by-event basis. In general, classifiers are easier to train, so this seems like a promising method.

Figure 19 shows the PNN architecture. Both events are fed through the same interior model in parallel. This is shown in the image as the “Common Interior Model.” The interior model consists of four hidden layers with 50 nodes each, and the ELU activation function is used for all layers. The interior model produces a single output for each input event, and this single output node uses the ReLU activation. The motivation for this is to think of the output for each event as its own anomaly score. Within the larger PNN, we then subtract these two output anomaly scores from each other. If the first event is more anomalous, the result should be negative and if the second is more anomalous, the result will be positive. The larger the difference in scores should tell us about the networks confidence in the relative ordering. Finally, to turn this into a classification problem, we apply the sigmoid function to the interior model difference, mapping large negative numbers to 0 and large positive values to 1. If the anomaly scores are the same (the difference is 0) the sigmoid gives a value of 0.5.

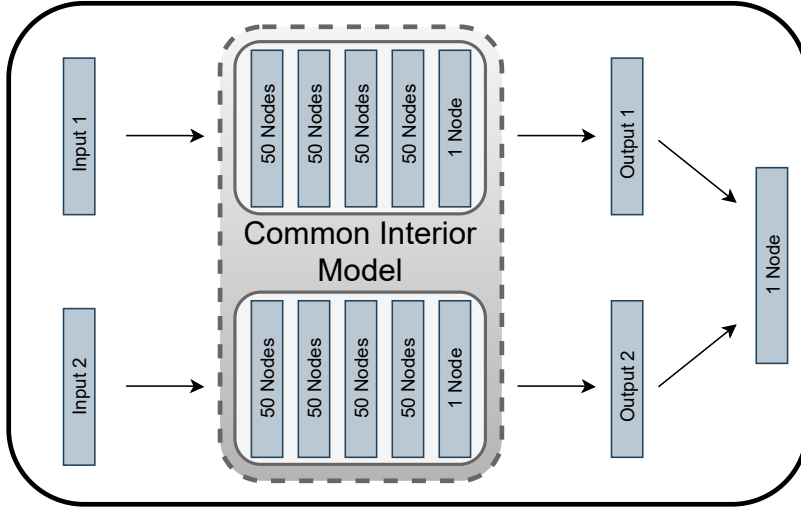


Figure 19. The architecture of the Paired Neural Network. The interior model consists of 4 hidden layers each with 50 nodes and using the ELU activation function. The interior model outputs a single node for each input and uses the ReLU activation function. The final output of the model is a single node which is the difference between the two interior model outputs and uses a sigmoid activation function. Our input data are the jet’s mass,  $p_T$ , and up to 14 EFPs.

To train the network, we continue the idea of classification and minimize the binary cross-entropy given by

$$L_{\text{PNN}} = -\frac{1}{N} \sum_k^N \left[ y_k \ln \left( f_P(X_k) \right) + (1 - y_k) \ln \left( 1 - f_P(X_k) \right) \right] \quad (4.9)$$

where  $k$  represents a specific pair of events, where the order matters. The value of  $y_k$  is the truth “label” for the pair of events as determined by the AE, i.e.  $y_k = 0(1)$  if the AE determines the event in Input 1 to be more (less) anomalous than the event in Input 2, and  $f_P(X_k)$  is the PNN’s output for the pair of events. Appendix B.2 provides the training details for the PNN.

After training the PNN on  $\sim 250,000$  pairs of events, we extract the interior model for use on single events. Thus, even though the training procedure requires pairs of events and was trained as a classifier, the interior model provides a function which takes in observables from a single event and outputs an anomaly score.

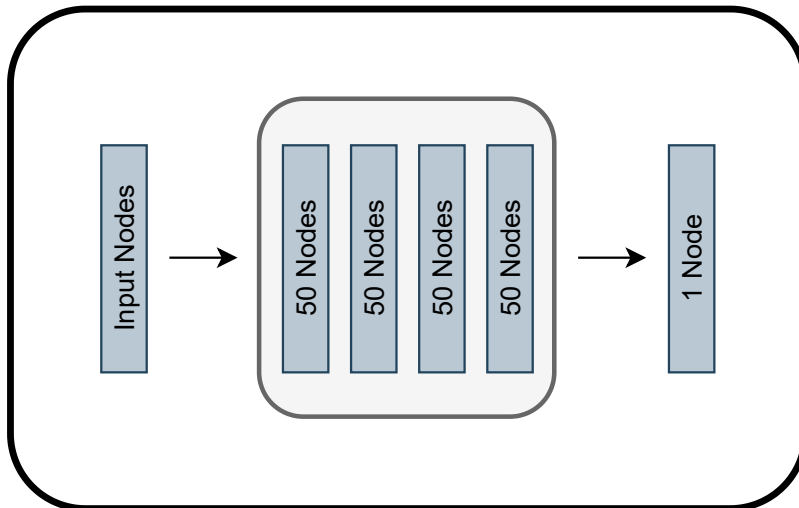


Figure 20. The architecture of the High- Level Neural Network. This network consists of four hidden layers, with each having 50 nodes and using the ELU activation function. The network output is a single node. Like the PNN, our input data are the jet’s mass,  $p_T$ , and up to 14 EFPs.

#### 4.2.2.4 High-Level Neural Network

The PNN described in the last section does not attempt to learn the actual anomaly score of the AE, but only the relative difference in the anomaly score between pairs of events. We also introduce a method which specifically aims to mimic the actual anomaly score of the AE. We call this network the High- Level Neural Network (HLN). In practice, the anomaly score (reconstruction error) from the AE spans many orders of magnitude, so we found better results when the HLN is trained to predict the log of the anomaly score rather than the score itself.

We find that a relatively simple neural network is able to achieve the task of reproducing the loss of the AE. Figure 20 shows the architecture we use for the HLN. The HLN consists of 4 hidden layers, with each hidden layer having 50 nodes. The final output of the network is a single node. All of the nodes in the hidden layers use the ELU activation function.

To train the HLN, we minimize the mean squared error between the (log of the) anomaly score of the AE and the output of the HLN. Specifically, we use a loss

function of,

$$L_{\text{HLN}} = \frac{1}{N} \sum_k^N \left[ f_H(X_k) - \ln \left( \frac{1}{N_p} \sum_j^{N_p} (f_A(I_k^j) - I_k^j)^2 \right) \right]^2 \quad (4.10)$$

where  $f_H(X_k)$  is the HLN's output given some input data  $X_k$  and  $f_A(I_k^j)$  is the AE's output given a pixel  $j$  in an image  $I_k^j$  for the  $k$ th event. When using the HLN as an anomaly detector, we use the model's output as the anomaly score. See App. B.2 for the HLN training details.

### 4.3 Results

In the previous section, we outlined two different architectures we could use to iteratively build neural networks whose decision functions would more closely resemble the AE's decision function. Here, we provide the results of the iterative procedure and analyze the specific EFPs that are selected to mimic the anomaly detector. We will find that the EFPs selected are composite observables built out of only six prime EFP factors. We show that using only the prime components gives very similar results. Finally, we demonstrate that using the EFPs with a traditional anomaly detection technique, the isolation forest, gives very poor results. The failure of the isolation forest when provided with the same basic physics observables highlights the benefits of using our mimicker networks.

#### 4.3.1 Background Decision Ordering

We start our iterative process by training both a PNN and HLN on jet mass and  $p_T$  for QCD events in the training set and then compute the ADO for each model. Of the  $\sim 5 \times 10^7$  pairs of events we use to compute the ADO, both the initial PNN and HLN correctly order  $\sim 72\%$  of the events relative to the reconstruction error of the AE. Next, we take all of the pairs which are misordered and compute the ADO



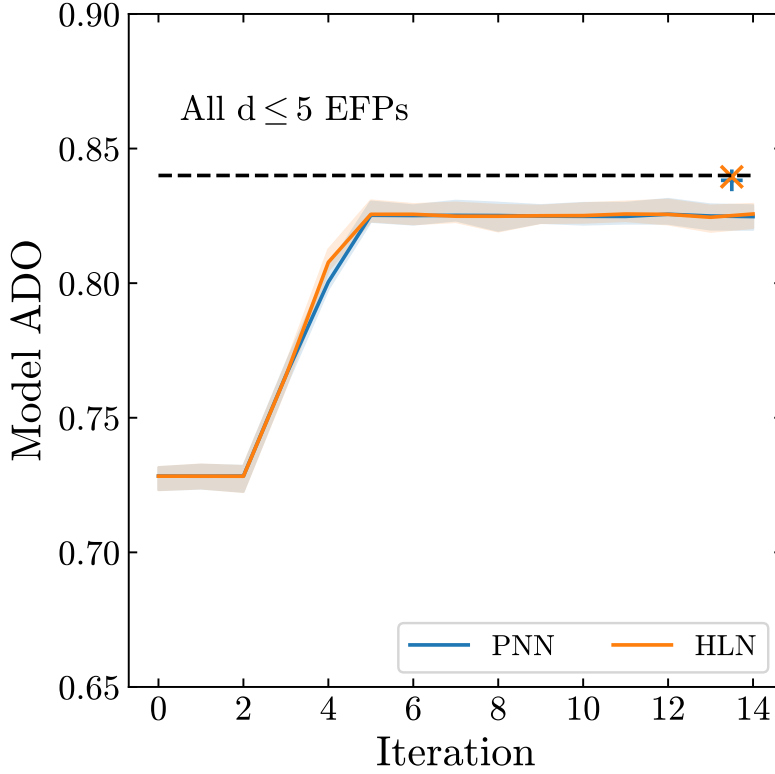


Figure 21. The ADOs for each PNN and HLN. The center line shows the ADO of the model that was used to select the EFPs. The shaded bands show the maximum and minimum ADO values obtained when recalculating the ADO an additional 50 times, using a different set of pairs of events each time. The  $x$ -axis denotes the iteration step of the iterative process. See Table 17 for the multigraph and mathematical representations of the selected EFPs and the iteration step at which they were added. The blue ‘+’ (orange ‘x’) shows the ADO of a PNN (HLN) trained on only the 5 prime EFPs picked out by each method (see Eq. 4.12). The ADO of each model trained on  $m, p_T$ , and all of the  $d \leq 5$  EFPs is the same to 3 significant digits, and is plotted as a single dashed line.

between all 102 EFPs and the AE. On this first iteration, we find that the observable with the highest ADO for both networks is EFP 2, given by

$$\text{EFP 2} = \sum_{a,b=1}^N z_a z_b \theta_{ab}^2. \quad (4.11)$$

This observable is then added to the list of inputs. So in the next iteration the input for each event is given by  $(m_J, p_T, \text{EFP 2})$ . We then repeat this process 14 more times, recording both the ADO of each network, as well as which EFP has the largest ADO for the pairs of events which are misordered by the respective networks.

Figure 21 shows the result of this iterative process. The solid lines show the ADO of the models we used to determine the next best observable to add; the shaded band shows the maximum and minimum value of the ADO for each model after recalculating the ADO an additional 50 times at each iteration using a different set of  $\sim 5 \times 10^7$  pairs of events. We also created PNN and HLN models trained on  $m, p_T$  and all  $d \leq 5$  EFPs. The ADOs of these two models agree to 3 significant digits and thus is plotted as the single dashed line in the panel. Since they use all of the EFPs, this line gives a sense of the highest ADO each model is capable of achieving, given our set of observables. The blue ‘+’ and orange ‘×’ will be discussed in Sec. 4.3.3. There are a few key takeaways from these plots. By the time the ADOs start to plateau, both the HLN and PNN are correctly ordering 83% of the pairs of events in the QCD sample relative to the AE. For the first two iterations, the model ADOs do not change. Looking at Table 17, we see that the first two EFPs are EFP 2 and [EFP 2]<sup>2</sup>, which are proportional to  $m^2/p_T^2$  and  $m^4/p_T^4$ . Since the initial inputs to both the PNN and HLN are mass and  $p_T$ , these observables contain no new information, and thus it makes sense that the model ADO does not improve. This redundancy of information follows since the EFPs are a linear basis of substructure observables, whereas our neural networks can utilize nonlinear combinations of its inputs. Despite their underlying philosophical differences—the HLN’s are trying to match the AE’s anomaly score, while the PNN is trying to match the DO of the AE—both methods select the same set of 14 EFPs in the same order. In Table 17, we list the multigraph and mathematical expression corresponding to each of these EFPs as well as the iteration step in which they were added. The agreement of the PNN and HLN approaches gives us confidence that these observables are important to detect jets which do not look like typical QCD jets. Also, since by the last iteration,

EFP No.	EFP Multigraph	EFP Expression	PNN Iteration	HLN Iteration
1		$\sum_{a,b=1}^N z_a z_b \theta_{ab}$	5	5
2		$\sum_{a,b=1}^N z_a z_b \theta_{ab}^2$	1	1
54		$\sum_{a,b,c,d=1}^N z_a z_b z_c z_d \theta_{ab} \theta_{cd}$	6	6
57		$\sum_{a,b,c,d=1}^N z_a z_b z_c z_d \theta_{ab}^2 \theta_{cd}^2$	2	2
65		$\sum_{a,b,c,d,e=1}^N z_a z_b z_c z_d z_e \theta_{ab}^2 \theta_{cd}^2 \theta_{de}^2$	3	3
70		$\sum_{a,b,c,d,e,f=1}^N z_a z_b z_c z_d z_e z_f \theta_{ab} \theta_{cd} \theta_{ef}$	7	7
85		$\sum_{a,b,c,d,e,f=1}^N z_a z_b z_c z_d z_e z_f \theta_{ab} \theta_{cd}^2 \theta_{ef}^2$	4	4
86		$\sum_{a,b,c,e,d,f,g=1}^N z_a z_b z_c z_d z_e z_f z_g \theta_{ab} \theta_{ac} \theta_{de} \theta_{fg}$	13	13
94		$\sum_{a,b,c,e,d,f,g=1}^N z_a z_b z_c z_d z_e z_f z_g \theta_{ab} \theta_{ac} \theta_{bc} \theta_{de} \theta_{fg}$	11	11
95		$\sum_{a,b,c,d,e,f,g,h=1}^N z_a z_b z_c z_d z_e z_f z_g z_h \theta_{ab} \theta_{cd} \theta_{ef} \theta_{gh}$	8	8
97		$\sum_{a,b,c,d,e,f,g,h=1}^N z_a z_b z_c z_d z_e z_f z_g z_h \theta_{ab} \theta_{bc} \theta_{cd} \theta_{ef} \theta_{gh}$	12	12
99		$\sum_{a,b,c,d,e,f,g,h=1}^N z_a z_b z_c z_d z_e z_f z_g z_h \theta_{ab}^2 \theta_{cd} \theta_{ef} \theta_{gh}$	14	14
100		$\sum_{a,b,c,d,e,f,g,h,i=1}^N z_a z_b z_c z_d z_e z_f z_g z_h z_i \theta_{ab} \theta_{ac} \theta_{de} \theta_{fg} \theta_{hi}$	10	10
101		$\sum_{a,b,c,d,e,f,g,h,i,j=1}^N z_a z_b z_c z_d z_e z_f z_g z_h z_i z_j \theta_{ab} \theta_{cd} \theta_{ef} \theta_{gh} \theta_{ij}$	9	9

Table 17. The EFP multigraphs and corresponding expressions for each of the EFPs selected by both the HLN and PNN. In the last two columns, we list the iteration step where the PNN or HLN selects the corresponding EFP.

the PNN and HLN have nearly reached the ADO of the dashed line, it suggests that the decision ordering of our mimickers has almost converged to what is possible with our set of EFPs.

### 4.3.2 Anomaly Detection

While both the HLN and PNN have demonstrated the ability to mimic the AE's anomaly score on QCD events, it's unclear if matching the decision ordering on in-distribution events will generalize to out-of-distribution events. In other words, having mimicked the AE on QCD background events with HLN and PNNs, we must

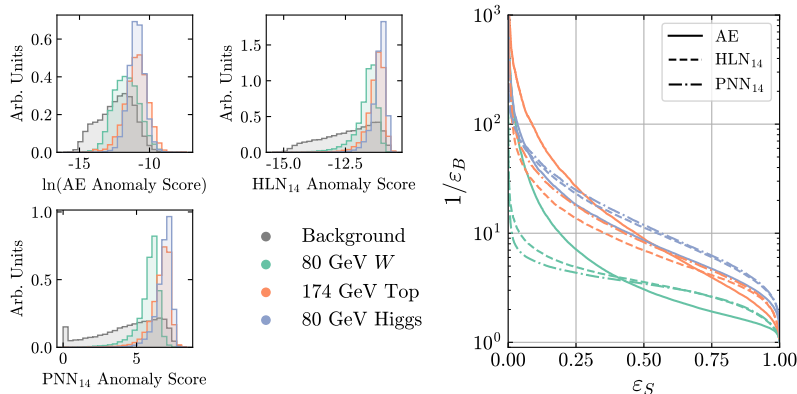
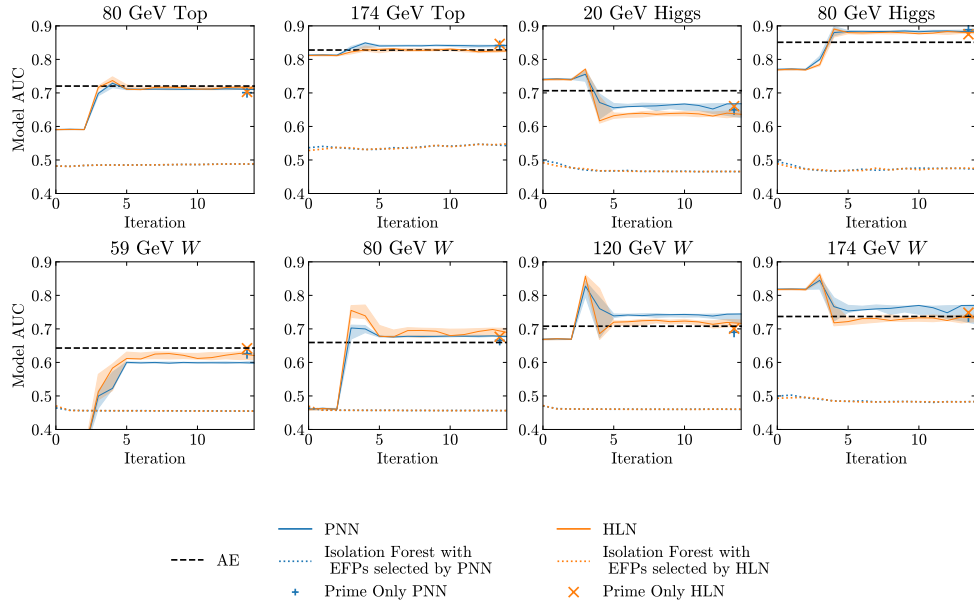


Figure 22. The performance of the AE, PNN<sub>14</sub>, and HLN<sub>14</sub> as anomaly detectors on the 80 GeV  $W$ , 174 GeV top, and 80 GeV Higgs. Note that the Higgs bosons are pair produced from the decay of a heavier Higgs, leading to potentially 4 prongs in the large-radius jet. The left panels show the normalized distribution of each method’s respective anomaly score for the background and each signal. The right panel shows the ROC curves for each signal, with the solid lines being the ROC curves for the AE, the dashed lines for HLN<sub>14</sub>, and the dashed-dot lines for PNN<sub>14</sub>.

test if this decision ordering transfers to boosted jet signals by comparing the AE, PNN, and HLN as anomaly detectors. To determine how well each network performs as an anomaly detector we use a popular metric, the AUC.

Figure 22 shows how the HLN and PNN on their final iteration compare to the autoencoder on the same three signals as Fig. 18. The left panels show the normalized distributions of each network’s anomaly scores for the background and three of the signals. The right panel then shows all of the ROC curves for each model on each signal. We can see that both the HLN and PNN do a good job of mimicking the anomaly detector on events with higher anomaly scores. But the long tails in each of the background distributions indicates that HLN and PNN struggle to match the AE on less anomalous events, explaining their poorer background rejection at low signal efficiency.

Figure 23 shows how the mimickers perform on all eight signals described in Sec. 4.1 at each step of the iterative progress. The dashed black line in each panel shows the AUC when using the reconstruction error of the AE as the anomaly score. The blue and orange curves show the results of the PNN and HLN, respectively, as a



**Figure 23.** AUCs for the PNN and HLN at each iteration for each of the eight signals reserved for testing. Note that the Higgs bosons are pair produced from the decay of a heavier Higgs, leading to potentially 4 prongs in the large-radius jet. The solid center lines are the AUC of the model used in the iterative process, the shaded bands show the maximum and minimum AUCs from retraining each network an additional 10 times. The dashed black line corresponds to the AE’s AUC. The dotted lines correspond to the isolation forest anomaly detectors and the blue ‘+’ (orange ‘x’) is the PNN(HLN) trained using mass,  $p_T$ , and the five prime factors in Eqn. 4.12.

function of the number of iterations for selecting extra observables. The solid center lines denote the AUC of the model used to select observables in the iterative process. The shaded bands show the maximum and minimum AUCs when retraining each network ten additional times, to give us a sense of how stable the training is. The bands are quite narrow, indicating that the results are robust to training uncertainties.

Like we saw with the ADOs in Fig. 21, the HLN and PNN perform similarly, despite their different approaches. For both the decision ordering and the AUCs, the results start to plateau around the fifth iteration. When the HLN and PNN AUC scores begin to plateau, we see that the value is similar to the AUC of the AE. This indicates that the HLN and PNN are performing comparably to the AE when all three are acting as anomaly detectors. It is surprising that mimicking the decision ordering on the in-distribution (QCD) events seems to also generalize to the relative

differences between the signals and the background. Some of the mimicking networks even exceed the anomaly detection capability of the AE they are trying to mimic for certain signals.

For some signals—specifically the 20 GeV Higgs, 80 GeV  $W$ , 120 GeV  $W$ , and 174 GeV  $W$ —we see a drop in AUC around the 3rd iteration for both the PNN and HLN. While such dips are not ideal, they are not completely unexpected. Our iterative process is trying to pick out the observables that help to best order the background events, with no attention paid to how effective they may or may not be to picking out signal events. So, for those three signals, it appears that the EFP added at the iteration where the AUC dips improves the ADO relative to the AE, but at the same time makes it more difficult for the HLNs and PNNs to distinguish those signal events from the background.

However, AUC is an inclusive figure of merit and, consequently, does not tell the whole story. As Fig. 22 highlights, networks with similar AUCs are not necessarily making the exact same decisions when used as anomaly detectors. Some more physically interpretable metrics are the background rejection ( $1/\varepsilon_B$ ) at fixed signal efficiency ( $\varepsilon_S$ ) and the signal efficiency at fixed background rejection. Table 18 shows the background rejection at two different fixed signal efficiencies—0.5 and 0.1—and the signal efficiency at two different fixed values of the background rejection—10 and 100—for all 8 signals and 5 different networks—the AE, HLN<sub>0</sub>, PNN<sub>0</sub>, HLN<sub>14</sub>, and PNN<sub>14</sub>.

There are a few key takeaways from this table. Looking at the signal efficiency at a fixed value of the background rejection, we can see that, in general, our mimicker networks need to operate at lower signal efficiencies to achieve the same background rejection as the AE. The exceptions here are the final iteration of the mimicker

80 GeV Top						174 GeV Top					
	AE	HLN <sub>14</sub>	PNN <sub>14</sub>	HLN <sub>0</sub>	PNN <sub>0</sub>		AE	HLN <sub>14</sub>	PNN <sub>14</sub>	HLN <sub>0</sub>	PNN <sub>0</sub>
$\epsilon_S(1/\epsilon_B = 10)$	0.252	<b>0.012</b>	0.114	<b>0.071</b>	<b>0.071</b>	$\epsilon_S(1/\epsilon_B = 10)$	0.470	0.357	0.428	0.146	0.148
$\epsilon_S(1/\epsilon_B = 100)$	0.022	<b>0.007</b>	<b>0.008</b>	<b>0.007</b>	<b>0.008</b>	$\epsilon_S(1/\epsilon_B = 100)$	0.088	0.016	0.022	0.013	0.013
$1/\epsilon_B(\epsilon_S = 0.5)$	4.24	4.03	3.95	2.29	2.29	$1/\epsilon_B(\epsilon_S = 0.5)$	8.93	6.94	8.26	5.96	6.00
$1/\epsilon_B(\epsilon_S = 0.1)$	26.5	12.0	11.3	<b>7.33</b>	<b>7.39</b>	$1/\epsilon_B(\epsilon_S = 0.1)$	87.6	28.6	38.0	12.8	12.9

20 GeV Higgs						80 GeV Higgs					
	AE	HLN <sub>14</sub>	PNN <sub>14</sub>	HLN <sub>0</sub>	PNN <sub>0</sub>		AE	HLN <sub>14</sub>	PNN <sub>14</sub>	HLN <sub>0</sub>	PNN <sub>0</sub>
$\epsilon_S(1/\epsilon_B = 10)$	0.240	<b>0.027</b>	<b>0.086</b>	<b>0.032</b>	<b>0.033</b>	$\epsilon_S(1/\epsilon_B = 10)$	0.446	0.549	0.565	<b>0.030</b>	<b>0.031</b>
$\epsilon_S(1/\epsilon_B = 100)$	0.025	<b>0.001</b>	<b>0.001</b>	<b>0.001</b>	<b>0.001</b>	$\epsilon_S(1/\epsilon_B = 100)$	0.036	0.022	0.020	<b>0.002</b>	<b>0.002</b>
$1/\epsilon_B(\epsilon_S = 0.5)$	4.06	3.39	4.14	4.87	4.91	$1/\epsilon_B(\epsilon_S = 0.5)$	8.58	11.3	11.9	4.67	4.70
$1/\epsilon_B(\epsilon_S = 0.1)$	25.7	<b>6.82</b>	<b>9.67</b>	<b>6.68</b>	<b>6.72</b>	$1/\epsilon_B(\epsilon_S = 0.1)$	42.4	46.1	50.1	<b>6.41</b>	<b>6.44</b>

59 GeV W						80 GeV W					
	AE	HLN <sub>14</sub>	PNN <sub>14</sub>	HLN <sub>0</sub>	PNN <sub>0</sub>		AE	HLN <sub>14</sub>	PNN <sub>14</sub>	HLN <sub>0</sub>	PNN <sub>0</sub>
$\epsilon_S(1/\epsilon_B = 10)$	0.155	<b>0.017</b>	<b>0.007</b>	<b>0.011</b>	<b>0.012</b>	$\epsilon_S(1/\epsilon_B = 10)$	0.190	<b>0.043</b>	<b>0.013</b>	<b>0.014</b>	<b>0.014</b>
$\epsilon_S(1/\epsilon_B = 100)$	0.015	<b>3E-4</b>	<b>3E-4</b>	<b>7E-4</b>	<b>7E-4</b>	$\epsilon_S(1/\epsilon_B = 100)$	0.028	<b>5E-4</b>	<b>4E-4</b>	<b>9E-4</b>	<b>9E-4</b>
$1/\epsilon_B(\epsilon_S = 0.5)$	2.86	2.76	2.62	1.40	1.40	$1/\epsilon_B(\epsilon_S = 0.5)$	3.06	3.57	3.44	1.77	1.77
$1/\epsilon_B(\epsilon_S = 0.1)$	16.1	<b>5.08</b>	<b>3.91</b>	<b>2.36</b>	<b>2.35</b>	$1/\epsilon_B(\epsilon_S = 0.1)$	22.4	<b>7.17</b>	<b>5.52</b>	<b>2.83</b>	<b>2.84</b>

120 GeV W						174 GeV W					
	AE	HLN <sub>14</sub>	PNN <sub>14</sub>	HLN <sub>0</sub>	PNN <sub>0</sub>		AE	HLN <sub>14</sub>	PNN <sub>14</sub>	HLN <sub>0</sub>	PNN <sub>0</sub>
$\epsilon_S(1/\epsilon_B = 10)$	0.244	<b>0.070</b>	<b>0.089</b>	<b>0.021</b>	<b>0.022</b>	$\epsilon_S(1/\epsilon_B = 10)$	0.289	0.124	0.190	<b>0.064</b>	<b>0.064</b>
$\epsilon_S(1/\epsilon_B = 100)$	0.040	<b>0.001</b>	<b>0.001</b>	<b>0.001</b>	<b>0.001</b>	$\epsilon_S(1/\epsilon_B = 100)$	0.052	<b>0.003</b>	<b>0.003</b>	<b>0.003</b>	<b>0.003</b>
$1/\epsilon_B(\epsilon_S = 0.5)$	3.71	4.01	4.76	2.97	2.97	$1/\epsilon_B(\epsilon_S = 0.5)$	4.40	4.21	5.53	6.05	6.10
$1/\epsilon_B(\epsilon_S = 0.1)$	32.9	<b>8.52</b>	<b>9.58</b>	<b>4.30</b>	<b>4.31</b>	$1/\epsilon_B(\epsilon_S = 0.1)$	42.4	11.4	14.7	<b>8.61</b>	<b>8.57</b>

Table 18. The background rejection ( $1/\epsilon_B$ ) at two different fixed signal efficiencies ( $\epsilon_S$ )—0.5 and 0.1—and the signal efficiency at two different fixed values of the background rejection—10 and 100—for all 8 anomalous signals. We present these metrics for 5 different networks, the AE, PNN<sub>0</sub>, HLN<sub>0</sub>, PNN<sub>14</sub>, and HLN<sub>14</sub>. The values shown in red are those where  $\epsilon_B > \epsilon_S$ .

networks when used as anomaly detectors for the 174 GeV Top and 80 GeV Higgs. These networks, when applied to these signals operate at comparable signal efficiencies to the AE for lower fixed values of the background rejection. Shifting now to the background rejection at fixed signal efficiency, we see that our mimicker networks compare favorably to the AE at higher signal efficiencies across all of the anomalous signals we consider, but fall behind the AE at lower signal efficiencies. Again, the exception here are the mimicker networks applied to the 80 GeV Higgs. As was observed earlier in Fig. 22, as we make tighter cuts on our mimicker networks, forcing them to operate at lower signal efficiencies, they begin to deem the background as being more anomalous than the signal when compared to the autoencoder. While this type of behavior would be difficult to deal with in a real analysis, it is not unique to our mimicker networks and is a challenge with anomaly detection in general. The cuts that result in  $\epsilon_B > \epsilon_S$  are highlighted in red in Tab. 18. Taken together, these indicate that most of the performance of our mimicker networks is coming at higher signal

efficiencies, and the long tails in their anomaly scores for the background distribution holds them back from exactly matching the AE.

Finally, by the endpoint of the iterative process, we had found that the PNN and HLN agreed on ordering of background events at about 83% when compared to the AE. Here, we see that in terms of the AUC metric, 83% mimicking transferred quite well to the use of these mimickers as simpler anomaly detectors with comparable performance. We expect the tendency for the mimicker networks to tag the background as being more anomalous than the signal at low signal efficiencies to subside as the ADO of the mimickers approaches 1.

### 4.3.3 Using Only Prime EFPs

In examining the EFPs selected to improve the decision ordering, we note that even though we use up to 14 EFPs, they only depend on six prime EFP factors:

$$\begin{array}{cccccc}
 \bullet & \bullet & \bullet & \bullet & \bullet & \bullet \\
 | & \circ & \text{---} & \circ & \triangle & \text{---} \\
 \bullet & \bullet & \bullet & \bullet & \bullet & \bullet
 \end{array}
 \tag{4.12}$$

Notably in these primes, the first and fifth prime factors are the energy correlation functions for two and three prong structures [184]. It is also interesting to note that these prime factors are nonzero only for  $\geq 2, 3$  prong structures. As the AE is learning to encode the predominantly 1-prong QCD events, it seems that it is losing information contained in these higher prong observables. With this loss of information, networks with direct access to these observables are able to explain the reconstruction error of the network.

The observation that the anomaly scores can be explained by composite operators which only have a few prime operators leads one to wonder if the prime EFPs are good enough. To test this, we trained both the PNN and the HLN using mass,  $p_T$ , and the six prime EFPs. The results are denoted in Fig. 21 and Fig. 23 by the blue



‘+’ and orange ‘×’, respectively. Not only do these “prime-only” networks perform comparably to each other, which matches the behavior we saw from the networks trained on the composite EFPs, but the prime-only and composite networks also perform comparably across all of the signals. The results in Fig. 21 show the ADO of the prime-only networks computed on the same pairs of events as the center line for the composite models. The ADO of the prime-only models has a similar spread as the composite models, and thus the two do indeed perform comparably. Taken together, this seems to indicate that the prime EFPs alone contain all of the necessary information to construct simple anomaly detectors capable of matching much more complex ones. While each of the prime EFPs on their own would have been selected eventually, these results also suggests a more efficient iterative procedure for creating HLN and PNN mimickers, where one uses the redundancy in the full space of EFPs to their advantage and allows the algorithm to explore the full space of composite EFPs, but only selects those containing new prime factors.

#### 4.3.4 Comparison with Isolation Forests

Through this iterative process, we’ve constructed two different types of dense neural networks that approximately match the AE not only in how their decision functions order background events, but also as anomaly detectors for classifying a variety of signals. It is clear then that the observables picked out by this procedure contain the information needed to match the AE on both fronts. One then wonders if an even simpler anomaly detector than the ones presented in Sec. 4.2 would give similar results. To investigate this possibility, we consider isolation forests as implemented by ISOLATION FOREST in SCIKIT-LEARN [173].

Isolation forests work by randomly selecting a feature from a given set of inputs, and then randomly selecting a split value for that feature. This splitting process is

repeated until each event the model is trained on has been isolated from the rest, resulting in a tree-like structure. We then build an ensemble, or “forest” of these classifiers. The anomaly score is the number of splittings needed to isolate each event, averaged over the entire ensemble. This kind of random partitioning tends to take fewer splittings to isolate anomalous events, so if the average number of splittings across a large ensemble is low, the event is likely to be anomalous. We wanted to see if the performance of the isolation forests saturate in the same way the HLN and PNNs did, so we trained a series of them and added the new observable picked out by either the HLN or PNN each time. The details of our specific implementation is given in App. B.2. Since the HLN and PNNs selected EFPs in a slightly different order, we trained 2 different sets of isolation forests. One set added observables in the order selected by the HLN, while the other added them in the order selected by the PNN.

Figure 23 shows how the isolation forests compare to the HLN, CNNs, and AE when used as a classifier on the 8 signals considered in this work. The blue dotted line shows the AUC of the isolation forests trained on the EFPs selected by the PNN, the orange dotted line corresponds to isolation forests trained on the EFPs selected by the HLN. For most of the signals, both isolation forests have an AUC of  $\sim 0.5$ , and are unable to match the performance of the HLN, PNN, or AE. This is a very interesting observation. The same small set of observables are able to lead to good anomaly detection when trying to match the decisions of the AE. However, as discussed above, these observables in some sense tell us what the AE is choosing to ignore when learning to reconstruct QCD images. Since these observables are not very descriptive for QCD events, the isolation forest does not have much to learn from. We expect the results would hold for other anomaly detection techniques trained on

the same observables. Thus, we suspect it is the mimicking aspect of our procedure which allows for good anomaly detection with the simple set of observables.

#### 4.4 Conclusion

In this paper, we have extended the results of Ref. [128] to build simpler, more interpretable anomaly detectors. Starting with a convolutional autoencoder, we iteratively built a network that mimics the autoencoder’s ordering of background events, where the network’s inputs are high-level variables taken from a set of Energy Flow Polynomials. We presented two network architectures for the mimickers, the High-Level Network and the Paired Neural Network. The High-Level Network aims to reproduce the reconstruction error of the autoencoder, while the Paired Neural Network takes in two events and is trained to order them like the autoencoder. Note that both the PNN and HLN are trained to order anomalous events from the physics observables, which is an inherently different task than the autoencoder, which was only trained to compress and decompress background data. This highlights the difference with Ref. [128], in which the black-box network and mimicking network have the same task of binary classification. Given this fundamental difference between our AE and mimicking networks, it is not obvious that employing the same strategy will work when trying to mimic the autoencoder’s ordering. However, we find that these two complementary approaches give similar performance,  $\sim 83\%$  agreement, when ordering background events and also pick out the same list of EFPs, suggesting the commonality of the information that is needed to order events like the autoencoder.

After mimicking the autoencoder on ordering of background events, we take these networks and apply them as anomaly detectors on eight different signals. Even though the mimickers and autoencoder have never seen these events, we find that the similarity in ordering transfers to these events, making the mimickers as good

(or better) than the autoencoder as an anomaly detector for seven of the eight signals. It is worth emphasizing how such results were not guaranteed to occur. The autoencoder, having been trained only on background events, has no concept of what is anomalous. So it is not obvious that mimicking the ordering of events for the background will generalize to anomalous events, especially given a large set of signal classes.

Since the high-level observables picked out by these mimickers rely only on six prime Energy Flow Polynomials, it indicates that the information required to order events like the autoencoder is reasonably small. However, since the isolation forests based on these high-level inputs did not perform as well, it shows that mimicking the autoencoder's background ordering is crucial in creating a simpler anomaly detector.

In terms of future directions, it would be interesting to extend the list of Energy Flow Polynomials to check that one can saturate the decision ordering of the autoencoder and to determine what prime Energy Flow Polynomials are needed for that. Applying this technique to other anomaly detection methods on the same dataset would help uncover what high-level variables are being used by these methods and could help in designing more powerful anomaly detectors. Finally, it would be interesting to see if one can extend this technique to cases where there is no known high-level variable basis (like the Energy Flow Polynomials) and to see to what extent decision ordering transfers to different signals. For instance, the methods which performed best on the Dark Machines anomaly score challenge [93, 116, 119] used variational autoencoder structures which only aimed to make a Gaussian latent space and did not try to reconstruct events. It would be very interesting to see what physics these methods are using, but there is no obvious basis of observables to use.

CHAPTER V  
CONCLUSIONS

### 5.1 Primary Observables for Top Quark Collider Signals

In this chapter, we have extended an approach [28] to determine the on-shell 3 and 4 point amplitudes that are needed for modeling general top quark phenomenology at colliders. These serve as an intermediary between the observables searched for by experimental analyses and the operators in effective field theories for the Standard Model. This involved characterizing the general amplitudes for processes involving four fermions or two fermions and two gauge bosons. We were able to characterize these respectively to dimension 12 and 13, finding the structure of primary and descendant amplitudes, where descendants are primaries multiplied by Mandelstam factors. Interestingly, we find two classes of interactions whose Hilbert series numerator has a complete cancellation in the numerator. This naïvely would suggest that there are no primary operators at a certain mass dimension, but in actuality there are an equal number of new primaries and redundancies that appear at that mass dimension. This illustrates the importance of using the Hilbert series in conjunction with the amplitudes, as they complement each other in this process. We also note that our approach is a complementary check to the existing results up to dimension 8 using spinor-helicity variables [26, 27] and extends the amplitude structure to higher dimension.

To provide an initial survey of the potential phenomenology, we've used perturbative unitarity to place upper bounds on the coupling strengths of these interactions. These depend on the scale where unitarity is violated  $E_{\text{TeV}} = E_{\text{max}}/\text{TeV}$ , with more stringent constraints as one increases  $E_{\text{TeV}}$ . Given the expected sample of top quarks at HL-LHC, we've estimated the coupling size needed for the top quark

decays to be seen over irreducible backgrounds. This allowed us to highlight the that top quark decays into both FCNC modes, like  $t \rightarrow c(\bar{\ell}\ell, h\gamma, hg, Z\gamma, Zg, \gamma\gamma, \gamma g)$ , and non-FCNC modes, like  $t \rightarrow b(W\gamma, Wg)$ , could be interesting to search for at the HL-LHC. Some of these highlighted modes occur at dimension 8 and 10 in SMEFT and thus would be interesting to explore how distinctive these new amplitudes are compared to existing searches. We leave such detailed phenomenology to future work.

To conclude, the high energy program at colliders is entering the phase of testing whether the Standard Model is indeed the correct description of physics at the TeV scale. To do so, we must look for new physics in the most general way, so that we can find such deviations or constrain them. On-shell amplitudes are a useful intermediary between experimental analyses and the parameterization of new physics by effective field theories. Finally, by determining the on-shell amplitude structure to high dimension and writing down a concrete basis for them, we hope this will allow the field to maximize its efforts to find what exists beyond the Standard Model.

## 5.2 Mass Agnostic Jet Taggers

The significance of a discovery or exclusion will always be the primary factor when determining which decorrelation method to use in an analysis. With this in mind, one potential concern with the data augmentation techniques is that they may reduce the statistical power of the data itself, especially when applied to data on the tails of the distribution. We do not expect this to be the case since the PCA based approach involves only linear transformations of the data and Planing only requires that the data used for training be reweighted. In future work, we will answer this question concretely, as part of a larger study where we explicitly look at a phenomenological proxy for the discovery significance that properly accounts for systematic errors and further optimizes the working point of the tagger.

One interesting extension of the techniques explored here would be to train networks on jets in a given mass range, and then use these networks to classify jets in an entirely different mass range. Neural networks offer a very flexible framework to train a wide variety of models, but are far less adaptable once trained. The techniques studied here distinguish signal from background with less reliance on the jet mass. Since they only rely on substructure information, and not the absolute scale of the jet, they should be applicable to other regions of the mass parameter space. Showing that such results are possible could increase the usage of such MV techniques in large experimental collaborations, such as those at the LHC.

Our comparisons used the same representation of the input data for all of the classifiers, namely the N-subjettiness basis. However, there have been many studies of jet taggers using other representations, such as images, sequences, or graphs. Mass decorrelation has been done in images with Planing [33] and Adversarial training [69], but it would be interesting to see how all of the techniques studied here could be applied to the different representations, and if any additional advantage is offered. Additionally, decorrelating in both the jet mass and the transverse momentum could make for a stable jet tagger (See Ref. [177] for multidimensional decorrelation with Planing).

In this work, we applied all our methods to decorrelate the classifiers from the jet mass by explicitly using the jet mass in the decorrelation procedure (flattening the jet mass distribution for Planing; binning in jet mass for PCA). However,  $\tau_{21}^{\text{DDT}}$  uses  $\rho = \log(m^2/p_T^2)$  in its analytic decorrelation. An interesting test would be to examine how the decorrelation techniques work using this value (or just  $p_T$ ) as opposed to the  $m_J$  alone. Additionally, it would be worthwhile studying how robust these techniques are in a more realistic experimental environment by testing how the classification and

decorrelation generalize to signals with mixed prongedness, and signal contamination. This is work we intend to do, and leave to future study.

New physics searches are challenging, especially when the processes are rare and the backgrounds plentiful. Rejecting background events is necessary, but *how* the background is removed is also important. Experimental efforts to look for new physics are greatly aided by easy-to-model backgrounds, so the need for techniques that preserve the profiles of the underlying background distributions cannot be understated.

In this work, we explored a variety of cutting-edge methods used in the classification of boosted objects. We started by looking at how standard single- and multi-variate techniques achieve better classification at the cost of increased background sculpting. These standard methods serve as a point of comparison to analytic [65] and multivariate [67, 64] methods designed specifically with mass decorrelation in mind. Previous studies of these techniques [70] focused only on their application to searches for two-body hadronic resonances. We extended these analyses to see how existing methods perform when tasked with classifying jets with more complex substructure. We also studied two data augmentation based techniques to decorrelate the classifier output from the mass of the jet, Planing and PCA-based rescaling, as well as two training augmentation based techniques, uBoost and Adversarial NNs.

All of the decorrelation techniques studied in this work reduce the extent to which the background is sculpted, and could therefore be used to increase sensitivity in a new physics search. We have shown that Planing and PCA give comparable performance to training augmentation based methods, while taking only a fraction of the time and computational overhead to train. These data augmentation techniques



could be useful in situations such as testing prototypes, where fast turnaround is desired.

### **5.3 Creating Simple, Interpretable Anomaly Detectors for New Physics in Jet Substructure**

In this chapter, we have extended the results of Ref. [128] to build simpler, more interpretable anomaly detectors. Starting with a convolutional autoencoder, we iteratively built a network that mimics the autoencoder’s ordering of background events, where the network’s inputs are high-level variables taken from a set of Energy Flow Polynomials. We presented two network architectures for the mimickers, the High-Level Network and the Paired Neural Network. The High-Level Network aims to reproduce the reconstruction error of the autoencoder, while the Paired Neural Network takes in two events and is trained to order them like the autoencoder. Note that both the PNN and HLN are trained to order anomalous events from the physics observables, which is an inherently different task than the autoencoder, which was only trained to compress and decompress background data. This highlights the difference with Ref. [128], in which the black-box network and mimicking network have the same task of binary classification. Given this fundamental difference between our AE and mimicking networks, it is not obvious that employing the same strategy will work when trying to mimic the autoencoder’s ordering. However, we find that these two complementary approaches give similar performance,  $\sim 83\%$  agreement, when ordering background events and also pick out the same list of EFPs, suggesting the commonality of the information that is needed to order events like the autoencoder.

After mimicking the autoencoder on ordering of background events, we take these networks and apply them as anomaly detectors on eight different signals. Even though the mimickers and autoencoder have never seen these events, we find that

the similarity in ordering transfers to these events, making the mimickers as good (or better) than the autoencoder as an anomaly detector for seven of the eight signals. It is worth emphasizing how such results were not guaranteed to occur. The autoencoder, having been trained only on background events, has no concept of what is anomalous. So it is not obvious that mimicking the ordering of events for the background will generalize to anomalous events, especially given a large set of signal classes.

Since the high-level observables picked out by these mimickers rely only on six prime Energy Flow Polynomials, it indicates that the information required to order events like the autoencoder is reasonably small. However, since the isolation forests based on these high-level inputs did not perform as well, it shows that mimicking the autoencoder's background ordering is crucial in creating a simpler anomaly detector.

In terms of future directions, it would be interesting to extend the list of Energy Flow Polynomials to check that one can saturate the decision ordering of the autoencoder and to determine what prime Energy Flow Polynomials are needed for that. Applying this technique to other anomaly detection methods on the same dataset would help uncover what high-level variables are being used by these methods and could help in designing more powerful anomaly detectors. Finally, it would be interesting to see if one can extend this technique to cases where there is no known high-level variable basis (like the Energy Flow Polynomials) and to see to what extent decision ordering transfers to different signals. For instance, the methods which performed best on the Dark Machines anomaly score challenge [93, 116, 119] used variational autoencoder structures which only aimed to make a Gaussian latent space and did not try to reconstruct events. It would be very interesting to see what physics these methods are using, but there is no obvious basis of observables to use.

## APPENDIX A

### SUPPLEMENTAL MATERIAL FOR MASS AGNOSTIC JET TAGGERS

#### A.1 Adversary decorrelation parameter

As mentioned in Sec. 3.2.3.2, adversarially-trained neural networks introduce a new positive hyperparameter,  $\lambda$ , which must be chosen by the user. Higher values of  $\lambda$  increase the importance of the adversary when minimizing the loss function of the tagger, which decorrelates the output from the tagger from the jet mass at the cost of worse classification when compared to standard neural networks.

In choosing a value of  $\lambda$  to use in our analysis, we examined the different metrics and found that  $\lambda = 50$  is where results start to saturate. Figure A.24 shows the results of this parameter sweep using the three metrics used in the main body of this work. The ROC curves for the 2-, 3-, and 4-prong signals are shown in the top row. Darker shades correspond to lower values of  $\lambda$ . As expected, using lower values of  $\lambda$  result in better classification. In the middle row, we have plotted the Bhattacharyya distance as a function of signal efficiency for every value of  $\lambda$ . The darkest curves look nearly identical to the Original NN results of Fig. 12, and sculpt the background the most, while the lightest curves (corresponding to higher values of  $\lambda$ ) sculpt the least. From this row, we can see that the mass decorrelation as measured by the Bhattacharyya distance saturate at  $\lambda = 50$ . The bottom row shows a parametric plot of the Bhattacharyya distance and the background rejection, made by scanning across the signal efficiencies. For a fixed level of background rejection, we again see that the decorrelating benefits of the adversarial approach saturate at  $\lambda = 50$ .

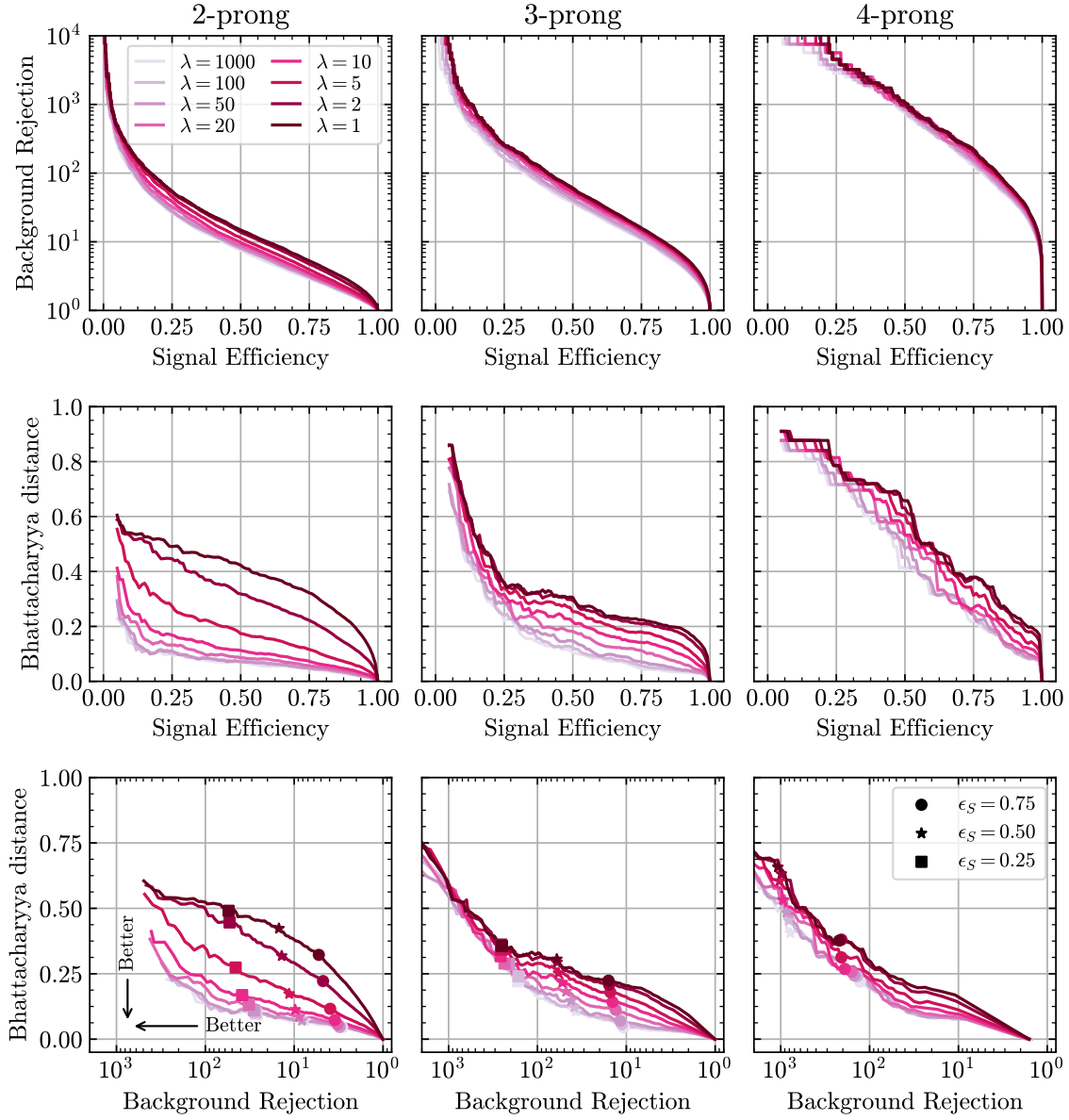


Figure A.24. The top row shows the ROC curves for all of the adversarially-trained neural networks tasked with distinguishing the 2-, 3-, and 4-prong signal jets from the QCD background. Lighter shades correspond to increasingly larger values of  $\lambda$ . Larger values of  $\lambda$  put an increased emphasis on making the network output less dependent on the mass, at the cost of worse classification. The middle row shows how the Bhattacharyya distance for the QCD background changes as tighter cuts are made on the network output. As expected, higher values of  $\lambda$  lead to less sculpting than lower values of  $\lambda$ . The bottom row shows a parametric plot of the Bhattacharyya distance for the QCD background versus the background rejection. The adversarially-trained networks are all able to achieve similarly large background rejections, but networks using higher values of  $\lambda$  are able to reject much of the background while preserving the profile of the underlying distribution. All three rows show that the benefits of adversarial training saturate at  $\lambda = 50$ .

## A.2 Comparison of histogram distances

We have used Bhattacharya distance in this work to quantify the sculpting of jet mass distribution from various jet tagging methods. This distance has the nice feature that it is normalized and therefore allows fair comparison across various methods. It is certainly not a unique choice. Another method used by ATLAS collaboration in Ref. [70] to quantify the mass distortion is the Jensen-Shannon distance, which is given as

$$d_{\text{JSD}}(P, Q) = \sqrt{\frac{d_{\text{KL}}(P, \frac{P+Q}{2}) + d_{\text{KL}}(Q, \frac{P+Q}{2})}{2}}, \quad (\text{A.1})$$

where  $d_{\text{KL}}$  is the Kullback-Leibler divergence, given by

$$d_{\text{KL}}(P, Q) = \sum_i p_i \log \frac{p_i}{q_i}, \quad (\text{A.2})$$

$p_i, q_i$  being the value of the distribution  $P, Q$  in bin  $i$ . For us,  $P$  is the background mass distribution before the application of a given tagger, and  $Q$  is the background mass distribution after the application of a given tagger. In Fig. A.25, we compare how the two distances  $d_{\text{B}}$  and  $d_{\text{JSD}}$  compare. We see that the two distances are very similar to each other for 2-pronged and 3-pronged signals, while have some differences in the 4-pronged case. The general shape is the same however, and one can be chosen over the other without biasing any inferences.

## A.3 Histogram Sculpting Comparison

Here we show a qualitative comparison of all of the decorrelation methods for all of the different pronged signals considered in the main body of this work. The figures are organized as follows: the leftmost column shows the single-variable benchmark,  $\tau_N^{(1)}/\tau_{N-1}^{(1)}$  ( $N = 2, 3, 4$  for 2-/3-/4-pronged signal), as well as the Designed

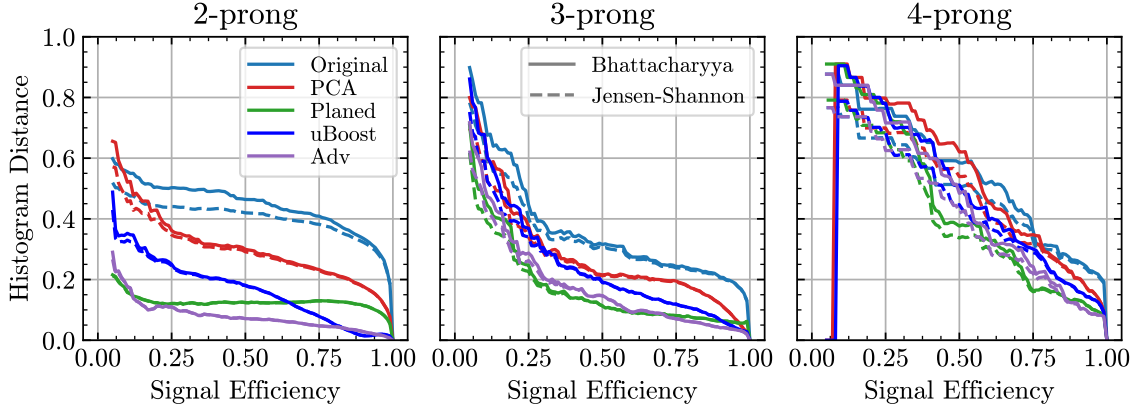


Figure A.25. Comparison of Bhattacharyya distance and Jensen-Shannon distance for 2-, 3-, and 4-pronged signals, as a function of signal efficiency for various decorrelation methods studied in this work. The general trend for both metrics is seen to be the same.

Decorrelated Tagger for the 2-prong signal; the middle column shows how the BDT benchmark sculpts the background, followed by all of the BDT based decorrelation methods studied in this work—uBoost, Planing, and PCA; the right column shows how the NN benchmark sculpts, followed by all of the NN based methods studied, namely Adversarial NNs, Planing, and PCA. A legend is provided in the lower left of each figure to remind the reader which colors correspond to which cuts on the signal efficiency,  $\varepsilon_S$ .

Figure A.26 shows the comparison of methods for the 2-pronged signal, Fig. A.27 shows this comparison for the 3-pronged signal, and Fig. A.28 shows the comparison for the 4-prong signal.

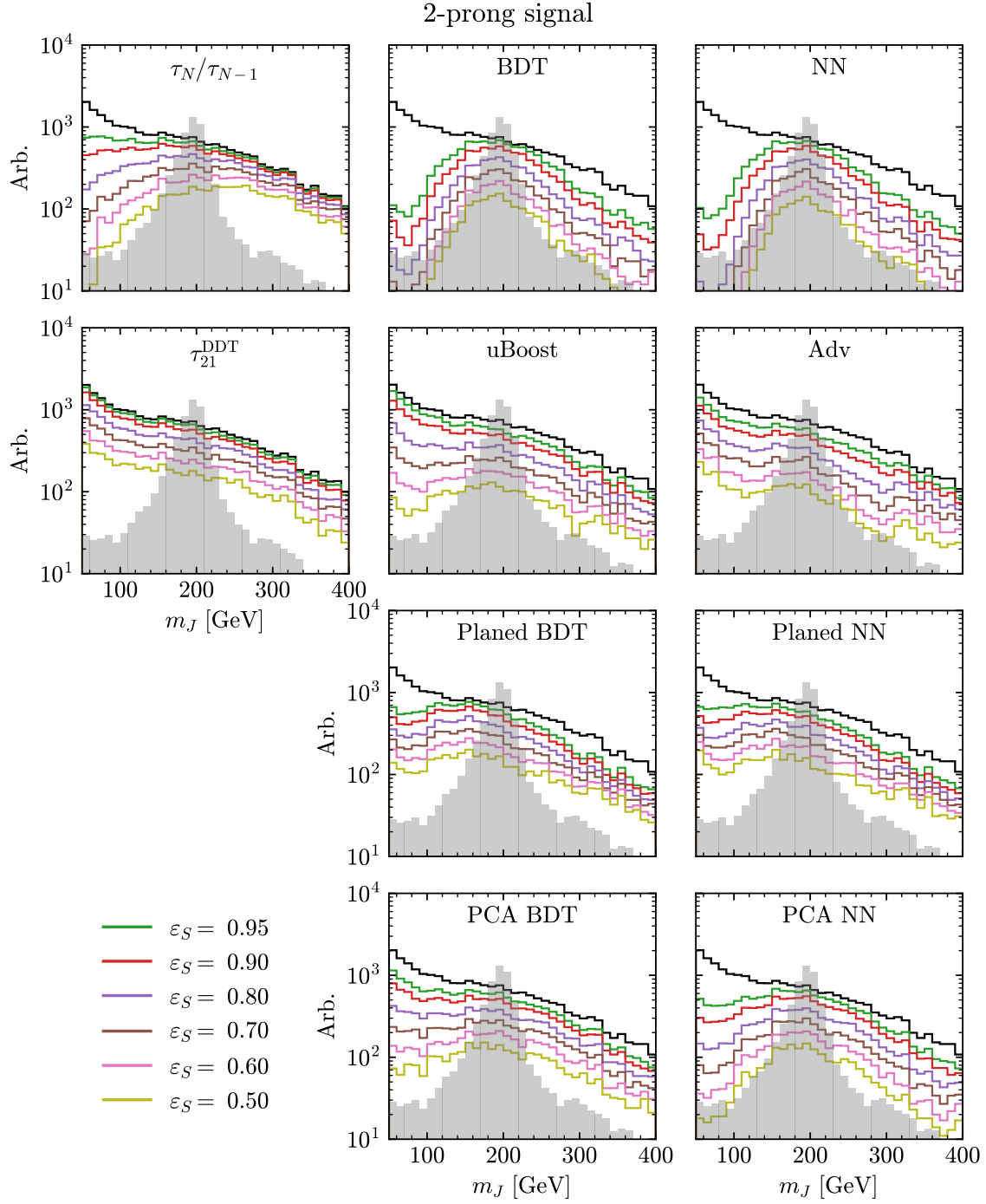


Figure A.26. Comparison of all decorrelation methods to the benchmarks for the 2-prong signal.  $\tau_N/\tau_{N-1}$  is  $\tau_2/\tau_1$ .

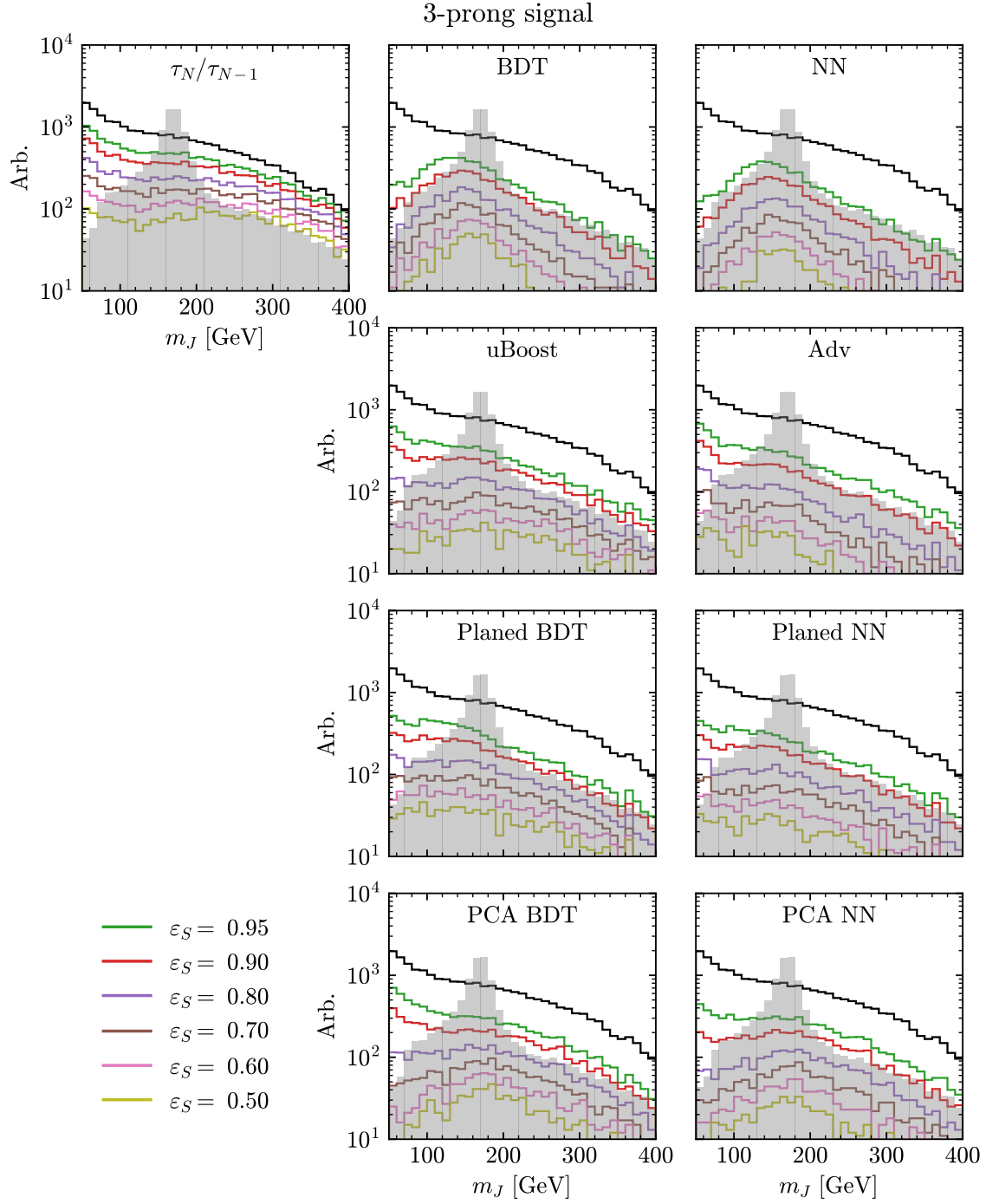


Figure A.27. Comparison of all decorrelation methods to the benchmarks for the 3-prong signal.  $\tau_N/\tau_{N-1}$  is  $\tau_3/\tau_2$ .



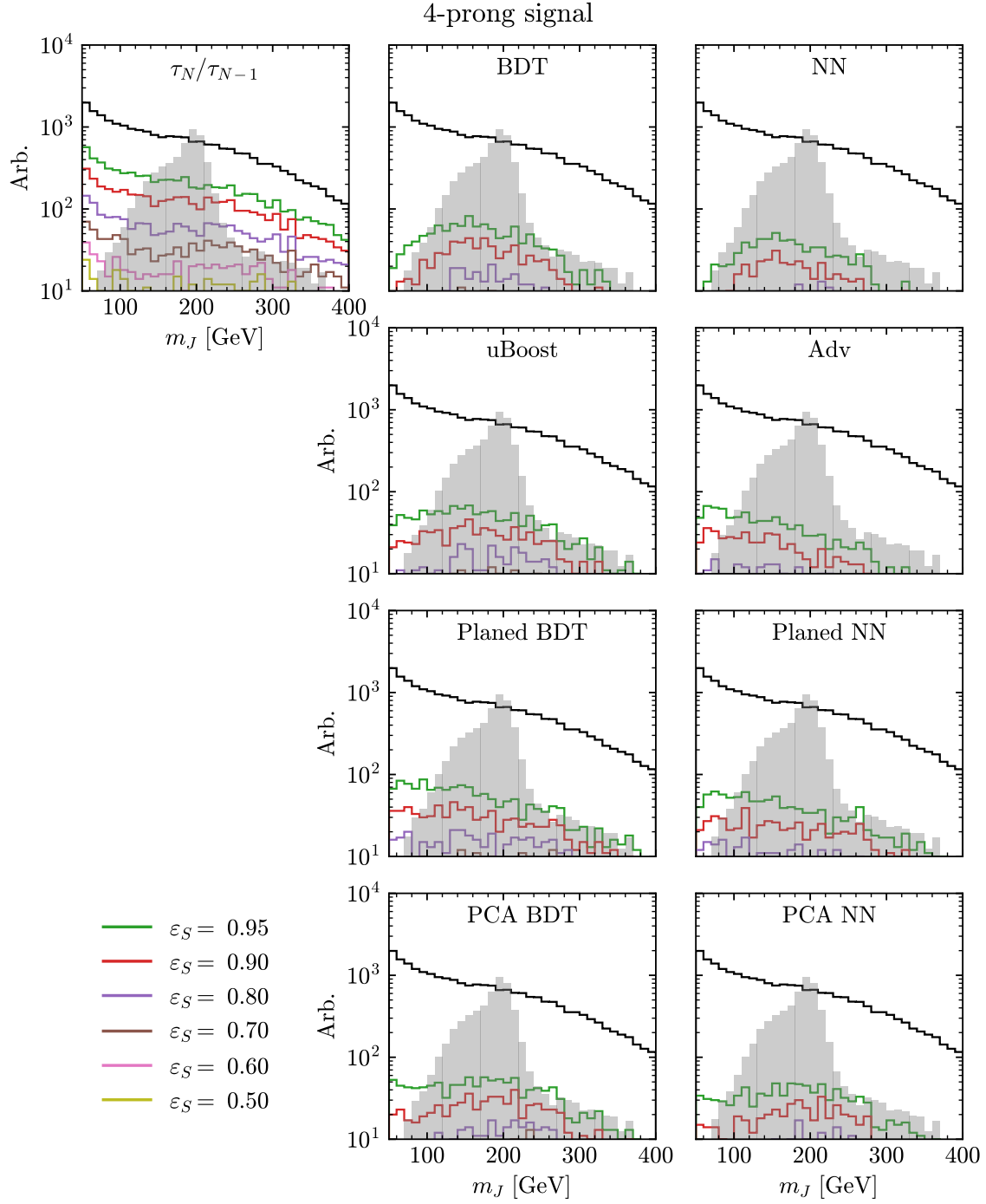


Figure A.28. Comparison of all decorrelation methods to the benchmarks for the 4-prong signal.  $\tau_N/\tau_{N-1}$  is  $\tau_4/\tau_3$ .

## APPENDIX B

### SUPPLEMENTAL MATERIAL FOR CREATING SIMPLE, INTERPRETABLE ANOMALY DETECTORS FOR NEW PHYSICS IN JET SUBSTRUCTURE

#### B.1 Simulation Details

In this appendix, we provide further details of the simulated public datasets we use in this work [103, 179, 180]. All of the QCD dijet,  $W$ , top, and Higgs samples are subject to the same selection criteria, showering, and detection simulation parameters. The background and anomalous events are generated using MADGRAPH [166] and PYTHIA8 [193], with detector effects being simulated by DELPHES [168]. The jets are then clustered with FASTJET [194, 195] using the anti- $k_T$  algorithm [196] with a cone size of  $R = 1.0$ . All events are required to have two hard jets, with the leading jet having  $p_T > 450$  GeV and the sub-leading jet having  $p_T > 200$  GeV. We then take only the leading jet in each event.

The QCD jets are created via  $pp \rightarrow jj$ . The  $W$  jets are created using  $pp \rightarrow W' \rightarrow W (\rightarrow jj) Z (\rightarrow \nu\bar{\nu})$  with  $m_{W'} = 1.2$  TeV. The top jets are produced via  $pp \rightarrow Z' \rightarrow t\bar{t}$  with  $m_{Z'} = 1.3$  TeV. Finally, the Higgs jets are produced with  $pp \rightarrow HH, H \rightarrow hh, h \rightarrow jj$  with  $m_H = 174$  GeV. For each of these signals, we only consider jets with  $p_T \in [550, 650]$  GeV. This same  $p_T$  cut is applied to the background training and testing sets.

#### B.2 Network Training Hyperparameters

Here, we provide the details of the training hyperparameters of the AE, PNN, HLN, and isolation forests. For all three deep neural network architectures, we use the REDUCELRONPLATEAU and EARLYSTOPPING callbacks from KERAS to dynamically reduce the learning rate and stop training early, respectively. All three neural networks are trained with the Adam optimizer [197].

For the AE, our training hyperparameters are:

- Train for 100 epochs with `EARLYSTOPPING` on the `validation_loss` with a patience of 10 epochs.
- Initial learning rate of  $10^{-3}$  with `REDUCELRONPLATEAU` on the `validation_loss` with a patience of 5 epochs.
- Batch size of 256.

For the HLN and PNN, our training hyperparameters are:

- Train for 200 epochs with `EARLYSTOPPING` on the `validation_loss` with a patience of 10 epochs.
- Initial learning rate of  $10^{-3}$  with `REDUCELRONPLATEAU` on the `validation_loss` with a patience of 5 epochs.
- Batch size of 256.

With the early stopping conditions, the AE trains in  $\sim 30$  epochs, the PNN trains in  $\sim 50$  epochs, and the HLN trains in  $\sim 60$  epochs.

For the isolation forests, our training hyperparameters are:

- 250 estimators in the ensemble.
- The `max_features` used to train each estimator is set to the number of inputs for each event.
- `contamination` is set to ‘`auto`’ since there is no way to determine what fraction of events can reliably be called outliers *a priori*.
- `bootstrap` is set to ‘`False`’, so individual trees are trained on random subsets of the data without replacement.

## REFERENCES CITED

- [1] **ATLAS** Collaboration, G. Aad *et al.*, “Observation of a new particle in the search for the Standard Model Higgs boson with the ATLAS detector at the LHC,” *Phys. Lett. B* **716** (2012) 1–29, arXiv:1207.7214 [hep-ex].
- [2] **CMS** Collaboration, S. Chatrchyan *et al.*, “Observation of a New Boson at a Mass of 125 GeV with the CMS Experiment at the LHC,” *Phys. Lett. B* **716** (2012) 30–61, arXiv:1207.7235 [hep-ex].
- [3] D. Hanneke, S. F. Hoogerheide, and G. Gabrielse, “Cavity Control of a Single-Electron Quantum Cyclotron: Measuring the Electron Magnetic Moment,” *Phys. Rev. A* **83** (2011) 052122, arXiv:1009.4831 [physics.atom-ph].
- [4] E. Corbelli and P. Salucci, “The extended rotation curve and the dark matter halo of M33,” *Monthly Notices of the Royal Astronomical Society* **311** (01, 2000) 441–447, <https://academic.oup.com/mnras/article-pdf/311/2/441/2881340/311-2-441.pdf>. <https://doi.org/10.1046/j.1365-8711.2000.03075.x>.
- [5] P. Natarajan, U. Chadayammuri, M. Jauzac, J. Richard, J.-P. Kneib, H. Ebeling, F. Jiang, F. van den Bosch, M. Limousin, E. Jullo, H. Atek, A. Pillepich, C. Popa, F. Marinacci, L. Hernquist, M. Meneghetti, and M. Vogelsberger, “Mapping substructure in the HST Frontier Fields cluster lenses and in cosmological simulations,” *Monthly Notices of the Royal Astronomical Society* **468** (02, 2017) 1962–1980, <https://academic.oup.com/mnras/article-pdf/468/2/1962/11210742/stw3385.pdf>. <https://doi.org/10.1093/mnras/stw3385>.
- [6] A. Refregier, “Weak gravitational lensing by large-scale structure,” *Annual Review of Astronomy and Astrophysics* **41** (2003) no. 1, 645–668, <https://doi.org/10.1146/annurev.astro.41.111302.102207>. <https://doi.org/10.1146/annurev.astro.41.111302.102207>.
- [7] D. Clowe, M. Bradač, A. H. Gonzalez, M. Markevitch, S. W. Randall, C. Jones, and D. Zaritsky, “A direct empirical proof of the existence of dark matter,” *The Astrophysical Journal* **648** (aug, 2006) L109–L113. <https://doi.org/10.1086%2F508162>.
- [8] **Planck** Collaboration, N. Aghanim *et al.*, “Planck 2018 results. VI. Cosmological parameters,” *Astron. Astrophys.* **641** (2020) A6, arXiv:1807.06209 [astro-ph.CO]. [Erratum: *Astron. Astrophys.* 652, C4 (2021)].

- [9] **WMAP** Collaboration, C. L. Bennett *et al.*, “Nine-Year Wilkinson Microwave Anisotropy Probe (WMAP) Observations: Final Maps and Results,” *Astrophys. J. Suppl.* **208** (2013) 20, [arXiv:1212.5225 \[astro-ph.CO\]](#).
- [10] **Super-Kamiokande** Collaboration, Y. Fukuda *et al.*, “Evidence for oscillation of atmospheric neutrinos,” *Phys. Rev. Lett.* **81** (1998) 1562–1567, [arXiv:hep-ex/9807003](#).
- [11] **SNO** Collaboration, Q. R. Ahmad *et al.*, “Direct evidence for neutrino flavor transformation from neutral current interactions in the Sudbury Neutrino Observatory,” *Phys. Rev. Lett.* **89** (2002) 011301, [arXiv:nucl-ex/0204008](#).
- [12] P. Fayet, “Spontaneously Broken Supersymmetric Theories of Weak, Electromagnetic and Strong Interactions,” *Phys. Lett. B* **69** (1977) 489.
- [13] **Particle Data Group** Collaboration, R. L. Workman *et al.*, “Review of Particle Physics,” *PTEP* **2022** (2022) 083C01.
- [14] **Muon g-2** Collaboration, T. Albahri *et al.*, “Measurement of the anomalous precession frequency of the muon in the Fermilab Muon  $g-2$  Experiment,” *Phys. Rev. D* **103** (2021) no. 7, 072002, [arXiv:2104.03247 \[hep-ex\]](#).
- [15] **CDF** Collaboration, T. Aaltonen *et al.*, “High-precision measurement of the  $W$  boson mass with the CDF II detector,” *Science* **376** (2022) no. 6589, 170–176.
- [16] W. Buchmuller and D. Wyler, “Effective Lagrangian Analysis of New Interactions and Flavor Conservation,” *Nucl. Phys. B* **268** (1986) 621–653.
- [17] B. Grzadkowski, M. Iskrzynski, M. Misiak, and J. Rosiek, “Dimension-Six Terms in the Standard Model Lagrangian,” *JHEP* **10** (2010) 085, [arXiv:1008.4884 \[hep-ph\]](#).
- [18] F. Feruglio, “The Chiral approach to the electroweak interactions,” *Int. J. Mod. Phys. A* **8** (1993) 4937–4972, [arXiv:hep-ph/9301281](#).
- [19] T. Cohen, N. Craig, X. Lu, and D. Sutherland, “Is SMEFT Enough?,” *JHEP* **03** (2021) 237, [arXiv:2008.08597 \[hep-ph\]](#).
- [20] R. S. Gupta, A. Pomarol, and F. Riva, “BSM Primary Effects,” *Phys. Rev. D* **91** (2015) no. 3, 035001, [arXiv:1405.0181 \[hep-ph\]](#).
- [21] M. Gonzalez-Alonso, A. Greljo, G. Isidori, and D. Marzocca, “Pseudo-observables in Higgs decays,” *Eur. Phys. J. C* **75** (2015) 128, [arXiv:1412.6038 \[hep-ph\]](#).
- [22] A. Greljo, G. Isidori, J. M. Lindert, and D. Marzocca, “Pseudo-observables in electroweak Higgs production,” *Eur. Phys. J. C* **76** (2016) no. 3, 158, [arXiv:1512.06135 \[hep-ph\]](#).

- [23] A. Falkowski, “Higgs Basis: Proposal for an EFT basis choice for LHC HXSWG,” <https://cds.cern.ch/record/2001958>.
- [24] G. Durieux, T. Kitahara, Y. Shadmi, and Y. Weiss, “The electroweak effective field theory from on-shell amplitudes,” *JHEP* **01** (2020) 119, [arXiv:1909.10551](https://arxiv.org/abs/1909.10551) [[hep-ph](#)].
- [25] G. Durieux, T. Kitahara, C. S. Machado, Y. Shadmi, and Y. Weiss, “Constructing massive on-shell contact terms,” *JHEP* **12** (2020) 175, [arXiv:2008.09652](https://arxiv.org/abs/2008.09652) [[hep-ph](#)].
- [26] Z.-Y. Dong, T. Ma, J. Shu, and Z.-Z. Zhou, “The New Formulation of Higgs Effective Field Theory,” [arXiv:2211.16515](https://arxiv.org/abs/2211.16515) [[hep-ph](#)].
- [27] H. Liu, T. Ma, Y. Shadmi, and M. Waterbury, “An EFT hunter’s guide to two-to-two scattering: HEFT and SMEFT on-shell amplitudes,” [arXiv:2301.11349](https://arxiv.org/abs/2301.11349) [[hep-ph](#)].
- [28] S. Chang, M. Chen, D. Liu, and M. A. Luty, “Primary Observables for Indirect Searches at Colliders,” [arXiv:2212.06215](https://arxiv.org/abs/2212.06215) [[hep-ph](#)].
- [29] P. Baldi, P. Sadowski, and D. Whiteson, “Searching for Exotic Particles in High-Energy Physics with Deep Learning,” *Nature Commun.* **5** (2014) 4308, [arXiv:1402.4735](https://arxiv.org/abs/1402.4735) [[hep-ph](#)].
- [30] J. Thaler and K. Van Tilburg, “Maximizing Boosted Top Identification by Minimizing N-subjettiness,” *JHEP* **02** (2012) 093, [arXiv:1108.2701](https://arxiv.org/abs/1108.2701) [[hep-ph](#)].
- [31] J. Thaler and K. Van Tilburg, “Identifying Boosted Objects with N-subjettiness,” *JHEP* **03** (2011) 015, [arXiv:1011.2268](https://arxiv.org/abs/1011.2268) [[hep-ph](#)].
- [32] L. G. Almeida, M. Backović, M. Cliche, S. J. Lee, and M. Perelstein, “Playing Tag with ANN: Boosted Top Identification with Pattern Recognition,” *JHEP* **07** (2015) 086, [arXiv:1501.05968](https://arxiv.org/abs/1501.05968) [[hep-ph](#)].
- [33] L. de Oliveira, M. Kagan, L. Mackey, B. Nachman, and A. Schwartzman, “Jet-images — deep learning edition,” *JHEP* **07** (2016) 069, [arXiv:1511.05190](https://arxiv.org/abs/1511.05190) [[hep-ph](#)].
- [34] P. Baldi, K. Cranmer, T. Faucett, P. Sadowski, and D. Whiteson, “Parameterized neural networks for high-energy physics,” *Eur. Phys. J.* **C76** (2016) no. 5, 235, [arXiv:1601.07913](https://arxiv.org/abs/1601.07913) [[hep-ex](#)].
- [35] J. S. Conway, R. Bhaskar, R. D. Erbacher, and J. Pilot, “Identification of High-Momentum Top Quarks, Higgs Bosons, and W and Z Bosons Using Boosted Event Shapes,” *Phys. Rev.* **D94** (2016) no. 9, 094027, [arXiv:1606.06859](https://arxiv.org/abs/1606.06859) [[hep-ex](#)].

- [36] J. A. Aguilar-Saavedra, J. H. Collins, and R. K. Mishra, “A generic anti-QCD jet tagger,” *JHEP* **11** (2017) 163, arXiv:1709.01087 [hep-ph].
- [37] A. Butter, G. Kasieczka, T. Plehn, and M. Russell, “Deep-learned Top Tagging with a Lorentz Layer,” *SciPost Phys.* **5** (2018) no. 3, 028, arXiv:1707.08966 [hep-ph].
- [38] S. Chang, T. Cohen, and B. Ostdiek, “What is the Machine Learning?,” *Phys. Rev.* **D97** (2018) no. 5, 056009, arXiv:1709.10106 [hep-ph].
- [39] T. Cohen, M. Freytsis, and B. Ostdiek, “(Machine) Learning to Do More with Less,” *JHEP* **02** (2018) 034, arXiv:1706.09451 [hep-ph].
- [40] L. M. Dery, B. Nachman, F. Rubbo, and A. Schwartzman, “Weakly Supervised Classification in High Energy Physics,” *JHEP* **05** (2017) 145, arXiv:1702.00414 [hep-ph].
- [41] S. Egan, W. Fedorko, A. Lister, J. Pearkes, and C. Gay, “Long Short-Term Memory (LSTM) networks with jet constituents for boosted top tagging at the LHC,” arXiv:1711.09059 [hep-ex].
- [42] G. Kasieczka, T. Plehn, M. Russell, and T. Schell, “Deep-learning Top Taggers or The End of QCD?,” *JHEP* **05** (2017) 006, arXiv:1701.08784 [hep-ph].
- [43] S. Choi, S. J. Lee, and M. Perelstein, “Infrared Safety of a Neural-Net Top Tagging Algorithm,” *JHEP* **02** (2019) 132, arXiv:1806.01263 [hep-ph].
- [44] J. H. Collins, K. Howe, and B. Nachman, “Anomaly Detection for Resonant New Physics with Machine Learning,” *Phys. Rev. Lett.* **121** (2018) no. 24, 241803, arXiv:1805.02664 [hep-ph].
- [45] K. Fraser and M. D. Schwartz, “Jet Charge and Machine Learning,” *JHEP* **10** (2018) 093, arXiv:1803.08066 [hep-ph].
- [46] P. T. Komiske, E. M. Metodiev, B. Nachman, and M. D. Schwartz, “Learning to classify from impure samples with high-dimensional data,” *Phys. Rev.* **D98** (2018) no. 1, 011502, arXiv:1801.10158 [hep-ph].
- [47] S. H. Lim and M. M. Nojiri, “Spectral Analysis of Jet Substructure with Neural Networks: Boosted Higgs Case,” *JHEP* **10** (2018) 181, arXiv:1807.03312 [hep-ph].
- [48] J. Lin, M. Freytsis, I. Moulton, and B. Nachman, “Boosting  $H \rightarrow b\bar{b}$  with Machine Learning,” *JHEP* **10** (2018) 101, arXiv:1807.10768 [hep-ph].
- [49] S. Macaluso and D. Shih, “Pulling Out All the Tops with Computer Vision and Deep Learning,” *JHEP* **10** (2018) 121, arXiv:1803.00107 [hep-ph].

- [50] M. Farina, Y. Nakai, and D. Shih, “Searching for New Physics with Deep Autoencoders,” [arXiv:1808.08992 \[hep-ph\]](#).
- [51] J. H. Collins, K. Howe, and B. Nachman, “Extending the search for new resonances with machine learning,” *Phys. Rev.* **D99** (2019) no. 1, 014038, [arXiv:1902.02634 \[hep-ph\]](#).
- [52] K. Datta, A. Larkoski, and B. Nachman, “Automating the Construction of Jet Observables with Machine Learning,” [arXiv:1902.07180 \[hep-ph\]](#).
- [53] A. Butter *et al.*, “The Machine Learning Landscape of Top Taggers,” [arXiv:1902.09914 \[hep-ph\]](#).
- [54] A. J. Larkoski, I. Moulton, and B. Nachman, “Jet Substructure at the Large Hadron Collider: A Review of Recent Advances in Theory and Machine Learning,” [arXiv:1709.04464 \[hep-ph\]](#).
- [55] D. Guest, K. Cranmer, and D. Whiteson, “Deep Learning and its Application to LHC Physics,” *Ann. Rev. Nucl. Part. Sci.* **68** (2018) 161–181, [arXiv:1806.11484 \[hep-ex\]](#).
- [56] B. Nachman, “Anomaly Detection for Physics Analysis and Less than Supervised Learning,” [arXiv:2010.14554 \[hep-ph\]](#).
- [57] L. Lehman and A. Martin, “Hilbert Series for Constructing Lagrangians: expanding the phenomenologist’s toolbox,” *Phys. Rev. D* **91** (2015) 105014, [arXiv:1503.07537 \[hep-ph\]](#).
- [58] B. Henning, X. Lu, T. Melia, and H. Murayama, “Hilbert series and operator bases with derivatives in effective field theories,” *Commun. Math. Phys.* **347** (2016) no. 2, 363–388, [arXiv:1507.07240 \[hep-th\]](#).
- [59] L. Lehman and A. Martin, “Low-derivative operators of the Standard Model effective field theory via Hilbert series methods,” *JHEP* **02** (2016) 081, [arXiv:1510.00372 \[hep-ph\]](#).
- [60] B. Henning, X. Lu, T. Melia, and H. Murayama, “2, 84, 30, 993, 560, 15456, 11962, 261485, ...: Higher dimension operators in the SM EFT,” *JHEP* **08** (2017) 016, [arXiv:1512.03433 \[hep-ph\]](#). [Erratum: *JHEP* 09, 019 (2019)].
- [61] B. Henning, X. Lu, T. Melia, and H. Murayama, “Operator bases,  $S$ -matrices, and their partition functions,” *JHEP* **10** (2017) 199, [arXiv:1706.08520 \[hep-th\]](#).
- [62] L. Graf, B. Henning, X. Lu, T. Melia, and H. Murayama, “2, 12, 117, 1959, 45171, 1170086, ...: a Hilbert series for the QCD chiral Lagrangian,” *JHEP* **01** (2021) 142, [arXiv:2009.01239 \[hep-ph\]](#).



- [63] L. Gráf, B. Henning, X. Lu, T. Melia, and H. Murayama, “Hilbert Series, the Higgs Mechanism, and HEFT,” [arXiv:2211.06275](#) [[hep-ph](#)].
- [64] C. Shimmin, P. Sadowski, P. Baldi, E. Weik, D. Whiteson, E. Goul, and A. Sogaard, “Decorrelated Jet Substructure Tagging using Adversarial Neural Networks,” *Phys. Rev.* **D96** (2017) no. 7, 074034, [arXiv:1703.03507](#) [[hep-ex](#)].
- [65] J. Dolen, P. Harris, S. Marzani, S. Rappoccio, and N. Tran, “Thinking outside the ROCs: Designing Decorrelated Taggers (DDT) for jet substructure,” *JHEP* **05** (2016) 156, [arXiv:1603.00027](#) [[hep-ph](#)].
- [66] I. Moutl, B. Nachman, and D. Neill, “Convolved Substructure: Analytically Decorrelating Jet Substructure Observables,” *JHEP* **05** (2018) 002, [arXiv:1710.06859](#) [[hep-ph](#)].
- [67] J. Stevens and M. Williams, “uBoost: A boosting method for producing uniform selection efficiencies from multivariate classifiers,” *JINST* **8** (2013) P12013, [arXiv:1305.7248](#) [[nucl-ex](#)].
- [68] G. Louppe, M. Kagan, and K. Cranmer, “Learning to Pivot with Adversarial Networks,” [arXiv:1611.01046](#) [[stat.ME](#)].
- [69] T. Heimel, G. Kasieczka, T. Plehn, and J. M. Thompson, “QCD or What?,” *SciPost Phys.* **6** (2019) no. 3, 030, [arXiv:1808.08979](#) [[hep-ph](#)].
- [70] **ATLAS Collaboration** Collaboration, “Performance of mass-decorrelated jet substructure observables for hadronic two-body decay tagging in ATLAS,” Tech. Rep. ATL-PHYS-PUB-2018-014, CERN, Geneva, Jul, 2018. <https://cds.cern.ch/record/2630973>.
- [71] G. Kasieczka *et al.*, “The LHC Olympics 2020 a community challenge for anomaly detection in high energy physics,” *Rept. Prog. Phys.* **84** (2021) no. 12, 124201, [arXiv:2101.08320](#) [[hep-ph](#)].
- [72] R. T. D’Agnolo and A. Wulzer, “Learning New Physics from a Machine,” *Phys. Rev. D* **99** (2019) no. 1, 015014, [arXiv:1806.02350](#) [[hep-ph](#)].
- [73] A. De Simone and T. Jacques, “Guiding New Physics Searches with Unsupervised Learning,” *Eur. Phys. J. C* **79** (2019) no. 4, 289, [arXiv:1807.06038](#) [[hep-ph](#)].
- [74] A. Casa and G. Menardi, “Nonparametric semisupervised classification for signal detection in high energy physics,” [arXiv:1809.02977](#) [[stat.AP](#)].
- [75] B. M. Dillon, D. A. Faroughy, and J. F. Kamenik, “Uncovering latent jet substructure,” *Phys. Rev. D* **100** (2019) no. 5, 056002, [arXiv:1904.04200](#) [[hep-ph](#)].

- [76] A. Mullin, S. Nicholls, H. Pacey, M. Parker, M. White, and S. Williams, “Does SUSY have friends? A new approach for LHC event analysis,” *JHEP* **02** (2021) 160, [arXiv:1912.10625 \[hep-ph\]](#).
- [77] R. T. D’Agnolo, G. Grosso, M. Pierini, A. Wulzer, and M. Zanetti, “Learning multivariate new physics,” *Eur. Phys. J. C* **81** (2021) no. 1, 89, [arXiv:1912.12155 \[hep-ph\]](#).
- [78] B. Nachman and D. Shih, “Anomaly Detection with Density Estimation,” *Phys. Rev. D* **101** (2020) 075042, [arXiv:2001.04990 \[hep-ph\]](#).
- [79] A. Andreassen, B. Nachman, and D. Shih, “Simulation Assisted Likelihood-free Anomaly Detection,” *Phys. Rev. D* **101** (2020) no. 9, 095004, [arXiv:2001.05001 \[hep-ph\]](#).
- [80] **ATLAS** Collaboration, G. Aad *et al.*, “Dijet resonance search with weak supervision using  $\sqrt{s} = 13$  TeV  $pp$  collisions in the ATLAS detector,” *Phys. Rev. Lett.* **125** (2020) no. 13, 131801, [arXiv:2005.02983 \[hep-ex\]](#).
- [81] B. M. Dillon, D. A. Faroughy, J. F. Kamenik, and M. Szewc, “Learning the latent structure of collider events,” *JHEP* **10** (2020) 206, [arXiv:2005.12319 \[hep-ph\]](#).
- [82] K. Benkendorfer, L. L. Pottier, and B. Nachman, “Simulation-assisted decorrelation for resonant anomaly detection,” *Phys. Rev. D* **104** (2021) no. 3, 035003, [arXiv:2009.02205 \[hep-ph\]](#).
- [83] V. Mikuni and F. Canelli, “Unsupervised clustering for collider physics,” *Phys. Rev. D* **103** (2021) no. 9, 092007, [arXiv:2010.07106 \[physics.data-an\]](#).
- [84] G. Stein, U. Seljak, and B. Dai, “Unsupervised in-distribution anomaly detection of new physics through conditional density estimation,” in *34th Conference on Neural Information Processing Systems*. 12, 2020. [arXiv:2012.11638 \[cs.LG\]](#).
- [85] J. Batson, C. G. Haaf, Y. Kahn, and D. A. Roberts, “Topological Obstructions to Autoencoding,” *JHEP* **04** (2021) 280, [arXiv:2102.08380 \[hep-ph\]](#).
- [86] A. Blance and M. Spannowsky, “Unsupervised event classification with graphs on classical and photonic quantum computers,” *JHEP* **21** (2020) 170, [arXiv:2103.03897 \[hep-ph\]](#).
- [87] B. Bortolato, B. M. Dillon, J. F. Kamenik, and A. Smolkovič, “Bump Hunting in Latent Space,” [arXiv:2103.06595 \[hep-ph\]](#).
- [88] J. H. Collins, P. Martín-Ramiro, B. Nachman, and D. Shih, “Comparing weak- and unsupervised methods for resonant anomaly detection,” *Eur. Phys. J. C* **81** (2021) no. 7, 617, [arXiv:2104.02092 \[hep-ph\]](#).

- [89] T. Dorigo, M. Fumanelli, C. Maccani, M. Mojsavska, G. C. Strong, and B. Scarpa, “RanBox: Anomaly Detection in the Copula Space,” [arXiv:2106.05747 \[physics.data-an\]](#).
- [90] S. Volkovich, F. De Vito Halevy, and S. Bressler, “A Data-Directed Paradigm for BSM searches,” [arXiv:2107.11573 \[hep-ex\]](#).
- [91] A. Hallin, J. Isaacson, G. Kasieczka, C. Krause, B. Nachman, T. Quadfasel, M. Schlaffer, D. Shih, and M. Sommerhalder, “Classifying Anomalies THrough Outer Density Estimation (CATHODE),” [arXiv:2109.00546 \[hep-ph\]](#).
- [92] T. Buss, B. M. Dillon, T. Finke, M. Krämer, A. Morandini, A. Mück, I. Oleksiyuk, and T. Plehn, “What’s Anomalous in LHC Jets?,” [arXiv:2202.00686 \[hep-ph\]](#).
- [93] T. Aarrestad *et al.*, “The Dark Machines Anomaly Score Challenge: Benchmark Data and Model Independent Event Classification for the Large Hadron Collider,” *SciPost Phys.* **12** (2022) 043, [arXiv:2105.14027 \[hep-ph\]](#).
- [94] J. Hajer, Y.-Y. Li, T. Liu, and H. Wang, “Novelty Detection Meets Collider Physics,” *Phys. Rev. D* **101** (2020) no. 7, 076015, [arXiv:1807.10261 \[hep-ph\]](#).
- [95] O. Cerri, T. Q. Nguyen, M. Pierini, M. Spiropulu, and J.-R. Vlimant, “Variational Autoencoders for New Physics Mining at the Large Hadron Collider,” *JHEP* **05** (2019) 036, [arXiv:1811.10276 \[hep-ex\]](#).
- [96] T. S. Roy and A. H. Vijay, “A robust anomaly finder based on autoencoders,” [arXiv:1903.02032 \[hep-ph\]](#).
- [97] A. Blance, M. Spannowsky, and P. Waite, “Adversarially-trained autoencoders for robust unsupervised new physics searches,” [arXiv:1905.10384 \[hep-ph\]](#).
- [98] M. Romão Crispim, N. F. Castro, R. Pedro, and T. Vale, “Transferability of Deep Learning Models in Searches for New Physics at Colliders,” *Phys. Rev. D* **101** (2020) no. 3, 035042, [arXiv:1912.04220 \[hep-ph\]](#).
- [99] O. Amram and C. M. Suarez, “Tag N’ Train: a technique to train improved classifiers on unlabeled data,” *JHEP* **01** (2021) 153, [arXiv:2002.12376 \[hep-ph\]](#).
- [100] M. Crispim Romão, N. F. Castro, J. G. Milhano, R. Pedro, and T. Vale, “Use of a generalized energy Mover’s distance in the search for rare phenomena at colliders,” *Eur. Phys. J. C* **81** (2021) no. 2, 192, [arXiv:2004.09360 \[hep-ph\]](#).
- [101] O. Knapp, O. Cerri, G. Dissertori, T. Q. Nguyen, M. Pierini, and J.-R. Vlimant, “Adversarially Learned Anomaly Detection on CMS Open Data: re-discovering the top quark,” *Eur. Phys. J. Plus* **136** (2021) no. 2, 236, [arXiv:2005.01598 \[hep-ex\]](#).

- [102] M. Crispim Romão, N. F. Castro, and R. Pedro, “Finding New Physics without learning about it: Anomaly Detection as a tool for Searches at Colliders,” *Eur. Phys. J. C* **81** (2021) no. 1, 27, [arXiv:2006.05432 \[hep-ph\]](#). [Erratum: *Eur.Phys.J.C* 81, 1020 (2021)].
- [103] T. Cheng, J.-F. Arguin, J. Leissner-Martin, J. Pilette, and T. Golling, “Variational Autoencoders for Anomalous Jet Tagging,” [arXiv:2007.01850 \[hep-ph\]](#).
- [104] C. K. Khosa and V. Sanz, “Anomaly Awareness,” [arXiv:2007.14462 \[cs.LG\]](#).
- [105] P. Thaprasop, K. Zhou, J. Steinheimer, and C. Herold, “Unsupervised Outlier Detection in Heavy-Ion Collisions,” *Phys. Scripta* **96** (2021) no. 6, 064003, [arXiv:2007.15830 \[hep-ex\]](#).
- [106] J. A. Aguilar-Saavedra, F. R. Joaquim, and J. F. Seabra, “Mass Unspecific Supervised Tagging (MUST) for boosted jets,” *JHEP* **03** (2021) 012, [arXiv:2008.12792 \[hep-ph\]](#). [Erratum: *JHEP* 04, 133 (2021)].
- [107] A. A. Pol, V. Berger, G. Cerminara, C. Germain, and M. Pierini, “Anomaly Detection With Conditional Variational Autoencoders,” in *Eighteenth International Conference on Machine Learning and Applications*. 10, 2020. [arXiv:2010.05531 \[cs.LG\]](#).
- [108] M. van Beekveld, S. Caron, L. Hendriks, P. Jackson, A. Leinweber, S. Otten, R. Patrick, R. Ruiz De Austri, M. Santoni, and M. White, “Combining outlier analysis algorithms to identify new physics at the LHC,” *JHEP* **09** (2021) 024, [arXiv:2010.07940 \[hep-ph\]](#).
- [109] S. E. Park, D. Rankin, S.-M. Udrescu, M. Yunus, and P. Harris, “Quasi Anomalous Knowledge: Searching for new physics with embedded knowledge,” *JHEP* **21** (2020) 030, [arXiv:2011.03550 \[hep-ph\]](#).
- [110] P. Chakravarti, M. Kuusela, J. Lei, and L. Wasserman, “Model-Independent Detection of New Physics Signals Using Interpretable Semi-Supervised Classifier Tests,” [arXiv:2102.07679 \[stat.AP\]](#).
- [111] D. A. Faroughy, “Uncovering hidden new physics patterns in collider events using Bayesian probabilistic models,” *PoS ICHEP2020* (2021) 238, [arXiv:2012.08579 \[hep-ph\]](#).
- [112] T. Finke, M. Krämer, A. Morandini, A. Mück, and I. Oleksiyuk, “Autoencoders for unsupervised anomaly detection in high energy physics,” *JHEP* **06** (2021) 161, [arXiv:2104.09051 \[hep-ph\]](#).

- [113] O. Atkinson, A. Bhardwaj, C. Englert, V. S. Ngairangbam, and M. Spannowsky, “Anomaly detection with convolutional Graph Neural Networks,” *JHEP* **08** (2021) 080, [arXiv:2105.07988 \[hep-ph\]](#).
- [114] B. M. Dillon, T. Plehn, C. Sauer, and P. Sorrenson, “Better Latent Spaces for Better Autoencoders,” *SciPost Phys.* **11** (2021) 061, [arXiv:2104.08291 \[hep-ph\]](#).
- [115] A. Kahn, J. Gonski, I. Ochoa, D. Williams, and G. Brooijmans, “Anomalous jet identification via sequence modeling,” *JINST* **16** (2021) no. 08, P08012, [arXiv:2105.09274 \[hep-ph\]](#).
- [116] S. Caron, L. Hendriks, and R. Verheyen, “Rare and Different: Anomaly Scores from a combination of likelihood and out-of-distribution models to detect new physics at the LHC,” [arXiv:2106.10164 \[hep-ph\]](#).
- [117] E. Govorkova *et al.*, “Autoencoders on FPGAs for real-time, unsupervised new physics detection at 40 MHz at the Large Hadron Collider,” [arXiv:2108.03986 \[physics.ins-det\]](#).
- [118] J. Gonski, J. Lai, B. Nachman, and I. Ochoa, “High-dimensional Anomaly Detection with Radiative Return in  $e^+e^-$  Collisions,” [arXiv:2108.13451 \[hep-ph\]](#).
- [119] B. Ostdiek, “Deep Set Auto Encoders for Anomaly Detection in Particle Physics,” *SciPost Phys.* **12** (2022) 045, [arXiv:2109.01695 \[hep-ph\]](#).
- [120] K. Fraser, S. Homiller, R. K. Mishra, B. Ostdiek, and M. D. Schwartz, “Challenges for Unsupervised Anomaly Detection in Particle Physics,” [arXiv:2110.06948 \[hep-ph\]](#).
- [121] A. A. Alemi, I. Fischer, J. V. Dillon, and K. Murphy, “Deep variational information bottleneck,” *CoRR* **abs/1612.00410** (2016) , 1612.00410. <http://arxiv.org/abs/1612.00410>.
- [122] S. Wunsch, R. Friese, R. Wolf, and G. Quast, “Identifying the relevant dependencies of the neural network response on characteristics of the input space,” *Comput. Softw. Big Sci.* **2** (2018) no. 1, 5, [arXiv:1803.08782 \[physics.data-an\]](#).
- [123] T. Roxlo and M. Reece, “Opening the black box of neural nets: case studies in stop/top discrimination,” [arXiv:1804.09278 \[hep-ph\]](#).
- [124] J. Gou, B. Yu, S. J. Maybank, and D. Tao, “Knowledge distillation: A survey,” *CoRR* **abs/2006.05525** (2020) , 2006.05525. <https://arxiv.org/abs/2006.05525>.
- [125] G. Agarwal, L. Hay, I. Iashvili, B. Mannix, C. McLean, M. Morris, S. Rappoccio, and U. Schubert, “Explainable AI for ML jet taggers using expert variables and layerwise relevance propagation,” *JHEP* **05** (2021) 208, [arXiv:2011.13466 \[physics.data-an\]](#).

- [126] F. Mokhtar, R. Kansal, D. Diaz, J. Duarte, J. Pata, M. Pierini, and J.-R. Vlimant, “Explaining machine-learned particle-flow reconstruction,” in *35th Conference on Neural Information Processing Systems*. 11, 2021. [arXiv:2111.12840](#) [physics.data-an].
- [127] J. Craven, V. Jejjala, and A. Kar, “Disentangling a deep learned volume formula,” *JHEP* **06** (2021) 040, [arXiv:2012.03955](#) [hep-th].
- [128] T. Faucett, J. Thaler, and D. Whiteson, “Mapping Machine-Learned Physics into a Human-Readable Space,” *Phys. Rev. D* **103** (2021) no. 3, 036020, [arXiv:2010.11998](#) [hep-ph].
- [129] J. Collado, J. N. Howard, T. Faucett, T. Tong, P. Baldi, and D. Whiteson, “Learning to identify electrons,” *Phys. Rev. D* **103** (2021) no. 11, 116028, [arXiv:2011.01984](#) [physics.data-an].
- [130] J. Collado, K. Bauer, E. Witkowski, T. Faucett, D. Whiteson, and P. Baldi, “Learning to isolate muons,” *JHEP* **21** (2020) 200, [arXiv:2102.02278](#) [physics.data-an].
- [131] P. T. Komiske, E. M. Metodiev, and J. Thaler, “Energy flow polynomials: A complete linear basis for jet substructure,” *JHEP* **04** (2018) 013, [arXiv:1712.07124](#) [hep-ph].
- [132] L. Bradshaw and S. Chang, “Primary Observables for Top Quark Collider Signals,” [arXiv:2304.06063](#) [hep-ph].
- [133] L. Bradshaw, R. K. Mishra, A. Mitridate, and B. Ostdiek, “Mass Agnostic Jet Taggers,” *SciPost Phys.* **8** (2020) no. 1, 011, [arXiv:1908.08959](#) [hep-ph].
- [134] L. Bradshaw, S. Chang, and B. Ostdiek, “Creating simple, interpretable anomaly detectors for new physics in jet substructure,” *Phys. Rev. D* **106** (2022) no. 3, 035014, [arXiv:2203.01343](#) [hep-ph].
- [135] S. Chang and M. A. Luty, “The Higgs Trilinear Coupling and the Scale of New Physics,” *JHEP* **03** (2020) 140, [arXiv:1902.05556](#) [hep-ph].
- [136] F. Abu-Ajamieh, S. Chang, M. Chen, and M. A. Luty, “Higgs coupling measurements and the scale of new physics,” *JHEP* **07** (2021) 056, [arXiv:2009.11293](#) [hep-ph].
- [137] F. Abu-Ajamieh, “The scale of new physics from the Higgs couplings to  $\gamma\gamma$  and  $\gamma Z$ ,” *JHEP* **06** (2022) 091, [arXiv:2112.13529](#) [hep-ph].
- [138] F. Abu-Ajamieh, “The scale of new physics from the Higgs couplings to  $gg$ ,” *Phys. Lett. B* **833** (2022) 137389, [arXiv:2203.07410](#) [hep-ph].

- [139] F. Maltoni, J. M. Niczyporuk, and S. Willenbrock, “The Scale of fermion mass generation,” *Phys. Rev. D* **65** (2002) 033004, [arXiv:hep-ph/0106281](#).
- [140] D. A. Dicus and H.-J. He, “Scales of fermion mass generation and electroweak symmetry breaking,” *Phys. Rev. D* **71** (2005) 093009, [arXiv:hep-ph/0409131](#).
- [141] J. A. Dror, M. Farina, E. Salvioni, and J. Serra, “Strong tW Scattering at the LHC,” *JHEP* **01** (2016) 071, [arXiv:1511.03674 \[hep-ph\]](#).
- [142] A. Falkowski and R. Rattazzi, “Which EFT,” *JHEP* **10** (2019) 255, [arXiv:1902.05936 \[hep-ph\]](#).
- [143] F. Maltoni, L. Mantani, and K. Mimasu, “Top-quark electroweak interactions at high energy,” *JHEP* **10** (2019) 004, [arXiv:1904.05637 \[hep-ph\]](#).
- [144] **CMS** Collaboration, A. Tumasyan *et al.*, “Search for Flavor-Changing Neutral Current Interactions of the Top Quark and Higgs Boson in Final States with Two Photons in Proton-Proton Collisions at  $\sqrt{s} = 13$  TeV,” *Phys. Rev. Lett.* **129** (2022) no. 3, 032001, [arXiv:2111.02219 \[hep-ex\]](#).
- [145] **CMS** Collaboration, A. Tumasyan *et al.*, “Search for flavor-changing neutral current interactions of the top quark and the Higgs boson decaying to a bottom quark-antiquark pair at  $\sqrt{s} = 13$  TeV,” *JHEP* **02** (2022) 169, [arXiv:2112.09734 \[hep-ex\]](#).
- [146] **ATLAS** Collaboration, G. Aad *et al.*, “Search for flavour-changing neutral-current interactions of a top quark and a gluon in pp collisions at  $\sqrt{s} = 13$  TeV with the ATLAS detector,” *Eur. Phys. J. C* **82** (2022) no. 4, 334, [arXiv:2112.01302 \[hep-ex\]](#).
- [147] **ATLAS** Collaboration, “Search for flavour-changing neutral-current couplings between the top quark and the photon with the ATLAS detector at  $\sqrt{s} = 13$  TeV,” [arXiv:2205.02537 \[hep-ex\]](#).
- [148] **ATLAS** Collaboration, “Search for flavour-changing neutral current interactions of the top quark and the Higgs boson in events with a pair of  $\tau$ -leptons in pp collisions at  $\sqrt{s} = 13$  TeV with the ATLAS detector,” [arXiv:2208.11415 \[hep-ex\]](#).
- [149] **CMS** Collaboration, “Search for flavor-changing neutral current interactions of the top quark in final states with a photon and additional jets in proton-proton collisions at  $\sqrt{s}=13$  TeV,” tech. rep., CERN, Geneva, 2023. <https://cds.cern.ch/record/2851857>.
- [150] **ATLAS** Collaboration, “Search for flavor-changing neutral-current couplings between the top quark and the  $Z$  boson with LHC Run 2 proton-proton collisions at  $\sqrt{s} = 13$  TeV with the ATLAS detector,” [arXiv:2301.11605 \[hep-ex\]](#).

- [151] J. A. Aguilar-Saavedra, “A Minimal set of top anomalous couplings,” *Nucl. Phys. B* **812** (2009) 181–204, [arXiv:0811.3842 \[hep-ph\]](#).
- [152] G. Durieux, F. Maltoni, and C. Zhang, “Global approach to top-quark flavor-changing interactions,” *Phys. Rev. D* **91** (2015) no. 7, 074017, [arXiv:1412.7166 \[hep-ph\]](#).
- [153] D. Barducci *et al.*, “Interpreting top-quark LHC measurements in the standard-model effective field theory,” [arXiv:1802.07237 \[hep-ph\]](#).
- [154] W. Altmannshofer, S. Gori, B. V. Lehmann, and J. Zuo, “UV physics from IR features: new prospects from top flavor violation,” [arXiv:2303.00781 \[hep-ph\]](#).
- [155] J. A. Aguilar-Saavedra, “Top flavor-changing neutral interactions: Theoretical expectations and experimental detection,” *Acta Phys. Polon. B* **35** (2004) 2695–2710, [arXiv:hep-ph/0409342](#).
- [156] **Top Quark Working Group** Collaboration, K. Agashe *et al.*, “Working Group Report: Top Quark,” in *Community Summer Study 2013: Snowmass on the Mississippi*. 11, 2013. [arXiv:1311.2028 \[hep-ph\]](#).
- [157] M. Schulze and Y. Soreq, “Pinning down electroweak dipole operators of the top quark,” *Eur. Phys. J. C* **76** (2016) no. 8, 466, [arXiv:1603.08911 \[hep-ph\]](#).
- [158] **CMS** Collaboration, A. Tumasyan *et al.*, “Search for charged-lepton flavor violation in top quark production and decay in pp collisions at  $\sqrt{s} = 13$  TeV,” *JHEP* **06** (2022) 082, [arXiv:2201.07859 \[hep-ex\]](#).
- [159] **CMS** Collaboration, S. Chatrchyan *et al.*, “Search for Baryon Number Violation in Top-Quark Decays,” *Phys. Lett. B* **731** (2014) 173–196, [arXiv:1310.1618 \[hep-ex\]](#).
- [160] W.-S. Hou, M. Nagashima, and A. Soddu, “Baryon number violation involving higher generations,” *Phys. Rev. D* **72** (2005) 095001, [arXiv:hep-ph/0509006](#).
- [161] Z. Dong, G. Durieux, J.-M. Gerard, T. Han, and F. Maltoni, “Baryon number violation at the LHC: the top option,” *Phys. Rev. D* **85** (2012) 016006, [arXiv:1107.3805 \[hep-ph\]](#).
- [162] K. Agashe, P. Du, S. Hong, and R. Sundrum, “Flavor Universal Resonances and Warped Gravity,” *JHEP* **01** (2017) 016, [arXiv:1608.00526 \[hep-ph\]](#).
- [163] K. S. Agashe, J. Collins, P. Du, S. Hong, D. Kim, and R. K. Mishra, “LHC Signals from Cascade Decays of Warped Vector Resonances,” *JHEP* **05** (2017) 078, [arXiv:1612.00047 \[hep-ph\]](#).



- [164] K. Agashe, J. H. Collins, P. Du, S. Hong, D. Kim, and R. K. Mishra, “Dedicated Strategies for Triboson Signals from Cascade Decays of Vector Resonances,” *Phys. Rev.* **D99** (2019) no. 7, 075016, [arXiv:1711.09920 \[hep-ph\]](#).
- [165] K. Agashe, J. H. Collins, P. Du, S. Hong, D. Kim, and R. K. Mishra, “Detecting a Boosted Diboson Resonance,” *JHEP* **11** (2018) 027, [arXiv:1809.07334 \[hep-ph\]](#).
- [166] J. Alwall, R. Frederix, S. Frixione, V. Hirschi, F. Maltoni, O. Mattelaer, H. S. Shao, T. Stelzer, P. Torrielli, and M. Zaro, “The automated computation of tree-level and next-to-leading order differential cross sections, and their matching to parton shower simulations,” *JHEP* **07** (2014) 079, [arXiv:1405.0301 \[hep-ph\]](#).
- [167] T. Sjostrand, S. Mrenna, and P. Z. Skands, “A Brief Introduction to PYTHIA 8.1,” *Comput. Phys. Commun.* **178** (2008) 852–867, [arXiv:0710.3820 \[hep-ph\]](#).
- [168] **DELPHES 3** Collaboration, J. de Favereau, C. Delaere, P. Demin, A. Giammanco, V. Lemaître, A. Mertens, and M. Selvaggi, “DELPHES 3, A modular framework for fast simulation of a generic collider experiment,” *JHEP* **02** (2014) 057, [arXiv:1307.6346 \[hep-ex\]](#).
- [169] S. D. Ellis, C. K. Vermilion, and J. R. Walsh, “Techniques for improved heavy particle searches with jet substructure,” *Phys. Rev.* **D80** (2009) 051501, [arXiv:0903.5081 \[hep-ph\]](#).
- [170] I. W. Stewart, F. J. Tackmann, and W. J. Waalewijn, “N-Jettiness: An Inclusive Event Shape to Veto Jets,” *Phys. Rev. Lett.* **105** (2010) 092002, [arXiv:1004.2489 \[hep-ph\]](#).
- [171] J. A. Aguilar-Saavedra, “Stealth multiboson signals,” *Eur. Phys. J.* **C77** (2017) no. 10, 703, [arXiv:1705.07885 \[hep-ph\]](#).
- [172] K. Datta and A. Larkoski, “How Much Information is in a Jet?,” *JHEP* **06** (2017) 073, [arXiv:1704.08249 \[hep-ph\]](#).
- [173] F. Pedregosa, G. Varoquaux, A. Gramfort, V. Michel, B. Thirion, O. Grisel, M. Blondel, P. Prettenhofer, R. Weiss, V. Dubourg, J. Vanderplas, A. Passos, D. Cournapeau, M. Brucher, M. Perrot, and E. Duchesnay, “Scikit-learn: Machine learning in Python,” *Journal of Machine Learning Research* **12** (2011) 2825–2830.
- [174] F. Chollet *et al.*, “Keras.” <https://keras.io>, 2015.

- [175] M. Abadi, A. Agarwal, P. Barham, E. Brevdo, Z. Chen, C. Citro, G. S. Corrado, A. Davis, J. Dean, M. Devin, S. Ghemawat, I. Goodfellow, A. Harp, G. Irving, M. Isard, Y. Jia, R. Jozefowicz, L. Kaiser, M. Kudlur, J. Levenberg, D. Mané, R. Monga, S. Moore, D. Murray, C. Olah, M. Schuster, J. Shlens, B. Steiner, I. Sutskever, K. Talwar, P. Tucker, V. Vanhoucke, V. Vasudevan, F. Viégas, O. Vinyals, P. Warden, M. Wattenberg, M. Wicke, Y. Yu, and X. Zheng, “TensorFlow: Large-scale machine learning on heterogeneous systems,” 2015. <https://www.tensorflow.org/>. Software available from tensorflow.org.
- [176] D. P. Kingma and J. Ba, “Adam: A method for stochastic optimization,” *arXiv:1412.6980* (2014) .
- [177] A. Andreassen and B. Nachman, “Neural Networks for Full Phase-space Reweighting and Parameter Tuning,” [arXiv:1907.08209](https://arxiv.org/abs/1907.08209) [hep-ph].
- [178] A. Rogozhnikov, A. Bukva, V. V. Gligorov, A. Ustyuzhanin, and M. Williams, “New approaches for boosting to uniformity,” *JINST* **10** (2015) no. 03, T03002, [arXiv:1410.4140](https://arxiv.org/abs/1410.4140) [hep-ex].
- [179] J. Leissner-Martin, T. Cheng, and J.-F. Arguin, “QCD Jet Samples with Particle Flow Constituents,” July, 2020. <https://doi.org/10.5281/zenodo.4641460>.
- [180] T. Cheng, “Test Sets for Jet Anomaly Detection at the LHC,” Mar., 2021. <https://doi.org/10.5281/zenodo.4614656>.
- [181] V. Mikuni, B. Nachman, and D. Shih, “Online-compatible Unsupervised Non-resonant Anomaly Detection,” [arXiv:2111.06417](https://arxiv.org/abs/2111.06417) [cs.LG].
- [182] <https://energyflow.network>.
- [183] D.-A. Clevert, T. Unterthiner, and S. Hochreiter, “Fast and accurate deep network learning by exponential linear units (elus),” 2016.
- [184] A. J. Larkoski, G. P. Salam, and J. Thaler, “Energy Correlation Functions for Jet Substructure,” *JHEP* **06** (2013) 108, [arXiv:1305.0007](https://arxiv.org/abs/1305.0007) [hep-ph].
- [185] A. J. Larkoski, I. Moulton, and D. Neill, “Power Counting to Better Jet Observables,” *JHEP* **12** (2014) 009, [arXiv:1409.6298](https://arxiv.org/abs/1409.6298) [hep-ph].
- [186] A. Banfi, G. P. Salam, and G. Zanderighi, “Principles of general final-state resummation and automated implementation,” *JHEP* **03** (2005) 073, [arXiv:hep-ph/0407286](https://arxiv.org/abs/hep-ph/0407286).
- [187] G. Gur-Ari, M. Papucci, and G. Perez, “Classification of Energy Flow Observables in Narrow Jets,” [arXiv:1101.2905](https://arxiv.org/abs/1101.2905) [hep-ph].

- [188] M. Jankowiak and A. J. Larkoski, “Jet Substructure Without Trees,” *JHEP* **06** (2011) 057, arXiv:1104.1646 [hep-ph].
- [189] I. Moutl, L. Necib, and J. Thaler, “New Angles on Energy Correlation Functions,” *JHEP* **12** (2016) 153, arXiv:1609.07483 [hep-ph].
- [190] CMS Collaboration, S. Chatrchyan *et al.*, “Search for a Higgs boson in the decay channel  $H$  to  $ZZ^{(*)}$  to  $q$  qbar  $\ell^- \ell^+$  in  $pp$  collisions at  $\sqrt{s} = 7$  TeV,” *JHEP* **04** (2012) 036, arXiv:1202.1416 [hep-ex].
- [191] A. J. Larkoski, J. Thaler, and W. J. Waalewijn, “Gaining (Mutual) Information about Quark/Gluon Discrimination,” *JHEP* **11** (2014) 129, arXiv:1408.3122 [hep-ph].
- [192] P. Gras, S. Höche, D. Kar, A. Larkoski, L. Lönnblad, S. Plätzer, A. Siódmok, P. Skands, G. Soyez, and J. Thaler, “Systematics of quark/gluon tagging,” *JHEP* **07** (2017) 091, arXiv:1704.03878 [hep-ph].
- [193] T. Sjöstrand, S. Ask, J. R. Christiansen, R. Corke, N. Desai, P. Ilten, S. Mrenna, S. Prestel, C. O. Rasmussen, and P. Z. Skands, “An introduction to PYTHIA 8.2,” *Comput. Phys. Commun.* **191** (2015) 159–177, arXiv:1410.3012 [hep-ph].
- [194] M. Cacciari, G. P. Salam, and G. Soyez, “FastJet User Manual,” *Eur. Phys. J. C* **72** (2012) 1896, arXiv:1111.6097 [hep-ph].
- [195] M. Cacciari and G. P. Salam, “Dispelling the  $N^3$  myth for the  $k_t$  jet-finder,” *Phys. Lett. B* **641** (2006) 57–61, arXiv:hep-ph/0512210.
- [196] M. Cacciari, G. P. Salam, and G. Soyez, “The anti- $k_t$  jet clustering algorithm,” *JHEP* **04** (2008) 063, arXiv:0802.1189 [hep-ph].
- [197] D. P. Kingma and J. Ba, “Adam: A Method for Stochastic Optimization,” arXiv:1412.6980 [cs.LG].